Mean-Field Stationary Diffusion: Polymers in steady-state systems

Promotor	prof.dr. G.J. Fleer persoonlijk hoogleraar bij de leerstoelgroep fysische chemie en kolloïdkunde, Wageningen Universiteit.
Copromotor	dr.ir. F.A.M. Leermakers universitair hoofddocent bij de leerstoelgroep fysische chemie en kolloïdkunde, Wageningen Universiteit.
Promotiecommissie	prof.dr. J.J.M. Slot Universiteit Twente en DSM-Research, Geleen.
	prof.dr. W.J. Briels Universiteit Twente.
	dr. G.T. Barkema Universiteit Utrecht.
	dr. J.H.J. van Opheusden Wageningen Universiteit.

Mean-Field Stationary Diffusion: Polymers in steady-state systems

Sonja Maria Scheinhardt-Engels

Proefschrift
ter verkrijging van de graad van doctor
op gezag van de rector magnificus
van Wageningen Universiteit,
prof.dr.ir. L. Speelman,
in het openbaar te verdedigen
op dinsdag 1 juni 2004
des namiddags te half twee in de Aula.

ISBN 90 8504 061 2

Voorwoord

Dit voorwoord wil ik graag benutten voor het bedanken van een aantal mensen die tijdens mijn promotieperiode in belangrijke mate hebben bijgedragen aan het tot stand brengen van dit proefschrift. Sommigen droegen hier heel direct aan bij, anderen meer indirect door het creëren van de juiste omgeving om mijn werk zo plezierig mogelijk te kunnen verrichten.

De meest directe bijdrage kwam natuurlijk van mijn begeleiders Frans Leermakers en Gerard Fleer. Frans zette de ruwe lijn van het onderzoek uit en kwam met allerlei ideeën voor verdere uitdieping. Gerard zette de puntjes op de i door zijn gedegen en kritische lezing van alle versies. Hij had altijd aanwijzingen voor een betere presentatie. In het geval van hoofdstuk 4 leidde dit tot een geheel ander verhaal, uiteindelijk toch nog zonder enige ellipsvergelijking. Frans en Gerard, bedankt voor alle hulp.

Ondanks de grondige lezing door Gerard droeg één van de commissieleden, Joost van Opheusden, nog enkele tekstuele verbeteringen aan, waar ik dankbaar gebruik van gemaakt heb. Ik wil ook graag de overige leden bedanken voor het zitting nemen in de promotiecommissie.

Jos van den Oever heeft zowel een directe als indirecte bijdrage aan dit proefschrift gehad. Zonder computer zou ik niet ver gekomen zijn en de grote rekenkracht die Jos verzamelde door alle PC's ingenieus te laten samenwerken heeft het een en ander mooi versneld. Ik heb ook vaak dankbaar gebruik gemaakt van al zijn andere computertips. Maar Jos, je indirecte bijdrage was ook belangrijk. Als kamergenoten hebben we de bekende AIO-frustraties gedeeld, maar ook veel gezelligheid gehad.

De werkomgeving van het laboratorium beviel me erg goed. Deze heb ik in het laatste jaar vanwege telewerken wel gemist. De labuitjes, de Veluweloop, het voetballen, roeien en fietsen waren mooie aanvullingen op de prettige contacten tijdens de werktijden. Hieraan hebben alle labgenoten bijgedragen.

Goede omstandigheden buiten de werkplek droegen indirect ook in belangrijke mate bij tot dit proefschrift. In het laatste jaar van mijn AIO-tijd, waarin de privé-omstandigheden minder goed waren, heb ik belangrijke steun van mijn familie (broers, zus, ooms en tantes) kunnen ervaren. Bedankt allemaal!

Mijn ouders hebben mij altijd vrij gelaten in alle keuzes die ik maakte. Nooit heb ik enige prestatiedrang ervaren. Die vrijheid en onvoorwaardelijke steun zijn essentiële ingredienten om promotiestress te relativeren. Ik had graag via deze weg mijn vader ook willen bedanken voor zijn aanstekelijke enthousiasme voor de muziek

die mij in het 'muziekwereldje' heeft gebracht. Gedurende de gehele AIO-tijd heeft dat muziekwereldje mij prettige afleiding gegeven.

In het studentenorkest van Enschede deelde ik met Bärbel niet alleen de muzieklessenaar, maar ook de laatste loodjes naar onze promoties. Edda, Wim en Niko zorgden, behalve voor gezellige weekends, soms ook ongemerkt voor een spurt in mijn onderzoek.

Degene die al mijn 'ups' en 'downs' echt heeft ondergaan is Werner. Vooral tijdens zo'n down-moment leek ik maar weinig waarde te hechten aan je vertrouwen in mijn onderzoek, maar het is toch heel belangrijk geweest. Dank je wel.

April 2004, Sonja.

Contents

Chapter 1

Introduction

1.1 Aim of this study

Much time is spent waiting for a system to reach equilibrium. In equilibrium, all properties such as temperature, pressure, and chemical potentials are constant in time and space. Equilibrium is the final state of all isolated systems and therefore of intrinsic interest. Moreover, equilibrium is a well-defined state and the most easy to understand. But what information can be obtained while waiting for a system to reach equilibrium? It is of great importance to understand how the molecules in a system move, swap, rotate, fold and unfold before they attain their equilibrium state. In other words, what are the dynamics of a system between its initial off-equilibrium state and its final equilibrium?

To illustrate the relevance of this question, take the example of a nicotine patch. This patch helps people who attempt to stop smoking to overcome the physical withdrawal symptoms. Initially the patch contains a certain amount of nicotine. The patch must be worn like a plaster onto the skin. The nicotine can then be transported through the skin into the body. If nothing would happen to the nicotine within the body, the equilibrium state would be the same concentration of nicotine within the patch and the body. However, the nicotine is metabolized fairly fast within the body so that the transport through the skin continues until the patch has discharged. For the development of such a nicotine patch, or of any other plaster that releases drugs in a steady flow, it is far more interesting to understand how the transport takes place than to describe the eventual (trivial) equilibrium state. The dynamics of the active molecules that diffuse through the various barriers (plaster membrane, skin, arterial cell membranes) are essential for the design of the patch material.

Transport processes are obvious examples to illustrate the relevance of investigations on molecular dynamics. However, even when the equilibrium state is the main goal, the dynamics between the initial state and the final equilibrium is of great importance. Understanding the dynamical process, such as the identification of the rate-limiting steps, may allow the manipulation and optimization of the time

needed to reach the desired equilibrium. For example, knowledge about the folding dynamics of catalysing enzymes helps to select the best process conditions for bread-making or industrial textile-treatments [1]. Although all systems have only one well-defined *thermodynamic* equilibrium, we could (when the dynamics of the process are understood) select the process conditions such that a distinct *mechanical* equilibrium state is reached. This may dramatically change the outcome of the process; a difference as large as the difference between graphite and diamond! Graphite and diamond are both crystalline forms of carbon. A large energy barrier must be overcome to produce graphite out of diamond. Nevertheless, graphite is the thermodynamic equilibrium and it will never spontaneously transform into any other state such as diamond. Many other compounds may form various crystal morphologies depending on the process conditions; only one of those is the thermodynamic equilibrium state. When the dynamics of crystal growth are understood, one may predict the final (mechanically and/or thermodynamically stable) crystal morphology. This knowledge may for example be applied to prevent the formation of obstructing crystals in industrial pipes.

The aim of the research described in this thesis is to develop a theoretical model by which not only the (thermodynamic) equilibrium can be studied, but also the dynamical process towards equilibrium. The equilibrium state is an appropriate starting point in the development of such a model. We may consider to extend an equilibrium model directly into a dynamical model covering the whole process between any arbitrarily chosen initial state and the final equilibrium. A dynamical model would describe the off-equilibrium state in which all properties such as concentrations and temperature may change both in time and in space. For such a model we would have to make assumptions about molecular motions, have an idea about the time interval in which physically critical steps occur (in order to allow time-discretization), and select interesting systems that show relevant and interesting dynamical features within a reasonable computation time. The development of a full dynamical model would be overambitious, because the properties of a system at a given time depend heavily on its history. There are however dynamical systems that do not have such history dependence, which are known as stationary states. In the stationary state the chemical potentials, temperature, pressure, and other properties may change in space, but not in time. The fluxes in stationary systems are constant in space as well. As a first (modest) step towards a full dynamical model, we aim at *the extension of an existing equilibrium model to a stationary state model*. As in a dynamical model, the stationary state model includes assumptions about the molecular motions. As in an equilibrium model, the result of the stationary state calculation is one well-defined state. In contrast to more complete dynamical models, the stationary state model does not need any discretization of the physical time and the computation time is short, comparable to the computation time for the equilibrium model.

In the following Section 1.2 we will define the stationary state and present some examples of stationary states. In Section 1.3 the equilibrium Scheutjens-Fleer model, which is the starting point of our stationary state model, is described. We

preview our stationary state model and the differences between that model and the equilibrium model in Section 1.4. Section 1.5 presents an outline of this thesis. After development of the stationary state model, we applied it to three-component systems for which we also calculated the equilibrium properties in order to understand and select interesting stationary systems.

1.2 Stationary states

1.2.1 General

All systems that are exposed to a time-independent input of some extra energy will develop stationary off-equilibrium states. There are many examples of systems that are in a stationary state. In industrial applications, fluids are driven by pumps in a stationary manner through pipes into continuously operating reaction vessels. Within these vessels the temperature is kept constant by means of a stationary heat flux in the heat exchanger. In living organisms, stationary state mechanisms are essential for the homeostasis, i.e., the maintenance of constant internal compositions[1]. One example of homeostasis is the electrolyte contents of a human cell. The cell interior needs a constant and specified concentration of sodium and potassium ions to operate properly. The exterior of the cell, for example the blood plasma, requires a much lower potassium concentration than the interior of the cell. Due to the concentration difference, the potassium ions diffuse passively out of the cell. This transport is opposed by the sodium/potassium pump which consumes energy to transport potassium back into the cell. This sodium/potassium pump is a stationary state mechanism which maintains the necessary concentration gradient of potassium over the cell membrane. Numerous metabolic pathways allow the maintenance of stationary concentration gradients of other components within the human body.

The general characteristic of stationary states (which are alternatively called 'steady states') is that all macroscopic quantities are constant in time. Thus, properties such as concentration gradients, temperature gradients and fluxes do not change without external intervention. The velocity of a fluid pumped through an industrial pipe may be stationary as long as nobody intervenes by adjusting the energy input that is provided by the pumps. The diffusion of potassium through the cell membrane is stationary until the sodium/potassium pump fails or until the potassium concentration in the blood plasma changes as a result of, for example, dietary intake. In other words, stationary states are characterized by a *constant* input of energy or material. If the input is suddenly raised or lowered, the stationary state is disturbed (although, after some time, a new but different stationary state will be established). The energy or material input could also be *constant and zero*. In that case we have a special stationary state, namely the equilibrium state. The

[1] In nature true stationary states do not occur, but in good approximation they may be treated as such.

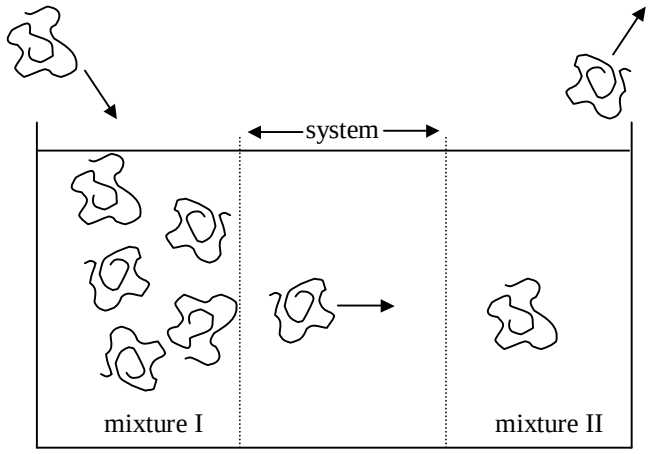

Figure 1.1. The stationary state considered in this thesis. Two bulk mixtures of constant (but different) compositions are brought into contact. The compositions of the bulk mixtures are maintained by continuous input and output of material. We focus on the transition region between the two bulk mixtures, denoted by 'system' in this figure.

interior and exterior of a cell are in equilibrium if they have equal concentrations of potassium and other components (assuming that the cell membrane is equally permeable to all ions and molecules occurring in the human body). No energy is needed to maintain such an equilibrium, as follows from the first and second laws of thermodynamics.

1.2.2 Stationary polymer systems

In this thesis, we concentrate on a particular type of off-equilibrium steady states, namely a system as presented in Figure 1.1. Two bulk mixtures with different compositions are brought into contact. Material will diffuse from the concentrated bulk mixture to the dilute bulk mixture. The compositions of the bulk mixtures are kept constant by continuous supply of material into the concentrated bulk mixture and continuous removal of material from the dilute bulk mixture. After some time, the region between the two bulk mixtures will show a stationary concentration gradient of the diffusing material. This is the region of interest. We aim at the development of a theoretical model by which we can investigate the concentration profiles within this region, also for more complex systems in which various compounds may diffuse in opposite directions. A system as depicted in Figure 1.1 models for example diffusion-limited catalysis: reactants diffuse from a large bulk solution towards the catalyst surface at which the concentration of the reactant remains constant through the reaction that takes place. Similar phenomena are relevant for electrode surfaces where components are reduced or oxidised.

The diffusing molecules that we are interested in are polymers. Polymers are

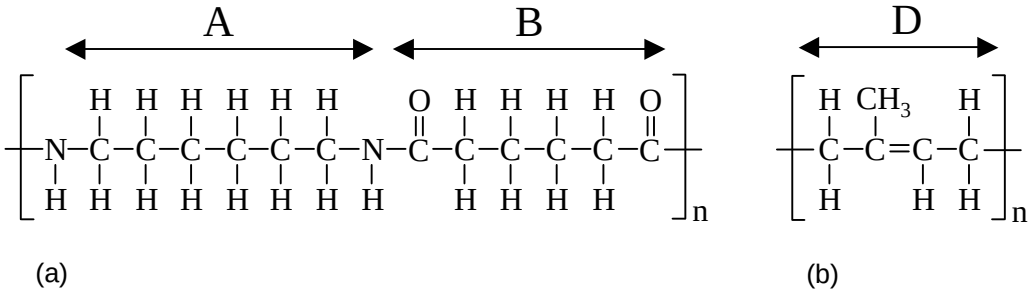

Figure 1.2. (a): Molecular structure of a copolymer (nylon), consisting of two types of monomers (A and B). (b): Molecular structure of a homopolymer composed of monomer D (natural rubber). The subscript n is the number of repeat units which is typically large ($n >> 1$).

long chains of repeating units, the monomers. A famous example of polymer material is the first synthetic polymer fibre: nylon. This strong material, used for panty hoses, shirts, and many other applications, was discovered when people searched for a substitute of natural silk. Figure 1.2a shows the molecular structure of this polymer. The nylon chain is an alternating sequence of two different monomers; it is therefore called a copolymer. Copolymer chains may have a much higher complexity than in nylon. Some natural copolymers, such as DNA or enzymes, appear to have a random sequence of various monomers. However, the sequence of monomers within these 'polymers of life' is critically defined for a proper functioning. Nature also produces much simpler polymers: natural rubber is an example of a homopolymer. It consists of only one monomer (see Figure 1.2b). Industrial polymers (plastics) are often homopolymers; however, the modern trend is towards so-called functional polymers with a more complex structure. Despite the simple molecular structure, homopolymers are intriguing objects of study. They reflect several universal characteristics of polymers, such as viscosity, strength, and elasticity.

1.2.3 Hindered polymer diffusion

In this study we focus on diffusing homopolymers. The theoretical model we developed to study stationary fluxes and concentration profiles also allows investigation of the conformations ('folding behaviour') of the homopolymers. This is particularly interesting when the diffusion of polymer chains is hindered due to the presence of a barrier, such as a membrane. Hindered diffusion occurs for example in drug-releasing plasters or in gel electrophoresis. In electrophoresis a mixture of different polymers is separated into its components by letting the polymers diffuse through a gel-like material in an electric field. The gel hinders the diffusion. Even in the absence of an electric field the various components could still be separated from each other in the gel when the various components have different flexibilities. Flexible chains will diffuse more rapidly through the labyrinth of the gel than stiff chains.

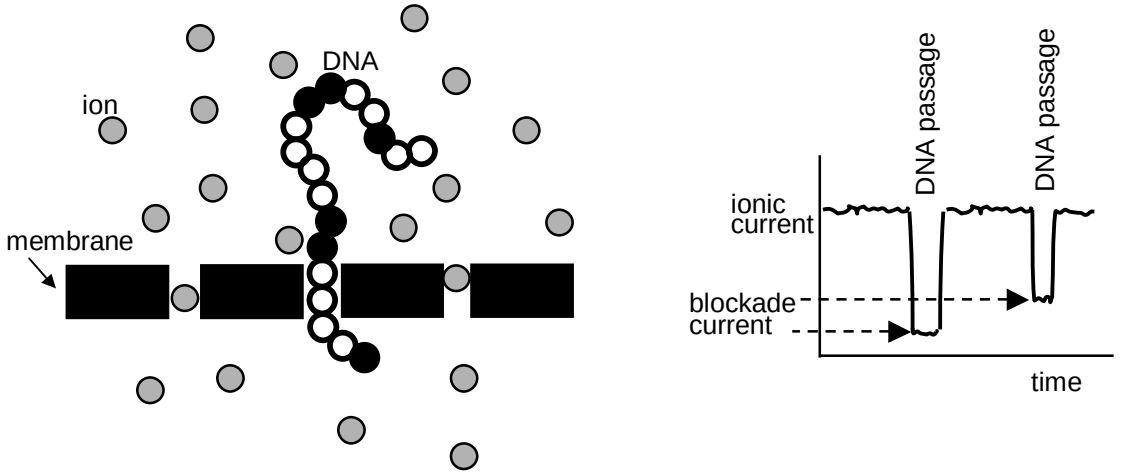

Figure 1.3. The reading of the genetic code written in the sequence of monomers in DNA-chains. The DNA-molecule blocks the passage of ions through the membrane, which can be measured as a drop in the ionic current during a specific time interval.

After some time, flexible chains have diffused further than stiff chains. The flexibility of a chain is reflected by the folding probabilities. Therefore, investigation of chain conformations during hindered diffusion is of interest for gel electrophoresis and some derived separation methods [2, 3]. In this thesis the driving force for diffusion does not arise from an electric field but from chemical potential differences. However, further extensions to our model are possible to describe the diffusion of charged molecules in an electric field.

Hindered chain diffusion is also a promising tool for the investigation of human genes. Genetic information is encoded by DNA, which is a sophisticated copolymer which nevertheless is made up of only four different monomers. The genetic code is the sequence of these four monomers within a DNA-chain. It has been suggested that the genetic code could be found by investigating the diffusion of the DNA-chain through a membrane [4]-[6]. This suggestion arose after diffusion experiments on homopolymers and simple copolymers. In these experiments an electric potential is applied over a membrane. The membrane is placed in an ionic solution as depicted in Figure 1.3*a*. Ions will diffuse through the membrane as a result of the electric field, and the ionic current can be measured. When a polymer chain is introduced at one side of the membrane, it may diffuse through the membrane and thereby either partially or completely block the ionic current during some time interval (see Figure 1.3*b*). It has been found in these experiments that the configuration of monomers within the polymer chain and the chain length determine the characteristics of the 'blockade current'. In other words, by recording the blockade current, it should be possible to predict the sequence of monomers in the chain. However, such predictions are only possible when the general physics of hindered polymer diffusion and its relation to chain folding are understood in more detail. The theoretical model

described in this thesis allows, in principle, a systematic study of the characteristics of hindered diffusion. This method for DNA-sequencing may therefore be a promising application for our stationary polymer diffusion model.

1.3 Equilibrium model

We aim at the development of a theoretical model for stationary systems. As discussed in Section 1.1 an equilibrium model might serve as an appropriate starting point. Since we are interested in polymer systems one might think of the well-known Flory-Huggins polymer theory as such a starting point [7, 8]. The Flory-Huggins theory derives thermodynamic quantities, for example phase diagrams, from the combinatorial entropy of mixing in combination with energetic contact interactions. However, this theory only applies to homogeneous bulk systems, whereas our stationary polymer model must allow the development of concentration gradients in the system. An equilibrium polymer model which accounts for inhomogeneities is therefore a more appropriate starting point for our objectives; this extension of the Flory-Huggins towards gradients was formulated by Scheutjens and Fleer. This generalisation was developed around 1980 and since then successfully extended and modified for a wide variety of systems [9]-[17]. All those systems have in common that they consider the equilibrium properties of polymers in blends or solutions, accounting for gradients near a surface or an interface. Examples of the properties that can be derived from calculations by the Scheutjens-Fleer model are concentration profiles, adsorption isotherms, adsorption layer structures, compositions of coexisting phases, characteristic thermodynamic quantities, and elastic (bending) properties of membranes, all at equilibrium.

As stated above, the Scheutjens-Fleer model is a generalisation of the Flory-Huggins theory. In both approaches, the free energy is a function of the distribution of the molecules. In the Flory-Huggins model, applying to bulk phases, this distribution is homogeneous. The Scheutjens-Fleer model allows the volume fractions of the components to be a function of position within the system. The objective of Scheutjens-Fleer calculations is to find the (average) distribution of the molecules (polymers, solvent, ions) in space for the equilibrium state. By an iterative procedure, the molecules are rearranged, that is, their concentration profiles and conformations are adjusted, until the minimum of the free energy is obtained. This state with minimum free energy defines the equilibrium; such a state does not consume or produce energy.

The positions of the molecules determine the force field that describes the forces acting on each molecule in the system. In other words, a Scheutjens-Fleer calculation starts with a guess for the distribution of the molecules in the system. The force field that results from this distribution gives rise to redistributions of the molecules in order to minimize the total free energy of the system. This redistribution, performed iteratively by the Scheutjens-Fleer method, gives rise to new force fields that again force the molecules to rearrange. The iterative procedure finishes when self-

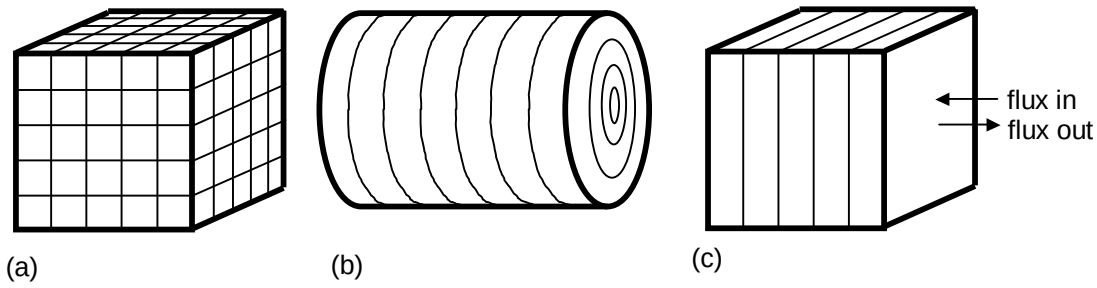

Figure 1.4. Examples of lattices in the equilibrium Scheutjens-Fleer model. (a): Three-dimensional cubic lattice. (b): Cylindrical lattice that reduces the three-dimensional space to two-dimensional calculations. (c): Lattice that reduces the three-dimensional space to one-dimensional calculations. This lattice has been used throughout this thesis. Indicated are the directions of material fluxes in our steady-state calculations.

consistency is obtained between the force field and the molecular distribution that corresponds to minimum free energy. The Scheutjens-Fleer model only considers *averaged* forces and therefore requires and calculates only the average distribution of the molecules in the system. This is called the mean-field approach. The average distribution is given in terms of the probabilities to find (portions of) the molecules at a specified position in space.

A few approximations are made to enable efficient calculations with the monomeric length as the yard-stick. First, the space to be filled with molecules is discretized as in a lattice. Thus, instead of referring to a particular position by its exact (continuum) coordinates, one refers to a lattice site. This allows discretization of the calculations. Moreover, it is straightforward to incorporate incompressibility constraints in lattice models, simply by requiring that all lattice layers are, on average, fully occupied by molecules. Figure 1.4 shows a few examples of lattices that can be used in the Scheutjens-Fleer model. All lattices allow three-dimensional folding of molecules, but in some lattices the concentrations are evaluated in only two dimensions (Figure 1.4b) or even in only one dimension (Figure 1.4c). In this thesis we use a lattice as depicted in Figure 1.4c, where only parallel layers are accounted for. This means that we compute only the average properties (volume fractions, interactions) in each lattice layer, which dramatically reduces the computation time and computer memory demands, and which allows the calculation of (only) the average molecular distributions. The constraint of incompressibility is translated into the requirement that the sum of all volume fractions within one lattice layer equals unity.

The Scheutjens-Fleer model efficiently describes the polymers as chains of segments (see Figure 1.5). Each segment may represent a few monomers. Thus the information about monomer properties is 'summarised' by the properties of such a segment. The properties of a segment are its ranking number in the chain and its interaction with other segments. (The size of a segment is always taken to be equal

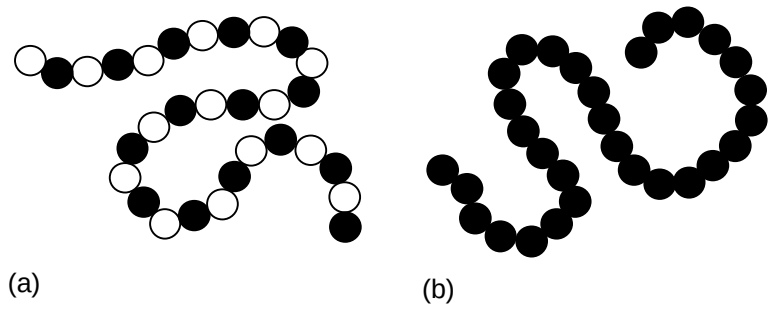

Figure 1.5. Representations of polymers by chains as in the Scheutjens-Fleer model. (a): An alternating copolymer (e.g. nylon, see Figure 1.2a). (b): A homopolymer (e.g. natural rubber, see Figure 1.2b).

to the size of one lattice site or the width of one lattice layer). For example, a group of monomers that together form a polar head of a copolymer may be represented by one segment of type A. The apolar tail of this copolymer may be represented by a number of segments of type B. Then the polymer chain is a surfactant given by the sequence A-B-B-B-B-B.... Segment types A are defined to have favourable energetic interactions with polar solvent segments, whereas segment types B will avoid contacts with those solvent segments. In all cases chain connectivity is maintained rigorously.

In the standard version of the model, the Scheutjens-Fleer model only includes nearest-neighbour energetic interactions between the segments (as in the Flory-Huggins theory). Then, segments residing in lattice layer z are assumed to feel only interactions with segments in the layers $z-1$, z, and $z+1$. As an example, the nearest-neighbour contacts for a segment in a two-dimensional space are indicated in Figure 1.6a. The interactions of a central segment A in layer $z=3$ with its neighbours is indicated by the arrows. This central segment in this example has three $A-B$ interactions and one $A-A$ interaction. Each $A-B$ contact results in a contribution χ_{AB} to the total energy of the central segment. The $A-A$ contact has the contribution χ_{AA}. (In fact, χ_{ij} is the so-called Flory-Huggins parameter which is defined to be zero for $i=j$ [18]). As illustrated in Figure 1.4c, in a layer system the exact positions of segments within layers $z-1$, z and $z+1$ are unknown; only the volume fractions of segment types in each layer are exactly defined. A segment in layer z is therefore assumed to interact with all segment types that occur in the layers $z-1$, z, and $z+1$, but mainly with the segment type that has the highest volume fraction in these layers. As discussed above, this is called the 'mean-field approach'; only the average force field is taken into account in the calculation of interactions. This approach is illustrated in Figure 1.6b for the two-dimensional space that corresponds to the lattice in Figure 1.6a. In the mean-field approach the central segment interacts mainly with A-segments in layer $z+1$, while the central segment in Figure 1.6a happens to interact with the B-segment in layer $z+1$. Due to the high volume fraction of A-segments in layer $z+1$, the central segment would

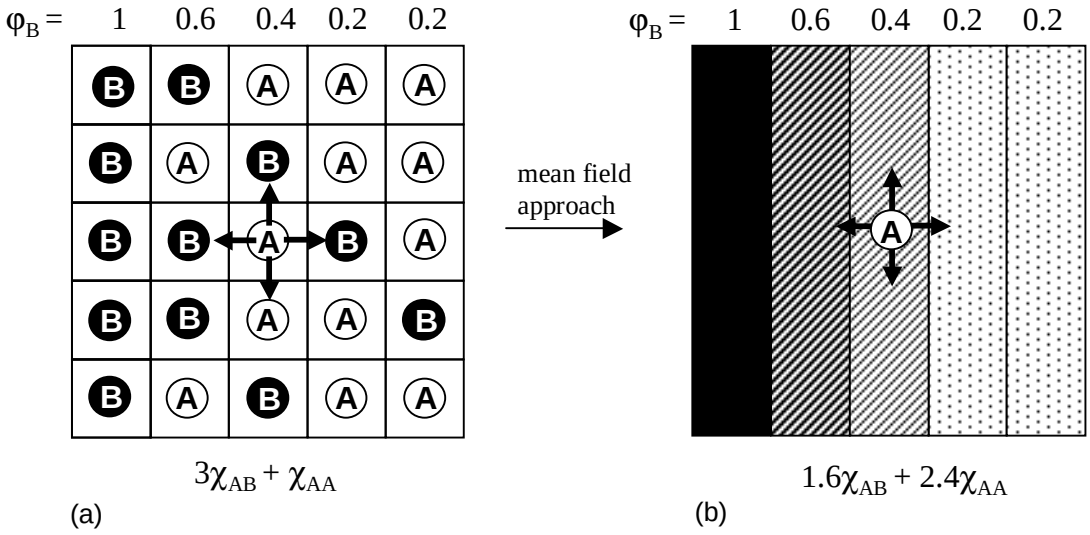

Figure 1.6. Nearest-neighbour interactions in two-dimensional space. (a): The central segment interacts with four segments. The volume fractions of B-segments are indicated as well as the four contributions to the total interaction energy of the central segment. (b): Mean-field approach for the same system as in (a). Again the contributions to the interaction energy are given.

have a higher probability to interact with A-segments than with the B-segment in layer $z+1$.

The optimal distribution of the molecules in the system is not only determined by the nearest-neighbour interactions, but also by the chain connectivities that highly affect the conformational entropy. The Scheutjens-Fleer results yield information about the preferred conformations (the way of folding) of the polymers in various regions of the system. For example, polymer conformations near an adsorbing surface will differ from the conformations in the bulk solution further from the surface. For an efficient calculation of the equilibrium distribution of the molecules, the Scheutjens-Fleer model allows (in its simplest form) backfolding of the polymer chains. That means that if the segment with ranking number s is in layer z, and the next segment $s+1$ is in layer $z+1$, then segment $s+2$ may be found in layer z as well (or in $z+1$ or $z+2$). Such exceptionally flexible chains greatly reduce the memory demands and computer calculation times, since one does not have to keep track of previous bond directions in order to decide on the direction of the next bond. Backfolding may be limited or prevented by some adjustments to the basic Scheutjens-Fleer model that reduce the chain flexibility [17].

The probability to find the chain segment with ranking number s in layer z is calculated in the standard Scheutjens-Fleer model by means of a propagation scheme that is closely connected to the Edwards diffusion equation [15]. Starting from the probability to find segment $s = 1$ in layer z_1, the propagation scheme

determines the probabilities to find segments $s = 2, 3, 4, ...$ of the same chain in any layer of the system. The Edwards diffusion equation yields a continuum description of the path followed by a diffusing Brownian particle. The diffusion path in the Edwards diffusion equation corresponds to the contour of the polymer that results from Scheutjens-Fleer's propagation scheme. In fact, the Scheutjens-Fleer model is a discrete version of the Edwards diffusion equation.

1.4 The MFSD-model

Our objective is to extend the equilibrium Scheutjens-Fleer model to a stationary model in which the polymers are allowed to diffuse between two bulk mixtures with arbitrarily chosen time-invariant compositions. The system of our interest is sketched in Figure 1.1. Instead of calculating the average molecular distribution that results in minimum free energy (as in the Scheutjens-Fleer model), we wish to calculate the average distribution that is consistent with constant, non-zero, material fluxes between the two bulk mixtures, whereby it is assumed that the compositions of the bulk mixtures are maintained by sufficient supply and removal of material. We call this extended Scheutjens-Fleer model the Mean-Field Stationary Diffusion (MFSD) model.

As in the Scheutjens-Fleer model, the system (which is the region between the two bulk mixtures) is described by a lattice. A lattice as depicted in Figure 1.4*c* is used throughout this thesis. The polymers are modelled as chains of connected segments. Only nearest-neighbour energetic interactions, described by the average force field, are taken into account. Chain connectivity is maintained and immediate step reversals (back-folding) are allowed. Unlike the Scheutjens-Fleer model, the MFSD-model does not only require that the system is incompressible, but also that the volume fractions are consistent with stationary diffusion and with the imposed compositions of the bulk mixtures. The polymer diffusion is stationary when the fluxes are constant in time and in space. Therefore, to obtain the stationary volume fraction profiles, we need to find expressions for the segmental fluxes. (Obviously, the same flux expressions could be applied if we would like to wait for equilibrium, that is, if our MFSD-model would be extended towards a dynamic model that follows the motions of molecules in a system that evolves towards equilibrium).

The flux expressions can only be found if some mechanism for the diffusion of segments is specified. We adopt the 'swap-mechanism', in which we assume that diffusion occurs through a sequence of position interchanges. The swap-mechanism is depicted in Figure 1.7. In this figure segment A diffuses to the right and segments B and C diffuse to the left, just by swapping their positions. The swapping process is directed by the driving force acting on each segment type that may possibly be involved in the swaps. The driving force for a particular segment type may vary as a function of position. The larger the driving force, the stronger the segment is pushed away. The driving force also determines the direction in which the segment is pushed; segments will usually be pushed towards a lattice layer in which their

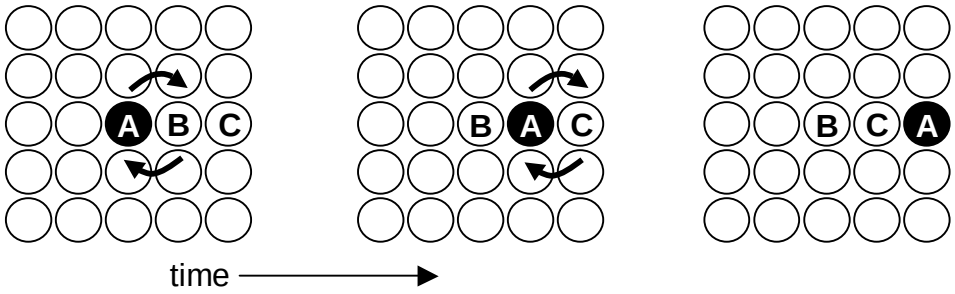

Figure 1.7. Two steps in the swapping diffusion mechanism. In the first step, segment A diffuses to the right and segment B to the left by interchanging their positions. Segment A diffuses further in the second step, and segment C diffuses to the left.

concentration is lower. However, contact interactions do also play a role. Some segment types may be intrinsically slower than others. The intrinsic segment mobility depends on the friction with other segments and on the length of the chain to which the segment belongs. The longer the chain, the slower the motion of the segments.

When more than two segment types are present in the system, a complex interplay between the driving forces on all segment types determines which segments interchange their positions. It is therefore usually difficult to predict the outcome of the diffusion process, in particular on the length scale of segments. We distinguish two theories that describe the complex interplay of the driving forces. The first is the slow-mode model [19]. According to this theory, a segment A prefers to swap positions with the segment type that has the highest mobility. The second approach is the fast-mode model [20, 21]. Here it is assumed that there exists a drift flux for all segment types: segments A are dragged along with the motions of other segment types. The resulting diffusion profiles may be highly dependent on the choice between either the fast-mode or slow-mode models. Some experiments are in favour of the slow-mode results [22, 23], others are more accurately represented by fast-mode results [24]-[27]. We have translated both theories, originally derived for binary diffusion, to multi-component diffusion in the framework of the Scheutjens-Fleer model, yielding flux equations that are the essential ingredients for the MFSD-method.

We do not only use the MFSD-model to calculate the stationary fluxes or concentration profiles between two arbitrarily chosen bulk mixtures, but also to derive the conformations of the moving chains. Knowledge about these conformations is of particular interest for separation techniques such as electrophoresis and for the development of 'DNA-reading' techniques such as depicted in Figure 1.3.

1.5 Outline of this thesis

Chapter 2 presents the details of the Mean-Field Stationary Diffusion (MFSD) model. It allows to study polymers that diffuse in a steady state between two mixtures of different compositions. The MFSD model is explicitly placed in the framework of its equilibrium counterpart, the Scheutjens-Fleer Self-Consistent-Field model. We show a few stationary diffusion profiles for athermal systems, calculated by use of the MFSD-model. We apply both the slow-mode and the fast-mode theories for the assumptions about the diffusion mechanism and we consider two expressions for the driving forces. The results of the numerical MFSD-model are verified by comparison with analytically calculated diffusion profiles. Such analytical calculations are only possible for simple systems in which the components are completely miscible (all $\chi_{ij} < 2/N$, where N is the chain length). Excellent agreement is found between MFSD-calculations and analytical results. It is shown for an athermal three-component system (all $\chi_{ij} = 0$) that uphill diffusion may occur, i.e., diffusion in the direction of increasing concentration gradient.

In Chapter 3 we apply the MFSD-model to study stationary *hindered* diffusion of polymers. A simple barrier with the characteristics of a fluid film ('membrane') is introduced in the system. This film acts as a barrier through the reduction of the space available for the diffusing polymers. We focus on the conformations of the polymers that reside partly within the barrier and partly outside the barrier. We find that the conformations of flexible polymers are heavily disturbed by the barrier. The results for simple barriers are compared with the predictions from a scaling model. We model the diffusion through a lipid bilayer by including a barrier that consists of two hydrophilic regions and a central hydrophobic region. Such a barrier forces the polymer chains to adjust their conformations a few times during their diffusion.

Chapter 4 considers the compositions of the two bulk mixtures in the MFSD-model that determine the driving forces on the diffusing polymers. These mixtures need to have stable compositions in order to allow unique solutions for the MFSD-calculations. A bulk mixture has a stable composition when there is no driving force for phase separation into two or more coexisting phases. The choice for the compositions of the bulk mixtures is therefore limited, the limits being given by the compositions of coexisting phases (the so-called binodal). The compositions of coexisting phases can conveniently be estimated by analytical approximations. In Chapter 4 we develop a new, more accurate, analytical estimation than the existing approximations. Our analytical expressions are based upon the flux expressions used in the MFSD-model.

In Chapter 5 we apply the equilibrium Scheutjens-Fleer model to study the adsorption or wetting on polymer/polymer interfaces. The adsorbing polymeric component C is equally soluble in both polymeric solvents A and B. We investigate the transitions between two modes, called partial and complete wetting. The transitions occur through variation of the solubility of component C or through variation of the mutual miscibility of the polymeric solvents. We find a large parameter

space for which the transition is second order, which is rarely found experimentally.

The results of Chapter 5 are used in Chapter 6 in which we apply the MFSD-model to study adsorption at *off-equilibrium* interfaces. As in Chapter 5 all three components are polymers with the same chain length and the adsorbing component C is equally soluble in the two demixing polymers A and B. Whereas in Chapter 5 the bulk mixtures at both sides of the A/B interface are coexisting phases, in Chapter 6 they are stable but do not coexist so that polymer A diffuses from the A-rich phase through the interface to the B-rich phase and polymer B diffuses in the opposite direction. We do not impose a concentration gradient on the adsorbing polymer C. We find interesting adsorption behaviour and stationary-flux characteristics. The adsorbed amount is a strong non-linear function of driving forces, A/B-miscibility and C-solubility. There is no unambiguous relation between the adsorbed amount of C and the stationary fluxes of A and B. These findings are related to the ternary phase composition diagrams.

All results and conclusions following from the research described in this thesis are summarised (in English and Dutch) after Chapter 6.

Chapter 2

Lattice mean-field method for stationary polymer diffusion

We present a method to study mean-field stationary diffusion (MFSD) in polymer systems. When gradients in chemical potentials vanish, our method reduces to the Scheutjens-Fleer self-consistent field (SF-SCF) method for inhomogeneous polymer systems in equilibrium. To illustrate the concept of our MFSD method, we studied stationary diffusion between two different bulk mixtures, containing, for simplicity, non-interacting homopolymers. Four alternatives for the diffusion equation are implemented. These alternatives are based on two different theories for polymer diffusion (the slow- and fast-mode theories) and on two different ways to evaluate the driving forces for diffusion, one of which is in the spirit of the SF-SCF method. The diffusion profiles are primarily determined by the diffusion theory and they are less sensitive to the evaluation of the driving forces. The numerical stationary state results are in excellent agreement with analytical results, in spite of a minor inconsistency at the system boundaries in the numerical method. Our extension of the equilibrium SF method might be useful for the study of fluxes, steady state profiles and chain conformations in membranes (e.g. during drug delivery) and for many other systems for which simulation techniques are too time-consuming.

Published in Physical Review E **68**, 011802 (2003).

2.1 Introduction

Polymeric interfaces [28], brushes [29], vesicles [30] and individual polyelectrolytes [31] are examples of systems that can be studied successfully by using the Scheutjens-Fleer self-consistent-field (SF-SCF) method [9, 10]. This is a numerical mean-field approach, yielding the (inhomogeneous) volume fractions and all thermodynamic properties for the systems *at equilibrium*. However, the *stationary states* of such systems are of great interest in the context of, for example, drug delivery over membranes, diffusion-controlled reactions at catalyst surfaces or diffusion over technical membranes in separation processes. To study such stationary polymer systems, the SF-SCF method needs to be extended by dynamic equations and new boundary conditions. We implemented such an extension for a relatively simple system, namely the diffusion layer between two different homogeneous mixtures, consisting of homopolymer blends or homopolymer solutions. Such a system is of interest for polymer diffusion at long time scales. Our method to study the stationary polymer diffusion will be referred to as the Mean-Field Stationary Diffusion (MFSD) method. Equilibrium SCF-methods have been extended to dynamic SCF-methods before, but our focus is different. The objective of previous extensions was to follow the evolution of a system towards its equilibrium or any other stationary state. Specifically, it was attempted by means of a dynamic version of the SF-SCF method to follow polymer adsorption processes from near-equilibrium towards equilibrium [32]. Two other methods (an off-lattice dynamic self-consistent-field method [33] and a dynamic density functional theory [34, 35]) were applied to study the process of spinodal decomposition in (co-)polymer blends. The dynamic density functional theory was also used to investigate the structure development of polymer adsorption layers [36] and, more relevant to our study, the interface formation by polymer interdiffusion [37]. Here we will not consider the evolution towards a stationary state but focus on a well-defined time-independent solution, that is, the (exact) stationary state itself. Obviously, this restriction allows more efficient computation algorithms than the dynamic methods that construct dynamical trajectories. Such methods need an additional noise term in the diffusion equations to allow the system to escape from local minima of the free energy profile [33, 35]. The density functional theory has recently also been applied to study just the stationary state, but only in the application to simple fluids [38]. As in the above mentioned dynamic mean-field theories, we do not consider hydrodynamic interactions. At present, particle-based simulation methods, which are rather time-consuming, are best suited to study polymer dynamics in the presence of hydrodynamic effects [39]. Our method can not deal with these hydrodynamic effects in full detail. However, the average effect of chain entanglements may easily be modelled in the MFSD method by introducing effective mobility parameters.

Polymer diffusion has attracted attention due to its occurrence and importance in many processes, such as phase-separation and spinodal decomposition, bio-adhesion, stabilization of polymer/polymer interfaces by copolymers, diffusion controlled reactions, etc. A large activity in theoretical work [19]-[21],[23],[40]-[46] accompanies the experimental studies [25]-[27], [47]-[50]in this field. The theoretical interest arises from the fundamental problem of linking together thermodynamic and kinetic properties of polymer mixtures. The mutual (or inter-)diffusion coefficient, governing the relaxation of concentration gradients by the mechanism of particle exchange, is usually written as a product of a thermodynamic factor $\mathcal{T}$ and a kinetic factor $\mathcal{K}$ [19, 20, 42, 44]. Interdiffusion is a collective process, in contrast to tracer or self-diffusion which concerns single-chain motions. The

driving force for the latter is entropy and the mechanism may be described by the Rouse [51] or reptation [52, 53] models. The tracer and self-diffusion coefficients are relatively easily obtained from experiments. A major topic of research has been on the question whether the mutual diffusion coefficient can be written in terms of these tracer diffusion coefficients.

Two (conflicting) attempts to find such a relation for binary systems are the slow-mode theory [19] and the fast-mode theory [20, 21]. The mutual diffusion coefficients of both theories have the same thermodynamic factor $\mathcal{T}$. However, the fast-mode theory predicts the kinetic factor $\mathcal{K}$ to depend linearly on the tracer diffusion coefficients, whereas according to the slow-mode theory the inverse of the kinetic factor depends linearly on the inverse of the tracer diffusion coefficients. This discrepancy originates from different assumptions concerning the compressibility of the system or, according to a statistical mechanical approach [41], from different assumptions concerning the friction coefficient between the diffusing components. Some experiments are in favour of the slow-mode theory [22, 23], but most experiments seem to be described best by the fast-mode theory [24]-[27]. However, it is stated in Ref. [45] that the initial concentration relaxations as measured in experiments may incorrectly *appear* to be fast-mode. Shearmur et. al. [48, 49] suggest that the preference for the fast-mode theory may arise from the fact that experiments are usually performed at temperatures far from the glass transition temperature. Their experiments follow slow-mode behaviour at low temperatures and fast-mode behaviour at high temperatures. They find a transition region in which neither of these theories applies. A few theories for polymer diffusion have been derived which reproduce the slow- and fast-mode results in some limiting cases. For example, a hybrid 'fast-slow' theory was proposed [40]. According to this theory, there exists a critical diffusion distance beyond which the diffusion changes from fast-mode behaviour to slow-mode behaviour. Jilge et. al. [42] adopted an approach which is similar to the fast-mode theory, but they took into account cross-coefficients and vacancy concentrations. The slow- and fast-mode results were obtained by making some approximations, but they concluded that in general no simple relation exists between the mutual diffusion and the tracer diffusions. More recently, Akcasu, Nägele and Klein (ANK) presented a statistical mechanical theory which reduces to the slow- and fast-mode models in the limits of, respectively, vanishing or large vacancy concentrations [54, 44]. According to the ANK-theory, a cooperative diffusion coefficient is involved in the mutual diffusion. The conclusions of this theory and of Shearmur's observations [49] are opposite to the predictions of Brereton [23] who constructed a linear combination of the slow- and fast-mode theory.

The above résumé illustrates that the behaviour of collectively diffusing polymers is still controversial. We do not aim at resolving this controversy. Instead, we show that it is possible to study stationary diffusion efficiently by our extension to the SF-SCF method. In principle, the flux-equations that are employed in our MFSD method can be chosen to conform any of the proposed theories in the literature. For our flux-equations, we have chosen the most widely used limiting cases: the slow- and fast-mode theories. The advantage of this choice is that the continuity equation can be solved analytically for some simple stationary systems. This allows the verification of the MFSD results. Using the MFSD method to solve the equation of continuity, the driving forces can be calculated exactly and the detailed conformations of chains may be studied. Moreover,

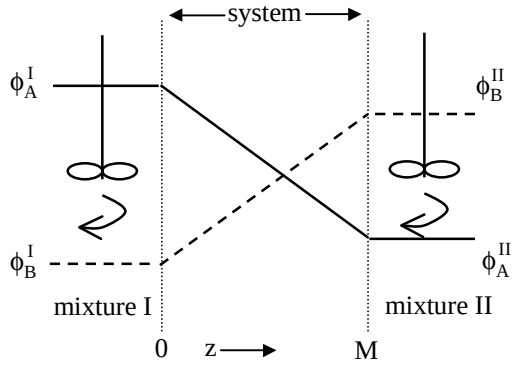

Figure 2.1. Schematic representation of the system of study. Stationary diffusion occurs between two infinitely large bulk mixtures I and II which are ideally stirred, so that the volume fractions in these mixtures are constant. The volume fraction profiles in the system are drawn as straight lines for simplicity.

MFSD calculations are much cheaper than simulations: it takes only minutes to calculate all characteristics of the desired stationary state. The equilibrium SF-SCF method, which is our starting point, has proven its applicability to many situations in which stationary diffusion may be of interest.

This paper is organized as follows: in the theoretical section (Section 2.2) we first describe the diffusion system for which we developed the MFSD method. We then outline the MFSD method itself, thereby showing that it is based upon the ideas of the equilibrium SF-SCF method. Attention is paid to the evaluation of the driving forces for diffusion (segment chemical potential gradients) and to the slow- and fast-mode flux expressions. These flux expressions were originally derived for binary mixtures, but they can easily be generalised to multicomponent systems, as we will demonstrate. We use each flux equation in combination with two ways to calculate the driving forces for diffusion, so that we obtain four models for the polymer diffusion. Section 2.3 presents the results of applying the MFSD method to these four diffusion models. We aim at showing the concept of the MFSD method. Therefore, we focus on the stationary diffusion profiles, although much more information may be extracted from the MFSD calculations. In Section 2.4 we discuss the performance of the MFSD method by comparing its numerical results with analytical results. Moreover, we discuss the general characteristics of the diffusion profiles in athermal binary and multicomponent systems. Section 2.5 summarizes our conclusions.

2.2 Theory

2.2.1 System

We developed the MFSD method for a set-up as shown in Figure 2.1. Two homogeneous polymer bulk mixtures, denoted I and II, are connected by a diffusion layer. Each of these two mixtures has its own composition, expressed in terms of volume fractions as ϕ_A^I,ϕ_B^I,ϕ_C^I... and ϕ_A^{II},ϕ_B^{II},ϕ_C^{II}..., respectively. Here A,B,C... denote the various ho-

mopolymers or solvent molecules in the mixtures. It is assumed that both mixtures are infinitely large and continuously stirred. As a result, these solutions or blends can be regarded as two bulk mixtures with invariant compositions. The actual system of interest is the layer between the two bulk mixtures. At each side of the system the volume fractions are known (namely ϕ^I and ϕ^{II}) and our MFSD method calculates the volume-fraction profiles in the diffusion layer for the stationary state, resulting from diffusion of the molecules for which $\mu^I \neq \mu^{II}$, where the μ's are the chemical potentials. The stationary state is defined by constant material fluxes, ensuring that there is no accumulation of any component within the system: $J_A(z,t) =$ constant in z and t. Note that the flux is taken to be dependent on the z-coordinate only, where z is the direction along the diffusion layer. This means that we use a one-dimensional mean-field method. The diffusion layer is divided in M lattice layers perpendicular to z.

At present, we model only homodisperse homopolymers and solvent molecules (regarded as monomers). A system containing copolymers would require a different approach for the boundary conditions. In the results Section 2.3 only athermal systems will be considered (i.e. all Flory-Huggins parameters χ are zero). In the present theoretical section, we treat the more general case of systems with interactions.

The calculation of the volume fractions (as functions of segment potentials) is dictated by the stationary condition. The derivation of the desired equation follows the steps from equilibrium SF-SCF theory, but requires a different Lagrange parameter as shown in Section 2.2.2. From the theory outlined in that section we find an expression for the exact segment chemical potential (Section 2.2.3) which is inserted into the Smoluchowski equation that describes the diffusion of the polymers in an external potential field (Section 2.2.4). In our case the external potential comprises contributions from segmental interactions and from the incompressibility constraint. The slow-mode and fast-mode theories are different in the way they deal with the incompressibility constraint. They thus yield different expressions for the segmental fluxes. In Section 2.2.4 these fluxes are derived in terms of chemical potential gradients and concentration-independent diffusion coefficients. In Section 2.2.8, we rewrite them in terms of concentration gradients and concentration-dependent diffusion coefficients for analytical purposes.

2.2.2 The MFSD method

The equilibrium SF-SCF method [15] provides an easy way to calculate volume fraction profiles for inhomogeneous (multicomponent) systems at equilibrium. The polymers in these systems are described as chains of segments (comparable with Kuhn segments). Since we are considering only homodisperse homopolymers the number of components is equal to the number of segment types and we can refer to a component just by referring to its constituent segment type A,B,$C\ldots$ The chain length of homopolymer A is given by N_A, i.e. the number of segments of type A that form the whole chain. The conformation of a chain is given by the position of each segment. The SF-SCF method optimises the partition function Q for a lattice in which each lattice site is occupied by a polymer segment, a monomer or a vacancy. Consider a 1-D system described by M lattice layers ($z = 1, \ldots, M$). Then the optimisation of the partition function must be performed under M constraints:

$$\sum_A \phi_A(z) = 1 \quad \forall z \in [1, M] \tag{2.1}$$

where the sum over A denotes summation over all components (or over all segments, which is identical in our system of homodisperse homopolymers). Therefore, M Lagrange-parameters $\alpha(z)$ are introduced in the equilibrium SF-SCF method, which are interpreted as the space-filling potentials. The requirements for equilibrium then become

$$\frac{\partial}{\partial n_j^c}\left[\ln Q + \sum_z \alpha(z)\left\{\sum_A \phi_A - 1\right\}\right] = 0 \quad \forall n_j^c \tag{2.2a}$$

$$\frac{\partial}{\partial \alpha(z)}\left[\ln Q + \sum_z \alpha(z)\left\{\sum_A \phi_A - 1\right\}\right] = 0 \quad \forall z \in [1, M] \tag{2.2b}$$

The parameter n_j^c denotes the number of molecules j in a specified conformation c. Obviously, Equation 2.2b ensures the constraint of incompressibility to be fulfilled. Equation 2.2a dictates the way in which the volume fractions ϕ must be calculated from given segment potentials to obtain the conformation distribution with minimal free energy. The volume fractions depend on the potentials, but the potentials are also dependent on the volume fractions, for example due to unfavourable segment-segment contacts. The equilibrium SF-SCF algorithm is an iterative procedure which leads to a fixed point for which the potentials are consistent with the volume fractions that obey the constraints.

In the MFSD method, the volume fractions are calculated similarly. Thus the volume fractions in the stationary state correspond to that conformation distribution of all molecules for which the free energy is minimal. We apply the SF-SCF free energy functional which is valid for equilibrium systems. It is common to use equilibrium functionals for off-equilibria, since usually the true free energy functionals are unknown [55]. We do not consider this as a approximation of serious error, since we are only interested in the steady state and not in the evolution towards the steady state. We thus do not need to include a noise term as is usually done in the density functional theory. There is a small difference between the calculation of ϕ in SF-SCF and in MFSD. This is due to the extended set of constraints for the stationary state. For the stationary state, we have the constraints

$$\phi_A(0) = \phi_A^I \quad \forall A \tag{2.3a}$$

$$\phi_A(M+1) = \phi_A^{II} \quad \forall A \tag{2.3b}$$

$$\sum_A \phi_A(z) = 1 \quad \forall z \in [1, M] \tag{2.3c}$$

$$\frac{\partial \phi_A(z)}{\partial t} = 0 \quad \forall A, z \in [1, M]. \tag{2.3d}$$

The first constraints (given by Equations 2.3a and 2.3b) are treated separately by the boundary conditions (see Section 2.2.7). The next M constraints (Equation 2.3c) are satisfied by additional stop-criteria for the iterations which must lead to the consistency between the potentials and the volume fractions (see Section 2.2.6). The number of constraints left is M*(number of segment types) (Equation 2.3d). We assume that there exists only one volume fraction profile, that satisfies all constraints and has the minimal free energy. If this profile is given by $\phi_A^{\mathrm{stat}}(z)$ the constraints in Equation 2.3d may be summarized by:

$$\phi_A(z) = \phi_A^{\mathrm{stat}}(z) \quad \forall A, z \in [1, M]. \tag{2.4}$$

The requirements for the stationary state become

$$\frac{\partial}{\partial n_j^c}\left[\ln Q + \sum_{A,z}\alpha_A(z)\left\{\phi_A^{\mathrm{stat}}(z) - \phi_A(z)\right\}\right] = 0 \quad \forall n_j^c \tag{2.5a}$$

$$\frac{\partial}{\partial \alpha_A(z)}\left[\ln Q + \sum_{A,z}\alpha_A(z)\left\{\phi_A^{\mathrm{stat}}(z) - \phi_A(z)\right\}\right] = 0 \quad \forall A, z \in [1, M]. \tag{2.5b}$$

We thus have the correct number of Lagrange parameters if we take $\alpha(z)$ to be dependent on the segment type. The volume fractions in the stationary state are calculated in the same way as in equilibrium, but now by introducing the new space filling potentials $\alpha_A(z)$ in the segment potentials $u_A(z)$. Following Ref. [14], we have

$$\frac{u_A(z)}{k_BT} = \alpha_A(z) + \sum_B \chi_{\mathrm{AB}}\left\langle\phi_B(z)\right\rangle + \frac{u_A^{\mathrm{ref}}}{k_BT}. \tag{2.6}$$

where the reference potential u_A^{ref} can be chosen arbitrarily. (In case of copolymers all constraints should be written in terms of ϕ_{Ai}, the volume fraction of segments A which are part of molecule i. The Lagrange parameters α (and therefore also the segment potentials u) would be dependent both on molecule type and on segment type. In SF-SCF, the segment potentials are always independent on the type of molecules [14]). Angular brackets are used to denote the contact-weighted average over three layers $z-1$, z, $z+1$:

$$\left\langle\phi_B(z)\right\rangle = \lambda_{-1}\phi_B(z-1) + \lambda_0\phi_B(z) + \lambda_1\phi_B(z+1). \tag{2.7}$$

The λ's account for the number of contacts between lattice sites. For a simple cubic lattice $\lambda_0 = 4/6$ and $\lambda_{-1} = \lambda_{+1} = 1/6$. The potentials $u_A(z)$ determine the Boltzmann-weighting factors $G_A(z)$, $G_A(z, s|1)$ and $G_A(z, s|N_A)$:

$$G_A(z) = \exp\left\{\frac{-u_A(z)}{k_BT}\right\} \tag{2.8a}$$

$$G_A(z, s|1) = G_A(z)\left\langle G_A(z, s-1|1)\right\rangle \tag{2.8b}$$

$$G_A(z, s|N_A) = G_A(z)\left\langle G_A(z, s+1|N_A)\right\rangle. \tag{2.8c}$$

The quantity $G_A(z, s|1)$ is the weighting factor for the last segment of a chain of length s, where segment s is in layer z, while segment 1 may be anywhere in the system. Similarly, $G_A(z, s|N_A)$ is the weighting factor for the first segment of a chain of length $N_A - s + 1$, where the first segment (s) is in layer z, while the last segment (N_A) may be anywhere. The starting conditions for Equations 2.8b and 2.8c are: $G_A(z, 1|1) = G_A(z)$ and $G_A(z, N_A|N_A) = G_A(z)$. In terms of these weighting factors, the volume fraction of segment s of component A in layer z must be calculated according to Equations 2.5a and 2.5b by

$$\phi_A(s, z) = C_A\frac{G_A(z, s|1)G_A(z, s|N_A)}{G_A(z)} \tag{2.9}$$

where C_A is a normalization constant. Ref. [14] considers different ways to normalize volume fractions in equilibrium SF-SCF, but the MFSD results are not influenced by the

choice for C_A, since the driving forces for diffusion are gradients which are independent on the constant C_A. Equation 2.9 can also be derived intuitively: the volume fraction of segment s in layer z is given by the normalized weighting factor for the probability to find s in z while both the first and the last segment of the chain may be anywhere in the lattice. The chain can be considered as consisting of two parts, one running from segments 1 to s and one from segment s to N_A. The desired weighting factor can thus be decomposed into the end-segment weighting factors for these parts (as in the numerator in Equation 2.9). The denominator of Equation 2.9 corrects for the double counting the effect of the potential field felt by segment s that connects the two chain parts.

2.2.3 Segment chemical potentials

Since the partition function is known in the SF-SCF and MFSD calculations, all desired thermodynamical quantities may be calculated. We are interested in the diffusion of segments due to imposed gradients in the chemical potentials. The segment chemical potential is defined as the derivative of the free energy with respect to the volume fraction of the segment under consideration. As shown in Appendix 2A the resulting expression is:

$$\frac{\mu_A^{\mathrm{SCF}}(z)}{k_BT} = \frac{\partial(F-F^*)/k_BT}{\partial\phi_A(z)} = -\frac{\partial(\ln Q - \ln Q^*)}{\partial\phi_A(z)} = \frac{\ln N_A C_A}{N_A} - \frac{u_A(z)}{k_BT} + \sum_B \chi_{\mathrm{AB}} \langle\phi_B(z)\rangle$$

so that the gradient of the segment chemical potential is easily calculated by

$$\begin{aligned}\nabla\frac{\mu_A^{\mathrm{SCF}}(z)}{k_BT} &= -\nabla\frac{u_A(z)}{k_BT} + \nabla\sum_B \chi_{\mathrm{AB}} \langle\phi_B(z)\rangle \\ &= -\nabla\alpha_A(z). \end{aligned} \tag{2.10}$$

By these expressions we take into account the inhomogeneity of the system. In the following, we will therefore refer to these potentials as the 'exact segment chemical potentials', or the 'SCF potentials'. Brochard [19] and Kramer [20], on the contrary, approximate the segment chemical potentials by $\mu_A^{\mathrm{app}} = \mu_A^{\mathrm{chain}}/N_A$, where N is the chain length and where μ^{chain} is obtained from the Flory-Huggins lattice theory [18]. This definition for the segment chemical potential is less accurate when the compositions change significantly within the region where the chain finds itself. Generalizing Brochard's and Kramers approach for binary systems to multicomponent homopolymer systems, we obtain for the segment chemical potential of segment type A:

$$\frac{\mu_A^{\mathrm{app}}}{k_BT} = \frac{\ln\phi_A}{N_A} + \frac{1}{N_A} - \sum_B \frac{\phi_B}{N_B} - \frac{1}{2}\sum_{BC}\left(\phi_B - \delta_{AB}\right)\chi_{\mathrm{BC}}\left(\phi_C - \delta_{AC}\right). \tag{2.11}$$

Here, δ_{AB} (δ_{AC}) is the Kronecker delta which is unity for $A = B$ ($A = C$) and zero otherwise. The independent variables of the segment chemical potentials are given by the volume fractions of all components except one, which we denote as component X. The volume fraction ϕ_X is of course equal to $1 - \sum_{B\neq X}\phi_B$. In order to write the flux in terms of ϕ-gradients instead of μ-gradients (for analytical purposes) we take the total differential of the approximate segment chemical potential:

$$\nabla\frac{\mu_A^{\mathrm{app}}}{k_BT} = \frac{1}{k_BT}\sum_{B\neq X}\left(\frac{\partial\mu_A^{\mathrm{app}}}{\partial\phi_B}\right)_{\phi_{C\neq B,X}}\nabla\phi_B \tag{2.12}$$

$$= \sum_B \left(\frac{\delta_{AB}}{\phi_A N_A} - \frac{1}{N_B} + \chi_{\mathrm{AB}} - \sum_C \phi_C \chi_{\mathrm{BC}} \right) \nabla \phi_B .$$

The gradients of the approximate and exact potentials are indistinguishable if there are only monomers or if the system is homogeneous.

2.2.4 Flux equations

One of the constraint-sets for MFSD, namely Equation 2.3d, can easily be translated in terms of material fluxes by the equation of continuity:

$$\frac{\partial \phi_A(z)}{\partial t} = 0 = -\nabla J_A(z) \tag{2.13}$$

where J_A is the flux of segments A. Obviously, in the stationary state, the fluxes are independent of time and position. For simplification, we do not explicitly write the z-dependence of the quantities in the following. We first present the derivation of the so-called slow-mode flux-expression within the framework of the MFSD method. These fluxes will then be rewritten in terms of Onsager coefficients. Using this short notation, the fast-mode flux expression can readily be derived.

Slow-mode flux

The starting point is the Smoluchowski equation [53]:

$$\frac{\partial \phi_A}{\partial t} = \nabla \frac{1}{\zeta_A} \left(k_B T \nabla \phi_A + \phi_A \nabla U_A \right). \tag{2.14}$$

Here, ζ_A is the monomer friction constant and U_A is the potential field felt by segments of type A. Two contributions to this potential can be distinguished: $U_A(z) = E_A(z) + P(z)$. There is a contribution E_A arising from molecular interactions with segments of other types:

$$E_A = k_B T \sum_B \chi_{\mathrm{AB}} \langle \phi_B \rangle . \tag{2.15}$$

The other contribution P is a pressure term due to the requirement of incompressibility, which causes the fluxes of different segment types to be coupled.

Comparing the Smoluchowski equation with Equation 2.13 yields for the flux of segments A:

$$J_A^s = -\frac{k_B T}{\zeta_A} \phi_A \left(\frac{1}{\phi_A} \nabla \phi_A + \nabla \sum_B \chi_{\mathrm{AB}} \langle \phi_B \rangle + \nabla P \right) \tag{2.16}$$

where we have substituted Equation 2.15. The superscript s refers to the slow-mode approach.

The derivative of ϕ_A is found by writing Equation 2.9 as

$$\frac{\phi_A(z,s)}{C_A} = G_A(z) \langle G_A(z, s-1|1) \rangle \langle G_A(z, s+1|N_A) \rangle , \tag{2.17}$$

so that

$$\frac{\nabla \phi_A}{C_A} = \nabla \left(G_A(z) \sum_s \langle G_A(z, s-1|1) \rangle \langle G_A(z, s+1|N_A) \rangle \right)$$

$$\approx \sum_s \langle G_A(z, s-1|1)\rangle \langle G_A(z, s+1|N_A)\rangle \nabla G_A(z). \tag{2.18}$$

In the last line, we used the so called Local Coupling Approximation (LCA), in which the kinetic coupling between segments is neglected: one segment of a chain is allowed to move independently from the motions of its neighbour segments. The LCA was also used by Fraaije in the density functional theory [34]. It might be a approximation with serious consequences (see Ref. [56] and the references therein), but it allows efficient computation and analytical comparisons. Pair correlation functions or a completely different approach would be needed to avoid the LCA [56]. Substitution of Equation 2.18 into the first term of Equation 2.16 yields:

$$\begin{aligned}\frac{\nabla\phi_A(z)}{\phi_A(z)} &= \frac{1}{G_A(z)}\nabla G_A(z)\\ &= \nabla \ln G_A(z).\end{aligned} \tag{2.19}$$

By inserting Equation 2.19 and the well-known Einstein relation for the diffusion coefficient ($D_A = k_BT/\zeta_A$) into Equation 2.16 one arrives at

$$\begin{aligned}J_A^s &= -D_A\phi_A\nabla\left(\ln G_A + \sum_B \chi_{\mathrm{AB}}\langle\phi_B\rangle + P\right)\\ &= -D_A\phi_A\nabla\left(\frac{\mu_A}{k_BT} + P\right).\end{aligned} \tag{2.20}$$

For the second version of Equation 2.20, Equation 2.8a in the form $u_A = -k_BT\ln G_A$ and Equation 2.10 for μ_A were used. The last unknown flux contribution ∇P is obtained by requiring

$$\sum_A J_A(z) = 0 \quad \forall z \in [1, M] \tag{2.21}$$

which is the incompressibility constraint. From Equations 2.20 and 2.21 it is found that

$$\nabla P = -\frac{1}{\sum_A D_A\phi_A}\sum_A D_A\phi_A\nabla\mu_A. \tag{2.22}$$

Substituting this into Equation 2.20 results after some rearrangement in the final expression for the slow-mode flux of segments A:

$$J_A^s(z) = -\frac{D_A\phi_A(z)}{\sum_C D_C\phi_C(z)}\sum_B D_B\phi_B(z)\nabla\left(\frac{\mu_A(z)-\mu_B(z)}{k_BT}\right). \tag{2.23}$$

Onsager coefficients

The flux is conveniently written in terms of Onsager coefficients $\Lambda_A(z)$, by which the single-chain dynamics enter the expressions for the collective dynamics. The Onsager coefficients as defined by Brochard [19] and Kramer [20] relate the unconstrained fluxes to their driving forces:

$$J_A^u = -\Lambda_A\nabla\mu_A. \tag{2.24}$$

The superscript u indicates that the incompressibility constraint is not yet taken into account. The Onsager coefficients are generally written in terms of segment mobilities $\tilde{B}_A$:

$$\Lambda_A = \tilde{B}_A \phi_A. \tag{2.25}$$

Combining this with Equation 2.24 for the unconstrained flux and comparing the result with Equation 2.20 where the constraint is given by the pressure term, it is found that $\tilde{B}_A = D_A/k_BT = 1/\zeta_A$. Using this relation for the mobility coefficient, the slow mode flux (Equation 2.23) may be written in terms of Λ's as

$$J_A^s = -\frac{\Lambda_A}{\sum_C \Lambda_C} \sum_B \Lambda_B \nabla \left(\mu_A - \mu_B\right). \tag{2.26}$$

In Appendix 2B we show that this flux expression obeys Onsager's reciprocal relations.

The relation $\tilde{B}_A = 1/\zeta_A$ is only valid for the Rouse regime. Other expressions for the mobility coefficients may also be used in Equation 2.26. If a polymer chain is longer than the entanglement length, Rouse behaviour may no longer be assumed; the average mobility of the segments will decrease due to the entanglements. According to Ref. [19], this leads to a correction factor $(N_e)_A / N_A$ so that $\tilde{B}_A = (N_e)_A / (N_A \zeta_A)$, where $(N_e)_A$ is the *effective* entanglement length of A chains in the mixture. In pure A, the entanglement length equals N_{e0}. If the chains are diluted by monomeric solvents, the constraints to the segment motions are less pronounced than in pure A, so that the effective entanglement length may be approximated as $(N_e)_A = N_{e0}(1-\phi_{\text{monomer}}(z))$, where ϕ_{monomer} is the total volume fraction of all monomer components.

Alternative expressions for the Onsager coefficient might be obtained by including the effect of chain connectivity (nonlocal coupling). Such Onsager coefficients are proportional to the pair-correlation function [33].

Fast-mode flux

The difference between the slow-mode model and the fast-mode model is the incorporation of vacancies. In the fast-mode model it is assumed that there exists a drift flux by the presence of vacancies:

$$J_A^f = -\Lambda_A \nabla \mu_A + \phi_A J_{\text{vac}}. \tag{2.27}$$

To obey the condition of incompressibility (Equation 2.21), the flux of the vacancies is taken as $J_{\text{vac}} = \sum_B \Lambda_B \nabla \mu_B$, so that

$$J_A^f = -\sum_B \left(\phi_B \Lambda_A \nabla \mu_A - \phi_A \Lambda_B \nabla \mu_B\right). \tag{2.28}$$

The superscript f indicates that it concerns the flux in the fast-mode model. In Appendix 2B Onsager's reciprocal relations are verified.

2.2.5 Four models

The combination of the multi-component slow-mode flux (Equation 2.26) with the approximate segment chemical potentials (Equation 2.12) is a generalization of the binary model developed by Brochard, Jouffroy and Levinson [19]. We refer to this model as the

BJL model. The combination of Equation 2.26 with exact segment chemical potentials (Equation 2.10) is called the **slow-mode SCF model** or the **SCF-BJL model**. Combining Equation 2.28 with the approximate segment chemical potentials is a generalization of the model developed by Kramer, Green and Palmstrøm [20]. We refer to this model as the **KGP model**. The combination of Equation 2.28 with exact segment chemical potentials is called the **fast-mode SCF model** or the **SCF-KGP model**.

2.2.6 Procedure and discretization

The stationary diffusion profiles are obtained by the following procedure. Segment weighting factors are calculated for mixtures I and II in accordance with the desired volume fractions in these bulk mixtures. Then the numerical iterations are started with an initial guess for the potentials $u_A(z)$. These are used to calculate the segment weighting factors within the diffusion layer. In this calculation the boundary conditions (Section 2.2.7) play a role. The weighting factors enable the computation of the volume fractions (Equation 2.9). These volume fractions are needed to check whether the stop-criteria for the stationary state are met. If not, a new iteration loop with newly chosen potentials $u_A(z)$ is started. This is repeated until the the volume fractions obey the constraints. One constraint is a constant material flux for every component (Equation 2.3d). Therefore the flux equation needs to be written in discrete form for use in the lattice model. The continuity equation for a lattice with a one-dimensional gradient reads

$$\frac{\partial \phi_A(z)}{\partial t} = J_A(z-1 \longrightarrow z) + J_A(z+1 \longrightarrow z). \tag{2.29}$$

As an example, we take the slow-mode flux expression, Equation 2.26, and rewrite it for convenience as:

$$J_A^s(z) = \sum_B \Omega_{AB}(z) \nabla(\Delta\mu_{AB}(z)) \tag{2.30}$$

where $\Delta\mu_{AB}$ is shorthand for $\mu_A - \mu_B$. Then $J_A(z-1 \longrightarrow z)$ in the lattice can be calculated as

$$J_A^s(z-1 \longrightarrow z) = \frac{1}{2} \sum_B \left[\Omega_{AB}(z-1) + \Omega_{AB}(z)\right] \frac{\Delta\mu_{AB}(z) - \Delta\mu_{AB}(z-1)}{z-(z-1)}. \tag{2.31}$$

The stop-criteria for the stationary diffusion become for all layers and for all components except one (say X):

$$\sum_B \left[\Omega_{AB}(z-1) + \Omega_{AB}(z)\right] \left[\Delta\mu_{AB}(z) - \Delta\mu_{AB}(z-1)\right] +$$

$$\left[\Omega_{AB}(z) + \Omega_{AB}(z+1)\right] \left[\Delta\mu_{AB}(z+1) - \Delta\mu_{AB}(z)\right] = 0 \tag{2.32a}$$

The stop criterion for component X is for all lattice layers:

$$\phi_X(z) = 1 - \sum_B \phi_B(z). \tag{2.32b}$$

2.2.7 Boundary conditions

The boundaries of the diffusion layer deserve some extra attention. Behind the boundaries ($z \leq 0$ and $z \geq M+1$) are bulk mixtures with specified volume fractions ϕ_A^I and ϕ_A^{II}. A property of any bulk system is the condition that $G_A^{\mathrm{b}}(z) = \text{constant} = \left\langle G_A^{\mathrm{b}}(z) \right\rangle$. As a result, $G_A^{\mathrm{b}}(z,s|1) = \left(G_A^{\mathrm{b}}\right)^s$ and $G_A^{\mathrm{b}}(z,s|N_A) = \left(G_A^{\mathrm{b}}\right)^{N_A-s+1}$. For homopolymers or monomers G_A^{b} is known:

$$G_A^{\mathrm{b}} = \left(\frac{\phi_A^{\mathrm{b}}}{\phi_A^{\mathrm{ref}}}\right)^{1/N_A}. \tag{2.33}$$

We choose to have an abrupt transition between the bulk mixtures and the system; if $z = 1$ is the first layer in the system, then $z = 0$ represents a true bulk. The consequence is an inconsistency at the boundaries and some 'forbidden' chain conformations, which will be discussed in a future publication. All results presented in this paper are obtained from the 'abrupt transition conditions'. We have used other boundary conditions as well (e.g. mirrors for the calculation of ϕ combined with bulk conditions for the calculation of the driving forces, or taking $G_A(z \leq 0, s) = G_A^I$ and $G_A(z \leq 0, s|1)$ still dependent on $G_A(z > 0, s^* < s, 1)$), but the influence on the resulting diffusion profiles is negligible.

2.2.8 Diffusion coefficients

An advantage of using the approximate segment chemical potentials, is that the flux-expressions in terms of μ-gradients can easily be rewritten in terms of ϕ-gradients. This allows the analytical description of the stationary diffusion profiles for some simple systems. Since we only consider athermal systems in the following and since we wish to avoid unnecessary multi-line equations, we assume that $\chi_{\mathrm{AB}} = 0$ for all A, B in the present paragraph. Generally, the flux-expression in terms of ϕ-gradients reads:

$$J_A = -\sum_B \tilde{D}_{AB}^{(X)} \nabla \phi_B \tag{2.34}$$

by which the mutual diffusion coefficients are defined. The superscript X indicates that all volume fractions, except that for the component containing segment type X, are taken as the independent variables for the flux. For example, the flux of segments A in a binary (A/B) system can be written in two ways:

$$J_A = -\tilde{D}_{AA}^{(B)} \nabla \phi_A = -\tilde{D}_{AB}^{(A)} \nabla \phi_B. \tag{2.35}$$

Brochard [19] derived for the mutual diffusion coefficient $\tilde{D}_{AA}^{(B)}$ for athermal binary systems:

$$\frac{\tilde{D}_{AA}^{s(B)}}{k_B T} = \frac{\Lambda_A \Lambda_B}{\Lambda_A + \Lambda_B} \left(\frac{1}{\phi_A N_A} + \frac{1}{\phi_B N_B}\right). \tag{2.36}$$

As discussed in Section 2.1 $(\tilde{D}_{AA}^{s(B)})^{-1}$ is proportional to $(1/\Lambda_A + 1/\Lambda_B)^{-1}$. By substituting Equation 2.12 into the slow-mode flux-equation 2.26 and after some rearrangement, the mutual diffusion coefficients for multicomponent systems in the BJL-model are found to be

$$\frac{\tilde{D}_{AB}^{s(X)}}{k_B T} = \frac{\Lambda_A}{\sum_C \Lambda_C} \left[\frac{\Lambda_X}{\phi_X N_X} - \frac{\Lambda_B}{\phi_B N_B} - \sum_Q \frac{\Lambda_Q}{\phi_A N_A} \left(\delta_{AX} - \delta_{AB}\right)\right]. \tag{2.37}$$

It is easily shown that for binary systems Brochard's mutual diffusion coefficient is recovered.

The mutual diffusion coefficients for the Kramer-model are obtained by inserting Equation 2.12 into the fast-mode flux-equation 2.28:

$$\frac{\tilde{D}_{AB}^{f(X)}}{k_B T} = \left(\phi_A \sum_C \Lambda_C - \Lambda_A\right)\left(\frac{1}{N_B} - \frac{1}{N_X}\right) - \phi_A\left(\frac{\Lambda_B}{\phi_B N_B} - \frac{\Lambda_X}{\phi_X N_X}\right) - \frac{\Lambda_A}{\phi_A N_A}\left(\delta_{AX} - \delta_{AB}\right) \tag{2.38}$$

so that $\tilde{D}_{AB}^{f(X)}$ is a linear combination of Λ's.

Obviously, if ϕ_X is not an independent variable of the flux, $\tilde{D}_{XX}^{(X)}$ and $\tilde{D}_{AX}^{(X)}$ should vanish, which is satisfied by Equations 2.37 and 2.38. $\tilde{D}_{AA}^{(X)}$ is always positive for $X \neq A$. For binary systems $\nabla\phi_A = -\nabla\phi_B$, thus according to Equation 2.35, we must find that $\tilde{D}_{AA}^{(B)} = -\tilde{D}_{AB}^{(A)}$, which can also be verified by Equations 2.37 and 2.38.

2.3 Results

We illustrate the concepts of the MFSD method by showing the stationary diffusion profiles for various athermal systems. Stationary diffusion profiles are the volume fractions for each component as function of the spatial parameter z, such that the two bulk mixtures have the desired composition and such that there is no accumulation of material anywhere between these bulk mixtures. We stress again that the stationary solution is the only solution of the MFSD method. We do not obtain the stationary profiles by following the physical trajectories towards the steady state, but directly by computing the volume fraction profiles that obey all conditions for the steady state. As outlined before, the method has been applied for four different diffusion models. We treat binary and multicomponent systems separately. All binary systems considered in this study have the boundary conditions $\phi_A^I = 0.99$ and $\phi_A^{II} = 0.01$. First the results are presented. After that, an attempt to rationalize them is given.

The most simple systems to study stationary diffusion are those for which all components have the same chain length N and the same mobility B. Figure 2.2 presents the MFSD stationary diffusion profile for such a system. It is seen that these simple systems give rise to linear volume fraction profiles in the stationary state, independent on the model used. The linear profiles turn into curved profiles if the components either have different N or B, as shown in Figure 2.3 and 2.4, respectively.

In Figure 2.3 we have plotted the stationary diffusion profiles for two systems: one system has $N_A/N_B = 5$, the other has $N_A/N_B = 250$. This figure shows that the BJL and KGP results (dashed curves) coincide if the components only differ in their chain lengths. The SCF-BJL and SCF-KGP models (solid curves) also yield indistinguishable profiles for such systems. However, the exact calculation of segment chemical potentials yields profiles which slightly differ from those calculated by approximated segment chemical potentials, in particular for increasing ϕ-gradients and decreasing N_A/N_B. The discrepancy at large $\nabla\phi$ is a result of the assumption of homogeneous mixtures in the Flory-Huggins expression for the approximated chemical potential. It is seen that the larger the ratio between the

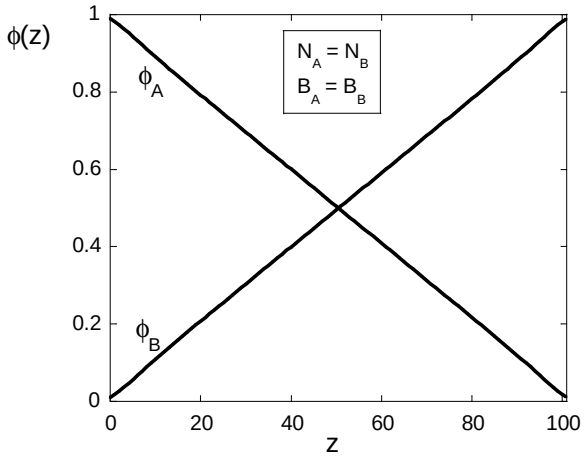

Figure 2.2. Stationary diffusion profiles in a binary system calculated with four different models. $N_A = N_B = N_{e0} = 100$, $\tilde{B}_A = \tilde{B}_B = 1$. All four models give the same result, with linear profiles.

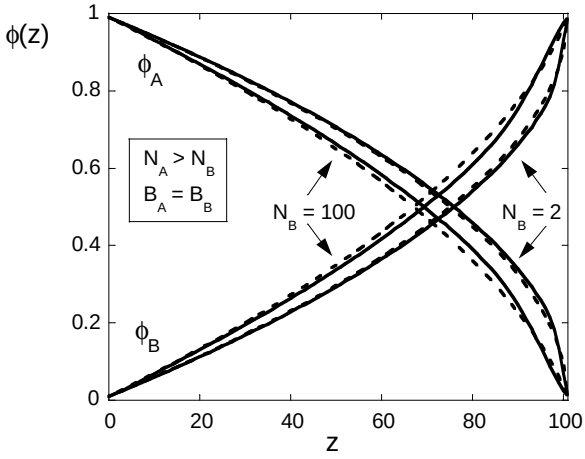

Figure 2.3. Stationary diffusion profiles in two binary systems calculated with four different models. $N_A = 500$, $N_B = 100$ or 2, $1/\zeta_A = 5$, $1/\zeta_B = 1$, $N_{e0} = 100$ so that $\tilde{B}_A = \tilde{B}_B = 1$. Solid lines correspond to calculations with SCF-potentials (SCF-BJL and SCF-KGP), dashed lines to approximate potentials (BJL and KGP).

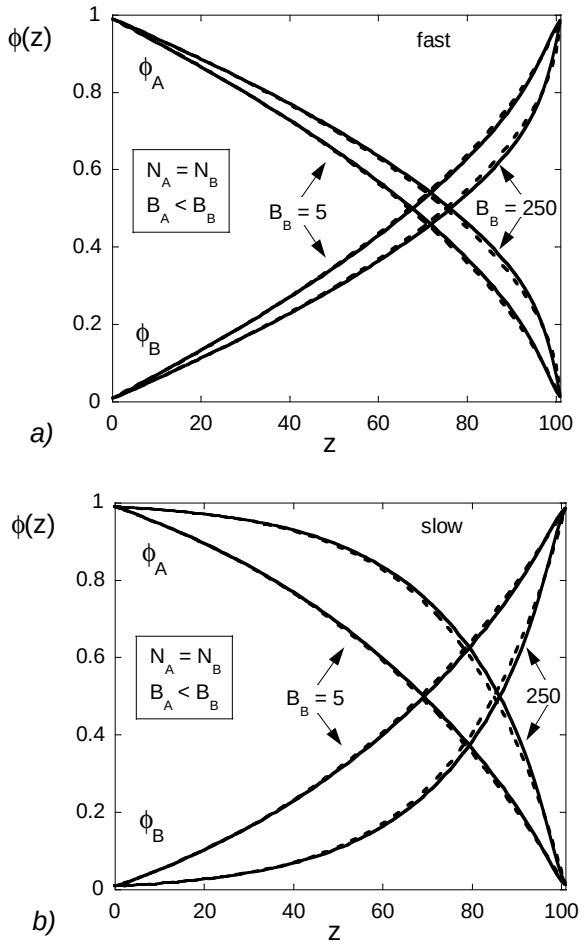

Figure 2.4. Stationary diffusion profiles in two binary systems calculated with four different models. $N_A = N_B = N_{e0} = 100$, $\tilde{B}_A = 1$ and $\tilde{B}_B = 5$ or 250. Solid curves correspond to SCF-potentials, dashed ones to approximate potentials. Figure *(a)* is obtained by the two fast-mode models, Figure *(b)* by the slow-mode models.

chain lengths, the more convex the profiles are. The volume fractions change rapidly near the bulk mixture that contains a large amount of short (and therefore, for given segment mobilities, more mobile) chains.

If the chain lengths are the same, while the segment mobilities are different, the profiles no longer coincide for any of the four models as is shown in Figure 2.4. For these systems, it is the diffusion mechanism (slow- or fast-mode) which mainly determines the stationary diffusion profiles; it is less important whether the segment chemical potentials are calculated exactly or not: KGP profiles compare very well with SCF-KGP profiles (Figure 2.4a), and BJL-profiles are similar to SCF-BJL profiles (Figure 2.4b). Since we have combined the profiles for two different systems in Figures 2.4a and b (namely for $\tilde{B}_B/\tilde{B}_A = 5$ and $\tilde{B}_B/\tilde{B}_A = 250$) it can directly be seen that the slow-mode expression is more sensitive to the segment mobilities than the fast-mode expression. The volume

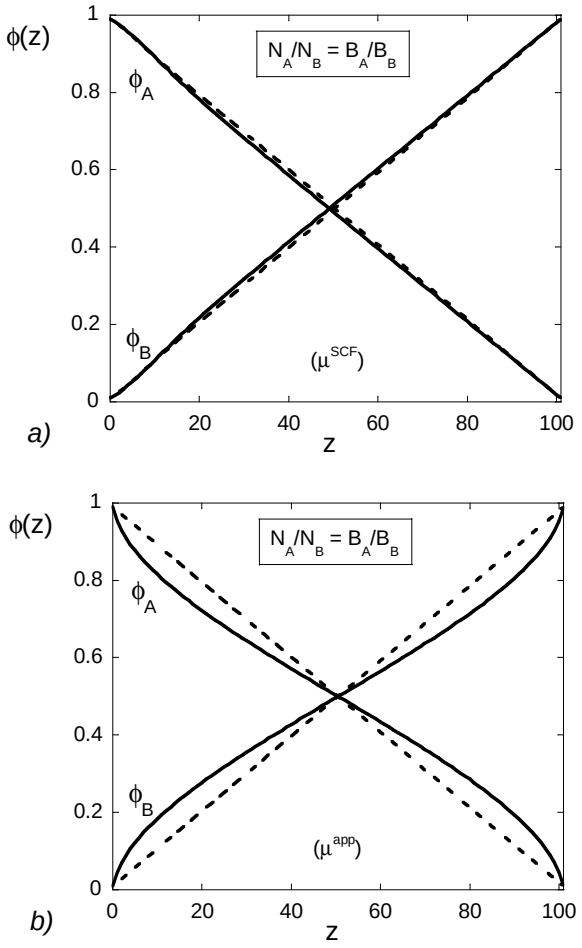

Figure 2.5. Stationary diffusion profiles in a binary system calculated with four different models. $N_A = 10$, $N_B = N_{e0} = 500$, $\tilde{B}_A = 1$, $\tilde{B}_B = 50$ so that $N_A/N_B = \tilde{B}_A/\tilde{B}_B$. Solid curves are calculated by the fast-mode models, dashed ones by the slow-mode models. For Figure *(a)* SCF-potentials are used, for Figure *(b)* approximate potentials.

fractions change rapidly near the bulk mixture that contains a large amount of components consisting of relatively mobile segments. This behaviour is more pronounced when the ratio between segment mobilities increases.

Comparing Figure 2.3 with Figure 2.4*a*, it appears that longer chains act as less mobile components. In particular, the stationary diffusion profiles calculated by the KGP model were found to be exactly the same for two binary systems (α) and (β) if $(N_A/N_B)^{(\alpha)} = \left(\tilde{B}_B/\tilde{B}_A\right)^{(\beta)}$ while $\left(\tilde{B}_B/\tilde{B}_A\right)^{(\alpha)} = 1 = (N_A/N_B)^{(\beta)}$. In other words, a system containing two components with different chain lengths but equal segment mobilities may be simulated by a system containing two monomers (or two polymers of the same length) with different segment mobilities. This is only true for the KGP model. This may suggest that the lower mobility of longer chains might be compensated by a higher mobility of its constituting segments. It would then be expected that the compo-

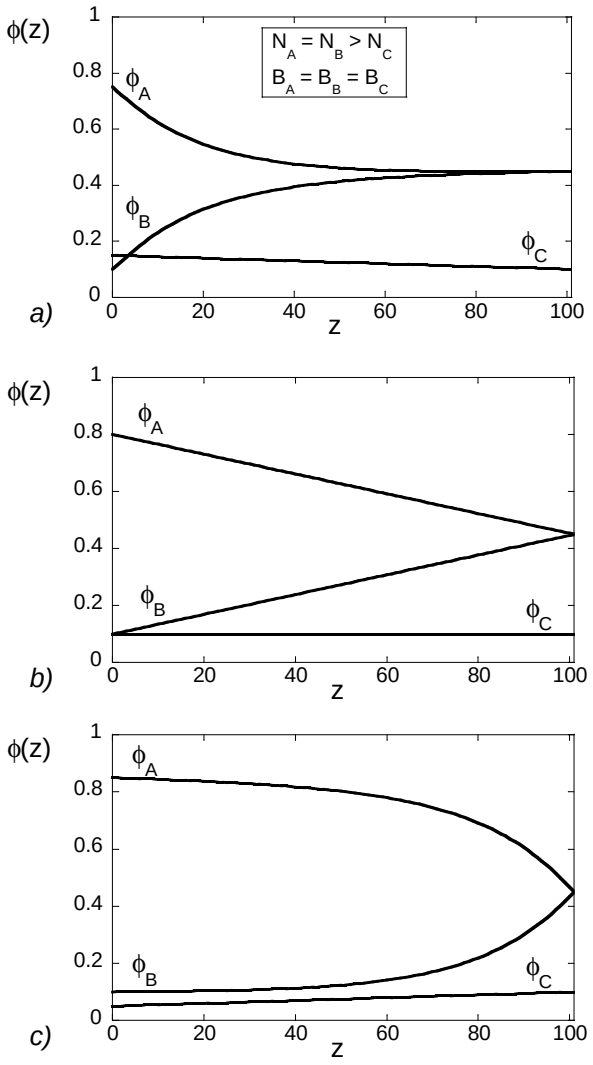

Figure 2.6. Stationary diffusion profiles in a ternary system containing two homopolymers (A and B) and one monomer (C). $N_A = N_B = N_{e0} = 100$, $N_C = 1$, $\tilde{B}_A = \tilde{B}_B = \tilde{B}_C = 1$. The only parameters that were varied in systems *(a)-(c)* are $\phi_A(0)$ and $\phi_C(0)$. All models give essentially the same results.

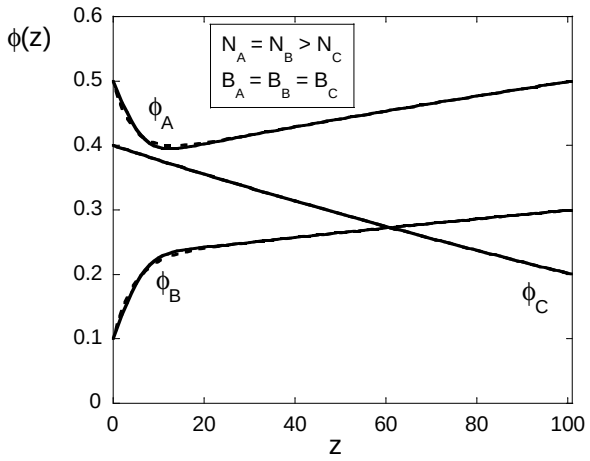

Figure 2.7. Stationary diffusion profiles in a ternary system containing one monomer (C) and two homopolymers (A and B) with equal chain lengths and segment mobilities, and equal ϕ_A but different ϕ_B at the boundaries. Note that $\phi_A(0) = \phi_A(M+1)$. $N_A = N_B = N_{e0} = 100$, $N_C = 1$, $\tilde{B}_A = \tilde{B}_B = \tilde{B}_C = 1$. Solid curves are obtained by the SCF-potentials, dashed ones by approximate potentials. No difference is found between the fast- or slow-mode mechanism.

nents would act as mutually indistinguishable if the system parameters were chosen such that $N_A/N_B = \tilde{B}_A/\tilde{B}_B$. Indistinguishable components would result in linear profiles (*cf* Figure 2.2). Figure 2.5 shows that this is true for the two slow-mode models, but not for the fast-mode models. Note that the fast-mode results change significantly when the exact segment chemical potentials are replaced by approximate ones. The discrepancy does not only occur for the largest ϕ-gradients. The comparison between the models for other choices of parameters generally yields the same conclusions as derived from Figure 2.5: usually the slow-mode results are less affected by the way to calculate the segment chemical potentials than the fast-mode results.

The four variants of the MFSD method were also used to calculate the stationary diffusion profiles for ternary systems: two equally long polymers in a solvent. The differences between the models are too small to be observed in the systems presented in Figure 2.6. This figure shows three systems which differ only slightly in the imposed volume fractions at the left-hand boundary ($z = 0$): $\phi_B(0) = 0.1$ in all cases and $\phi_A(0) = 0.75$ (top), 0.8 (middle), and 0.85 (bottom). It is seen that these small differences result in very different profiles. The solvent (monomer) has a rather flat and approximately linear profile in all cases. The largest ϕ-gradients of the polymers are found at the highest monomer concentration.

Another striking example of a ternary system is presented in Figure 2.7. Despite the fact that the imposed values for ϕ_A are the same at both sides of the system ($\phi_A(0) = \phi_A(M+1)$), this component has large gradients within the system. The profiles are the same for the fast- and slow-mode calculations, as was the case for binary systems in which all segments had the same mobilities. Small differences occur if the segment chemical potentials are not calculated exactly. However, the longer the polymer chains,

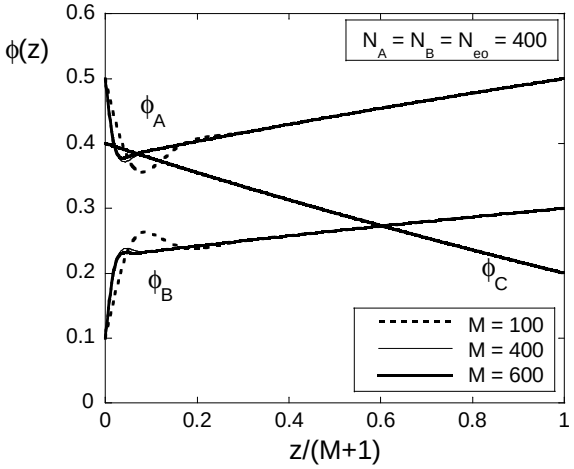

Figure 2.8. The same system as in Figure 2.7 for longer chains ($N_A = N_B = N_{e0} = 400$) and for various system sizes M, calculated by the SCF potentials. Volume fractions are now plotted versus the normalized z-variable. Increasing the system size above $M = N$ does not change the shape of the profiles significantly.

the larger these differences become (not shown).

As explained in Section 2.2.7, our boundary conditions are such that in the vicinity of the bulk mixtures some chain conformations could not occur. The stationary diffusion profiles do not suffer from these boundary conditions; the profiles scale accordingly with the system size as long as the system is not too small in comparison with the chain lengths. This is shown in Figure 2.8, where we plotted the diffusion profiles versus the normalized distance parameter $z/(M+1)$. The diffusion profiles are not influenced by the size of the system if $M \approx N$, where N is the length of the longest polymer chains. Note that we find oscillating volume fraction profiles if the chains are long compared to the system size ($N = 400$, $M = 100$) and when the driving forces are calculated exactly. Using the approximate segment chemical potentials does not give oscillating profiles.

2.4 Discussion

From Equations 2.26 and 2.28 it is easily concluded that the slow-mode and fast-mode models are indistinguishable for $\Lambda_A(z)/\phi_A(z) = \Lambda_B(z)/\phi_B(z)\ \forall A, B, z$ which means $\tilde{B}_A(z) = \tilde{B}_B(z) = \tilde{B}(z)\ \forall A, B, z$. This can only be true if $\tilde{B}$ is independent of z. Figures 2.2, 2.3, 2.7 and 2.8 show that this exact agreement between the slow- and fast-mode models is indeed found. In the remainder of this discussion, we first discuss some analytical descriptions and then focus on the general characteristics of binary and multicomponent systems.

2.4.1 Comparison with analytical results

Due to our choice of simple systems, we can compare the MFSD-results with analytical results. Analytical expressions for $\phi_A(z)$ are obtained by solving Equation 2.34 in combination with the diffusion coefficients of either the BJL model or the KGP model.

Suppose that all components have the same mobility B (so that the BJL and KGP models are identical) and the same chain length N. The flux is then simply given by $J_A(z) = -\frac{\tilde{B}k_BT}{N}\nabla\phi_A(z)\ \forall A, z$. To satisfy the condition of constant fluxes, the analytical expressions for ϕ are linear functions of z. The MFSD-result obeys this linear behaviour for all four models as shown in Figure 2.2.

For binary systems $\phi_A(z)$ can be obtained by solving $-\int \tilde{D}_{AA}^{(B)}\mathrm{d}\phi_A = J_Az+k_1$. Expressions for $\tilde{D}_{AA}^{(B)}$ for various simple cases are given in Table 2.1. When $\tilde{B}_A = \tilde{B}_B$ and $N_A \neq N_B$, $\tilde{D}_{AA}^{(B)}$ is given by $\tilde{D}_{AA}^{(B)} = a - b\phi_A$ with $a = \tilde{B}k_BT/N_A$ and $b = \tilde{B}k_BT(1/N_A - 1/N_B)$. The result for $N_A > N_B$ is

$$\phi_A(z) = \frac{a}{b} - \frac{1}{b}\sqrt{a^2 + 2b(k_1 + J_Az)}. \tag{2.39}$$

The integration constant k_1 and the flux J_A can be found from the known values of $\phi_A(0)$ and $\phi_A(M+1)$. Due to the condition that $N_A > N_B$, the sign of the square root term is unambiguously determined. The volume fraction profile of the short-chain component simply follows from $\phi_B = 1 - \phi_A$.

In case of equal chain lengths but $\tilde{B}_A \neq \tilde{B}_B$, we find for the BJL-model $\tilde{D}_{AA}^{(B)} = a/(c\phi_A + \tilde{B}_B)$, with $a = \tilde{B}_A\tilde{B}_Bk_BT/N$ and $c = \tilde{B}_A - \tilde{B}_B$. Thus, for $\tilde{B}_B > \tilde{B}_A$, the stationary volume fraction profile is

$$\phi_A(z) = \frac{k_2}{c}\,\exp\left\{-\frac{cJ_A}{a}z\right\} - \frac{\tilde{B}_B}{c} \tag{2.40}$$

with $k_2 = \exp\{-ck_2^{'}/a\}$. The same system has for the KGP-model $\tilde{D}_{AA}^{(B)} = a - c\phi_A$ with $a = \tilde{B}_Ak_BT/N$ and $c = (\tilde{B}_A - \tilde{B}_B)k_BT/N$, so that

$$\phi_A(z) = \frac{a}{c} - \frac{1}{c}\sqrt{a^2 + 2c(k_3 + J_Az)}. \tag{2.41}$$

Analytical explicit expressions for $\phi_A(z)$ do not exist for arbitrarily chosen chain lengths and segment mobilities are chosen arbitrarily. In Figure 2.9 the analytical expressions 2.39, 2.40 and 2.41 are plotted together with the corresponding results from the MFSD method. They match each other exactly.

In Appendix 2C, we show that for the three-component system in Figure 2.7 with $\tilde{B}_A = \tilde{B}_B = \tilde{B}_C$, $N_A = N_B$ and $N_A > N_C$, the analytical expressions for the volume fractions read:

$$\begin{aligned}
\phi_A(z) &= \frac{aJ_A}{bJ_C}\,[d(z) - 1] + k_5\,\exp\{-d(z)\} \\
\phi_B(z) &= \frac{aJ_B}{bJ_C}\,[d(z) - 1] - k_5\,\exp\{-d(z)\} \\
\phi_C(z) &= \frac{a}{b}\,[d(z) - 1] + 1
\end{aligned} \tag{2.42}$$

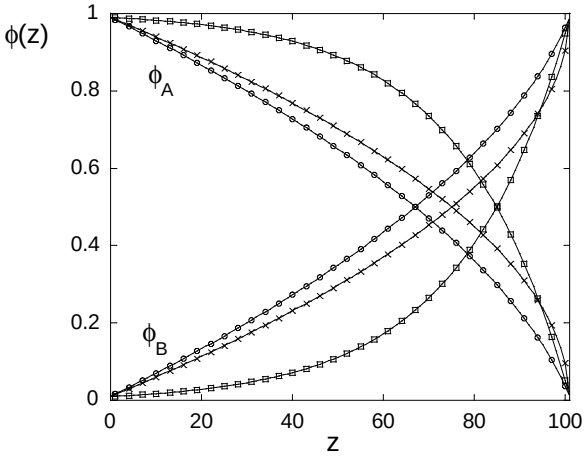

Figure 2.9. Comparison of results from the MFSD method (markers) with the corresponding analytical results (curves) in different binary systems. In all cases $M = 100$, $N_B = 100$ and $\tilde{B}_A = 1$. The circles are for the BJL and KGP model with $N_A/N_B = 5$ and $\tilde{B}_A = \tilde{B}_B$. The squares are for the BJL model with $N_A = N_B$ and $\tilde{B}_B/\tilde{B}_A = 250$. The crosses are for the KGP model with $N_A = N_B$ and $\tilde{B}_B/\tilde{B}_A = 250$.

where $a = \tilde{B}k_BT/N_A$, $b = \tilde{B}k_BT(1/N_A - 1/N_C)$, $d(z) = \frac{1}{a}\sqrt{s+tz}$, $s = a^2 + 2bk_4$, $t = -2bJ_C$ and $J_C = -J_A - J_B$. J_A, J_B and the integration constants k_4 and k_5 are given by the compositions of the bulk mixtures. These equations reproduce the profiles in Figure 2.7 (including the minimum in ϕ_A) with the same accuracy as shown for binary systems in Figure 2.9.

The exact agreement between the analytical profiles and the MFSD results proves the proper performance of the MFSD method. In addition, they show that the abrupt transition between the system and the bulk mixtures in the MFSD method does not disturb the diffusion profiles. However, if the system is small compared to the longest chains, small discrepancies may occur between the analytical results and the MFSD results.

2.4.2 General characteristics of binary systems

We now focus on general characteristics of the diffusion profiles for binary systems. It is convenient to analyze how $\nabla\phi$ should change with ϕ according to the flux-expressions for the approximate models, since this behaviour of $\nabla\phi$ can readily be checked by plots of diffusion profiles. Since $\nabla\phi_A = -J_A/\tilde{D}_{AA}^{(B)}$ and $J_A =$ constant we have

$$\frac{\partial\nabla\phi_A}{\partial\phi_A} = -\frac{\nabla\phi_A}{\tilde{D}_{AA}^{(B)}}\frac{\partial\tilde{D}_{AA}^{(B)}}{\partial\phi_A}. \tag{2.43}$$

Given that $\tilde{D}_{AA}^{(B)}$ is positive, it is concluded that for binary systems $\frac{\partial\tilde{D}_{AA}^{(B)}}{\partial\phi_A}$ and $\frac{\partial|\nabla\phi_A|}{\partial\phi_A}$ must have opposite signs. In Table 2.1 different classes of binary systems are distinguished by different combinations of parameters. For each class and for both approximate models

Table 2.1. Stationary binary systems: ϕ-derivatives of the diffusion coefficients and ϕ-gradients. The expressions for $\tilde{D}_{AA}^{(B)}$ were obtained from Equations 2.36-2.38 after inserting $\Lambda_A = \tilde{B}_A\phi_A$ and $\Lambda_B = \tilde{B}_B\phi_B$ (Equation 2.25).

		$N_A = N_B = N$ $\tilde{B}_A = \tilde{B}_B = \tilde{B}$ (Fig. 2.2)	$N_A = xN_B$ $\tilde{B}_A = \tilde{B}_B = \tilde{B}$ (Fig. 2.3)	$N_A = N_B = N$ $\tilde{B}_B = x\tilde{B}_A$ (Fig. 2.4)
BJL-model[19]	$\tilde{D}_{AA}^{(B)}$	$\frac{\tilde{B}k_BT}{N}$	$\frac{\tilde{B}k_BT}{N_A}(\phi_B + x\phi_A)$	$\frac{\tilde{B}_Bk_BT}{N}\frac{1}{(\phi_A + x\phi_B)}$
	$\frac{\partial\tilde{D}_{AA}^{(B)}}{\partial\phi_A}$	0	$\frac{\tilde{B}k_BT}{N_A}(x-1)$	$\frac{\tilde{B}_Bk_BT}{N}\frac{(x-1)}{(\phi_A + x\phi_B)^2}$
	$\frac{\partial\lvert\nabla\phi_A\rvert}{\partial\phi_A}$	0	$\begin{cases} <0 \text{ for } N_A > N_B \\ >0 \text{ for } N_A < N_B \end{cases}$	$\begin{cases} <0 \text{ for } \tilde{B}_A < \tilde{B}_B \\ >0 \text{ for } \tilde{B}_A > \tilde{B}_B \end{cases}$
KGP-model[20]	$\tilde{D}_{AA}^{(B)}$	$\frac{\tilde{B}k_BT}{N}$	$\frac{\tilde{B}k_BT}{N_A}(\phi_B + x\phi_A)$	$\frac{\tilde{B}_Ak_BT}{N}(\phi_B + x\phi_A)$
	$\frac{\partial\tilde{D}_{AA}^{(B)}}{\partial\phi_A}$	0	$\frac{\tilde{B}k_BT}{N_A}(x-1)$	$\frac{\tilde{B}_Ak_BT}{N}(x-1)$
	$\frac{\partial\lvert\nabla\phi_A\rvert}{\partial\phi_A}$	0	$\begin{cases} <0 \text{ for } N_A > N_B \\ >0 \text{ for } N_A < N_B \end{cases}$	$\begin{cases} <0 \text{ for } \tilde{B}_A < \tilde{B}_B \\ >0 \text{ for } \tilde{B}_A > \tilde{B}_B \end{cases}$

the sign of $\frac{\partial|\nabla\phi_A|}{\partial\phi_A}$ is evaluated by first writing the general expression for $\tilde{D}_{AA}^{(B)}$ and then calculating its derivative with respect to ϕ_A. We first note that the KGP model yields the same stationary diffusion profiles for the second (Figure 2.3) and third (Figure 2.4) classes if $(N_A/N_B)_{\text{equal }\tilde{B}} = (\tilde{B}_B/\tilde{B}_A)_{\text{equal }N}$, as can be seen from the diffusion coefficients in the second and third columns of Table 2.1. This implies that the mobility of a chain can effectively be changed by either its chain length or the segment mobility. The general conclusion which can be drawn from Table 2.1 is that the larger the fraction of relative mobile component, the steeper the volume fraction profiles for stationary diffusion: it is observed that $\frac{\partial|\nabla\phi_A|}{\partial\phi_A}$ is positive if ϕ_A is the relative mobile component. The first column shows that if both components have the same mobilities, the gradients of the volume fractions are constant. The second column implies an increasing $\nabla|\phi|$ for increasing volume fraction of the shorter, and therefore more mobile, homopolymer. These columns refer to classes of systems for which the slow-mode and the fast-mode fluxes are the same, in accordance with previous statements. The third column in Table 2.1 refers to systems for which the slow-mode and fast-mode models no longer coincide, but the general conclusion remains valid for both models.

Barrer [57] and Crank [58] also present stationary diffusion profiles for diffusion coefficients that are concentration-dependent. Their general conclusion is that the concentration profiles are convex towards the z-axis if $\partial\tilde{D}_{AA}^{(B)}/\partial c_A < 0$, and convex away from the z-axis if $\partial\tilde{D}_{AA}^{(B)}/\partial c_A > 0$. Our results are in agreement with their conclusion, but we can

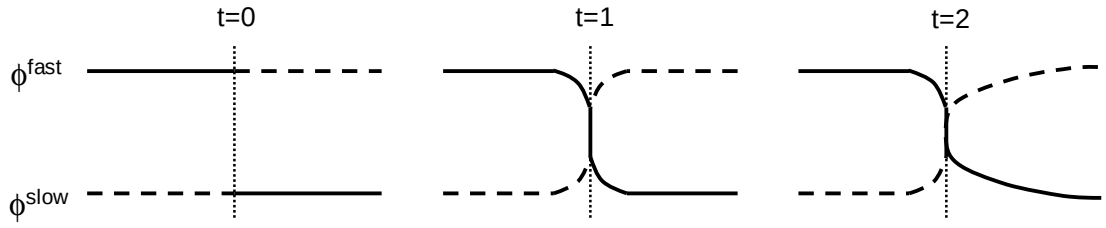

Figure 2.10. Schematic picture of the developing diffusion profiles for fast component diffusing to the right and slow component to the left.

state more specifically that the profiles are convex towards the ϕ-axis if $\partial\phi^{\text{fast}}/\partial z < 0$ and vice versa, where ϕ^{fast} refers to the relative mobile component. This general behaviour can be understood by considering how these stationary profiles develop from the initial profile at $t = 0$ which is assumed to be discontinuous at $z = \frac{1}{2}M$ (see Figure 2.10*(a)*). Suppose the major component at the left side of the system consists of relative mobile A-segments, whereas at the right mainly low-mobile B-segments are present. From Table 2.1 it follows that $\partial\tilde{D}/\partial\phi^{\text{fast}} < 0$ so that the diffusion coefficient is smaller at the left than at the right. Segments A start diffusing to the right by exchanging their positions with segments B. At first instance, the ϕ-gradients at both sides will be similar: $\nabla\phi_A(z = \frac{1}{2}M - \epsilon) \approx \nabla\phi_A(z = \frac{1}{2}M + \epsilon)$ (Figure 2.10*((b))*. However, the gradient at $z = \frac{1}{2}M + \epsilon$ vanishes more rapidly than at $z = \frac{1}{2}M - \epsilon$ due to the larger diffusion coefficient (Figure 2.10*(c)*). This results in flatter profiles at low concentration of mobile component.

Comparing the approximate models with the exact models, we found two situations in which discrepancies may occur. First, discrepancies occurred if the system was small compared to the chain lengths. The oscillations in Figure 2.8 were only found if the driving forces are calculated by the exact segment chemical potentials and if the chains are long compared to the system size. The smaller the system or the longer the chains, the larger the gradients in the region in which the chains find themselves. In other words, the assumption of local homogeneity, as used for the approximate segment chemical potentials, is incorrect for such small systems with long chains. Secondly, discrepancies between approximate and exact *fast-mode* calculations occurred if the components had both dissimilar chain lengths and dissimilar segment mobilities (e.g. Figure 2.5). In general, agreement was found between BJL and SCF-BJL for such systems. In other words: the fast-mode model seems to be more sensitive to the calculation of the driving force than the slow-mode model. Probably, the error in $\nabla\mu_A$ is compensated by the error in $\nabla\mu_B$ in calculations applying the slow-mode fluxes, since the driving forces appear as $\nabla(\mu_A - \mu_B)$ in these flux expressions (*cf* Equation 2.26). On the contrary, in the KGP-model, the errors in $\nabla\mu$ are weighted by segment mobilities due to the terms $\tilde{B}_A\nabla\mu_A - \tilde{B}_B\nabla\mu_B$ in the flux expressions (Equation 2.28).

2.4.3 General characteristics of multicomponent systems

Figure 2.6 can now be understood from Table 2.1. Since the homopolymer components in Figure 2.6*b* are indistinguishable, the chemical potential of the monomer component

is constant. Effectively, this system refers to binary diffusion of two homopolymers with equal chain lengths and mobilities, for which the profiles must be linear. At first instance Figure 2.6*a* and *c* may also be interpreted as the stationary diffusion profiles for binary mixtures, one component being the monomer, the other the combination of both polymers. Indeed, as predicted by Table 2.1, the profiles change rapidly at high monomer concentrations. This is not only true for the monomer and the total of the two polymers, but also for the individual polymer components. This can be understood from the observation that the polymers are identical and they have a similar absolute difference between ϕ^I and ϕ^{II}. As a result, they must behave similarly and with opposite gradients.

A first remark for the three-component system in Figure 2.7 concerns the behaviour of polymer A. Despite the equal volume fractions in both bulk mixtures, its volume fraction within the system is not constant. Due to the requirement of stationary diffusion, the flux of segments A needs to be constant throughout the system. For this particular system, J_A is found to be negative; A-segments diffuse from right to left. This implies that for small values of z the A-segments diffuse against a concentration gradient. This phenomenon is called 'uphill diffusion'. It is found only in multicomponent systems and must be due to either diffusive coupling of components (large $|\tilde{D}_{AB}^{(X)}|$ for $A \neq B$) or negative 'main diffusion coefficients' $\tilde{D}_{AA}^{(X)} < 0$. In our system, $\tilde{D}_{AA}^{s(C)} = \tilde{D}_{AA}^{f(C)} = \phi_A[1/N_C + \phi_B/(\phi_A N_A)] \approx \phi_A > 0$ and $\tilde{D}_{AB}^{s(C)} = \tilde{D}_{AB}^{f(C)} = \phi_A[1/N_C - 1/N_B] \approx \phi_A$ (see Equations 2.37 and 2.38). The relatively large cross diffusion coefficient $\tilde{D}_{AB}^{(C)}$ drives the flux of A-segments towards the region of low ϕ_B. Experimental evidence for uphill diffusion has been reported frequently for metallic systems and in the context of geological studies [59]-[61] in which all diffusing components have nearly equal sizes. Negative main diffusion coefficients have been measured in ternary surfactant mixtures [62]. Uphill diffusion has been found in theoretical studies as well [63, 38] for example as a result of interparticle interactions. We are not aware of any reports on uphill diffusion only due to chain-length effects. (Remind that we consider athermal systems). Note that A-segments have $\phi_A(0) = \phi_A(M+1)$, but $\mu_A^{chain}(0) < \mu_A^{chain}(M+1)$ as a result of the different monomer contents at both sides.

The profile of the monomer can be understood by considering the system as a binary mixture, since the polymers are indistinguishable. The monomer concentration must therefore change rapidly at the left side, where its concentration is maximal.

2.5 Conclusions

The equilibrium Scheutjens-Fleer method has been extended to create a new framework for the modelling of stationary diffusion in polymer systems. The numerical algorithm converges fast and smoothly to stationary volume fraction profiles that obey the imposed volume fractions at the system boundaries. It is important to note that, although we implemented the transition between the bulk mixtures and the gradients in a rather rough way, the diffusion profiles did not suffer from it. Two theories, presented in the literature for binary homopolymer diffusion and referred to as 'slow mode' and 'fast mode', respectively, were combined with two methods to calculate the segment chemical potentials. This yielded four models for the fluxes. The parameters for the flux-equations are the Flory-Huggins interaction parameters χ, the chain lengths of the components N_A, the entanglement length of the components N_e and the mobilities of the constituent segments

$1/\zeta_A$. In general, the diffusion profiles were more sensitive to the applied theory (slow mode or fast mode) than to the calculation of segment chemical potentials. However, results from the two slow-mode models are more similar than those from the two fast-mode models. By analytical analysis of diffusion coefficients, we were able to verify the usually asymmetric diffusion profiles. We have thereby verified the MFSD method since the analytical results matched exactly the results from the MFSD method. It has been found for stationary diffusion profiles that the volume fractions change more rapidly at the location where the amount of mobile components is larger. The mobility of components is determined both by the segment mobilities and by their chain lengths. We only studied athermal systems, but mutually interacting components might be studied as well by the MFSD method. It is therefore possible to study interfaces in the presence of concentration gradients, as well as diffusion through pores of membranes that energetically interact with some components. Another interesting aspect of the MFSD method is that it provides information about the chain conformations; this information was not discussed in the present paper and will be presented elsewhere.

Appendix 2A Derivation of the segment chemical potential in the MFSD-method

The segment chemical potential is defined as the derivative of the free energy with respect to the volume fraction:

$$\frac{\mu_A(z)}{k_BT} = \frac{\partial(F - F^*)/k_BT}{\partial\phi_A(z)} \tag{2A.1}$$

According to statistical thermodynamics, the free energy is given by

$$\frac{F - F^*}{k_BT} = -\ln\frac{Q}{Q^*}, \tag{2A.2}$$

where Q is the canonical partition function, defined by $Q = \Omega\exp\{-U/k_BT\}$, with Ω the degeneracy for the system with energy U. In Equation 2A.2, F^* and Q^* are the free energy and the partition function for a set of reference states. Each reference state is a pure amorphous bulk state. The number of reference states equals the number of molecule types in the system under consideration. Thus a system containing two molecular types i and j has two reference states: one with $\phi_i^* = 1$, the other with $\phi_j^* = 1$. The partition function for the set of reference states, Q^*, is defined as $Q^* = \Pi_i Q_i^*$, where the product is taken over all molecule types i. The free energy in Equation 2A.2 can then be rewritten by using

$$\ln Q = \ln\frac{\Omega}{\Omega^*} - \frac{U - U^*}{k_BT} + \ln Q^*, \tag{2A.3}$$

with $U^* = \sum_i U_i^*$. The total energy U of the system under consideration is easily obtained by introduction of the Flory-Huggins interaction parameters χ_{AB}:

$$\frac{U}{k_BT} = \frac{1}{2}\sum_{z,A,B}\phi_A(z)\chi_{\mathrm{AB}}\left\langle\phi_B(z)\right\rangle. \tag{2A.4}$$

The reference state i of molecules i has total energy U_i^*:

$$\frac{U_i^*}{k_BT} = \frac{n_i N_i}{2} \sum_{A,B} \phi_{Ai}^* \chi_{\mathrm{AB}} \phi_{Bi}^* = \frac{1}{2} \sum_{z,A,B} \phi_{Ai}(z) \chi_{\mathrm{AB}} \phi_{Bi}^*. \tag{2A.5}$$

Here, ϕ_{Ai} is the volume fraction of segments A that belong to molecule type i. Both the reference state i and the system under consideration contain n_i molecules of type i. The number of A segments in the reference state i is therefore equal to the number of A segments in all molecules i in the system: $n_i N_i \phi_{Ai}^* = \sum_z \phi_{Ai}(z)$. The expressions for the degeneracies Ω and Ω_i^* in Equation 2A.3 is derived by counting the number of different ways in which a collection of molecules can be placed in the lattice [14]. The resulting logarithm for Ω/Ω^* can be approximated by Sterling's formula ($\ln X! = X \ln X - X$) as

$$\ln \frac{\Omega}{\Omega^*} = \sum_{i,c} n_i^c \ln \frac{\lambda^c}{n_i^c N_i}, \tag{2A.6}$$

where n_i^c is the number of molecules of type i with conformation c, and where λ^c is a product of the weighting factors λ_0 and λ_1 that occur in molecular conformation c. Substituting Equations 2A.3 and 2A.6 into Equation 2.3a, using $\phi_{Ai}(z) = \sum_c n_i^c N_{Ai}^c(z)$ and defining the segment potential as $u_{Ai}(z) = k_BT\alpha_{Ai}(z) + \partial U/\partial\phi_A(z) + u_{Ai}^{\mathrm{ref}}$ yields

$$\ln \frac{n_i^c}{\lambda^c} = \ln C_i - \sum_{z,A} \frac{u_A(z)}{k_BT} N_{Ai}(z). \tag{2A.7}$$

In this expression, the constant C_i only depends on the type of molecule and on the choice for the reference potentials u_{Ai}^{ref}. This constant appears in the calculation of the volume fractions as a normalisation constant (*cf* Equation 2.9). When the system under consideration is in equilibrium with a homogeneous bulk mixture in which the reference potentials equal zero, the normalisation constant is given by $C_i = \phi_i^{\mathrm{bulk}}/N_i$.

The free energy of the inhomogeneous system can be written by combination of Equations 2A.2-2A.7 as:

$$\begin{aligned} \frac{F - F^*}{k_BT} &= \sum_{z,A,i} \frac{\phi_{Ai}(z)}{N_i} \ln N_i C_i - \sum_{z,A,i} \phi_{Ai}(z) \frac{u_{Ai}(z)}{k_BT} \\ &\quad + \frac{1}{2} \sum_{z,A,B} \phi_A(z) \chi_{\mathrm{AB}} \langle \phi_B(z) \rangle - \frac{1}{2} \sum_{z,A,B,i} \phi_{Ai}(z) \chi_{\mathrm{AB}} \phi_{Bi}^*. \end{aligned} \tag{2A.8}$$

When the system under consideration contains only homopolymers the last term vanishes. This is because if homopolymer chains of type i are constituted of segments of type A, then $\phi_{Bi} = 0$ for all $B \neq A$ and because $\chi_{\mathrm{AA}} = 0$. For a homopolymer system the segment chemical potential of segment type A becomes according to Equation 2A.1:

$$\begin{aligned} \frac{\mu_A}{k_BT} &= \frac{\partial}{\partial \phi_A} \left(\sum_{z,A} \frac{\phi_A(z)}{N_A} \ln N_A C_A - \sum_{z,A} \phi_A(z) \frac{u_A(z)}{k_BT} + \frac{U}{k_BT} \right) \\ &= \frac{1}{N_A} \ln N_A C_A - \frac{u_A(z)}{k_BT} + \sum_B \chi_{\mathrm{AB}} \langle \phi_B(z) \rangle . \end{aligned} \tag{2A.9}$$

Note that all volume fractions were made mutually independent by the introduction of the Lagrange parameters $\alpha_A(z)$ so that $\partial\phi_i/\partial\phi_j$ equals one for $i = j$ and zero otherwise, and $\partial\alpha_i(z)/\partial\phi_j(z) = 0$ for all i, j.

We may also calculate the segment chemical potentials in the homogeneous bulk mixtures I and II. These mixtures are in equilibrium with a homogeneous bulk mixture in which $\phi_A = \phi_A^{\text{ref}}$ and $u_A^{\text{ref}} = 0$ for all segment types $A, B, ...$ In other words, $C_A = \phi_A^{\text{ref}}/N_A$ and (using Equation 2.33):

$$\frac{u_A^I}{k_BT} = -\ln G_A^I = -\frac{1}{N_A}\ln\frac{\phi_A^I}{\phi_A^{\text{ref}}}, \tag{2A.10}$$

For the segment chemical potentials in mixture I we obtain from Equation 2A.9:

$$\frac{\mu_A^I}{k_BT} = \frac{1}{N_A}\ln\phi_A^I + \sum_B \chi_{\text{AB}}\phi_B^I. \tag{2A.11}$$

These chemical potentials differ from the segment chemical potentials in the Flory-Huggins theory for homogeneous bulk mixtures. The segment chemical potential according to the Flory-Huggins theory is defined as $N_A\mu_A^{\text{app}} = \partial F^{\text{FH}}/\partial n_A$. As explained in Chapter 4 in the derivation of Equation 4.2 the segment chemical potential μ_A^{app} is then calculated as

$$\mu_A^{\text{app}} = f + (1-\phi_A)\frac{\partial f}{\partial\phi_A} \tag{2A.12}$$

where $f = F^{\text{FH}}/\sum_A n_A N_A$ and where the volume fractions are mutually dependent.

Appendix 2B Onsager's reciprocal relations

Mass transport driven by chemical potential gradients may be written in the standard form of Onsager's phenomenological equations:

$$J_A = -\sum_B L_{AB}\nabla\mu_B \tag{2B.1}$$

where L_{AA} are the main transport coefficients and L_{AB} are the cross-coefficients describing the coupling between the fluxes. According to Onsager's reciprocal relations we should have $L_{AB} = L_{BA}\ \forall A, B$.

The slow mode flux of Equation 2.26 may be written in the form of Equation 2B.1 by realizing that the summation in Equation 2.26 may also be taken over all segment types except A and by using $\sum_{B\neq A}\Lambda_B = \sum_B \Lambda_B - \Lambda_A$. We then obtain for the slow-mode transport coefficients:

$$L_{AA}^s = \frac{\Lambda_A^2}{\sum_C \Lambda_C} - \Lambda_A \tag{2B.2a}$$

$$L_{AB}^s = \frac{\Lambda_A\Lambda_B}{\sum_C \Lambda_C} \tag{2B.2b}$$

so that Onsager's reciprocal relations are obeyed.

For rewriting the fast mode flux of Equation 2.28 we first add the term $\Lambda_A\sum_B \phi_B\nabla\mu_B$. This term equals zero according to Gibbs-Duhem relation $\sum_B \phi_B \mathrm{d}\mu_B = 0$. Rewriting the

extended Equation 2.28 in the form of Equation 2B.1 yields for the fast mode transport coefficients:

$$L^f_{AA} = \Lambda_A(2\phi_A - 1) \tag{2B.3a}$$

$$L^f_{AB} = \phi_A\Lambda_B + \phi_B\Lambda_A \tag{2B.3b}$$

so that again Onsager's reciprocal relations are obeyed.

Appendix 2C Derivation of Equation 2.42

For a three-component system with $N_A = N_B$ and $\tilde{B}_A = \tilde{B}_B = \tilde{B}_C$, we have a set of two independent fluxes which may be written by the help of Equations 2.34 and either 2.37 or 2.38 as:

$$J_A = -a\nabla\phi_A + b\phi_A\nabla(\phi_A + \phi_B) \tag{2C.1}$$

$$J_B = -a\nabla\phi_B + b\phi_B\nabla(\phi_A + \phi_B) \tag{2C.2}$$

where $a = \tilde{B}k_BT/N_A$ and $b = \tilde{B}k_BT(1/N_A - 1/N_C)$. We want to solve this set for $\phi_A(z)$ and $\phi_B(z)$ with $0 \leq \phi_A(z) + \phi_B(z) \leq 1$ for $z \in [0, M+1]$. The values for $\phi_A(0)$, $\phi_B(0)$, $\phi_A(M+1)$ and $\phi_B(M+1)$ are known.

Summation of the differential equations and defining $\phi_A(z) + \phi_B(z) = h(z)$, we find for $h(z)$:

$$h(z) = \frac{a}{b} \pm \frac{1}{b}\sqrt{a^2 + 2b(k_4 - J_Cz)}. \tag{2C.3}$$

The integration constant k_4 and the flux $J_C = -(J_A + J_B)$ can be calculated from $h(0)$ and $h(M+1)$. $h(z)$ must be positive and for our specific case ($N_A > N_C$) we have $a > 0$ and $b < 0$. Therefore, we must select the minus sign in Equation 2C.3.

Using $h(z)$, we can now solve $\phi_A(z)$ from Equation 2C.1 by the standard procedures of separation of variables and variation of parameters. This introduces a new constant k_5. k_5 and J_A may be calculated from ϕ_A in $z = 0$ and $z = M+1$. J_B is then known from the values for J_C and J_A. $\phi_B(z)$ is simply the difference between $h(z)$ and $\phi_A(z)$, and $\phi_C(z) = 1 - h(z)$.

Chapter 3

Polymer conformations in stationary diffusion through a barrier

The transport of macromolecules through confined space, such as a membrane or a slit, is of interest for biological, industrial and scientific applications. Hindered transport is influenced by the conformations of the diffusing macromolecules. We studied the conformations of homopolymers that diffuse through a barrier from one unconfined bulk mixture to another. By the use of the Mean-Field Stationary Diffusion method we were able to model the barrier in direct contact with the unconfined bulk and to investigate the average conformational properties of an unlimited number of molecules. The membrane is modelled as a region with a reduced available space for diffusing components. This barrier membrane disturbs the ideal coil structure of the polymers dramatically. We either find weakly deformed coils or dramatically deformed conformations, namely inhomogeneous flower conformations. The degree of deformation depends on barrier height, barrier interactions, polymer concentration and driving force, but not on the chain length or barrier width. The latter parameters only affect the fraction of all chains that deform. Our results are particularly important for the experimental characterisation of membrane morphologies, whereby the maximum pore size of a membrane is derived from the size of the largest polymers that are able to cross the membrane. It is thereby usually assumed that the polymers maintain a spherical coil conformation. Our results show that this assumption is incorrect.

3.1 Introduction

When molecules have to travel through a barrier such as a hole, a porous material, or a membrane, we have a case of hindered diffusion or translocation. Hindered macromolecular translocation is a rate-limiting event in various biological processes. For example, the synthesis of proteins in biological cells is preceded by the passage of macromolecular translated gene material (m-RNA) through the nuclear pores. Subsequently, the newly synthesized proteins often have to be transported from one side of a membrane to the other to perform their task. Another example is the injection of macromolecular genetic material (DNA) from a virus head into the host cell [64]. The rate-limiting macromolecular translocation is also of great importance for new drug delivery methods whereby complex molecules have to diffuse through the skin of a patient into the blood stream [65]. Apart from the biologically inspired interest, there is an economically driven interest in hindered macromolecular diffusion. Important technical processes such as separation steps (e.g., by electrophoresis or gel permeation chromatography) and catalytic reactions may heavily depend on the transport characteristics of macromolecules through a barrier. Direct industrial interest in this field may also arise from the synthesis of nanocomposites of polymer and silicate layers. These nanocomposites can be formed by the so-called intercalation process whereby polymers diffuse from their melt into the porous structure of a substrate [66]. Hindered diffusion may be relevant in other fields. Membrane scientists exploit hindered macromolecular diffusion to study the morphology of porous material in solute retention measurements [67]. Scientists in biotechnology attempt to elucidate the sequence of nucleic acids in DNA by making use of the physically and chemically determined translocation time of DNA through an appropriate membrane channel [6, 68, 69].

The hindrance in macromolecular diffusion may originate from hydrodynamic resistance, from volume exclusion or from both. Volume exclusion simply means that part of the total volume is taken by other material; that part is then not available for the macromolecular species.

Interesting aspects of hindered diffusion are the migration times of macromolecules through a barrier and the partitioning of the macromolecules between a porous material and the bulk solution. Even if we only focus on the hindrance through volume exclusion, both aspects still depend on many variables, for example on the length, composition, and flexibility of the translocating macromolecule and on barrier characteristics such as pore sizes, pore distributions, and chemical interactions with translocating molecules. All these variables have in common that they determine the conformation that the macromolecule can or must adopt to be able to diffuse from one side of the barrier to the other.

In the present paper we limit ourselves to the computational study of volume exclusion effects on the conformations of the macromolecules (in our case homopolymers) that are forced to diffuse through a barrier by an imposed concentration gradient. Our results are of direct interest to various modes of barrier crossing, but particularly so for the characterisation of membranes. A standard method to estimate the maximum pore size in a technical membrane is to determine the size of the largest polymer that is able to cross the membrane. It is then generally assumed that the polymers maintain their bulk coil conformation during the translocation and the maximum pore size is related to the size of those coils [67, 70]. We show that already in very simple systems the coil conformation may be significantly disturbed, even in the absence of convection-induced deformation [71]. For sufficiently high barriers, we find so-called flower conformations, where one part

of the chain is stretched, and the other part has a (perturbed) coil conformation. Similar conformations have been found in experiments on long DNA molecules driven from one entropic trap to another [3, 72, 73]. Such conformations, in particular the coil-to-flower transitions, have been studied before at liquid/liquid interfaces [74]-[76]. Flowers have also been found in Monte Carlo simulations of a chain near the exit of a pore [77]. An advantage of our method over Monte Carlo or other simulations is that we obtain the statistical average properties of a macroscopic system in a very efficient way. Our mean-field calculations cover the complete configurational space in a CPU time of minutes. Monte Carlo or Molecular Dynamics simulations are in principle more accurate to follow the transport of a selected molecule, but only a few molecules can be included in the simulations. The study of confined polymers is usually restricted to partition studies [78, 79], to concentration profiles [80]-[82], or to conformational studies of chains that are fully inserted in the confinement [83]-[86]. Chains in a bulk mixture that are in contact with a confinement are studied as well [87]-[90], but little attention has been paid to the conformations [77, 91, 92]. Some studies focus on the probability to cross a barrier by considering the barrier as an infinitely thin sheet that is only penetrable via a hole [93]-[95]. This allows the generalisation of the Kramers approach for barrier crossing, whereby assumptions are needed for the shape of the potential energy curve. In our approach, we fill the gap between the studies on bulk conformations and studies on completely confined conformations at equilibrium; we study the conformations in systems where bulk and barrier are in direct contact and where the number of (diffusing) molecules is unlimited. We do not need to make assumptions about potential energy curves. The potential energy in our approach directly follows from two barrier parameters: its width and its porosity. The latter is represented by the volume fraction taken by barrier material.

The structure of this chapter is as follows: in Section 3.2 we explain the relevant details of the statistical method used to obtain the polymer conformations. As a result of this method, our barrier is of a special character since we can not assign a specific pore size distribution. Section 3.3 presents and discusses the effects of polymer properties and barrier characteristics on the conformations of translocating chains. Section 3.4 summarizes our conclusions.

3.2 Method

3.2.1 General

We use a numerical lattice model to obtain the conformations of polymers that diffuse over a barrier. That model is based upon the rules of statistical thermodynamics. Originally, Scheutjens and Fleer developed the model for equilibrium polymer systems containing interfaces [9], but recently we extended it with dynamics equations to enable the modelling of stationary diffusion as well [96]. We call this extension the Mean-Field Stationary Dynamics (MFSD) method.

In the MFSD method, the polymers are described as a chain of segments, as in the original theory. The length of the chains is measured by the number of segments N. Homopolymers are chains of only one segment type, copolymers are made up of different segment types. Each segment takes one site on a three-dimensional (3D) lattice. A 3D lattice with $K \times L \times M$ sites may be seen as M layers in the z-direction, where each

layer has $K \times L$ lattice sites whose positions are given by coordinates x and y. In our 1D calculations, we are only interested in the fraction of sites in each layer taken by segments of type A, the fraction taken by segments of type B,...etc. Thus, the exact distribution of the different segment types within such a layer is not taken into account, which is typical for a 'mean-field' method. The only relevant position variable is the coordinate z that runs from 0 to M. Moreover, the lattice does not have any boundaries in the other directions ($K \to \infty$ and $L \to \infty$).

The MFSD-method generates segment weighting factors $G_A(z) = \mathrm{e}^{-u_A(z)/k_BT}$, where u is the segment potential. Both G and u are functions of z and the segment type A. These segment weighting factors are the essential information to calculate the chain conformations. They determine the probability for a certain segment to be found at a certain position z. The chain connectivity and the (average) interactions with all other segments are taken into account, as well as some imposed constraints. These constraints are the following: (i) the system is completely filled with segments and thereby incompressible, (ii) the volume fraction of each polymer at $z = 0$ and $z = M$ is fixed at a certain value, and (iii) the system is in a stationary state, so the volume fractions do not change in time. For a particular stationary-state solution the density profile in the system is chosen such that the free energy is minimal. In other words, the optimisation of the partition function under these constraints determines how the volume fractions are calculated from a given set of segment weighting factors. On the other hand, the segment weighting factors depend on the volume fractions through, for example, contact interactions, which are modelled through Flory-Huggins parameters χ. The MFSD-method is a self-consistent field calculation that starts with a choice for the segment potentials u and thus for the weighting factors, then calculates from these the volume fractions in a way that is imposed by the optimisation of the partition function, and subsequently adjusts the segment weighting factors iteratively until the values for the volume fractions are such that all constraints are obeyed.

In the next section we define the system. Special attention is paid to the properties of the barrier. We then explain in Section 3.2.3 how to obtain information about the chain conformations from the segment weighting factors.

3.2.2 System, dynamics and barrier

The system used to study hindered diffusion of polymers is presented in Figure 3.1. Two mixtures I and II, for which we may choose any composition, are brought into contact. These mixtures are ideal sinks and sources for the components in the system, i.e., their compositions do not change in time. If these mixtures have equal compositions and if these compositions correspond to the stable one-phase region in a phase diagram, the system represents the equilibrium state of a bulk mixture. When the mixtures have different compositions, the components will diffuse in the direction determined by the chemical potentials of the segments. We only consider stationary diffusion, with the material fluxes constant in time and space. In other words, there is no time-dependent accumulation of material anywhere in the system. Accumulation in space can occur, as shown later in Figure 3.2.

The flux equations for two different diffusion mechanisms, the slow-mode mechanism and the fast-mode mechanism, are presented elsewhere [96, 97]. These mechanisms become

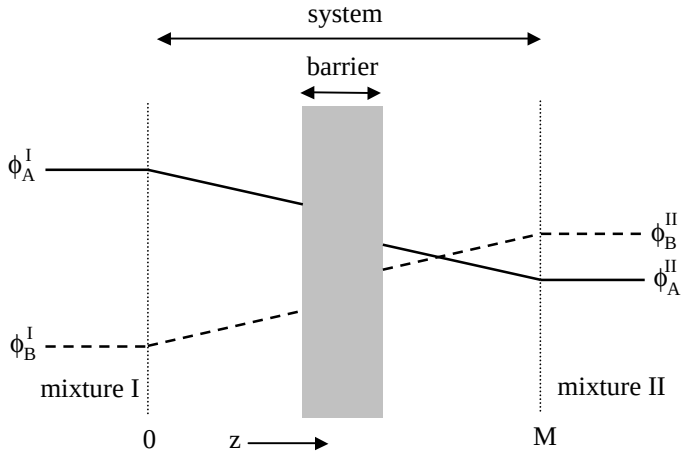

Figure 3.1. The system for hindered diffusion of polymers. The compositions of mixtures I and II are kept at a constant value. The diffusion profile in the system is such that the material fluxes are constant throughout the system. The characteristics of the barrier are discussed in the text.

identical if all segment types have equal mobility coefficients, as will be assumed in the present study. Both diffusion mechanisms may then be described as a 'swap'-mechanism; segments of different types diffuse by exchanging their positions. When we also assume that entanglement effects on the diffusion may be ignored, the flux of segments of type A is given by

$$J_A(z) = -\tilde{B} \sum_j \phi_A(z)\phi_j(z)\nabla \left(\mu_A(z) - \mu_B(z)\right). \tag{3.1}$$

Here, $\tilde{B}$ is the segment mobility coefficient, ϕ_A is the volume fraction of segment type A and $\mu_A(z)$ is the segment chemical potential, calculated as the derivative of the free energy with respect to the number of A-segments in layer z.

The polymers must diffuse over a barrier, which may be located anywhere in the system (cf. Figure 3.1). In the present study, we simply construct the barrier by limiting the available space for the diffusing components. This is achieved by requiring that in a number of lattice layers a certain volume fraction ϕ^* is taken by barrier material ($\phi^* < 1$). The width of the barrier is given by the specified number of lattice layers containing barrier material. The 'height' of the barrier is varied for all diffusing components collectively by varying ϕ^*. The height of the barrier may also be varied for a specific component i by varying the chemical interactions between the barrier material and that component. These interactions are quantified by the Flory-Huggins parameter χ_{i*}. We do not ascribe any structure to the barrier, for instance by specifying specific pore sizes or pore shapes. Due to the 1D mean-field calculations, we can only specify the volume fraction of ϕ^* in layer z and not the distribution of barrier material within that layer. In a 2D version of the MFSD method it would be possible to model, for example, a cylindrical pore.

For a description of the nature of the barrier, we may imagine the barrier as a fluid film, bounded by infinitely thin semi-permeable membranes. These membranes are permeable (in fact even invisible) to all components in mixtures I and II, but completely impermeable

to the barrier material, which is the component that builds up the fluid layer. Thus, these membranes allow a sharp interface between the fluid film and the polymer blends outside the barrier. The fluid film acts as a solvent in which the solubility of the components is suddenly decreased compared to the solubility outside the barrier region. The easiest way to show this solubility drop is by considering the diffusion in a special homopolymer blend. In that blend all polymers have the same chain length and there are no contact interactions; $N_i = N$, $\chi_{\mathrm{ij}} = 0$ and $\chi_{\mathrm{i}^*} = 0$ for all components i and j (athermal system). We used the MFSD-method to calculate the stationary volume fraction profiles in this system in the presence of a barrier. The resulting diffusion profiles are plotted in Figure 3.2. (In the absence of any barrier, we would obtain linear volume fraction profiles in the stationary diffusion regime, even when there would exist concentration gradients [96]). From the volume fractions just outside the barrier and just inside the barrier for profiles as in Figure 3.2 we found that the effect of the barrier is given by a solubility drop, quantified by the partitioning coefficient

$$K_i^{\mathrm{par}} = \frac{\phi_i^{\mathrm{in}}}{\phi_i^{\mathrm{out}}} = 1 - \phi^* \quad \forall i, \tag{3.2}$$

where ϕ^{in} and ϕ^{out} are evaluated at the first barrier layer and at the layer adjacent to the barrier, respectively. There is no such simple relation between the barrier volume fraction and the partitioning coefficient for polymer solutions (where the chain lengths of polymer and solvent are greatly different) or for systems that have a solubility gap ($\chi > \chi^{\mathrm{crit}}$). A more detailed description of the diffusion profiles and flux characteristics is beyond the focus of the present chapter.

The underlying principle of our barrier is the entropy effect (if all χ-parameters are taken zero). Chains that approach the barrier experience a sudden decrease in the number of possible conformations, similar to chains close to a solid wall or inside a cylindrical pore. This is clearly seen by the occurrence of a depletion layer at the outside of the barrier for polymers in solution. The depletion results from the reluctance of polymer chains to reside within the region that limits their entropy. Figure 3.2*a* depicts the volume fraction profiles throughout the system containing a barrier with two different heights. This figure plots the volume fraction profiles for a homopolymer with length $N_A = 1000$ in a solvent with $N_B = 1$. There are no contact interactions; $\chi_{\mathrm{AB}} = \chi_{\mathrm{A}^*} = \chi_{\mathrm{B}^*} = 0$. In Figure 3.2*b* we zoom in into the region just outside the barrier. The curves in this figure illustrate the similarity between the depletion layer next to a solid wall (dotted curve) and the depletion layers next to the (fluid) barrier. The dotted curve was obtained by standard Scheutjens-Fleer calculations. The solid curves in Figure 3.2 were calculated by MFSD-calculations. The depletion at the solution sides resembles the depletion due to the solid wall if the barrier is sufficiently dense, in other words if ϕ^* is sufficiently large. In fact, for the solid wall we have $\phi^* = 1$. At solid walls, the profile of the depletion layer is known to be given approximately by $\phi_A(z) = \phi_A^{\mathrm{bulk}} \tanh^2\left(\frac{z+p}{\xi}\right)$, where the so-called proximal length p is related to the adsorption energy of the wall and where ξ is the correlation length in the bulk [98, 99]. It can be anticipated that a similar equation can be derived for the depletion layer at the barrier, where p will be related to ϕ^* and thereby to the potential energy associated with the barrier (u_A^* in Section 3.3.7).

The entropic effect of the barrier is also illustrated by the 'accumulation layer' (in contrast to the depletion layer) just inside the barrier (see Figure 3.2*c*). Chains that

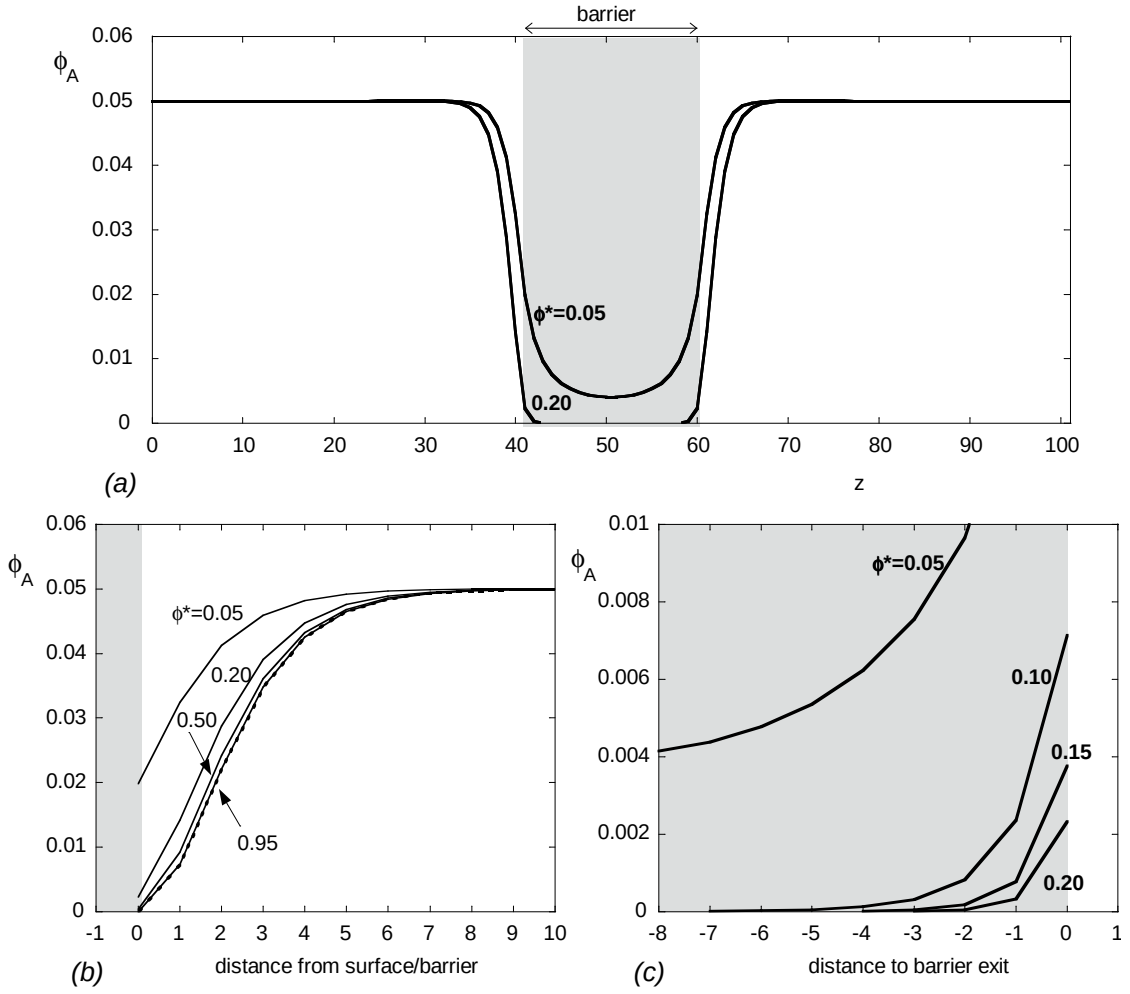

Figure 3.2. Volume fraction profiles in the presence of a fluid barrier or a solid wall. (a): Profiles in the total system for $\phi^* = 0.05$ and $\phi^* = 0.20$. (b): Depletion layers near a solid wall (dotted curve) and near a fluid barrier with varying barrier densities. (c): Accumulation layer within a fluid barrier with varying barrier densities. The parameters are: $N_A = 1000$, $N_B = 1$, $\chi_{\mathrm{AB}} = \chi_{\mathrm{A}^*} = \chi_{\mathrm{B}^*} = 0$, $\phi_A^{\mathrm{bulk}} = \phi_A^I = \phi_A^{II} = 0.05$.

reside within the barrier experience a sudden increase of their conformation possibilities when they approach the exit of the barrier. Therefore, there is an excess of polymer near the exit of the barrier with respect to the amount of polymer in the centre of the barrier. The depletion layer and accumulation layer are not symmetrical with respect to the barrier/blend transition, since ϕ_A^{bulk}, which appears in the equation for the depletion profile, is independent of ϕ^*, whereas ϕ_A^*, the volume fraction in the barrier interior, decreases with increasing ϕ^*. The analogy between the accumulation layer just inside the barrier and the adsorption layer next to an adsorbing wall is also interesting. The equation $\phi_A(z) = \phi_A^{\mathrm{bulk}} \coth^2\left(\frac{z+p^*}{\xi^*}\right)$ may serve as an 'educated guess' for the accumulation profile, where p^* is related again to ϕ^* and ξ^* to the correlation length for chains in the barrier.

3.2.3 Evaluation of chain conformations

Information about the chain conformations may be obtained through the concept of 'conditional volume fractions'. We first explain how the usual (unconditional) volume fractions are computed.

The MFSD-method calculates the segment weighting factors $G_i(z,s)$. The subscript i refers to the molecule type, z is the position coordinate, and s is the ranking number of the segment in the chain. The parameter s runs from 1 to N_i. Since we consider monomers or monodisperse homopolymers, segments of type A always belong to only one molecule type. The definition of the weighting factor is:

$$G_A(z,s) = \exp -\frac{u_A(z)}{k_B T}. \tag{3.3}$$

Here, k_B is the Boltzmann constant, T the temperature, and $u_A(z)$ is the segment potential felt by segment A in z. The segment potential depends on the interactions with other segment types and on the space-filling potential α_A:

$$\frac{u_A(z)}{k_B T} = \alpha_A(z) + \sum_B \chi_{\mathrm{AB}} \left\langle \phi_B(z) - \phi_B^{\mathrm{ref}} \right\rangle. \tag{3.4}$$

The space-filling potential α_A ensures that the lattice is completely filled. For example, a polymer melt near a non-interacting solid wall needs low values for α in the lattice layer next to that wall, otherwise the components would avoid this lattice layer due to the entropy loss of polymers. In the standard Scheutjens-Fleer method, α_A does not depend on the segment type and the subscript A can be dropped. In MFSD, the space-filling potential only depends on segment types if mixtures I and II have different compositions. The volume fraction ϕ_B^{ref} refers to a reference mixture which can be chosen arbitrarily. The angular brackets in $\langle \phi_B(z) \rangle$ generally denote the average over three layers $z-1$, z, $z+1$:

$$\langle \phi_B(z) \rangle = \lambda_{-1}\phi_B(z-1) + \lambda_0 \phi_B(z) + \lambda_1 \phi_B(z+1). \tag{3.5}$$

The average over the three layers is weighted by λ's which account for the number of contacts for a segment in layer z. For a cubic lattice $\lambda_0 = \lambda_{z\to z} = 4/6$ and $\lambda_{-1} = \lambda_{z\to z-1} = \lambda_{z\to z+1} = \lambda_1 = 1/6$.

From $G_A(z,s)$ we may calculate the end-segment weighting factors $G_A(z,s|1)$ for chains ('walks') starting from $s=1$ and $G_A(z,s|N_A)$ for walks starting from $s=N_A$. Here, $G_A(z,s|1)$ is the weighting factor for the last segment of a chain of length s, where segment s is in layer z, and segment 1 may be anywhere in the system. Similarly, $G_A(z,s|N_A)$ is the weighting factor for the first segment of a chain of length $N_A - s + 1$, where the first segment (s) is in layer z, and the last segment (N_A) may be anywhere. The end-segment weighting factors follow from the segment weighting factors $G_A(z,s)$ according to a propagation scheme which incorporates the chain connectivity. The starting conditions are $G_A(z,1|1) = G_A(z,1)$ and $G_A(z,N_A|N_A) = G_A(z,N_A)$, and for the consecutive segments we have

$$G_A(z,s|1) = G_A(z,s)\,\langle G_A(z,s-1|1)\rangle \tag{3.6a}$$

$$G_A(z,s|N_A) = G_A(z,s)\,\langle G_A(z,s+1|N_A)\rangle \tag{3.6b}$$

Note that this (first-order Markov) propagation scheme allows immediate step reversals. A more refined scheme is possible [17], but is not used in the present study.

By combining two end-segment weighting factors we can calculate $\phi_A(z,s)$, the volume fraction in layer z for segment s of molecule A. Connecting the chain parts from 1 to s and from s to N_A and correcting for the double counting of segment s we find

$$\phi_A(z,s) = C_A \frac{G_A(z,s|1)G_A(z,s|N_A)}{G_A(z,s)}. \tag{3.7}$$

where C_A is a normalisation factor given by the composition of the reference mixture.

Expressions for so-called 'conditional volume fractions' can be derived in a similar way. An example of a conditional volume fraction is $\phi_A(z,s|z',s')$. This evaluates the volume fraction $\phi_A(z,s)$ for a chain that has segment s' in layer z':

$$\phi_A(z,s|z',s') = C_A \frac{G_A(z',s'|1)G_A(z,s|z',s')G_A(z,s|N_A)}{G_A(z,s)G_A(z',s')} \quad \text{for } s' \leq s \tag{3.8a}$$

$$\phi_A(z,s|z',s') = C_A \frac{G_A(z,s|1)G_A(z,s|z',s')G_A(z',s'|N_A)}{G_A(z,s)G_A(z',s')} \quad \text{for } s' \geq s \tag{3.8b}$$

The propagation scheme of Equation 3.6 is used to calculate $G_A(z,s|z',s')$, but the starting conditions are

$$G_A(z,s'|z',s') = \begin{cases} G_A(z',s') & \text{for } z = z' \\ 0 & \text{for } z \neq z' \end{cases} \tag{3.9}$$

The segment weighting factors and conditional volume fractions are calculated slightly differently near the two bulk mixtures at the boundaries of the system. As stated in Chapter 2 we have an inconsistency at the boundaries at $z = 0$ and $z = M$. Appendix 3A explains the consequences for the calculation of the conditional volume fractions and for the the chain conformations near the boundaries. One expects artifacts if there exist large density gradients near the boundaries. We consider systems where these gradients are typically small so that these problems do not affect our results. Moreover, we are interested in the conformations of chains for layers far from the system boundaries at $z = 0$ and $z = M$.

3.3 Results and discussion

3.3.1 General conformational changes

We start with the description of the general conformational changes during stationary hindered diffusion of polymer chains. Figure 3.3 presents the system under consideration: the two bulk mixtures are in equilibrium. They contain a polymer component with chain length $N_A = 100$ and volume fraction $\phi_A = 0.05$ in a monomeric solvent ($N_B = 1$, $\phi_B = 0.95$). There are no contact interactions ($\chi_{ij} = 0$). The barrier in the centre of the system reduces the available space by 20% ($\phi^* = 0.20$) for 19 of the 149 lattice layers. The volume fraction profiles in Figure 3.3 show that the polymer volume fraction ϕ_A^* (nearly) vanishes in the barrier region. Also, the concentration of solvent decreases significantly, from $\phi_B = \phi_B^{\text{bulk}} = 0.95$ to a value $1 - \phi^* - \phi_A^* \approx 0.8$.

The chain conformations can be monitored by considering the conditional volume fractions $\phi_A(z,s|z',s')$. For convenience we normalise these volume fractions as

$$P_A(z,s|z',s') = \frac{\phi_A(z,s|z',s')}{\sum_{z=0}^{M} \phi_A(z,s|z',s')}, \tag{3.10}$$

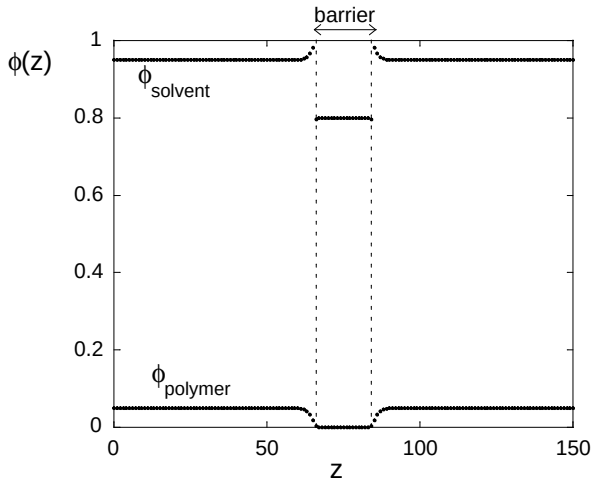

Figure 3.3. The volume fraction profiles in a simple system for which we illustrate the general chain deformations in stationary diffusion: polymers ($N_A = 100$) in solution ($N_B = 1$), $\phi^* = 0.20$, barrier width=19, $\phi_A^I = \phi_A^{II} = 0.05$, $\chi_{\mathrm{AB}} = \chi_{\mathrm{A}^*} = \chi_{\mathrm{B}^*} = 0$.

so that we obtain the 'conditional segmental probabilities'. The profiles of these probabilities are plotted in Figure 3.4. The difference between the four diagrams in this figure is the position of segment $s' = 1$. In each diagram the profiles for various values of s are plotted. Obviously the curves flatten for increasing $|s - s'|$, as is clearly seen in Figure 3.4*a*. The Gaussian profiles in Figure 3.4*a* illustrate that the chains that have their first segments sufficiently far from the barrier ($s' = 1$ in $z' = 30$) adopt a coil structure. Closer to the barrier, the coil starts to deform in order to avoid the barrier region ((Figure 3.4*b*). Interesting conformational deformations occur for chains that have some segments within the barrier as in Figures 3.4*c* and 3.4*d*. If $s' = 1$ is in the centre of the barrier ($z' = 75$), the next segments are forced to be in the adjacent layers. The higher the segment number, the larger its preferred distance from $z' = 75$. Thus, the chain stretches. For sufficiently high ranking numbers, the chain escapes from the barrier, either at the left or at the right side of the barrier. The part of the chain that has escaped from the barrier remains close to the barrier. We call these conformations 'flowers' as sketched in Figure 3.5. The stem of the flower is formed by the stretched part of the chain within the barrier. The part of the chain that has escaped forms the crown of the flower. For the system presented in Figure 3.3, where $\Delta\phi = \phi^{II} - \phi^I = 0$, most chains stretch to the left if $s = 1$ is at the left of the barrier centre and most to the right if $s = 1$ is at the right of the centre. Both directions are equally probable if $s = 1$ is at the centre.

To investigate whether some segments are preferred over other segments in lattice layer z we calculate the segmental preferences $p(z, s)$:

$$p(z, s) = N_A \frac{\phi_A(z, s)}{\phi_A(z)}. \tag{3.11}$$

The preference $p(z, s)$ equals unity for all s if all segments of polymer A have the same probability in layer z (which is the case in the homogeneous bulk solution). The contour

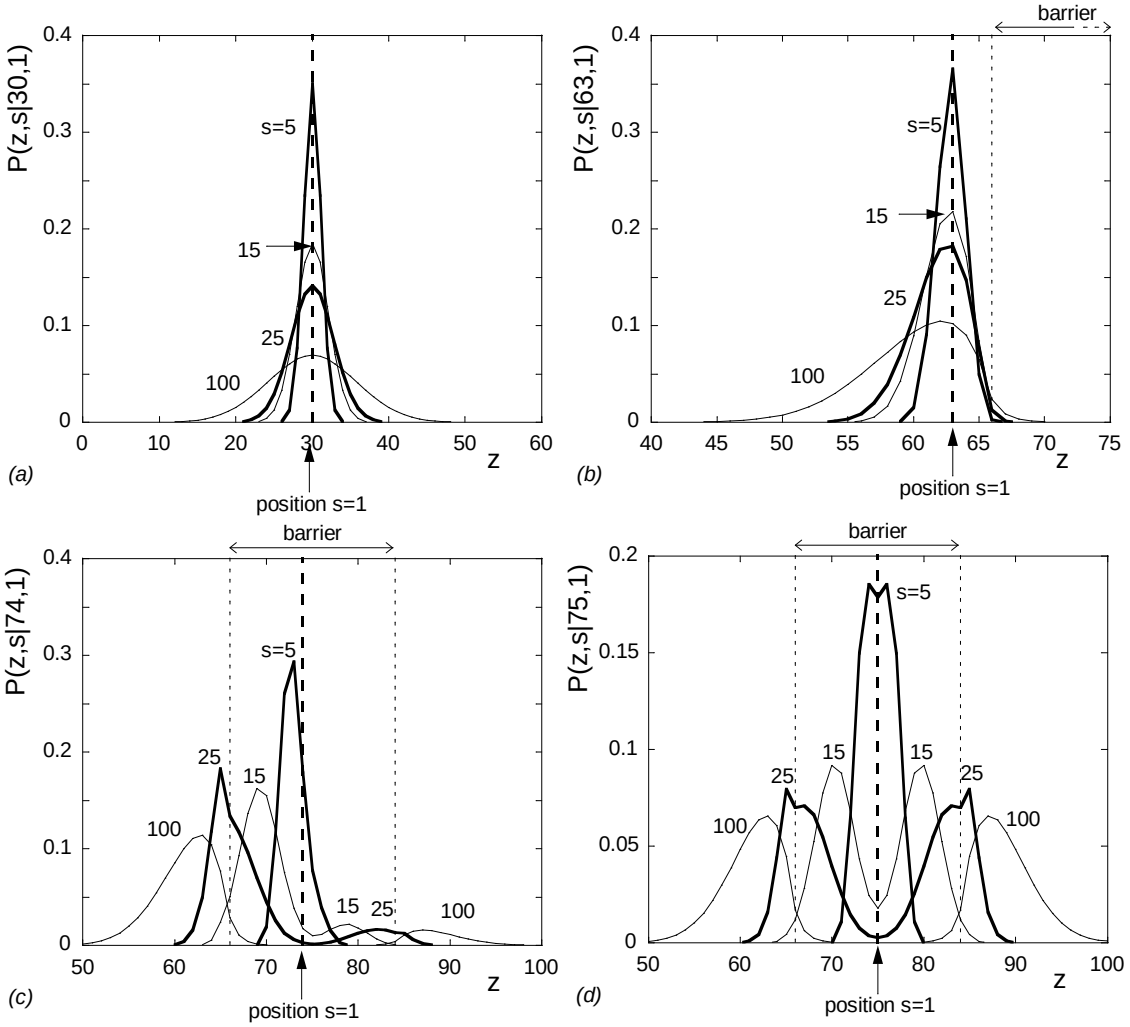

Figure 3.4. The conditional segmental probability profiles for the system of Figure 3.3, with the centre of the barrier in $z = 75$. *(a)*: Conformations far from the barrier, *(b)*: conformations near the barrier, *(c)*: conformations for first segment within the barrier ($s' = 1$ at $z' = 74$), *(d)*: conformations for first segment in the centre of the barrier ($s' = 1$ at $z' = 75$).

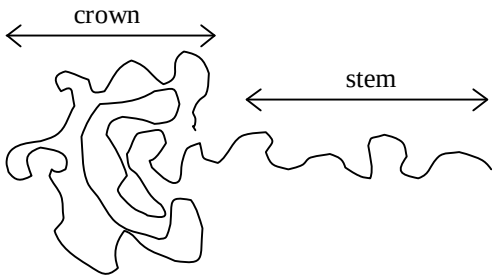

Figure 3.5. Sketch of the flower conformation that a chain adopts at the transition between the barrier and the solution, where the stem is found within the barrier and the crown outside the barrier.

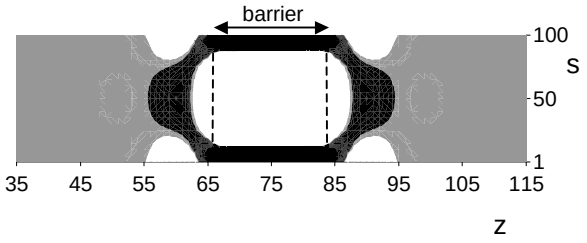

Figure 3.6. Segmental preferences for the system of Figure 3.3. Grey regions: $0.995 < p(z,s) < 1.005$, white regions: $p(z,s) < 0.995$, black regions: $p(z,s) > 1.005$.

plot in Figure 3.6 presents the values of $p(z,s)$ as a function of s and z. Dark regions in this plot indicate a preference ($p(z,s) > 1$) and white regions a shortage ($p(z,s) < 1$) of segment s. In the grey regions there exists no (significant) preference. The symmetry in Figure 3.6 in the direction of z is due to the identical bulk compositions. The symmetry in the direction of s is due to the properties of homopolymers; segments $s = 1$ and $s = N_A$ have the same distribution. The barrier clearly exhibits a preference for end segments (s close to 1 or close to N_A). Middle segments are underrepresented. Outside the barrier, distortions of segmental contributions are found only close to the barrier. It is seen that chains tend to direct their ends towards the barrier. These chains are prepared for barrier entrance in such a way that so called 'hair pin' conformations are avoided. Such hair pin conformations would have some middle segments within the barrier and two tails sticking out of the barrier.

The highly preferred flower-conformations, combined with the preference for end segments in the centre of the barrier, suggest that chains that permeate through the barrier must suddenly change the direction of their flower. However, in equilibrium systems, such translations will be rare, since there is no chemical potential gradient which forces the chains to diffuse. In the next sections we discuss the influence of various variables on the chain conformations, where we also consider stationary diffusion between two bulk systems that are not in equilibrium.

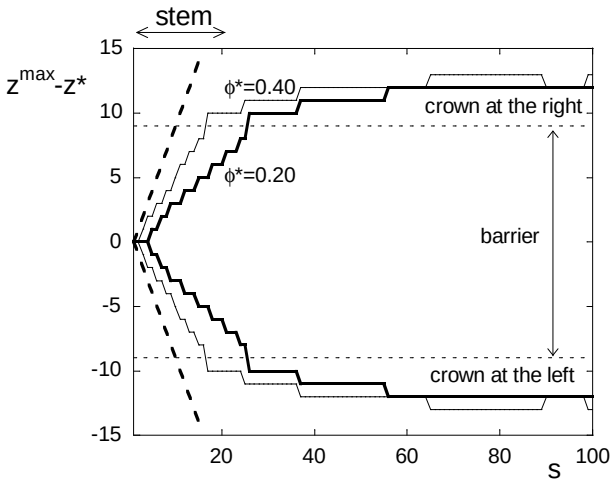

Figure 3.7. Location of the maxima of $\phi_A(z, s|75, 1)$ showing the chain stretching for chains that have their first segment in the centre of the barrier. The system is the same as in Figure 3.3. Chain stretching is maximal if the slope equals that of the dashed line. The blob size ξ of the stretched stem is equal to the slope $\mathrm{d}s/\mathrm{d}z$ of the linear part for small s.

3.3.2 Barrier height

The height of the barrier can simply be adjusted by varying ϕ^*. It may be expected that the stem of the flower conformations will stretch stronger for higher ϕ^*. Chain stretching can be quantified by the notion of blob size ξ. The stem of the flower is described as a chain of blobs that behave Gaussian on their own length scale. The stronger the stretching, the smaller the blob size. By calculating $\phi(z, s|z', s')$ for z' within the barrier region, we may obtain the first segment number s_{out} that escapes from the barrier and to take part in the crown of the flower starting at $z = z_{\mathrm{out}}$. The S segments between s' and s_{out} form the stem that stretches over $Z = |z' - z_{\mathrm{out}}|$ layers. The blob size can then be calculated as $\xi = S/Z$; here ξ acts as a stretching parameter. A simple scaling argument for the blob size will be discussed in Section 3.3.7.

We find the first segment that prefers to escape from the barrier by calculating the positions of the local maxima of $\phi(z, s|z', s')$. In Figure 3.7 the positions of these local maxima are plotted as a function of s for a system as in the Figure 3.3, with $\phi^* = 0.20$ ($s_{\mathrm{out}} = 25$) and $\phi^* = 0.40$ ($s_{\mathrm{out}} = 17$). The first segment of each chain is in the centre of the barrier, thus a chain may stretch either to the right or to the left, so that we have two curves for each ϕ^* in Figure 3.7. The higher the ranking number s, the further out the maximum of $\phi(z, s|z', s')$ is found. Outside the barrier, the position of the maximum is independent of s (for $s > s_{\mathrm{out}}$), meaning that the crown is an unperturbed coil. Figure 3.7 shows that the higher ϕ^*, the smaller $s' - s_{\mathrm{out}}$, thus the stronger the stretching of the chain. The slopes of Figure 3.7 represent the blob sizes of the stretched part of the chain. Figure 3.8 presents these blob sizes as function of ϕ^*. The barrier must be sufficiently high to find chain deformations. With increasing ϕ^*, the concentration of polymer in the centre of the barrier decreases faster than the blob size. Thus the number of chains in the barrier must decrease if the barrier height increases.

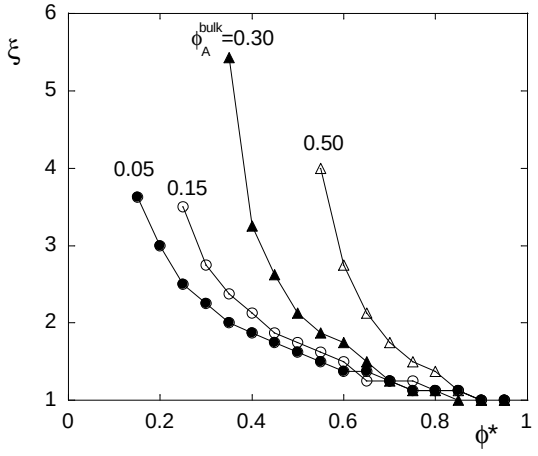

Figure 3.8. Blob sizes as a function of barrier height for various bulk concentrations of polymer ($\phi_A^{\text{bulk}} = \phi_A^I = \phi_A^{II}$). The other parameters are the same as for Figure 3.3. Curves have been drawn to guide the eye.

3.3.3 Interactions inside the barrier

The barrier height can be adjusted for a specific component i by adjusting the contact interaction between i and the barrier, as expressed by the parameter $\chi_{\text{i}*}$. The volume fractions of other components in the system will also be influenced, but each component may react differently, depending for example on its chain length. For a polymer solution with $N_A = 100$ and $N_B = 1$ we varied either $\chi_{\text{A}*}$ with $\chi_{\text{B}*} = 0$ or we varied $\chi_{\text{B}*}$ with $\chi_{\text{A}*} = 0$. Increasing $\chi_{\text{A}*}$ for given ϕ^* has the effect of increasing the barrier. As expected, Figure 3.9 shows that the stretching is stronger (smaller blob size) for higher barriers, i.e. for higher $\chi_{\text{A}*}$. As we will see in Figure 3.13, the blob size increases for increasing $\chi_{\text{A}*}$, which lowers the barrier for the polymer A. With increasing $\chi_{\text{A}*}$ the polymer is not only forced to stretch more strongly, but also to increase its fraction of stretched chains. A measure for this fraction is

$$f_{\text{out}}(N_A|z', s') = \sum_{z \notin \text{barrier}} P_A(z, N_A|z', s') \tag{3.12}$$

since (most of) the stretched chains will have $s = N_A$ outside the barrier. The fraction of chains with $s = N_A$ outside the barrier is plotted as a function of $\chi_{\text{A}*}$ also in Figure 3.9. Note that $f_{\text{out}}(N_A|z', s')$ is only a rough measure for the fraction of stretching chains, since also coil conformations around $z' = 75$ have a small contribution to $f_{\text{out}}(N_A|z', s')$. The fraction suddenly decreases with decreasing $\chi_{\text{A}*}$ at the moment that we can not longer identify the blob size. The blob size can not be identified any more if the stretching is so weak that $\phi_A(z, s|75, 1)$ only has a visible maximum for $z = z'$.

The interactions with the barrier are not only felt within the barrier, but also by segments in the two solution layers adjacent to the barrier. We therefore may expect a significant effect of $\chi_{\text{A}*}$ and $\chi_{\text{B}*}$ on the segment preferences $p(z, s)$ in these layers. The segmental contributions to the volume fractions are plotted in contour plots for various $\chi_{\text{A}*}$ in Figure 3.10. For comparison, Figure 3.11 shows similar contour plots for a

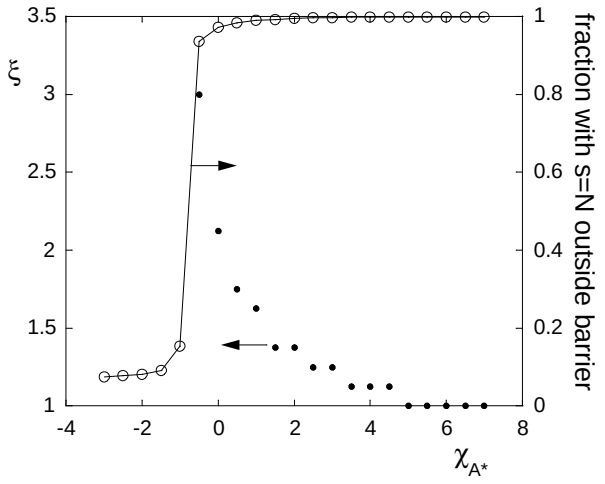

Figure 3.9. The blob size as a function of χ_{A^*} (black dots) and the fraction of chains that have their end segment outside the barrier if their first segment is in the centre (open circles and line). Parameters: $N_A = 100$, $N_B = 1$, $\phi_A^I = \phi_A^{II} = 0.05$, $\phi^* = 0.30$, barrier width = 19 lattice layers, $\chi_{AB} = \chi_{B^*} = 0$.

polymer solution next to a solid impenetrable wall for different polymer-wall interactions. Figure 3.10*a* is nearly the same as Figure 3.6. Both figures are characteristic for systems containing flowers. The segmental contributions to the volume fractions outside the barrier are comparable to those near a low-attractive, inert or rejective solid wall (see Figure 3.11 for $\chi_{A^*} = -1$ or $\chi_{A^*} = 0$). We obtain a segment preference pattern as for a polymer adsorbing on a solid wall if we increase the affinity of the barrier material to $\chi_{A^*} = -1.3$ (Figure 3.10*b* and Figure 3.11 for $\chi_{A^*} = -2$ or $\chi_{A^*} = -1.5$). The preference for middle segments next to the barrier or the wall can be explained by the presence of tails with their ends relatively far from the surface [10]. Therefore, middle segments are preferentially adsorbed, and the chain parts with the end segments stick into the solution. Increasing the attractiveness further results in patterns that are unique for low barriers. In contrast to flower-forming barriers, the low barriers prefer middle segments (Figure 3.10*c*). Despite the reduced available space, the barrier region is made attractive for polymer segments by the negative value of χ_{A^*}. This can clearly be seen in Figure 3.12, where we evaluated the direction of the chains by calculating the fractions of chains with $s = 1$ in z' that have their last segment either left or right of z':

$$f_{\text{left}}(N_A|z',1) = \sum_{z=0}^{z'-1} P_A(z, N_A|z',1), \tag{3.13a}$$

$$f_{\text{right}}(N_A|z',1) = \sum_{z=z'+1}^{M} P_A(z, N_A|z',1). \tag{3.13b}$$

Without any distortion, both directions are equally probable as can be seen for z' at some distance from the barrier in Figures 3.12*b* and 3.12*c*. With some simple statistics it is

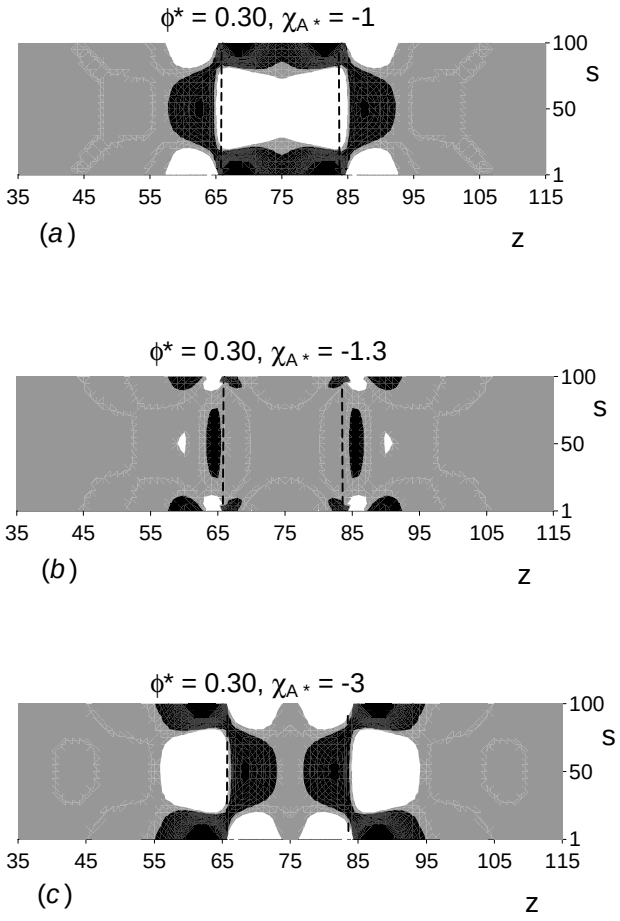

Figure 3.10. Contour plots of $p(z, s)$ for the system of Figure 3.9 with *(a)*: $\chi_{\mathrm{A}*} = -1$, *(b)*: $\chi_{\mathrm{A}*} = -1.3$, *(c)*: $\chi_{\mathrm{A}*} = -3$.

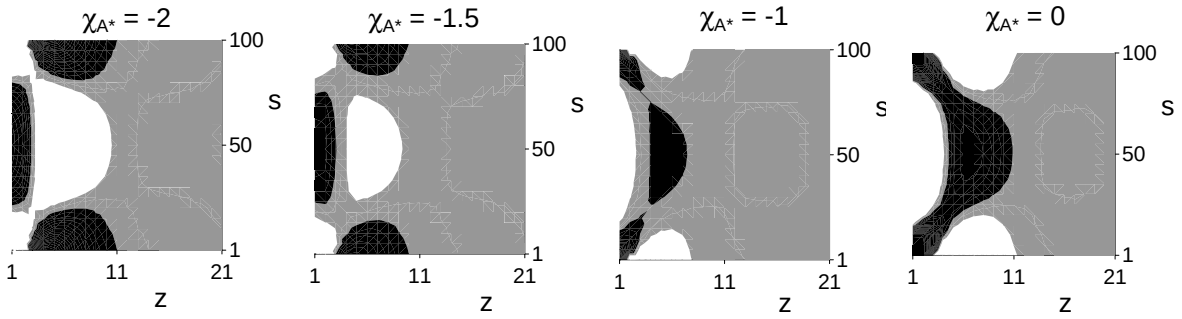

Figure 3.11. Contour plots of $p(z, s)$ for a polymer solution near a solid wall at $z = 0$. The interactions between the polymer and the wall are indicated. $N_A = 100$, $N_B = 1$, $\phi_A^{\mathrm{bulk}} = 0.05$, $\chi_{\mathrm{AB}} = \chi_{\mathrm{B}*} = 0$.

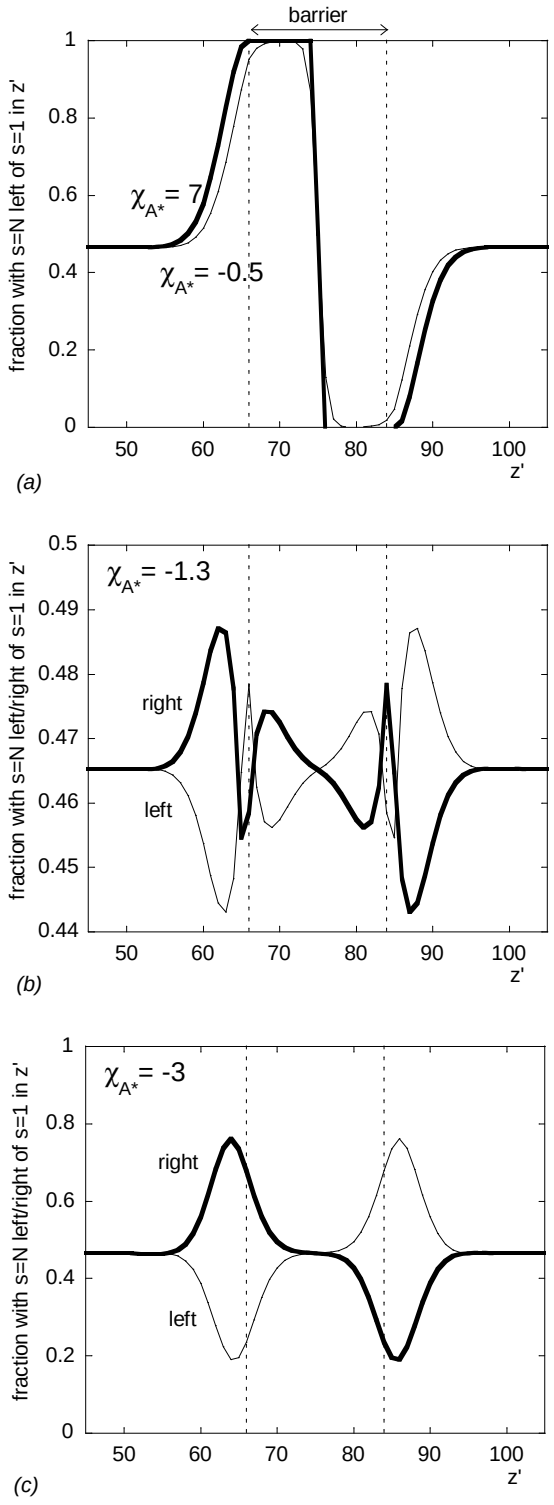

Figure 3.12. The directions of chains that have their first segment in layer z' for different values of χ_{A*}. The system is the same as for Figures 3.9 and 3.10.

found that about $46,5\%$ of unperturbed coils have $N_A = 100$ at the left of $s = 1$, and an equal percentage have $N_A = 100$ at the right. These percentages are calculated as $\frac{1}{2} * [1 - P_A(z', N_A|z', 1)]$ with

$$P_A(z', s|z', 1) = \sum_{i=0}^{i\max} \lambda_0^{(s-1-2i)} \lambda_1^{2i} \binom{s-1}{2i} \binom{2i}{i}, \tag{3.14}$$

where $i\max$ equals $\frac{1}{2}(s-1)$ for s odd and $\frac{1}{2}s-1$ for s even. For the derivation of Equation 3.14 see Appendix 3B. Figure 3.12a refers to flower-forming barriers. For convenience, only the fraction of chains going to the left is shown. Chains with their first segment within the barrier escape from the barrier. In accordance with the observation in Figure 3.4, the flowers change their direction for $s = 1$ in the centre of the barrier. Chains that have their first segment near the barrier have a disturbed coil conformation to avoid the barrier. Figure 3.12b corresponds to Figure 3.10b, which resembles an attractive solid wall. Indeed, we see in Figure 3.12b that polymers that approach the barrier are attracted by the barrier. Chains with one of their ends within the barrier prefer to reside within the barrier, taking advantage of the attractive barrier material (by the negative term $\chi_{A*}\phi^*$ in Equation 3.4). Only when they have their first segment in the first layer of the barrier, they prefer to escape, taking advantage of the available space and a smaller contribution of attractive barrier material (the term $\lambda_1\chi_{A*}\phi^*$ in Equation 3.4). For $\chi_{A*} = -3$, as in Figure 3.12c the barrier is attractive for all chains, also if $s = 1$ is in the first layer of the barrier.

3.3.4 Polymer concentration

The chain deformations depend on the concentration of polymer, as shown already in Figure 3.8. Figure 3.13 shows both the blob size and $f_{\text{out}}(N_A|75, 1)$ as a function of ϕ_A^{bulk} for two values of χ_{B*}. From this figure it is observed that the larger the bulk concentration of polymer, the smaller the chain deformations. The blob size increases and the fraction of stretching chains decreases with increasing polymer concentration (see also Section 3.3.7). The highest polymer concentration is obtained for pure polymer melt ($\phi_A^{\text{bulk}} = 1$) or for a polymer blend where all components have equal chain lengths. In the polymer melt we only see coil deformations if the polymer resides close to the exit of the barrier region or if the barrier width is small compared to the coil size, e.g. if the barrier constitutes 10 layers and $N = 100$. In case of a polymer solution, the solvent competes with the polymer component to fill the barrier region and it wins due to the entropy loss for polymers. This greatly reduces the concentration of polymer within the barrier compared to systems with pure polymer. When, in the presence of a solvent, the polymer can avoid the barrier, it does so by adopting flower conformations. When, in the absence of a solvent, the polymer is forced to fill the barrier, its volume fraction does not reduce sufficiently to adopt flower conformations. Note, especially from Figure 3.8 but also from Figure 3.13, that flowers usually occur for $\chi_{A*} = \chi_{B*} = 0$ only if $\phi_A^{\text{bulk}} < \phi^*$.

Since the chain conformations depend on the polymer concentration ϕ_A^* within the barrier, it may be expected that the parameter χ_{AB} also influences the conformations. This parameter describes the polymer-solvent interactions. When χ_{AB} is sufficiently high, there will be a miscibility gap. Phase separation will occur for a range of concentrations of polymer A in the solvent B. An interface may develop somewhere between the two bulk

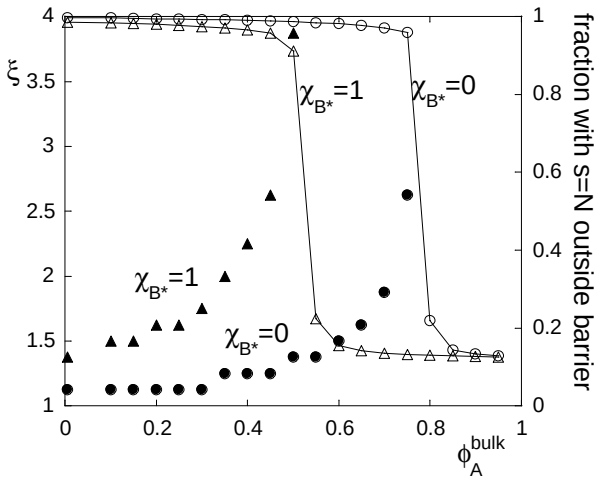

Figure 3.13. The blob size as a function of $\phi_A^{\text{bulk}} = \phi_A^I = \phi_A^{II}$ (black marks) and the fraction of chains that have their end segment outside the barrier if their first segment is in the centre of the barrier (open marks with lines). Circles: $\chi_{\text{B}^*} = 0$, triangles: $\chi_{\text{B}^*} = 1$. $N_A = 100$, $N_B = 1$, $\phi^* = 0.80$, barrier width = 19 lattice layers, $\chi_{\text{AB}} = \chi_{\text{A}^*} = 0$.

mixtures I and II, with a polymer-rich phase at one side of the interface and a solvent-rich phase at the other. The position of this interface is affected by the position of the barrier. In other words, ϕ_A^* (and thus the average chain conformation) depends on the position of the barrier relative to the position of the liquid/liquid interface.

3.3.5 Driving force

The driving force for diffusion can simply be varied by adjusting the composition of one of the bulk mixtures. Obviously, this also changes the polymer concentration in the barrier region. In Figure 3.14 the volume fraction profile for the polymer is shown for three values of $\Delta\phi_A = \phi_A^{II} - \phi_A^I$, with $\phi_A^I = 0.05$ and $\phi^* = 0.50$. Depending on the barrier height (ϕ^*) and the driving force $\Delta\phi_A$, the volume fraction profiles remain flat outside the barrier (as for $\Delta\phi_A = 0.40$ in Figure 3.14), or they may have three different gradients at the left, the right, and in the interior of the barrier (as for $\Delta\phi_A = 0.50$ and $\Delta\phi_A = 0.90$ in Figure 3.14). If the barrier is sufficiently high or the driving force is not too large ($\Delta\phi_A \leq 0.4$ in Figure 3.14), the volume fraction profile remains flat and the discontinuities at the barrier boundaries account for the transition between low and high ϕ_A of the bulk mixtures.

Flower conformations are only found if the gradient of $\phi_A(z)$ is small outside the barrier. When $\phi_A^I \neq \phi_A^{II}$ the blob size depends on the direction of the stretched stem. This is illustrated by the conditional segmental probability profiles in Figure 3.15 where ϕ^* and $\Delta\phi_A$ are chosen such that the volume fraction profile ϕ_A remains flat outside the barrier. Moreover, $\phi_A^I < \phi_A^{II}$. In this figure it is seen that if $s = 1$ is at $z = 90$, the flower may stretch both to the right and to the left. From the asymmetry of the $s = 5$ and $s = 15$-profiles with respect to $z' = 90$ it is observed that a stem going to the left stretches stronger than a stem going to the right, thus the flowers to the left have a

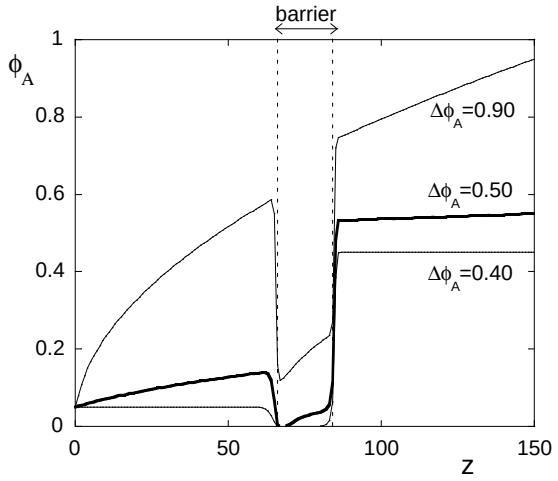

Figure 3.14. Volume fraction profiles for varying $\Delta\phi_A$. $N_A = 100$, $N_B = 1$, $\phi^* = 0.50$, barrier width = 19 layers, $\chi_{\mathrm{AB}} = \chi_{\mathrm{A}^*} = \chi_{\mathrm{B}^*} = 0$.

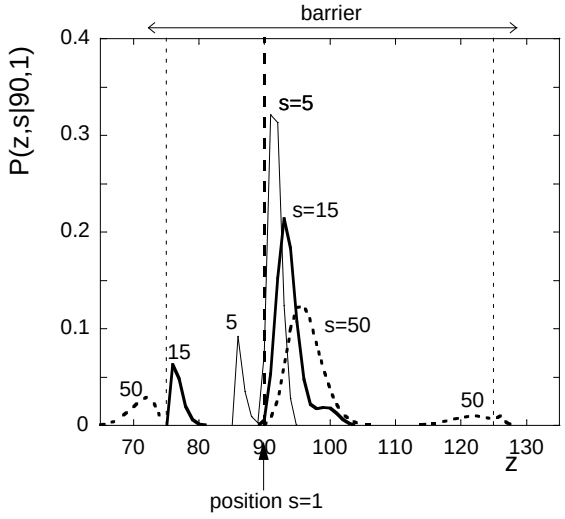

Figure 3.15. The conditional segmental probability profiles for a system with $\Delta\phi_A = 0.80$, showing the occurrence of deformed coils and flowers. The other parameters are $\phi_A^I = 0.10$, $\phi_A^{II} = 0.90$, $\phi^* = 0.95$, $N_A = 100$, $N_B = 1$, barrier width = 51 layers, $\chi_{\mathrm{AB}} = \chi_{\mathrm{A}^*} = \chi_{\mathrm{B}^*} = 0$.

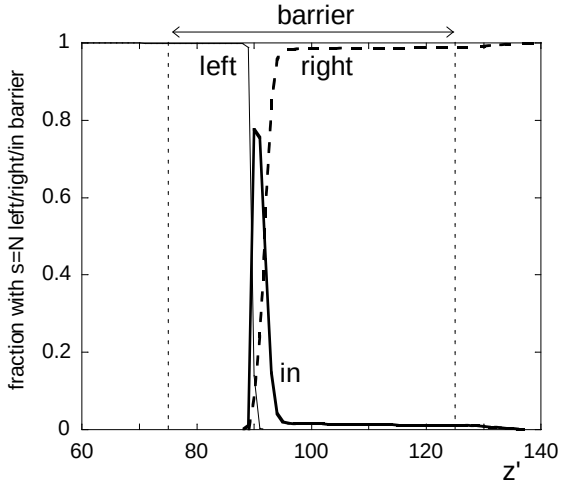

Figure 3.16. Fraction of chains that have their last segment either left or right of the barrier or in the barrier, given that their first segment is in layer z'. The system is the same as in Figure 3.15.

smaller blob size than the flowers to the right. This is due to the fact that the barrier potential u_A^* differs at the left and right side of the barrier: $u_A^* = u_A(\text{in}) - u_A^I$ is larger than $u_A^* = u_A(\text{in}) - u_A^{II}$ (see also Section 3.3.7). However, given the direction of the flower, the blob size is independent of the position of $s' = 1$.

Apart from flower conformations, we may also find deformed coils within the barrier. In these conformations, the chains remain in the barrier, but prefer a direction towards the higher ϕ_A^{bulk}. Such a conformation is shown in Figure 3.15 by the central peak in $P_A(z, s|90, 1)$ for $s = 50$. The two other peaks for $s = 50$ correspond to flower conformations.

In Figure 3.16 we plotted for every position of $s = 1$ the fraction of chains that have $s = N_A$ at the left of the barrier, within the barrier, or at the right of the barrier. These fractions were calculated analogously to Equation 3.12:

$$f_{\text{left}}(N_A|z', s') = \sum_{z=0}^{z_B-1} P_A(z, N_A|z', s'), \tag{3.15}$$

where z_B denotes the first barrier layer. It is clearly seen that the flowers reverse their direction from the left to the right if the first segment is still at the left of the barrier centre when $\phi_A^{II} > \phi_A^I$. We found that the direction is reversed if $s' = 1$ passes the layer z for which $\phi_A(z)$ is minimal. It is also visible that the flowers to the left do usually not occur simultaneously with other conformations. The fraction of chains with both $s' = 1$ and N_A within the barrier refer to the disturbed coil conformations. These conformations occur generally near the layer z for which the flowers reverse their direction.

3.3.6 Chain length

In this section we focus on the effect of the chain length on the conformations. We calculated the blob sizes in systems with varying chain lengths and barrier widths. One

could expect that long chains could permit smaller blob sizes, because the stretching can be compensated by a crown with a larger number of segments. We found that the blob size is independent of chain length or barrier width. It turns out that for $\chi_{\mathrm{AB}} = \chi_{\mathrm{A}^*} = \chi_{\mathrm{B}^*} = 0$ the blob size is only determined by ϕ^*, ϕ_A^I, and ϕ_A^{II}.

The requirement for chain stretching is that the chain must be sufficiently long compared to the barrier width so that there is a significant number of segments left for the crown of the flower to compensate the entropy loss due to stretching (see also the scaling analysis in Section 3.3.7). For example, when $\phi^* = 0.93$ and $\phi_A^I = \phi_A^{II} = 0.90$, chains with $N = 100$ in solution need about 50 segments to stretch through 24 barrier layers to escape from the barrier (not shown). If the chains in this system are replaced by shorter chains with $N = 70$, flowers do no longer occur (not shown) because the remaining number of 20 segments available for the crown of the flower is too small to compensate for the entropy loss in the stretched stem. Chains with $N = 70$ have a coil conformation in the barrier.

If short chains stretch, they stretch with the same blob size as longer chains, but the fraction of polymers in the barrier that deforms into a flower conformation is smaller for shorter chains. This can be shown by studying polymer chains with $N_A \geq 80$ that have segment $s' = 40$ somewhere within the barrier. We calculated for these chains the fraction with segment $s = 1$ at the left of the barrier, as well as the fraction with segment $s = 79$ at the left of the barrier. Along the contour of the chain these segments are equally far from $s' = 40$, but segment $s = 79$ is found more frequently outside the barrier than segment $s = 1$. Thus, the longer tail stretches more frequently then a shorter tail. The longer the chain, the larger the fraction with $s = 79$ at the left of the barrier. These results are presented in Figure 3.17, where we calculated the first term of Equation 3.12 as a function of s for $s' = 40$ fixed at $z' = 72$ (a few layers left of the barrier centre) for different chain lengths. The right-hand part of this figure shows the average conformation of these chains. The long tail forms a flower (stretched stem plus crown outside), the short tail only an (inside) crown. The chains thus have a 'double-crown' conformation. From the diagram in Figure 3.17 it is observed that the short tails have a constant (small) fraction outside the barrier, independent of N_A. The long tails have a larger fraction outside the barrier that increases with increasing N_A until $N_A = 200$, where nearly all chains have a double-crown conformation.

3.3.7 Scaling analysis

In this section we interpret our results with a scaling analysis of the flower conformation, analogous to that given in Ref. [74] for flower conformations due to an external step potential u. For sufficiently high barriers that cause the volume fraction profile of polymer A to be nearly flat, we can define a potential u_A^* corresponding to such an external step potential: $u_A^* = u_A(\mathrm{in}) - u_A(\mathrm{out})$, where $u_A(\mathrm{in})$ and $u_A(\mathrm{out})$ are given by Equation 3.4 for the appropriate z. If the bulk mixtures I and II have equal compositions there exists equilibrium and all space filling potentials α are independent of segment type (see Chapter 2). An expression for $\alpha(z)$ can easily be obtained for a monomeric component B, since it follows from Equations 3.7 and 3.3 that $u_B/k_BT = \ln(\phi_B(z)/\phi_B^{\mathrm{ref}})$. Assuming that $\phi_A(\mathrm{in}) \approx 0$ and that $\phi_A(\mathrm{out})$ $(= \phi_A^I)$ does not depend on position, and considering only

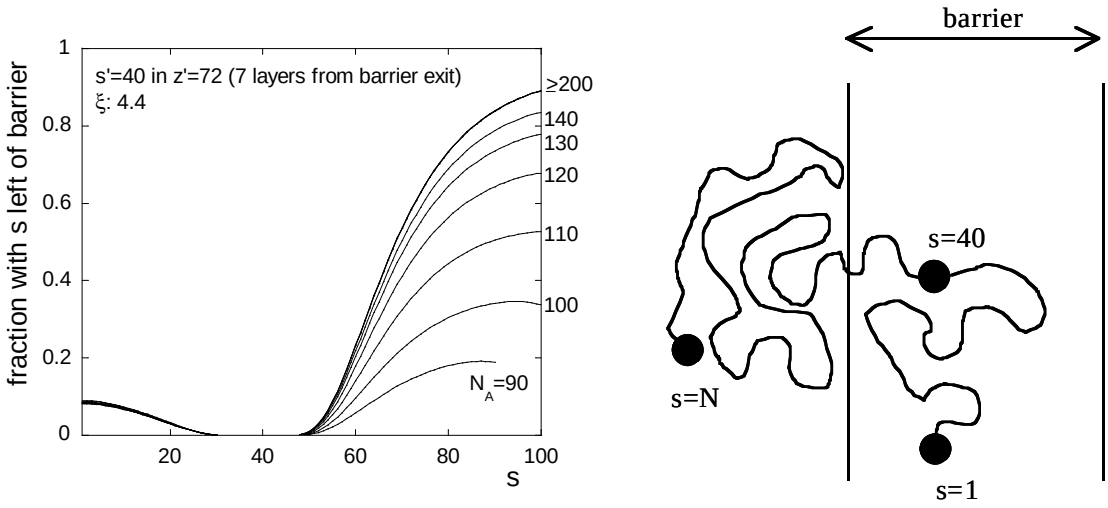

Figure 3.17. Fraction of chains with different N_A that have segment s at the left of the barrier as a function of s, given that their segment $s' = 40$ is in layer $z' = 72$ (just left of the barrier centre). The barrier extends over the layers $z = 66-84$. At the right, the conformation is shown that occurs frequently for sufficiently large N_A; if segment $s = 40$ is fixed within the barrier segments $s = 1$ to $s = 50$ are usually found within the barrier as well. The other segments form a crown outside the barrier. The system parameters are $N_B = 1$, $\phi^* = 0.35$, $\phi_A^I = \phi_A^{II} = 0.30$, $\chi_{\mathrm{AB}} = \chi_{\mathrm{A}^*} = \chi_{\mathrm{B}^*} = 0$.

binary mixtures, we obtain for the potential felt by A-segments:

$$\frac{u_A^*}{k_B T} = -\ln\frac{1-\phi^*}{1-\phi_A^I} + 2\chi_{\mathrm{AB}}\phi_A^I + \phi^*(\chi_{\mathrm{A}^*} - \chi_{\mathrm{B}^*} - \chi_{\mathrm{AB}}), \tag{3.16}$$

which is now independent of the position inside the barrier.

The free energy in units of $k_B T$ for a flower with S segments residing in the barrier and $N_A - S$ segments outside the barrier with respect to a unperturbed coil in the barrier reads for Gaussian chains of sufficiently high lengths [74]

$$F = \frac{3}{2}\frac{Z^2}{S} - (N_A - S)u_A^* \tag{3.17}$$

where Z is the number of lattice layers taken by the flower stem in the barrier. From Equation 3.17 it is seen that when the stretching energy ($\frac{3}{2}Z^2/S$) is compensated by the gain in energy due to the crown ($-(N_A - S)u_A^*$), this free energy is zero. By definition, $F = 0$ means that the free energy of the flower equals the free energy of coils in the barrier. The coil conformations in the barrier and the flower conformations are in equilibrium if $\partial F/\partial S = 0$ and $F = 0$. This is referred to as the binodal point in Ref. [74]. The flower conformation is found to be in equilibrium with the coil if $Z = N_A\sqrt{u_A^*/6} = Z^{\mathrm{bin}}$ and $S = \frac{1}{2}N_A = S^{\mathrm{bin}}$.

From the ratio between Z^{bin} and S^{bin} we can derive the scaling of the blob size ξ. The stem of a flower is a string of n blobs, each of which has a stretching energy of 1 $k_B T$.

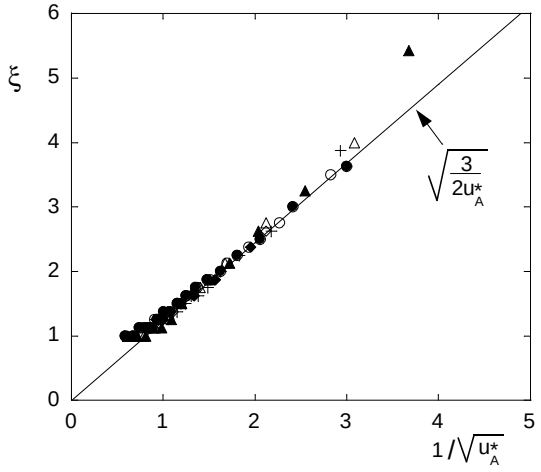

Figure 3.18. The blob size ξ versus $1/\sqrt{u_A^*}$ for the equilibrium systems considered in the previous sections. The expression for u_A^* is given by Equation 3.16. Filled circles: Figure 3.8, $\phi_A^{\text{bulk}} = 0.05$. Open circles: Figure 3.8, $\phi_A^{\text{bulk}} = 0.15$. Filled triangles: Figure 3.8, $\phi_A^{\text{bulk}} = 0.30$. Open triangles: Figure 3.8, $\phi_A^{\text{bulk}} = 0.50$. Filled diamonds: Figure 3.9. Open diamonds: Figure 3.13, $\chi_{\text{B}*} = 0$. Crosses: Figure 3.13, $\chi_{\text{B}*} = 1$.

The stretching energy of the whole stem (nk_BT) should correspond to $(Z^2/S)k_BT$, hence $n = Z^2/S$. The number of segments per blob g is given by $S/n = S^2/Z^2$. Since the chain remains Gaussian on the length scale of a blob, the blob size ξ must scale as $\sqrt{g}$, like the radius of gyration of a Gaussian chain scales as $\sqrt{N_A}$. The blob size is therefore found to scale as $\xi = S/Z = S^{\text{bin}}/Z^{\text{bin}} \propto 1/\sqrt{u_A^*}$. In the previous section it was confirmed that ξ does not depend on the chain length. Given this scaling behaviour of $Z/S = 1/\xi$, it is easily verified that S^{bin} and Z^{bin} are upper limits: the free energy of coil conformations is lower than for flower conformations if either $S > S^{\text{bin}}$ or $Z > Z^{\text{bin}}$.

In Figure 3.18 we check the scaling behaviour of ξ for the blob sizes as reported in the previous sections. Only the equilibrium systems (where mixtures I and II have equal compositions) are considered. The blob sizes reported in Section 3.3.2 and Figure 3.8 are a function of u_A^* through its dependence on ϕ^* (see Equation 3.16). In Section 3.3.3 and Figure 3.9 the potential u_A^* varies with $\chi_{\text{A}*}$ and in Section 3.3.4 and Figure 3.13 it varies with ϕ_A^{bulk}. Indeed the correct scaling is found in Figure 3.18 for all variations of u_A^*.

In Section 3.2.2 we discussed the accumulation layers in the interior of the barrier (see Figure 3.2). We suggested a description of the volume fraction profile in terms of p^* that should be related to u_A^*. We have found that p^* scales as $1/\sqrt{u_A^*}$ (not shown).

To verify the scaling of Z^{bin} with u_A^*, we used plots as in Figure 3.12. As an approximation for Z^{bin} we took the largest value of Z for which all chains have a direction towards the barrier exit (fraction =1). This is of course an underestimation of the true Z^{bin} for which the flowers are in equilibrium with the coil conformation. For $\chi_{\text{A}*} = -0.5$ in Figure 3.12*a* we would assign a value of $73 - 65 = 8$ to Z^{bin}. To check the scaling of Z^{bin} we chose the barrier width very large (151 layers) to ensure that chains residing in the left side of the barrier were not affected by the exterior solution at the right of the

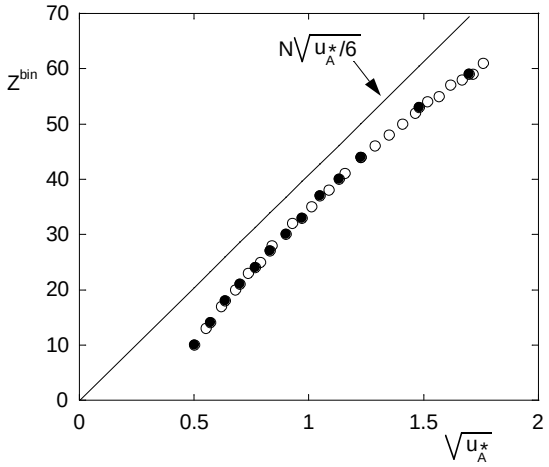

Figure 3.19. The value of Z^{bin} (underestimated as explained in the text) scales approximately as $N_A\sqrt{u_A^*/6}$. Parameters: $N_A = 100$, $N_B = 1$, $\phi_A^I = \phi_A^{II} = 0.10$, barrier width=151 layers. Filled circles: $\chi_{\mathrm{A}*} = 0$, varying ϕ^*. Open circles: $\phi^* = 0.80$, varying $\chi_{\mathrm{A}*}$.

barrier. The values obtained for Z^{bin} by variation of ϕ^* and $\chi_{\mathrm{A}*}$ are plotted as a function of $\sqrt{u_A^*}$ in Figure 3.19. The correct scaling is found with, indeed, a slight underestimation of the numerical Z^{bin}.

When $\phi_A^I \neq \phi_A^{II}$, there is not a single barrier potential, but two different ones. We may approximate these again as two step functions from one potential level to another if it is assumed that the volume fraction profiles are nearly flat (such as the profile for $\Delta\phi_A = 0.40$ in Figure 3.14). A local equilibrium is assumed between mixture I and the left part of the barrier and a distinct local equilibrium between mixture II and the right part of the barrier. For $\phi_A^I < \phi_A^{II}$ we obtain $u_A^*(\mathrm{left}) > u_A^*(\mathrm{right})$. The larger step potential at the left corresponds to a smaller blob size for flowers stretching to the left than for flowers stretching to the right. This is indeed found as discussed in Section 3.3.5. The scaling behaviour of Z^{bin} predicts $Z_{\mathrm{left}}^{\mathrm{bin}} > Z_{\mathrm{right}}^{\mathrm{bin}}$. This prediction is not confirmed by the MFSD-results. This is shown in Figure 3.20 for a system with $u_A^*(\mathrm{left}) > u_A^*(\mathrm{right})$. Figure 3.20*b* presents the volume fraction profile of the chains in such a system with a large barrier ($\phi* = 0.95$, width=151 layers). The solid curve in Figure 3.20*a* shows the fraction of chains in that system that have a direction to the left as a function of the position of the first segment. Considering the solid curve it is found that the flowers in the left-hand side of the barrier have $Z^{\mathrm{bin}} \approx 15$ and the flowers in the right-hand side $Z^{\mathrm{bin}} \approx 28$, thus $Z_{\mathrm{left}}^{\mathrm{bin}} < Z_{\mathrm{right}}^{\mathrm{bin}}$. If we could indeed accurately describe the potential profile by two step potentials $u_A^*(\mathrm{left})$ and $u_A^*(\mathrm{right})$, we would expect $Z_{\mathrm{left}}^{\mathrm{bin}} = Z_{0.1}^{\mathrm{bin}}$ and $Z_{\mathrm{right}}^{\mathrm{bin}} = Z_{0.9}^{\mathrm{bin}}$. The definitions of $Z_{0.1}^{\mathrm{bin}}$ and $Z_{0.9}^{\mathrm{bin}}$ are depicted in Figure 3.20*a*: they are the values of Z^{bin} for $\phi_A^I = \phi_A^{II} = 0.10$ and $\phi_A^I = \phi_A^{II} = 0.90$ respectively. We indeed obtain $Z_{\mathrm{right}}^{\mathrm{bin}} = Z_{0.9}^{\mathrm{bin}}$, but $Z_{\mathrm{left}}^{\mathrm{bin}} < Z_{0.1}^{\mathrm{bin}}$. Apparently, at the left-hand side the segment potential $u_A(z)$ is a stronger function of z than at the right-hand side. As a consequence, the step potential $u_A^*(\mathrm{left})$ is a poor description of the profile for $u_A(z)$. As noted in Section 3.3.5 the chains reverse their direction for the layer where $\phi_A(z)$ is minimal. In Figure 3.20 the

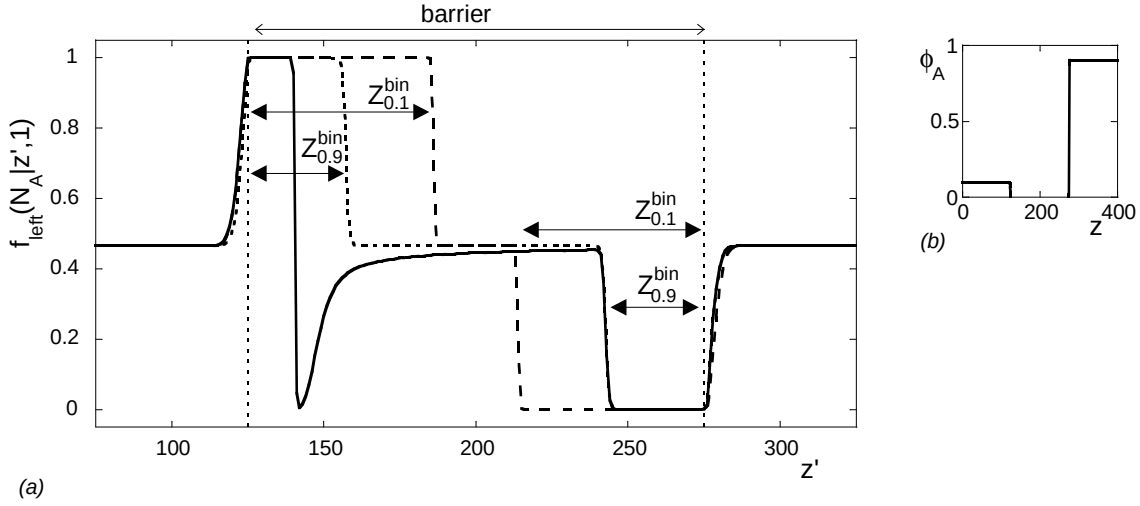

Figure 3.20. Comparison of expected and actual values of $Z^{\rm bin}$ for a system with $u_A^*(\text{left}) > u_A^*(\text{right})$. Figure *a* presents for three systems the fraction of chains that have $s = N_A$ left of $s' = 1$ where the position of s' is given by z'. The solid curve in Figure *a* corresponds to the system presented by the polymer volume fraction profile in Figure *b* where $\phi_A^I = 0.10$ and $\phi_A^{II} = 0.90$. The dotted curve in Figure *a* corresponds to a system with $\phi_A^I = \phi_A^{II} = 0.90$ and the dashed curve to a system with $\phi_A^I = \phi_A^{II} = 0.10$. The other parameters are $N_A = 100$, $N_B = 1$, $\phi* = 0.95$, $\chi_{\rm AB} = \chi_{\rm A*} = \chi_{\rm B*} = 0$.

minimum in $\phi_A(z)$ occurs for $Z < Z_{0.1}^{\rm bin}$. It was discussed in Chapter 2 that the volume fraction profiles change more rapidly if the concentration of mobile component is higher. In Figure 3.20 the left-hand side of the barrier contains more relatively mobile solvent B than the right-hand side. The concentration $\phi_A(z)$ will therefore change more rapidly at the left-hand side than at the right-hand side.

In conclusion, when $\phi_A^I \neq \phi_A^{II}$, the barrier potentials $u_A^*(\text{left})$ and $u_A^*(\text{right})$ can be used to predict the blob sizes $\xi_{\rm left}$ and $\xi_{\rm right}$, but not to predict the stem lengths $Z_{\rm left}^{\rm bin}$ and $Z_{\rm right}^{\rm bin}$. The step sizes $u_A^*(\text{left})$ and $u_A^*(\text{right})$ are good approximations for the barrier potentials, but only for a small number of layers within the barrier.

3.3.8 Conformations in a model lipid bilayer

Our barrier is a liquid-like film. Biologically more interesting systems would need a barrier consisting of polymers that are able to adjust their conformations in response to the transport of other molecules. We can approximate such a system by considering a liquid-like barrier that consists of three different regions to mimic a lipid bilayer. In the present section we consider such a lipid-like bilayer in between two homogeneous phases, just to illustrate the possibilities of the MFSD method. We here present the results for polymers (A) that diffuse in water (B) through a barrier as plotted in Figure 3.21. In this example, the barrier has the following characteristics: five hydrophilic layers

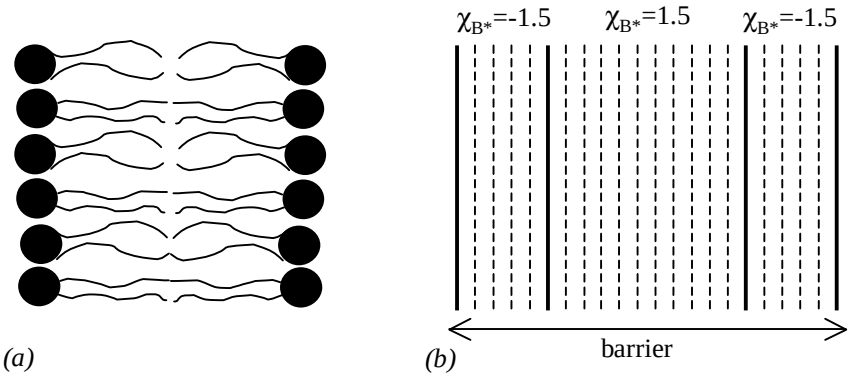

Figure 3.21. A lipid bilayer (a) is modelled by a barrier consisting of three different regions (b), where each region has its own interaction χ_{B^*} with water. The interactions with the polymer (χ_{A^*}) are taken to be zero.

($\chi_{\mathrm{B}^*_1} = -1.5$), 11 hydrophobic layers ($\chi_{\mathrm{B}^*_2} = 1.5$) and again five hydrophilic layers ($\chi_{\mathrm{B}^*_3} = -1.5$). The polymer-barrier interactions are taken zero and the polymer-water interaction has the arbitrarily chosen value of $\chi_{\mathrm{AB}} = 0.62$ such that there is a miscibility gap between $\phi_A = \phi_A^\alpha = 0.0312$ and $\phi_A = \phi_A^\beta = 0.18602$ [97]. The volume fraction of barrier material is chosen to be $\phi^* = 0.70$ for all three barrier sublayers; for comparison we show also results for a dilute barrier with $\phi^* = 0.05$. We imposed a concentration gradient over the system: $\phi_A^I = 0.01$ and $\phi_A^{II} = 0.30$. Figure 3.22a shows the volume fraction profiles in the absence of the bilayer, both for $\chi_{\mathrm{AB}} = 0$ and $\chi_{\mathrm{AB}} = 0.62$. For $\chi_{\mathrm{AB}} = 0$ the profile varies smoothly from $\phi_A = 0.01$ at $z = 0$ to $\phi_A^I = 0.30$ at $z = M = 150$. The slope of $\phi_A(z)$ is larger near $z = 0$ than near $z = M$ due to the larger volume fraction of relatively mobile water near $z = 0$ (see Chapter 2). For $\chi_{\mathrm{AB}} = 0.30$ there is a steep variation around $z = 10$, because a phase separation interface develops in which the major part of the total increase $\Delta\phi_A = 0.30 - 0.01 = 0.29$ occurs. This interface is closer to $z = 0$ than to $z = M$ because $|\phi_A^\alpha - \phi_A^I| < |\phi_A^{II} - \phi_A^\beta|$. The effect of the model lipid bilayer on the volume fraction profiles is shown in Figure 3.22b. If the barrier is low ($\phi^* = 0.05$), the phase separation interface is still visible around $z = 10$. If the barrier is high ($\phi^* = 0.70$), ϕ-gradients only occur near or within the barrier region.

The segmental contributions to the polymer volume fraction are plotted in Figure 3.23 for $\phi^* = 0.70$. Outside the barrier region the same preferences are obtained as for flower-forming barriers. However, within the barrier, there exists a preference for middle segments. Small asymmetries with respect to the centre of the barrier ($z = 75$) occur due to the gradient in $\phi_A(z)$. From Figure 3.24 we derive the conformations of chains that diffuse through the lipid-like barrier with $\Delta\phi_A = 0.29$ and $\chi_{\mathrm{AB}} = 0.62$. In Figure 3.24$a$ we plotted the fraction of chains with a direction to the left as a function of the position of the first chain segment. We follow the chains during their diffusion from $z = M$ towards $z = 0$. Most chains that approach the barrier from the right ($85 < z' < 100$) avoid the barrier region by adopting a conformation with $s = N_A$ located at the right of $s = 1$. If the diffusing chains enter the barrier they first encounter the hydrophilic region for $80 \leq z' \leq 85$. Polymer segments avoid this region by escaping either to the right out of the barrier (for $83 < z' \leq 85$) or to the left into the hydrophobic part of the

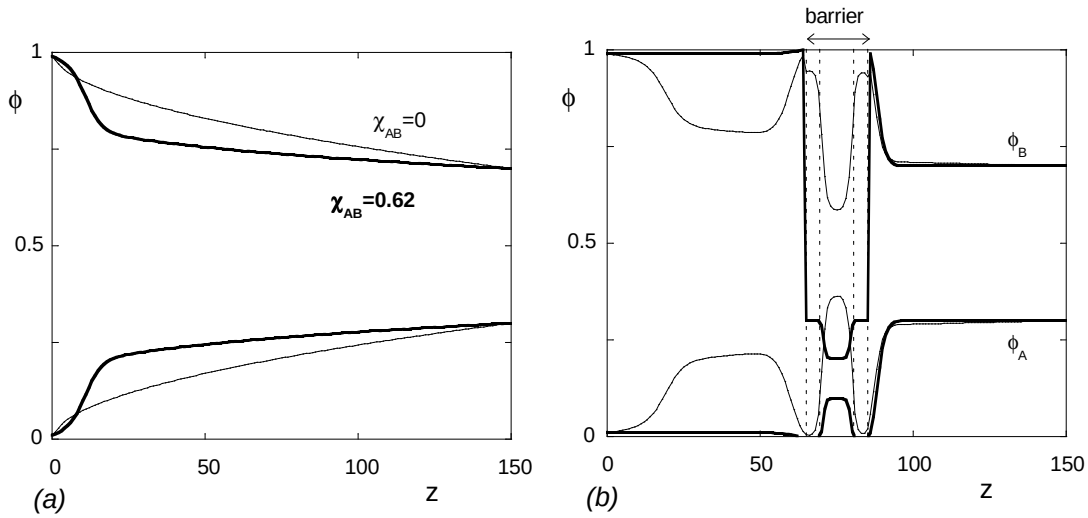

Figure 3.22. Volume fraction profiles ϕ_A for the polymer (bottom) and ϕ_B for the solvent (top), for $N_A = 100$, $N_B = 1$, $\phi_A^I = 0.01$, $\phi_A^{II} = 0.30$. *(a)*: In the absence of a barrier, $\chi_{\rm AB} = 0$ (thin curves) or $\chi_{\rm AB} = 0.62$ (thick curves). *(b)*: In the presence of a model lipid bilayer (see Figure 3.21) in the centre and $\chi_{\rm AB} = 0.62$, $\phi^* = 0.05$ (thin curves) or $\phi^* = 0.70$ (thick curves).

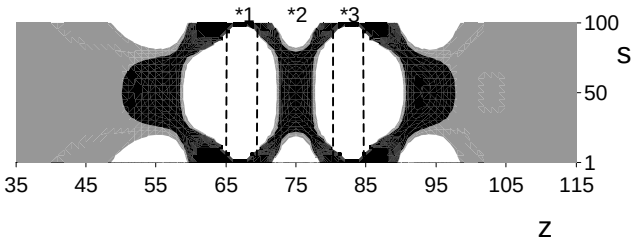

Figure 3.23. The segmental contributions to the polymer volume fraction for the polymer profile given by the thick curve in Figure 3.22*b*.

barrier (for $81 \leq z' < 83$). In Figure 3.24*b* we plotted the conditional segment probability $P_A(z, N_A|83, 1)$, i.e. the probability to find $s = N_A$ in z if segment $s = 1$ is in the centre of the hydrophilic region. The two possible escapes from the hydrophilic region are clearly seen. When chains continue to diffuse they enter the hydrophobic region of the barrier ($70 \leq z' \leq 80$). Figure 3.24*a* indicates that if the first segment of a chain resides within that hydrophobic region, the last segment is kept in the same region. This is confirmed by the conditional segment probability $P_A(z, N_A|75, 1)$ plotted in Figure 3.24*c*. When the chains enter the second hydrophilic region ($65 \leq z' < 70$) with their first segment, they again have two possibilities to escape. According to Figure 3.24*a* they fold into the hydrophobic region for $67 < z' \leq 69$. They escape from the barrier if $65 \leq z' < 67$. The conditional segment probability $P_A(z, N_A|67, 1)$ in Figure 3.24*d* shows that most chains with $s = 1$ in $z = 67$ escape from the hydrophilic region by folding into the hydrophobic

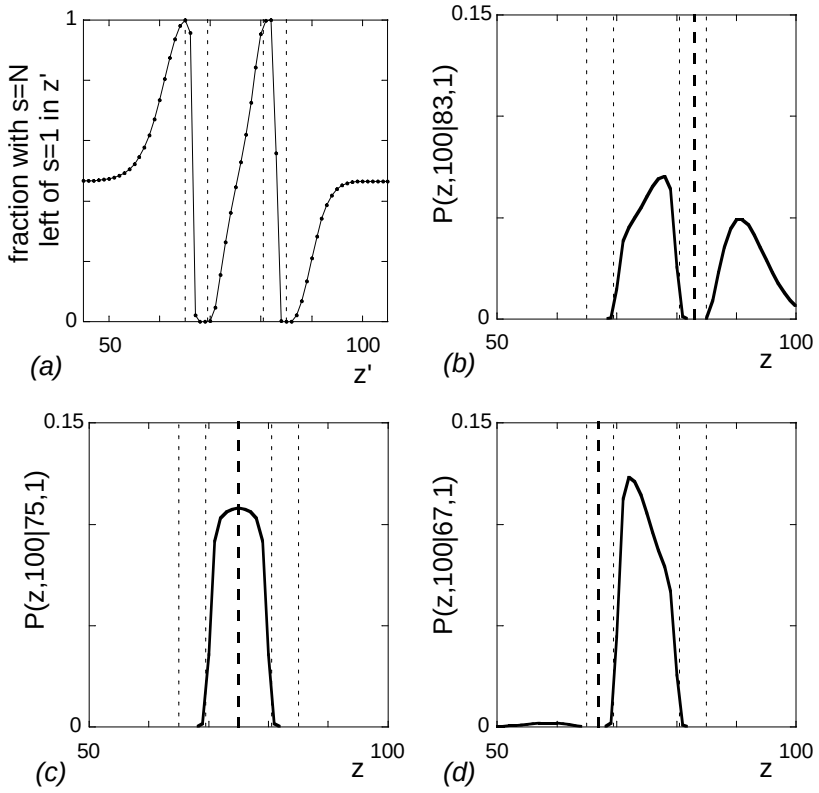

Figure 3.24. Conformational properties of chains in the same system as presented by the thick curves in Figure 3.22*b*. *(a)*: Fraction of chains that is directed to the left as a function of the position of segment $s = 1$. *(b)-(d)*: Probability to find segment $s = N_A$ in z for chains that have their first segment in the layer that is indicated by the thick dashed line: in the centre of the first hydrophilic barrier region *(b)*, in the centre of the hydrophobic barrier region *(c)*, or in the centre of the second hydrophilic region *(d)*.

region. Due to the low polymer content at the left of the barrier, only a small amount of chains escapes out of the barrier. In contrast, a considerable portion of chains is able to escape from the barrier if $s = 1$ resides within the other hydrophilic part (Figure 3.24*b*).

3.4 Conclusions

We modelled the stationary hindered diffusion of polymers through a barrier by the Mean-Field Stationary Diffusion (MFSD) method. The barrier is in principle a liquid film with a given (excluded) volume fraction ϕ^* that is inaccessible to polymer and solvent. The liquid film is made to resemble a lipid bilayer by subdividing the barrier into three (or more) parts and choosing the appropriate interaction parameters. The MFSD method computes the weighting factors for polymer segments or monomers such that the free energy is minimal for given bulk compositions, chemical interactions and barrier properties. From

these weighting factors we derive the conformational distributions of the polymers. The polymer chains near or within the barrier region generally show large deformations as compared to the coil conformations that are found further from the barrier. Chains near the barrier tend to avoid the barrier by deforming their coil conformation. Within a sufficiently high barrier they adopt so called flower conformations, where part of the chain (the stem) is stretched to allow the rest of the chain (the crown) to escape from the barrier. Within the barrier also deformed coil conformations may occur, namely when $\Delta\phi \neq 0$, where the chain does not escape, but still folds towards the exit of the barrier.

We quantified the deformations by defining a stretching parameter, expressed as the blob size. This blob size is calculated as the number of segments in the stretched part of the chain (the stem) divided by the length of the stem. The blob size decreases with increasing barrier height (that is, with increasing ϕ^*, increasing polymer-barrier repulsion, or increasing solvent-barrier attraction). The blob size increases with increasing polymer concentration within the barrier. In the absence of solvent, we only found deformed conformations when the chains are long compared to the barrier width. The blob sizes of polymers in solution are independent of chain length or barrier width. However, for shorter chains a smaller portion prefers the flower conformation than for longer chains. We have interpreted these observations by means of a Gaussian scaling model. Blobs can be distinguished only when the conformations of chains are heavily perturbed. Smaller perturbations (for example of chains at a liquid/liquid interface) can be made visible by evaluating the preferred direction of the chains. In this study the preferred direction was evaluated by calculating the fraction of chains with their first segment in a given layer z' that have their last segment either left or right of z'.

Near the barrier some segment ranking numbers are preferred over other ranking numbers, depending on the repulsions or attractions between the segments and the barrier material. The patterns for segmental preferences near the barrier are usually the same as the patterns near a solid wall. However, the segment preferences differ if ϕ^* and χ_{A*} are sufficiently low so that the barrier becomes an attractive region for the polymer. Then middle segments are preferred within the barrier, whereas the end segments are preferred within the barrier if ϕ^* is high or if polymer-barrier repulsions are small or absent. This preference for end segments within the barrier indicates that hair pin conformations are avoided.

The MFSD-method is a suitable and efficient tool to study the polymer conformations during (hindered) transport. A future refinement would be the implementation of a barrier that itself consists of (co)polymers which can not escape from the barrier region and whose conformations adjust when other (co)polymers or salts diffuse through them.

Appendix 3A Conformations near boundaries

The conditional volume fractions $\phi_A(z, s|z', s')$ can be calculated by means of Equations 3.8 and 3.9. However, the starting conditions in Equation 3.8 have to be slightly adjusted if part of a chain might reside in one of the bulk solutions at $z = 0$ and $z = M$. Moreover, the expression for the conditional volume fraction in Equation 3.8 is not valid for $z = 0$ or $z = M$. In this appendix we present the proper starting conditions and the expressions for $\phi_A(0, s|z', s')$ and $\phi_A(M, s|z', s')$.

The deviation from Equations 3.8 and 3.9 arises from the bulk properties in the

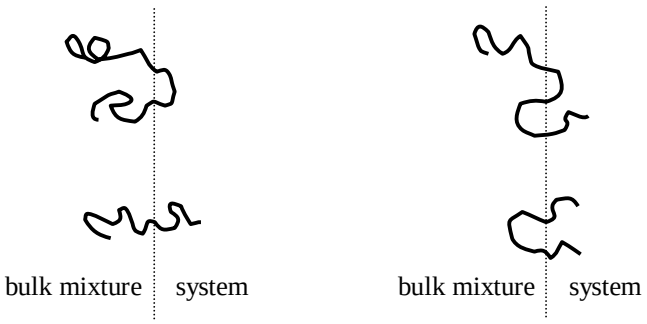

(a) correct *(b)* incorrect

Figure 3.25. Examples of chain conformations near the system boundaries that are either included accurately *(a)* or inaccurately *(b)* in the MFSD calculations.

layers $z = 0$ and $z = M$. Instead of calculating $G_A(0,2|1)$ according to Equation 3.6 as $G_A(0,2|1) = G_A(0,2)\{\lambda_{-1}G_A(-1,1) + \lambda_0 G_A(0,1) + \lambda_1 G_A(1,1)\}$ we assume real bulk characteristics in layer $z = 0$ so that $G_A(0,2|1)$ is computed as $[G_A(0)]^2$ (where $G_A(0) = G_A^I$), since in a bulk mixture G_A should be independent of position. More generally

$$G_A(0,s|1) = [G_A(0)]^s, \tag{3A.1a}$$

$$G_A(0,s|N_A) = [G_A(0)]^{N_A-s+1}, \tag{3A.1b}$$

and analogous expressions for $G_A(M,s|1)$ and $G_A(M,s|N_A)$ (with $G_A(M) = G_A^{II}$). The consequence is that some chain conformations near the boundaries are not accurately accounted for. For example, in the calculation of $\phi(1,s)$ we include the possibility that segment $s-1$ finds itself in the bulk mixture ($z = 0$). The term $C\lambda_{-1}G(0,s-1|1)G(1,s|N)$ in Equation 3.7 accounts for this conformation. Due to the assumed bulk properties of layer $z = 0$, this term is calculated as $C\lambda_{-1}[G(0)]^{s-1}G(1,s|N)$. This implies that conformations for which segment $s-1$ is in $z = 0$ and $s' < s-1$ is in $z > 0$ are not accounted for with the correct weight. Figures 3.25*a* and 3.25*b* show some conformations that are calculated correctly and incorrectly, respectively.

These boundary conditions have some effect on the computation of the conditional volume fractions. In short, we have to take care of the following additional rules if Equation 3.8 is applied:

$$G_A(1,s)\lambda_{-1}G_A(0,s-1|z',s') = 0 \quad \text{for } z' > 0, s' \le s-1 \tag{3A.2a}$$

$$G_A(1,s)\lambda_{-1}G_A(0,s+1|z',s') = 0 \quad \text{for } z' > 1, s' \ge s+1 \tag{3A.2b}$$

Similar rules apply for the transition between layer $M-1$ and M. Moreover, new equations are needed for the conditional volume fractions in the bulk mixtures. For bulk mixture I (layer $z = 0$) these equations read:

$$\phi_A(0,s|z',s') = C_A \frac{G_A(z',s'|1)}{G_A(z',s')} \sum_{\sigma=s'}^{s-1} G_A(1,\sigma|z',s')\lambda_{-1}[G_A(0)]^{N_A-\sigma} \quad \text{for } s' < s \tag{3A.3a}$$

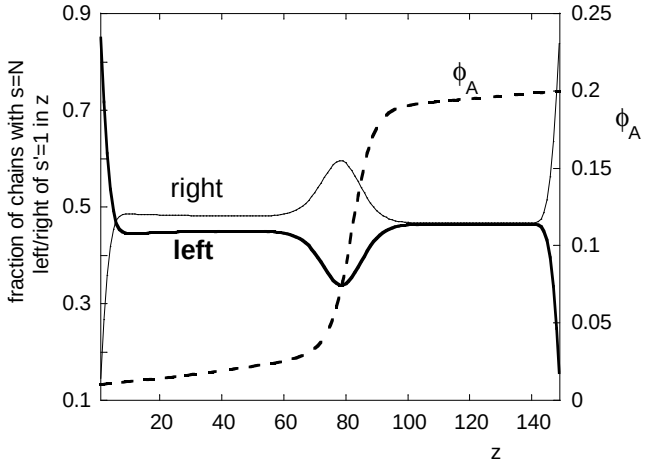

Figure 3.26. The fraction of chains that have a direction to the left or to the right if segment $s = 1$ is in layer z. The dashed curve is the volume fraction profile of the polymer. Parameters: $N_A = 100$, $N_B = 1$, $\chi_{AB} = 0.62$, $\phi_A^I = 0.01$, $\phi_A^{II} = 0.20$.

$$\phi_A(0,s|z',s') = C_A \frac{G_A(z',s'|N_A)}{G_A(z',s')} \sum_{\sigma=s+1}^{s'} G_A(1,\sigma|z',s')\lambda_{-1}[G_A(0)]^{\sigma-1} \quad \text{for } s' > s \tag{3A.3b}$$

The noticeable effect of the boundary conditions is that if a chain from the system enters the bulk with one of its tails, it will not be able to leave the bulk with that tail; the bulk soaks up the tail. This soaking effect is clearly seen in Figure 3.26 where the direction of chains is plotted as a function of the position of the first segment. The interface in Figure 3.26 influences the preferred direction of the chains only in the interfacial region. Chains in the solvent-rich phase fold into the direction of the polymer-rich phase to obey the requirement of suddenly increasing polymer concentration.

The soaking effect of the bulk mixtures is not accompanied by preferences for certain segment numbers. Only if $\nabla\phi$ is large near $z = 0$ or $z = M$, there may exist segment preferences near the bulk mixtures in which $\nabla\phi$ suddenly needs to vanish. In all systems discussed in this chapter, the bulk effects on the chain conformations are too small to influence the conformations of chains that diffuse through the barrier in the centre of the system.

Appendix 3B Derivation of Equation 3.14

The probability that segments with ranking numbers 1 and s reside within the same lattice layer z' is denoted by $P_A(z',s|z',1)$. We are interested in the value for $P_A(z',s|z',1)$ in a homogeneous mixture (bulk) in which $G_A(z,s) = G_A(z) =$ constant. Therefore, the contribution of a certain chain conformation to $P_A(z',s|z',1)$ is completely determined by the bond parameters λ_0 and $\lambda_1(=\lambda_{-1})$ (see Equation 3.5) that are associated with the $s-1$ bonds between segments 1 and s. For example, a conformation that has all segments

1, 2, 3,..., s within the same lattice layer has a contribution λ_0^{s-1} to $P_A(z', s|z', 1)$. Other conformations may have bonds that connect segments between two adjacent lattice layers. The weight of these bonds is λ_1 per bond. For chain conformations that contribute to $P_A(z', s|z', 1)$ the number of such layer-crossing bonds must always be an even number, otherwise segments 1 and s will not be found in the same layer. The number of layer-crossing bonds is counted as $2i$ in Equation 3.14 which results in the factor λ_1^{2i}. The remaining $s - 1 - 2i$ bonds do not cross the layers and have a weight λ_0. There are $\binom{s-1}{2i}$ possibilities to select the layer-crossing bonds. Only half of these layer-crossing bonds may have an arbitrary direction, either to the right or to the left. The other half of these bonds must have the opposite direction. This is accounted for by the factor $\binom{2i}{i}$ in Equation 3.14.

Chapter 4

Stationary dynamics approach to analytical approximations for polymer coexistence curves

Phase separation in polymer blends is an important process. However, the compositions of the coexisting phases can only be predicted by numerical methods. We provide simple analytical expressions which serve as good approximations for the compositions after phase separation of binary homopolymer blends. These approximations are obtained by a stationary dynamics approach: we calculate the compositions of two polymer mixtures such that the stationary diffusion between these distinguishable mixtures vanishes. For the diffusion equations we employ composition-dependent diffusion coefficients, as derived according to the slow- and fast-mode theory from the Flory-Huggins free energy. The analytical results are in good agreement with exact (numerically calculated) binodal compositions. Our coexistence curves are more accurate than some conventional approximations. Another advantage of the stationary dynamics approach is that it is not only applicable to binary polymer blends or polymer solutions, but also to symmetrical multicomponent blends. The same diffusion coefficients may be used to obtain the exact spinodal compositions in multicomponent systems.

Published in Physical Review E **69**, 021808 (2004).

4.1 Introduction

Phase equilibria in polymer solutions and polymer blends are of great interest since in many instances different macromolecular species are combined to obtain materials with favourable properties. The implications of the phase behaviour, such as the stability of polymer solutions and blends, is important not only in manufacturing and processing of materials, but also in their applications.

Different approaches have been developed to study the phase behaviour theoretically, aimed at finding more general characteristics than experiments allow. In the 1940s Flory [100, 7] and Huggins [8] described polymer mixtures by a random mixing approach on a lattice, a model which is nowadays known as the Flory-Huggins theory. The Flory-Huggins theory is still widely applied to understand phase behaviour, it is used as a reference to newly developed models and it has served as the basis of new approaches. For example, the theory has been extended to compressible systems by Sanchez and Lacombe [101] and, impelled by experiments, the Flory-Huggins interaction parameter χ has been proposed to be a function of temperature [102]-[107], concentration [102]-[106][108], chain length [108, 109], and/or chain architecture [105, 107, 110, 111]. A generalization of the Flory-Huggins theory, which is known as the lattice cluster theory and which may include details of monomeric shapes [111] was developed by Dudowicz and Freed [112]. An improvement on Flory-Huggins' random mixing approach has been suggested by Gujrati, in the form of a recursive lattice approach [113, 114]. The Flory-Huggins theory and its derivatives aim at the description of the full thermodynamics of polymer mixtures; the coexistence curves are just examples of the information which may be extracted from these theories. The great interest in the phase diagrams has led to a variety of simulation methods which were exclusively developed for the determination of coexistence curves. De Pablo et. al. present a clear overview of the simulation methods [115]. One easy and robust way to obtain the compositions of coexisting phases is by Panagiotopoulos' Gibbs ensemble simulations [116, 117]. This method needs n simulation boxes if n phases may coexist at the imposed temperature and overall composition. The Monte Carlo movements in the simulation allow subsequently the displacement of particles (NVT-simulations), adjustment of the volumes (NPT-simulations) and of the number of particles (μVT-simulations) in each of these n boxes. The boxes are in contact due to the condition that particles and volume are exchanged, so that N,V and T are constant for the total of all boxes. Equilibrium is obtained when the pressure and chemical potentials are the same in all boxes. The computation time may be decreased by performing the simulation on a lattice, but then the volume exchanges need some extra attention [118, 119]. The strength of the Gibbs ensemble method lies in the absence of interfaces: only bulk phases are simulated. One single simulation box containing two coexisting phases plus the interface in between would soon suffer from finite-size effects, especially near the critical point. However, problems arise in the Gibbs ensemble method when it is applied to macromolecules, since particle exchanges become extremely difficult. The acceptance probability of these exchanges may increase if chains are inserted by a growth-process, known as the configurational-bias method [120, 121]. Other approaches to circumvent the insertion problem were proposed by Escobedo [122] and by Brennan and Madden [123]. The Gibbs ensemble simulation result is a good starting point for the Gibbs-Duhem integration scheme [124]-[126], which constitutes an efficient search for coexisting phases.

There are some attempts to find the coexistence curve by simulations in one cell only.

The configurational-bias-vaporization method [127, 128] and the adhesive-wall method [129] simulate the coexisting phases with their interface. The histogram reweighing method [130, 131] is a powerful tool to find the coexistence curves by a limited number of simulations in which the interfaces need not be present.

This large number of attempts to find coexistence curves in polymer fluids indicates the importance of the issue. One general feature of such simulation methods is that one needs to start with a good estimate of the compositions of the coexistent phases. Such an initial guess might be obtained from a series of (time-consuming) trial simulations (e.g. by Virtual Gibbs ensemble simulations [132]) or from simple analytical expressions. Some analytical expressions are available in the literature. We review them in the following section. In Section 4.3 we explain our 'stationary dynamics approach' to obtain new analytical approximations for coexistence curves. In this approach, we look for the compositions of two mixtures at which the stationary flux between these mixtures vanishes. We show that this approach in principle yields the exact binodal compositions when the equations are solved numerically. However, when the equations are solved analytically only an approximation is obtained due to the analytically inaccessible discontinuity in the diffusion profiles. We apply this approach to binary and symmetric multicomponent blends. Our analytical coexistence curves from the stationary dynamics approach are compared with other approximations and with exact results in Section 4.4. It is found that our approach, which is applicable for a wide range of polymer blends, yields better approximations than those available from literature. Spinodal curves are strongly related to the coexistence curves. Section 4.5 shows that the exact spinodals of binary and multicomponent polymer blends may be obtained from our flux expressions. The last section (4.6) summarizes our findings.

4.2 Analytical binodal compositions

In this section, we focus on binary blends of homopolymers A and B. The approximations that are available from the literature apply the Flory-Huggins theory to find an expression for the chemical potential. This theory is simple and sometimes of limited use for experimental purposes, but it is still widely applied to understand phase behaviour. It is used as a reference for newly developed models and it has served as the basis of new approaches [102, 107, 108, 112, 113]. Our stationary dynamics approach is not limited to the use of Flory-Huggins theory. We use this only to compare with the approximations available in the literature.

The free energy of mixing per lattice site for incompressible homopolymer mixtures in the Flory-Huggins model is:

$$\frac{f}{k_BT} = \frac{g}{k_BT} + \text{constant} = \sum_i \frac{\phi_i}{N_i} \ln \phi_i + \frac{1}{2} \sum_{i,j} \phi_i \chi_{ij} \phi_j. \tag{4.1}$$

Here, ϕ_i and N_i denote the volume fraction and the chain length (that is, the number of constituent segments) of polymer i, respectively, and the parameters χ_{ij} quantify the repulsive ($\chi > 0$) or attractive ($\chi < 0$) net interactions between segments i and j. Solvents are simply described as molecules with $N = 1$. Due to the assumption of incompressibility, the Helmholtz (f) and Gibbs (g) free energies differ only by a constant.

We are looking for the binodal compositions, i.e., the volume fractions of both components in the two phases (α and β) that coexist at thermal equilibrium, for a given set of χ's. These compositions will be denoted, for polymer A, by ϕ_A^α and ϕ_A^β. Thermal equilibrium implies equal chemical potentials in both phases: $\mu_A^{\text{chain},\alpha} = \mu_A^{\text{chain},\beta}$ and $\mu_B^{\text{chain},\alpha} = \mu_B^{\text{chain},\beta}$. These chemical potentials follow from the standard procedure: $\mu_A^{\text{chain}} = \frac{\partial G}{\partial n_A}$, where n_A is the number of A-molecules. Using $\phi_A = \frac{n_A N_A}{n_A N_A + n_B N_B}$ and $G = (n_A N_A + n_B N_B)g$ it is then easy to obtain $\mu_A^{\text{chain}}/N_A = g + (1-\phi_A)\frac{\partial g}{\partial \phi_A}$ so that

$$\frac{\mu_A^{\text{chain}}}{k_B T} = \ln \phi_A + \left(1 - \frac{N_A}{N_B}\right)\phi_B + N_A \chi \phi_B^2 \tag{4.2}$$

where the pure phase A was taken as the reference point. The expression for μ_B^{chain} is obtained by interchanging the subscripts A and B. Obviously, in a binary mixture $\phi_B = 1 - \phi_A$. One relation between ϕ_A^α and ϕ_A^β follows from $\mu_A^{\text{chain},\alpha} = \mu_A^{\text{chain},\beta}$:

$$\ln \frac{\phi_A^\alpha}{\phi_A^\beta} + \left(1 - \frac{N_A}{N_B}\right)(\phi_A^\beta - \phi_A^\alpha) + N_A \chi \left[\phi_A^\alpha(\phi_A^\alpha - 2) - \phi_A^\beta(\phi_A^\beta - 2)\right] = 0 \tag{4.3}$$

and a second relation, obtained from $\mu_B^{\text{chain},\alpha} = \mu_B^{\text{chain},\beta}$, is found by interchanging the subscripts A and B in Equation 4.3 and substituting $\phi_B = 1 - \phi_A$. A numerical method is needed to find ϕ_A^α and ϕ_A^β from these two relations. Even for the simplest case of symmetrical polymer blends (i.e. $N_A = N_B = N$), which includes mixtures of monomers ($N = 1$), the binodal compositions are not analytically accessible. In this symmetrical case $\phi_A^\beta = 1 - \phi_A^\alpha$ and Equation 4.3 reduces to

$$\chi N = \frac{1}{2\phi_A^\alpha - 1} \ln\left(\frac{\phi_A^\alpha}{1 - \phi_A^\alpha}\right). \tag{4.4}$$

Numerical methods need good initial guesses to avoid divergence [133], for which analytical approximations are very helpful. We review three analytical approximations for the binodal compositions taken from the literature. Only one of these is generally applicable, the others are either for symmetrical blends ($N_A = N_B = N$) or for polymer solutions ($N_B = 1$) only.

In the following discussion we need some extra quantities which may easily be derived from the Flory-Huggins free energy expression for a binary system. These are the spinodal compositions $\phi_A^{\text{spin}} = 1 - \phi_B^{\text{spin}}$ that follow from the spinodal condition ($\frac{\partial^2 G}{\partial \phi^2} = 0$) and the critical composition and critical interaction parameter which are given by the critical condition ($\frac{\partial^2 G}{\partial \phi_A^2} = \frac{\partial^3 G}{\partial \phi_A^3} = 0$):

$$\phi_A^{\text{spin}} = k \pm \frac{b}{\sqrt{2}} \tag{4.5}$$

$$\phi_A^{\text{crit}} = k_{\text{crit}} \tag{4.6}$$

$$\chi_{\text{crit}} = \frac{1}{2}\left(\frac{1}{\sqrt{N_A}} + \frac{1}{\sqrt{N_B}}\right)^2. \tag{4.7}$$

Here, we introduced parameters k and b defined by

$$k = \frac{1}{2} + \frac{1}{4\chi}\left(\frac{1}{N_A} - \frac{1}{N_B}\right) \tag{4.8}$$

$$b^2 = 2k^2 - \frac{1}{\chi N_A}. \tag{4.9}$$

The parameter k_{crit} is the value of parameter k after substitution of $\chi = \chi_{\mathrm{crit}}$ into Equation 4.8:

$$k_{\mathrm{crit}} = \frac{\sqrt{N_B}}{\sqrt{N_A} + \sqrt{N_B}}. \tag{4.10}$$

4.2.1 Approximation for symmetrical blends

We first consider an analytical approximation for binodal compositions in blends that consist of two homopolymers with equal chain lengths ($N_A = N_B = N$). The compositions are calculated by minimization of a Ginzburg-Landau expansion for the Flory-Huggins free energy [134]. The minimization is preceded by expanding the entropic contribution in terms of the order parameter $\Psi = \phi - \phi^{\mathrm{crit}}$, which must be close to zero. This means that the system should be not far from its critical point. The minimization itself is carried out according to variational calculus. The result is therefore the coexistence curve according to a free energy functional that merely serves as an upper bound for the real free energy. Here we are only interested in the approximation for the binodal compositions,

$$\phi^{\mathrm{VdW}} = \frac{1}{2} \pm \sqrt{\frac{3}{8}(\chi N - 2)}, \tag{4.11}$$

but the procedure provides the complete composition profile between two liquid phases. It is known as the Van der Waals-theory of liquid/liquid interfaces.

4.2.2 Approximation for polymer solutions

For a polymer A in a solvent B we have $N_A = N$ and $N_B = 1$. The analytical approximation considered here provides only the binodal composition of the polymer-rich phase. The key element of this approximation is the assumption that the polymer-rich phase β coexists with a very dilute phase α which is essentially pure solvent. In other words, μ_B^{chain} is assumed to be equal to zero in both phases so that the composition of the concentrated phase must obey

$$\frac{\mu_B^{\mathrm{chain},\beta}}{k_B T} = \frac{\mu_B^{\mathrm{chain},\alpha}}{k_B T} = \ln\left(1 - \phi_A^\beta\right) + \left(1 - \frac{1}{N}\right)\phi_A^\beta + \chi(\phi_A^\beta)^2 = 0. \tag{4.12}$$

This assumption results in an underestimation of the polymer content in the concentrated phase, in particular for small values of χ and for chains that are relatively short. This can immediately be seen by inspection of μ_B^{chain} as a function of ϕ_A [123]. An analytical approximation for Equation 4.12 in the long-chain limit is obtained by neglecting the term $\frac{1}{N}$ and expanding the logarithm, assuming small ϕ_A even in the polymer-rich phase, which is valid for $N \to \infty$ and small $(\chi - \chi_{\mathrm{crit}}) = (\chi - \frac{1}{2})$. If the expansion is truncated after the term proportional to $(\phi_A^\beta)^3$, we obtain for the binodal composition of the polymer-rich phase:

$$\phi_A^{\mathrm{sol}(i)} = 3(\chi - \frac{1}{2}). \tag{4.13}$$

Truncation after the next term still results in an analytical expression:

$$\phi_A^{\mathrm{sol}(ii)} = \frac{2}{3}\left(-1 + \sqrt{1 + 9(\chi - \frac{1}{2})}\right). \tag{4.14}$$

Due to the truncation, these approximations are overestimations of the underestimating Equation 4.12. The result of this error-compensation will be shown in Section 4.4. The assumption that a concentrated polymer solutions coexists with pure solvent forms the basis for an osmotic Gibbs ensemble simulation technique that circumvents the necessity for insertion and deletion of macromolecules [123].

4.2.3 Approximation for all binary mixtures

Sanchez [135] has derived an approximation for Flory-Huggins coexistence curves that is valid both for symmetrical and asymmetrical binary blends as well as for polymer solutions. His derivation is based upon a Landau-type expansion of the free energy around the critical interaction parameter χ^{crit} and the critical composition ϕ_A^{crit}. He assumed that close to the critical point the binodal compositions are equidistant from the critical composition: $\phi_A^{\alpha} - \phi_A^{\mathrm{crit}} = \phi_A^{\beta} - \phi_A^{\mathrm{crit}}$. Combining the Landau-expansion with this assumption, the equilibrium condition ($\mu_A^{\mathrm{chain},\alpha} = \mu_A^{\mathrm{chain},\beta}$), and the spinodal condition ($\frac{\partial^2 G}{\partial \phi^2} = 0$) results in a simple relationship between the coexistence curve and the spinodal, which is known as the root-three rule:

$$\frac{\Delta\phi_A^{\mathrm{bin}}}{\Delta\phi_A^{\mathrm{spin}}} = \sqrt{3} \tag{4.15}$$

where $\Delta\phi_A^{\mathrm{bin}} = \phi_A^{\alpha/\beta} - \phi_A^{\mathrm{crit}}$ and $\Delta\phi_A^{\mathrm{spin}} = \phi_A^{\mathrm{spin1/spin2}} - \phi_A^{\mathrm{crit}}$. Here, $\phi_A^{\alpha/\beta}$ means either ϕ_A^{α} or ϕ_A^{β}. Substituting Equation 4.5 and 4.6 into Equation 4.15 yields for the root-three approximation for binodal compositions (denoted by $\phi_A^{(\sqrt{3})}$):

$$\phi_A^{(\sqrt{3})} = k_{\mathrm{crit}} + \sqrt{3}(k - k_{\mathrm{crit}}) \pm \frac{1}{2} b\sqrt{6}. \tag{4.16}$$

4.3 Stationary dynamics approximation

Our approach to find an approximation for the coexistence curve for given χ is completely different from the approaches in Section 4.2. We consider two polymer mixtures that differ in their compositions and that are brought into contact as shown in Figure 4.1. It is assumed that these mixtures are infinitely large and ideally stirred, so that their compositions do not change in time. Generally, a diffusion flux will occur between these mixtures, driven by the concentration gradients, or, more precisely, by the chemical potential gradients. This is the key idea of our approach: *if the compositions of the mixtures are chosen such that the mixtures represent coexisting phases, there is no diffusion flux.* This statement can not be inverted: the diffusion flux may also be absent for other compositions than that of coexisting phases, the trivial case being equal compositions for both mixtures. In the stationary situation, there is no accumulation of material within the contact zone between the two mixtures, and the fluxes are constant in time. Thus we can assign one value to the flux of each polymer in the stationary state. Our approach

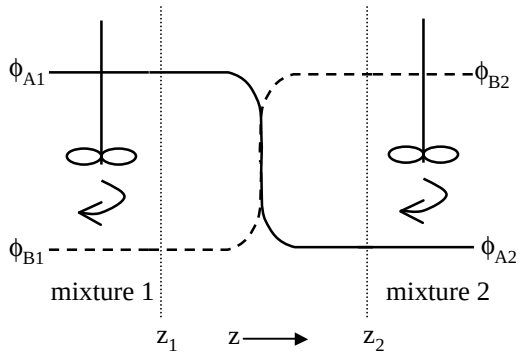

Figure 4.1. Schematic picture of the system that is used to obtain approximations for binodal compositions: two ideally stirred mixtures in contact and a composition profile in between. There is no flux if the mixtures are coexistent at equilibrium.

is to find those compositions that result in vanishing stationary fluxes for all polymers. A similar idea forms the basis of a numerical algorithm to obtain phase diagrams [136]. The analytical approximations for binodal compositions that we find from this stationary dynamics approach (SDA) will be denoted by ϕ_A^{SDA}.

We first need to derive expressions for the segment fluxes (Section 4.3.1), where we consider only one-dimensional diffusion perpendicular to the interface between the two mixtures. We will present the equations for stationary fluxes according to two different diffusion mechanisms. The assumptions about the diffusion mechanism are critical; they do not have an effect on the exact numerical results, but they determine whether it is possible to obtain an approximation for the coexistence curve.

The flux can be written in terms of Onsager coefficients and driving forces so that we generally have

$$J = -f(\phi)\nabla\mu \qquad \Leftrightarrow \qquad J\mathrm{d}z = -f(\phi)\mathrm{d}\mu. \tag{4.17}$$

The function $f(\phi)$ depends on the diffusion mechanism as will be seen in Section 4.3.2. In the stationary state, the flux is a constant so that integration of Equation 4.17 from $z = z_1$ to $z = z_2$ yields for vanishing stationary fluxes

$$[z_2 - z_1]\, J^{\mathrm{stat}} = -\int_{z_1}^{z_2} f(\phi)\mathrm{d}\mu = 0 \tag{4.18}$$

At least one of the solutions of this equation yields the exact binodal compositions, independent of the function $f(\phi)$. This is because $\int_{\mu=\alpha}^{\mu=\alpha} f(\phi)\mathrm{d}\mu$ always equals zero; one of the solutions of Equation 4.18 is found for $\mu(z_1) = \mu(z_2)$, which is the requirement for binodal compositions at z_1 and z_2. However, an analytical approach requires the fluxes to be rewritten in terms of diffusion coefficients $\tilde{D}$:

$$[z_2 - z_1]\, J^{\mathrm{stat}} = -\int_{z_1}^{z_2} \tilde{D}(\phi)\mathrm{d}\phi = -\int_{z_1}^{z_2} f(\phi)\frac{\partial\mu}{\partial\phi}\mathrm{d}\phi = 0. \tag{4.19}$$

Now the function $f(\phi)$ determines (together with the chosen expression for the chemical potential) whether this equation can be solved analytically or not, and if it can be

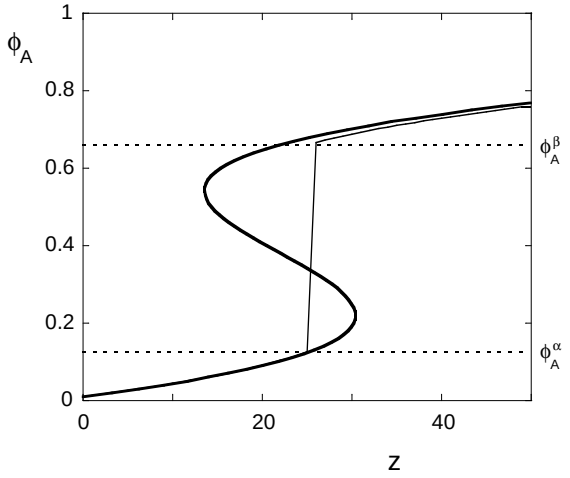

Figure 4.2. Stationary volume fraction profiles between two stable mixtures calculated numerically (thin curve) and analytically (thick curve). $N_A = 30$, $N_B = 10$, $\chi = 0.14$.

solved analytically, it determines the accuracy of the approximation. If the function $f(\phi)$ is a constant, Equation 4.19 requires a numerical calculation. If $f(\phi)$ is not a constant, analytical solutions may be possible, but numerical calculations still yield the exact binodals, since Equation 4.19 is equivalent to Equation 4.18. The discrepancy between the numerical and analytical solutions of Equation 4.19 originates from the shape of the volume fraction profiles between z_1 and z_2; numerical profiles show a discontinuity while the analytical profiles have a loop. This is shown in Figure 4.2 for a binary system. The numerical profiles are calculated by the Mean-Field Stationary Diffusion method (Chapter 2,[96]) and the analytical profiles by solving Equation 4.19 with the help of a simple form for the diffusion coefficient, presented later in Equation 4.27. The analytical computation yields the inverse of the volume fraction profile, $z(\phi_A)$, instead of $\phi_A(z)$. Since analytical solutions will never yield the discontinuous jumps, we only obtain an approximation for the exact binodals by analytically solving Equation 4.19. The discontinuous jumps are a consequence of our simple definition for the segmental chemical potential, necessary for the analytical approach; this definition yields the correct value in the bulk phases but implies a simplification in the interfacial region. A more sophisticated expression of this potential, presented in Chapter 2, yields continuous profiles without any loop.

We will see in Section 4.3.2 that Equation 4.18 or 4.19 is a sufficient condition for vanishing stationary fluxes between positions z_1 and z_2, but only a necessary condition for coexisting phases at these positions. We will need an additional criterion for coexistence.

4.3.1 Flux expressions

The expressions for the fluxes between polymer mixtures can be derived along the lines of the well-known fast-mode [20, 21] and slow-mode [19] models. Experimentalists have tried to verify the predictions of each model, but there is no definite preference for any of them: some experiments are more consistent with the slow-mode model [22, 23], others

with the fast-mode model [26, 27]. For a more detailed discussion, see Chapter 2.

The diffusion models were originally developed for binary blends, but may easily be generalized to multicomponent blends as shown in Chapter 2. Here, we only present the results. In order to describe the diffusion on the scale of segments, the *segment* chemical potentials μ are needed. They are simply calculated by dividing the chemical potential of a chain μ^{chain} by the number of chain segments N. This is an approximation since it is assumed that all segments of one chain have the same environment, although in the interfacial region the mixture is inhomogeneous on the length scale of the chain. In both diffusion models the segment fluxes satisfy the relation

$$\sum_i J_i = 0 \tag{4.20}$$

where the summation is taken over all segment types i. According to the slow-mode model, the system is incompressible and it is assumed that segments A diffuse by exchanging their positions with the positions of segments of type B,C,D.... The fluxes are then given by

$$J_A^s = -\Lambda_A \nabla \mu_A + \frac{\Lambda_A}{\sum_i \Lambda_i} \sum_j \Lambda_j \nabla \mu_j. \tag{4.21}$$

The fast-mode model assumes that there is an additional flux of segments due to drift flow. This results in fluxes that are expressed by

$$J_A^f = -\Lambda_A \nabla \mu_A + \phi_A \sum_j \Lambda_j \nabla \mu_j. \tag{4.22}$$

The difference between these two equations is thus a different prefactor of $\sum \Lambda \nabla \mu$: the volume fraction in Equation 4.22, and an "Onsager fraction" in Equation 4.21. In the above equations Λ_A is an Onsager coefficient, which can be expressed in terms of the mobility coefficient $\tilde{B}_A$ of segments A:

$$\Lambda_A(z) = \tilde{B}_A \phi_A(z) \tag{4.23}$$

The mobility coefficients may reflect the influence of entanglements on the dynamics of chains. This can be accounted for by considering the mobility coefficients to be a function of the monomer concentrations and chain lengths [20, 96]. However, in this study we consider the mobility coefficients $\tilde{B}$ as being constant. Since we are interested in equilibrium properties of the blends, the choice of mobility coefficients should not be critical. In Section 4.3.3 we explore the influence of segment mobilities on the approximations for binodal compositions. Note that the slow-mode and fast-mode expressions become identical if all segments have the same mobility $\tilde{B}_A = \tilde{B}_B = \cdots = \tilde{B}$.

In the following we apply the stationary dynamics approach to binary and multicomponent blends. We simply use the Flory-Huggins expression for the segment chemical potential, since it allows direct comparison with the approximations discussed in Section 4.2. In principle, any expression for the segment chemical potential could be chosen, as long as Equation 4.19 can be solved analytically.

4.3.2 Application to binary blends, $\tilde{B}_A = \tilde{B}_B$

We first apply the stationary dynamics approach to binary blends. For binary blends with $\tilde{B}_A = \tilde{B}_B = \tilde{B}$ we have according to Equations 4.21 and 4.22

$$J_A^s = J_A^f = -\tilde{B}\phi_A\phi_B\nabla(\mu_A - \mu_B). \tag{4.24}$$

Thus a vanishing stationary flux corresponds to:

$$J_A^{\text{stat},s} = J_A^{\text{stat},f} = -\frac{\tilde{B}}{[z_2 - z_1]}\int_{z_1}^{z_2}\phi_A\phi_B\mathrm{d}(\mu_A - \mu_B) = -\frac{\tilde{B}}{[z_2 - z_1]}\int_{z_1}^{z_2}\phi_A\mathrm{d}\mu_A = 0. \tag{4.25}$$

For the third equality we used the Gibbs-Duhem equation ($\sum_i \phi_i \mathrm{d}\mu_i = 0$) and $\phi_A + \phi_B = 1$. We see that the flux vanishes if $\mu_A(z_1) - \mu_B(z_1) = \mu_A(z_2) - \mu_B(z_2)$, or in other words if $\Delta\mu_A = \Delta\mu_B$, where $\Delta\mu = \mu(z_2) - \mu(z_1)$. This occurs (i) if mixtures 1 and 2 are identical, (ii) if they are coexistent or, (iii) if the driving force for diffusion of segments A is non-zero and the same (equal and in the same direction) as for segments B. In the third scenario none of the segments will be able to diffuse due to the incompressibility constraint (Equation 4.20). This scenario can only occur if at least one of the two mixtures is not stable (i.e. inside the binodal), since different stable mixtures always have different chemical potentials if the mixtures are non-coexistent.

Comparing Equation 4.25 with Equation 4.18 we find that in this case the function $f(\phi)$ in Equation 4.18 is given by

$$f(\phi_A) = \tilde{B}\phi_A \tag{4.26}$$

and by using Equation 4.19 and the Flory-Huggins chemical potential we find for $\tilde{D}(\phi)$:

$$\frac{\tilde{D}(\phi_A)}{k_BT} = f(\phi_A)\frac{\partial}{\partial\phi_A}\frac{\mu_A}{k_BT} = \tilde{B}\phi_A\phi_B\left(\frac{1}{\phi_A N_A} + \frac{1}{\phi_B N_B} - 2\chi\right). \tag{4.27}$$

The function $f(\phi_A)$ is linear in ϕ_A, which allows an analytical expression for the stationary flux according to $J = -\int \tilde{D}\mathrm{d}\phi_A$:

$$J_A^{\text{stat}} = \tilde{C}\left(\phi_{A1} - \phi_{A2}\right)\left(\phi_{A1}^2 + \phi_{A1}\phi_{A2} + \phi_{A2}^2 - 3k(\phi_{A1} + \phi_{A2}) + 3k^2 - \frac{3}{2}b^2\right), \tag{4.28}$$

where $\tilde{C} = \frac{2}{3}\tilde{B}\chi k_BT/[z_2 - z_1]$. There may exist many combinations of ϕ_{A1} and ϕ_{A2} for which the stationary flux vanishes. One of these combinations is the trivial case of identical blends ($\phi_{A1} = \phi_{A2}$), another combination must be the coexisting blends ($\phi_{A1} = \phi_A^\alpha$ and $\phi_{A2} = \phi_A^\beta$ or vice versa), the remaining combinations must have either $\phi_A^\alpha < \phi_{A1} < \phi_A^\beta$ or $\phi_A^\alpha < \phi_{A1} < \phi_A^\beta$ or both.

To find the best approximation for coexisting phases at z_1 and z_2, we need an extra criterion in addition to the requirement

$$\phi_{A1}^2 + \phi_{A1}\phi_{A2} + \phi_{A2}^2 - 3k(\phi_{A1} + \phi_{A2}) + 3k^2 - \frac{3}{2}b^2 = 0, \tag{4.29}$$

in particular for $N_A \neq N_B$. Therefore it is convenient to inspect the general plot of the stationary flux versus the composition of mixture 2 for given ϕ_{A1} (see Figure 4.3). If both

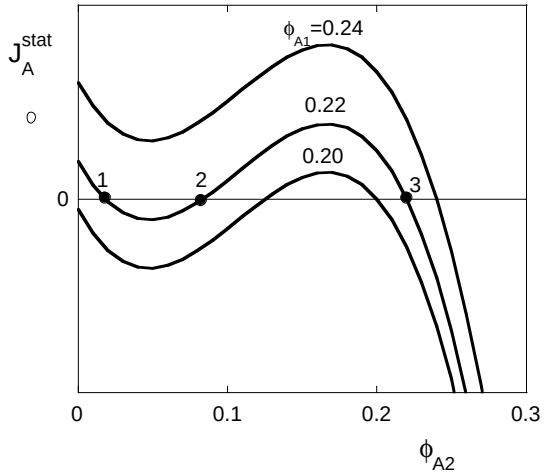

Figure 4.3. Analytically calculated stationary flux as function of the composition of mixture 2 for different compositions of mixture 1, as indicated by the value of ϕ_{A1}. $N_A = 100$, $N_B = 1$, $\chi = 0.63$.

mixtures are stable, we have $J_A^{\text{stat}} > 0$ (diffusion to the right) for $\phi_{A2} < \phi_{A1}$ and $J_A^{\text{stat}} < 0$ (diffusion to the left) for $\phi_{A2} > \phi_{A1}$. If one of the mixtures is unstable (inside the binodal curve) the stationary flux may be negative for $\phi_{A2} < \phi_{A1}$ and positive for $\phi_{A2} > \phi_{A1}$ depending on the chemical potentials of all components. Differentiating Equation 4.28 with respect to ϕ_{A2} at constant ϕ_{A1} gives $\partial J_A^{\text{stat}}/\partial\phi_{A2} = 0$ when $\phi_{A2} = k \pm b/\sqrt{2}$. Comparing this with Equation 4.5, we see that the minimum and maximum in Figure 4.3 correspond to the spinodal composition of mixture 2. Also, $\partial^2 J_A^{\text{stat}}/\partial\phi_{A2}^2 = 0$ for $\phi_{A2} = k$; the inflection point lies halfway between the two local extremes. Hence, the positions of the two extremal points and the inflection point in between do not depend on ϕ_{A1}. In fact, upon changing ϕ_{A1} the curves translate vertically, as follows from Equation 4.28.

Depending on the choice for ϕ_{A1} the curve has either one, two, or three zero points. These points are indicated by the numbers 1, 2, and 3 for $\phi_{A1} = 0.22$. Point 3 corresponds to $\phi_{A2} = \phi_{A1}$, points 1 and 2 can be found by solving the quadratic equation 4.29. If mixture 1 has a binodal composition ($\phi_{A1} = \phi_A^\alpha$) the three zero points are $\phi_{A2} = \phi_A^\alpha$ (point 3), $\phi_{A2} = \phi_A^\beta$ (point 1), and $\phi_A^\beta < \phi_{A2} < \phi_A^\alpha$ (point 2). This zero point 2 gives the necessary condition for coexisting phases in addition to Equation 4.29. It must represent the situation that $\Delta\mu_A = \Delta\mu_B \neq 0$. The additional condition is that ϕ_{A2} must have a certain given value (that of zero point 2), so that Equation 4.29 is obeyed only if mixture 1 has a binodal composition. We look for the appropriate value of zero point 2 in Section 4.3.2 after exploring the approximation for symmetrical systems in the following section.

$\tilde{B}_A = \tilde{B}_B$ and $N_A = N_B$

In a symmetrical binary blend, both components have the same chain length. For such systems, we do not explicitly need the plot of J_A^{stat} versus ϕ_{A2}: the extra criterion for coexistence is simply $\phi_A^\beta = \phi_B^\alpha = 1 - \phi_A^\alpha$. Substitution of $\phi_{A2} = 1 - \phi_{A1}$ and $N_A = N_B = N$ into Equation 4.29 yields the analytical approximation for binodal compositions

in symmetrical binary blends in which $\tilde{B}_A = \tilde{B}_B$:

$$\phi_A^{\mathrm{SDA}} = k \pm \frac{1}{2} b\sqrt{6} = \frac{1}{2} \pm \sqrt{\frac{3\chi N - 6}{4\chi N}}. \tag{4.30}$$

For symmetrical blends $k = k_{\mathrm{crit}} = \frac{1}{2}$, so that for these blends our approximation is identical to the root-three rule approximation (Equation 4.16).

Although we did not need the plot of J_A^{stat} versus ϕ_{A2} for the additional criterion, we can of course still relate this plot to ϕ_A^{SDA}. The inflection point of $J_A^{\mathrm{stat}}(\phi_{A2})$ for symmetrical blends does not only lie exactly halfway between the spinodal compositions, but also halfway between the binodal compositions, since $\left|\phi_A^{\alpha} - \phi_A^{\mathrm{spin1}}\right| = \left|\phi_A^{\beta} - \phi_A^{\mathrm{spin2}}\right|$. In other words, for symmetrical systems the zero point 2 in Figure 4.3 is also the inflection point. Thus, for symmetrical blends the stationary flux vanishes if mixture 1 has a binodal composition, and mixture 2 has either the same composition (point 3), or the coexisting composition (point 1), or the composition of the inflection point ($\phi_{A2} = k$, point 2). Hence, instead of selecting $\phi_{A2} = 1 - \phi_{A1}$ as the additional criterion, we could have selected $\phi_{A2} = k$. Indeed, substitution of $\phi_{A2} = k = k_{\mathrm{crit}} = \frac{1}{2}$ into Equation 4.29 yields the same approximation for the binodal compositions as presented by Equation 4.30.

$\tilde{B}_A = \tilde{B}_B$ and $N_A \neq N_B$

We do not have a simple relation between ϕ_A^{α} and ϕ_A^{β} for $N_A \neq N_B$ which could be used as the necessary criterion in addition to Equation 4.29. We propose two alternative additional criteria for vanishing fluxes if mixture 1 has a binodal composition: $\phi_{A2} = k$ or $\phi_{A2} = k_{\mathrm{crit}}$. For $N_A = N_B$ these criteria are identical and they yield the approximation as presented in Equation 4.30. Both criteria obey the requirement that $J_A^{\mathrm{stat}}(\phi_{A2})$ has three intersections with the line $J_A^{\mathrm{stat}} = 0$ if mixture 1 has a binodal composition, since both k and k_{crit} are somewhere between the two spinodal compositions which correspond to the local extreme of the curve.

The first choice for the additional criterion ($\phi_{A2} = k$) is related to the inflection point of $J_A^{\mathrm{stat}}(\phi_{A2})$. By taking this criterion, we assume that we must vertically translate the curve $J_A^{\mathrm{stat}}(\phi_{A2})$ until the inflection point is also a zero point of J_A^{stat}. The other zero points are then supposed to be the binodal compositions.

The alternative choice for the additional criterion ($\phi_{A2} = k_{\mathrm{crit}} = \phi_A^{\mathrm{crit}}$) is related to the observation in Equation 4.25 that the stationary flux vanishes if $\Delta\mu_A = \Delta\mu_B$. By taking this criterion we assume that both components in a mixture with a binodal composition feel the same driving force for diffusion when the other mixture has a critical composition. This is equivalent to the assumption that the chemical potential difference between the two components, $\mu_A - \mu_B$, is equal in the binodal and the critical compositions.

We also based the selection of these two criteria on numerical calculations of the stationary flux. By use of the Mean-Field Stationary Diffusion method (Chapter 2) the flux can be calculated exactly according to Equation 4.18. In these numerical calculations (also based upon the Flory-Huggins free energy functional), mixture 1 was kept at the binodal composition ϕ_A^{α}. We varied the composition of mixture 2 between $\phi_{A2} = k_{\mathrm{crit}}$ and $\phi_{A2} = k$. Figure 4.4 presents the results for various systems with $N_A > N_B$ and $\tilde{B}_A = \tilde{B}_B$. Each curve is in fact part of a curve as presented in Figure 4.3, viz. the part close to point 2. The two main intersections with the horizontal axis would occur for

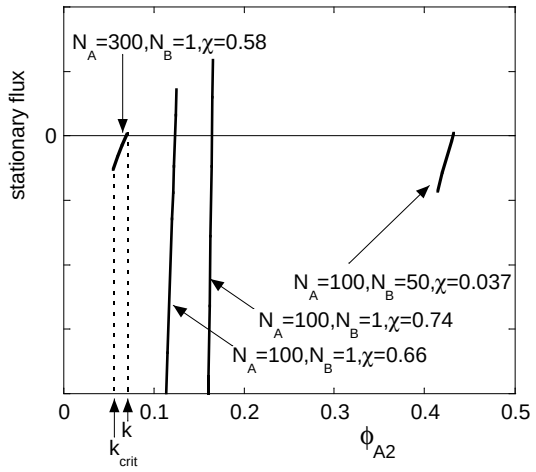

Figure 4.4. The exact stationary flux between two mixtures for four different systems. In all systems, one mixture (ϕ_{A1}) has a binodal composition. The composition ϕ_{A2} of the other mixture increases from $k_{\rm crit}$ to k. For the four combinations of N_A, N_B, and χ given in the figure (from left to right) $k_{\rm crit} = 5.46 \cdot 10^{-2}$, $9.09 \cdot 10^{-2}$, $9.09 \cdot 10^{-2}$, 0.414 and $k = 7.04 \cdot 10^{-2}$, 0.125, 0.166, 0.432. The exact stationary flux always vanishes for some value of ϕ_{A2} in between these limits.

$\phi_{A2} = \phi_A^\alpha$ and $\phi_{A2} = \phi_A^\beta$. Indeed, the third intersection of the stationary flux with the horizontal axis occurs for $k_{\rm crit} < \phi_{A2} < k$.

To select the best of our two additional criteria, we observe that the first ($\phi_{A2} = k$) yields the same result as obtained in Equation 4.30: $\phi_A^{\rm SDA} = k \pm \frac{1}{2} b\sqrt{6}$. A weak aspect of this criterion is that the resulting binodal compositions are both equally far from the spinodal compositions, which is not true for real binodal compositions. We therefore select the alternative ($\phi_{A2} = k_{\rm crit}$) as the necessary condition for a binodal composition of the mixture at the right hand side. Substitution of $\phi_{A2} = k_{\rm crit}$ into Equation 4.29 yields the stationary dynamics approximation for binodal compositions in binary blends with $N_A \neq N_B$ and $\tilde{B}_A = \tilde{B}_B$:

$$\phi_A^{\rm SDA} = \frac{1}{2}\left(3k - k_{\rm crit} \pm \sqrt{6b^2 - 3(k - k_{\rm crit})^2}\right). \tag{4.31}$$

We have compared this approximation with the approximation obtained from $\phi_{A2} = k$ in plots similar to those to follow in Section 4.4. Indeed, $\phi_{A2} = k_{\rm crit}$ yields a better approximation than $\phi_{A2} = k$ although the numerically calculated flux has zero point 2 closer to k than to $k_{\rm crit}$.

4.3.3 Application to binary blends, $\tilde{B}_A \neq \tilde{B}_B$

The segment mobilities enter the expressions for the stationary flux via the function $f(\phi)$, and may thereby determine whether an analytical prediction of the binodal compositions is possible or not.

Slow-mode diffusion mechanism

From Equation 4.21 we find for the slow-mode flux

$$[z_2 - z_1]J_A^{\mathrm{stat},s} = -\tilde{B}_A\tilde{B}_B \int_{z_1}^{z_2} \frac{\phi_A\phi_B}{\tilde{B}_A\phi_A + \tilde{B}_B\phi_B}\mathrm{d}(\mu_A - \mu_B). \tag{4.32}$$

The function $f(\phi_A)$ is found by applying the Gibbs-Duhem equation to Equation 4.32:

$$f(\phi_A) = \tilde{B}_A\tilde{B}_B\frac{\phi_A}{\phi_A(\tilde{B}_A - \tilde{B}_B) + \tilde{B}_B} \tag{4.33}$$

This function does not allow the analytical solution of $J^{\mathrm{stat}} = -\int \tilde{D}\mathrm{d}\phi = 0$, in contrast to the function $f(\phi)$ in Equation 4.26, which is linear in ϕ_A and follows from Equation 4.33 by substituting $\tilde{B}_A = \tilde{B}_B$.

If segments B are almost immobile compared to segments A, i.e. in the limit of $\tilde{B}_A/\tilde{B}_B \to \infty$, we obtain $f(\phi_A) \to \tilde{B}_B$. The diffusion may thus be described by the diffusion of only one (the slowest) component. Density gradients are immediately relaxed by the other component. Since $f(\phi_A)$ is a constant, $J^{\mathrm{stat}} = -\int \tilde{D}\mathrm{d}\phi$ would again require a numerical calculation. In the limit of $\tilde{B}_B/\tilde{B}_A \to \infty$ it is found that $f(\phi_B) \to \tilde{B}_A$.

Fast-mode diffusion mechanism

The fast-mode stationary flux for binary systems is given by

$$[z_2 - z_1]J_A^{\mathrm{stat},f} = -\tilde{B}_A\int_{z_1}^{z_2}\phi_A\phi_B\mathrm{d}\mu_A + \tilde{B}_B\int_{z_1}^{z_2}\phi_A\phi_B\mathrm{d}\mu_B, \tag{4.34}$$

so that we find for $f(\phi_A)$:

$$f(\phi_A) = \tilde{B}_A\phi_A + (\tilde{B}_B - \tilde{B}_A)\phi_A^2. \tag{4.35}$$

In combination with the Flory-Huggins potentials, this function only provides an analytical solution for $J^{\mathrm{stat}} = -\int \tilde{D}\mathrm{d}\phi = 0$ if $N_A = N_B$.

4.3.4 Application to symmetrical multicomponent blends

We now consider symmetrical systems containing K components. The symmetry in these systems arises from requirements on chain lengths and interaction parameters: $N_i{=}N\ \forall i$ and $\chi_{ij}{=}\chi\ \forall i, j \neq i$. Moreover, we assume $\tilde{B}_i{=}\tilde{B}\ \forall i$. At the corners of the K-phase region the volume fractions of $(K-1)$ components are equal to ϕ^{co}, and one component has volume fraction $1-(K-1)\phi^{\mathrm{co}}$. It is our aim to find ϕ^{co} as function of χN. The exact solution is numerically available from ([137]):

$$\frac{1}{1-K\phi^{\mathrm{co}}}\ln\left[\frac{1}{\phi^{\mathrm{co}}} - (K-1)\right] = \chi N. \tag{4.36}$$

For our approach we write the flux by use of either Equation 4.21 or 4.22 and the Gibbs-Duhem equation as

$$J_A = -\tilde{B}\phi_A\nabla\mu_A = -\sum_i f(\phi_A)\left(\frac{\partial\mu_A}{\partial\phi_i}\right)_{\phi_{j\neq i,n}}\nabla\phi_i. \tag{4.37}$$

In analogy to the approach for binary blends, we find for the mutual diffusion coefficients $\tilde{D}_{Ai}^{(K)}$, defined by $J_A = -\sum_i \tilde{D}_{Ai}^{(K)} \nabla\phi_i$:

$$\frac{\tilde{D}_{Ai}^{(K)}}{\tilde{B}k_BT} = \phi_A\phi_i\chi - \phi_A\phi_K\chi + (\delta_{AK} - \delta_{Ai})(\phi_A\chi - \frac{1}{N}). \tag{4.38}$$

The Kronecker delta δ_{AB} equals unity for $A = B$ and is zero otherwise. The superscript (K) indicates that ϕ_K is written as $1 - \sum_{i\neq K} \phi_i$, which is necessary in the calculation of the total differential in Equation 4.37.

We assume that we should always find the same compositions for the coexisting phases independent on the profiles of components $B, C \cdots, K-1$ at the interface between these phases. In other words, we substitute $\nabla\phi_i = 0$ for all $i \neq A, K$ into Equation 4.37 so that $J_A = -\tilde{D}_{AA}^{(K)} \nabla\phi_A$. We need to calculate ϕ^{co} for which $\int_{z_1}^{z_2} \tilde{D}_{AA}^{(K)} \mathrm{d}\phi_A = 0$. After the integration we substitute $\phi_{A1} = \phi_{K2} = \phi^{\mathrm{co}}$, $\phi_{A2} = \phi_{K1} = 1 - (K-1)\phi^{\mathrm{co}}$ and $\phi_{i1} = \phi_{i2} = \phi^{\mathrm{co}}\ \forall i \neq A, K$. Again (as for the binary systems, Equation 4.28) the result is a cubic equation in ϕ^{co}. One root of this polynomial is known: the flux should at least vanish if all components have the same volume fractions, thus $\phi^{\mathrm{co}} = \frac{1}{K}$. The two remaining roots are then found to be

$$\phi^{\mathrm{co}} = \frac{1}{2K^2}\left\{6 - K \pm \sqrt{3K^2(3 - \frac{8}{\chi N}) + 12(3-K)}\right\} \tag{4.39}$$

Only one of these two roots is a valid approximation (unless $K = 2$ for which ϕ^{co} reduces to Equation 4.30). Since the K-phase region increases with χN, ϕ^{co} must decrease with χN. We must therefore use the minus-sign in Equation 4.39.

We can also find approximations for the compositions at the corners of $(K-1)$-phase regions (for $K > 2$). At these corners, one minority component has volume fraction ϕ^{m}, $(K-2)$ components have volume fractions ϕ^{co} and the volume fraction of the last component is $1 - \phi^{\mathrm{m}} - (K-2)\phi^{\mathrm{co}}$. We want to obtain ϕ^{co} as a function of ϕ^{m} and χN. The exact solution can be calculated numerically from ([137]):

$$\frac{1}{1 - \phi^{\mathrm{m}} - (K-1)\phi^{\mathrm{co}}} \ln\left[\frac{1-\phi^{\mathrm{m}}}{\phi^{\mathrm{co}}} - (K-2)\right] = \chi N. \tag{4.40}$$

Taking the integral of the mutual diffusion coefficient and substituting two corner compositions into the result yields a cubic equation in ϕ^{co}. One root is given by $\phi^{\mathrm{co}} = (1-\phi^{\mathrm{m}})/(K-1)$. The others are:

$$\phi^{\mathrm{co}} = \frac{\phi^{\mathrm{m}}}{1-K} + \frac{1}{2(K-1)^2}\left\{7 - K \pm \sqrt{24(1-K)\phi^{\mathrm{m}} + (7-K)^2 + 8(K-1)^2(1 - \frac{3}{\chi N})}\right\} \tag{4.41}$$

This reduces to Equation 4.39 for $\phi^{\mathrm{m}} = \phi^{\mathrm{co}}$.

4.4 Results

The performance of our approximations for the binodal compositions can easily be evaluated by comparing them with the numerically calculated binodal and with other approximations. In this section, we only consider our approximations for systems with equal segment mobilities for all components, so that the fast- and slow-mode models are identical.

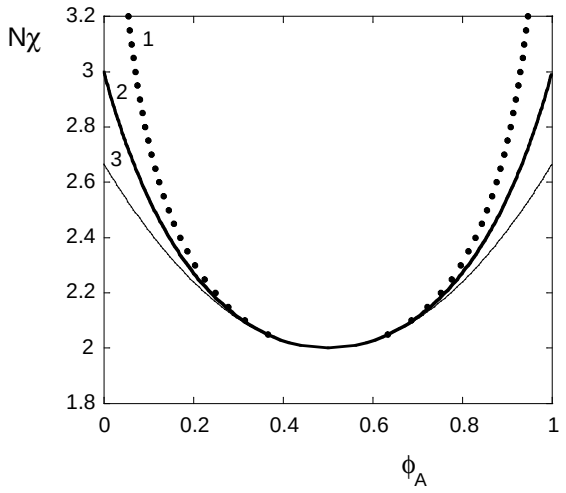

Figure 4.5. Comparison of exact and approximated coexistence curves for binary homopolymer systems with $N_A = N_B = N$. Curve 1 is the exact binodal (Equation 4.4), curve 2 is our analytical approximation (Equation 4.30) which in this case equals the root-three rule approximation (Equation 4.16), curve 3 is the analytical Van der Waals-approximation (Equation 4.11).

4.4.1 Symmetric binary blends

In Figure 4.5 we have plotted three binodals (coexistence curves). The use of the variable χN allows to cover all possible symmetrical binary systems at once. Curve 1 is the exact binodal, curve 2 is our approximation (Equation 4.30), which in this case equals the root-three rule approximation, and curve 3 is the approximation obtained by the Van der Waals theory of fluid interfaces (Equation 4.11). It is seen that all approximations perform well for systems not too far from their critical point ($\chi N = 2$) and that our approximation (or the root-three rule) is significantly more accurate than Van der Waals' approximation for larger χN.

4.4.2 Asymmetrical binary blends

Figures 4.6*a-d* illustrate the performance of our approximation for some typical examples of asymmetrical binary blends. The dots in these figures always represent the exact binodals, the solid curves correspond to our approximation given by Equation 4.31, and the dashed curves to the root-three rule. In Figure 4.6*a* the chain lengths do not differ too much, and our approximation almost coincides with the root-three result. Moreover, the accuracy of our approximation is comparable to that for symmetrical systems. With increasing N_A/N_B the discrepancy between our approximation and the root-three result increases, in particular for the branch of the coexistence curve that corresponds to the phase that is relatively rich in the longer chains. Our approximation is more accurate for this branch. For the other branch (dilute in the longer chains), the root-three rule is slightly more accurate than our approximation, but the difference is very small. Both

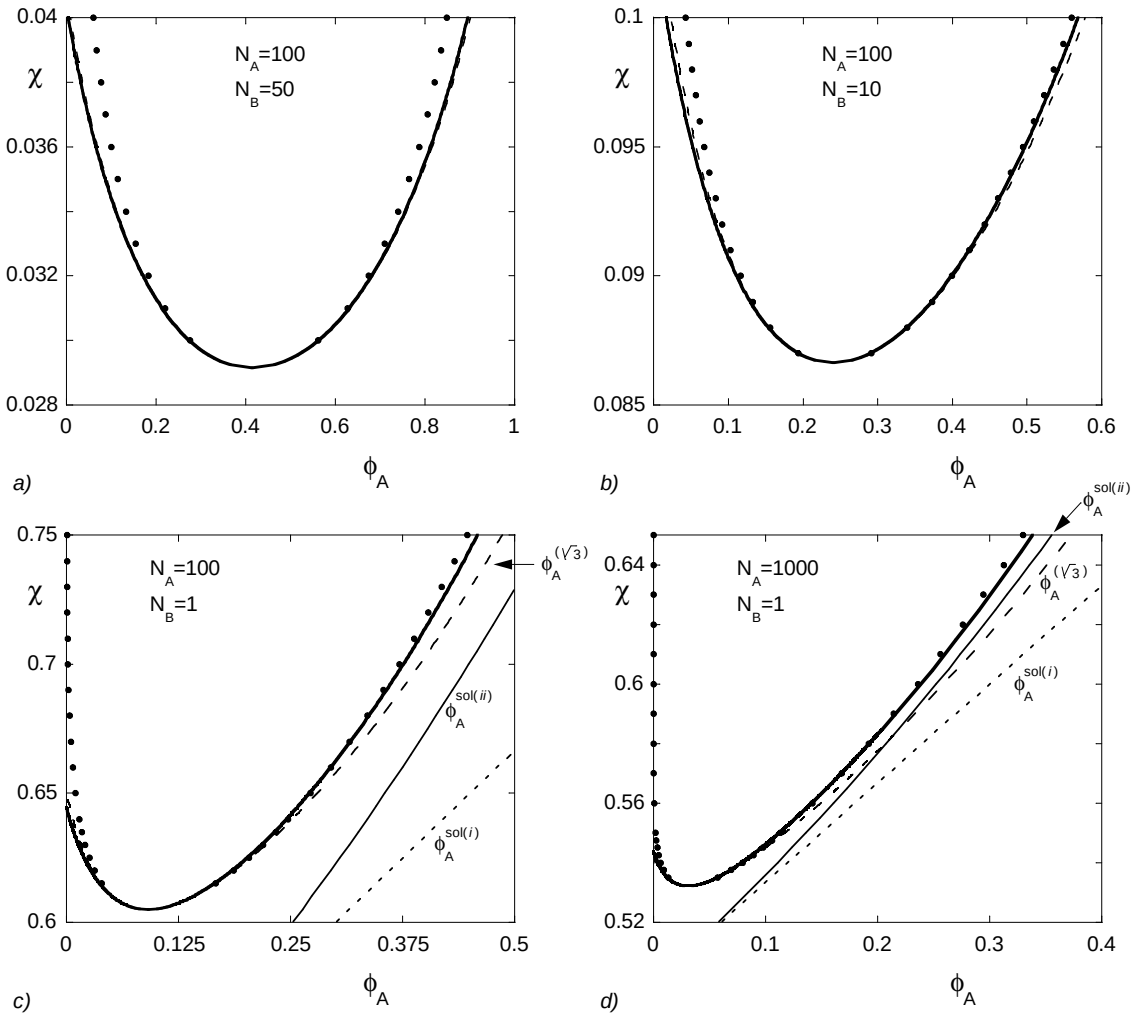

Figure 4.6. Comparison of our approximation Equation 4.31 (thick solid curves) with the exact binodal (dots), the root-three rule of Equation 4.16 (dashed curves), and the solution approximations of Equations 4.13 and 4.14 (dotted and thin solid curves respectively).

approximations for the diluted branch fail for high χ, since they predict negative volume fractions.

We can also compare our approximation with the approximations for polymer solutions (Equations 4.13 and 4.14). In Figures 4.6*c* and *d* ($N_B = 1$), where the polymer in solution has chain lengths 100 and 1000 respectively, we see that our approximation is much more accurate than $\phi_A^{\mathrm{sol}(i)}$ and $\phi_A^{\mathrm{sol}(ii)}$ (dotted lines). The accuracies of $\phi_A^{\mathrm{sol}(i)}$ and $\phi_A^{\mathrm{sol}(ii)}$ increase with N_A. We may substitute $N_A \to \infty$ into Equations 4.12 -4.15 and 4.31 and then write for each approximation χ as function of ϕ_A. In Figure 4.7 the results for infinitely long chains in a monomeric solvent are compared for all approximations. Taking the most accurate equation (the underestimating Equation 4.12) as the reference, it is concluded that our stationary dynamics approach yields the best approximations also for $N_A \to \infty$.

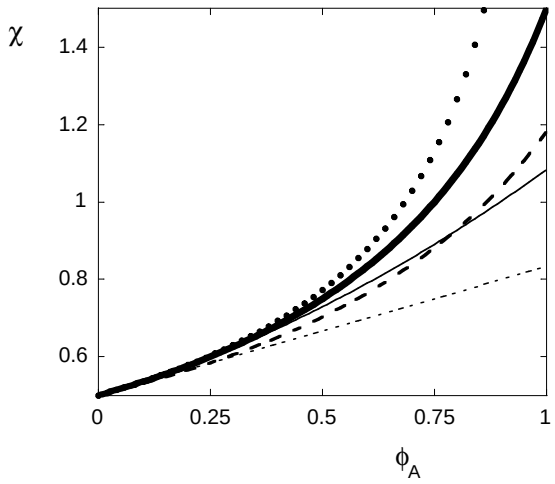

Figure 4.7. Comparison of all approximations for polymer solutions: $N_A \to \infty$, $N_B = 1$. Curves correspond to Equations 4.12-4.15 and 4.31 for the concentrated phase β, which yield $\chi^{\text{ref}} = -\frac{1}{\phi_A^2}(\phi_A + \ln(1-\phi_A))$ (dots), $\chi^{\text{sol}(i)} = \frac{1}{3}\phi_A + \frac{1}{2}$ (dotted line), $\chi^{\text{sol}(ii)} = \frac{1}{4}\phi_A^2 + \frac{1}{3}\phi_A + \frac{1}{2}$ (thin solid curve), $\chi^{(\sqrt{3})} = \frac{\sqrt{3}}{2(\sqrt{3}-\phi_A)}$ (dashed curve), $\chi^{\text{SDA}} = \frac{3}{6-4\phi_A}$ (thick solid curve).

4.4.3 Symmetric multicomponent blends

In Figure 4.8 we compare our approximation (Equation 4.41) with the exact results (Equation 4.40) for 2-phase regions in symmetrical 3-component blends. The smaller χN, the better our approximation. The product χN needs to be sufficiently large for the existence of a 3-phase region. Figure 4.9 gives the result for the lowest possible χN, which is $2\ln 4 = 2.77$ [137]. In this case there is a large discrepancy between our approximation (Equation 4.39) and the exact result (Equation 4.36), in line with the conclusion above that our model becomes worse for high χN.

4.5 Spinodal compositions derived from flux expressions

Spinodal compositions are strongly related to the binodal compositions. In phase diagrams, the stable and metastable mixtures are separated by the binodal line, while the metastable and unstable mixtures are separated by the spinodal line. Spinodal compositions are sometimes calculated numerically [137], although they may be calculated analytically (also for multicomponent systems) by Gibbs' determinant approach [138]. We show that exactly the same spinodal compositions are obtained by means of our flux-expressions.

Suppose that at some value of z the volume fractions and their gradients are such that $J_i(z) = 0$ for all i. (Note that we now turn to z-dependent fluxes, in contrast to the stationary fluxes considered in the search for binodal compositions). At this z a

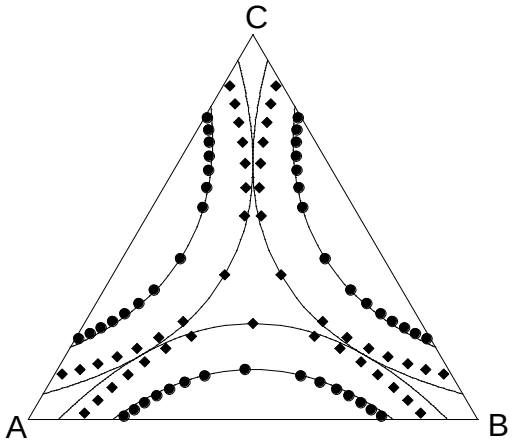

Figure 4.8. Two-phase regions in symmetrical three-component blends ($K = 3$). Comparison of our approximation (curves) with exact results (dots: $\chi N = 2.3$ and squares: $\chi N = \frac{8}{3}$).

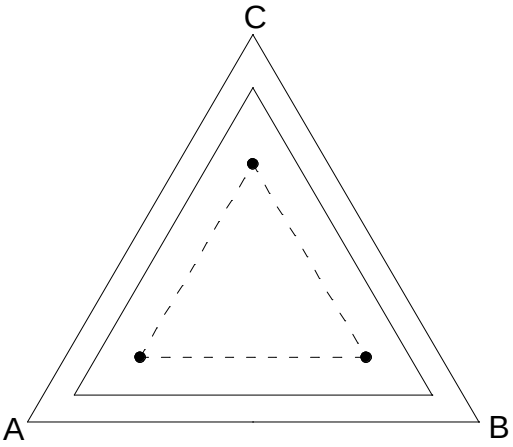

Figure 4.9. Three-phase region in a symmetrical three-component blend for lowest value of χN leading to phase separation, i.e. $\chi N = 2 \ln 4$ [137]. Comparison of our approximation (line) with exact results (dots).

component does not 'know' in which direction it should diffuse, although there may still exist gradients in the segment chemical potentials. This indicates that the composition of the blend at z may obey the spinodal conditions. Here we show that indeed the spinodal is found by requiring that all fluxes are zero at the same position z.

We first consider binary blends. The slow- and fast-mode fluxes (Equations 4.21 and 4.22) may be written in terms of only one segment chemical potential by applying the

Gibbs-Duhem equation:

$$J_A^s(z) = -\tilde{D}_{AA}^{s(B)}(z)\nabla\phi_A(z) = -\frac{\tilde{B}_B}{\Lambda_A(z)+\Lambda_B(z)}\Lambda_A(z)\nabla\mu_A(z) \tag{4.42}$$

$$J_A^f(z) = -\tilde{D}_{AA}^{f(B)}(z)\nabla\phi_A(z) = -\tilde{B}_B\left(\frac{\phi_A(z)}{\tilde{B}_A}+\frac{\phi_B(z)}{\tilde{B}_B}\right)\Lambda_A(z)\nabla\mu_A(z). \tag{4.43}$$

Due to the condition in Equation 4.20, both components have zero flux at $z = z^*$ if

$$\tilde{D}_{AA}^{(B)}(z^*) = f(z^*)\frac{\partial\mu_A(z^*)}{\partial\phi_A} = 0. \tag{4.44}$$

The function $f(z)$ is different for the slow- and fast mode models. It is determined by the factors in front of $\nabla\mu_A$ in Equations 4.42 and 4.43 respectively. We conclude from Equation 4.44 that the fluxes are zero only for the trivial solution ($\phi_A(z^*) = 0 \Rightarrow f(z^*) = 0$) or for the spinodal condition ($\frac{\partial^2 F}{\partial\phi_A^2} = 0 \Leftrightarrow \frac{\partial\mu_A}{\partial\phi_A} = 0$).

Multicomponent blends containing $n+1$ components have $J_i(z^*) = 0$ for all i if

$$|\tilde{\mathsf{D}}| = 0. \tag{4.45}$$

$\tilde{\mathsf{D}}$ is a matrix with dimensions $n \times n$. Its elements are the mutual diffusion coefficients $\tilde{D}_{ij}^{(n+1)}$ for either the slow mode or the fast mode model. Following the procedure for binary blends, these diffusion coefficients are written as:

$$\tilde{D}_{ij}^{s(n+1)} = \Lambda_i\left(x_{ij} + \sum_{k=1}^{k=n+1}\frac{1}{\Lambda_k}\sum_{l=1}^{n}(\tilde{B}_{n+1}-\tilde{B}_l)\phi_l x_{lj}\right) \tag{4.46}$$

$$\tilde{D}_{ij}^{f(n+1)} = \Lambda_i\left(x_{ij} + \frac{1}{\tilde{B}_i}\sum_{l=1}^{n}(\tilde{B}_{n+1}-\tilde{B}_l)\phi_l x_{lj}\right) \tag{4.47}$$

These expressions are found by substituting the Gibbs-Duhem equation and the total differential of μ_i into the flux equations 4.21 and 4.22. Here, x_{ij} is an element of the $(n \times n)$-matrix $\mathsf{X_n}$ and it is equal to $\left(\frac{\partial\mu_i}{\partial\phi_j}\right)_{\phi_m \neq j}$. After some matrix manipulations (see Appendix 4A) it is found that the fluxes are all equal to zero if

$$|\tilde{\mathsf{D}}^{\mathsf{s}}| = \tilde{B}_{n+1}\sum_{k=1}^{n+1}\frac{1}{\Lambda_k}\left(\prod_{l=1}^{n}\Lambda_l\right)|\mathsf{X_n}| = 0 \tag{4.48}$$

$$|\tilde{\mathsf{D}}^{\mathsf{f}}| = \tilde{B}_{n+1}\sum_{k=1}^{n+1}\frac{\phi_k}{\tilde{B}_k}\left(\prod_{l=1}^{n}\Lambda_l\right)|\mathsf{X_n}| = 0. \tag{4.49}$$

Since all terms in the summations are definite positive, the fluxes are found to be zero only if any of the components vanish or if

$$|\mathsf{X_n}| = 0 \tag{4.50}$$

which is exactly the spinodal condition for homopolymer blends containing $n+1$ components [138]. Both diffusion mechanisms result in the same spinodal. It is easily verified that Equations 4.48 and 4.49 are indistinguishable if all segments have the same mobilities, that they reduce to Equation 4.44 for binary blends, and that their solutions are independent of the segment mobilities.

4.6 Conclusions

The stationary dynamics approach is in principle an exact approach to obtain the compositions of coexisting phases. The binodal curves result from calculating the compositions of two distinguishable mixtures such that (i) there is no diffusion between these mixtures in the stationary state and (ii) an appropriate additional criterion is satisfied. For binary blends with $N_A = N_B$ this additional criterion is $\phi_A^\beta = 1 - \phi_A^\alpha$. In our approximations we took as a general additional criterion (both for symmetrical and asymmetrical binary blends) that the stationary flux also vanishes between a binodal mixture and a critical mixture, assuming that for this situation the chemical potential differences are approximately equal for both components.

The stationary dynamics approach becomes an approximation when the fluxes, written in terms of diffusion coefficients, are calculated analytically instead of numerically. The analytically calculated function $z(\phi_A)$ is not an injection if $\chi > \chi_{\text{crit}}$ (i.e. one value of z may have several values for ϕ_A) so that the analytical volume fraction profile between two mixtures is necessarily unrealistic. The expressions for the diffusion coefficients require a choice for the diffusion mechanism as well as a choice for the chemical potentials as a function of the volume fractions. These choices determine whether an analytical approach is possible or not, and the diffusion mechanism determines the accuracy of the approximated binodals, although the numerical results will always remain exact. The slow- or fast-mode diffusion mechanism in combination with the Flory-Huggins chemical potential yields an analytical approximation for the binodals when all segments have the same mobilities. This approximation for symmetrical blends ($N_A = N_B$) is equal to the root-three approximation, and more accurate than the Van der Waals-approximation. For blends with $N_A \neq N_B$, our approximation is more accurate than the root-three rule as for the composition of the phase that is relatively rich in the longer chains, and comparable as for the other (diluted) phase. Our stationary dynamics approximation is also more accurate than the approximations for polymer solutions obtained by assuming that the dilute phase is essentially pure solvent. The stationary dynamics approach also yields approximations for coexisting phases in symmetrical multicomponent systems, but the accuracy decreases as the number of coexisting phases increases. Our approximations may serve as good initial guesses for the search of coexisting phases by numerical calculations or simulations. Probably, the stationary dynamics approach may also yield analytical approximations if it is combined with other diffusion mechanisms than the fast- or slow-mode mechanisms or when it is applied to another chemical potential than the Flory-Huggins potential.

We also analyzed the fast- and slow-mode flux expressions for a specific non-stationary situation. If two mixtures have arbitrary compositions, it may occur that all fluxes are zero at some moment t^* at some position z^* between these mixtures. This occurs if the composition at t^* and z^* corresponds to a spinodal composition. Therefore, the spinodal compositions may be calculated for systems with $n+1$ components from the condition $|\tilde{\mathsf{D}}_\mathsf{n}| = 0$, where the matrix $\tilde{\mathsf{D}}_\mathsf{n}$ contains $n \times n$ diffusion coefficients $\tilde{D}$. Both the slow-mode and the fast-mode models yield exactly the same spinodal as calculated by Gibbs' condition $|\mathsf{X}_\mathsf{n}| = 0$, with elements $x_{ij} = \partial\mu_i/\partial\phi_j$.

Appendix 4A Calculation of $|\tilde{\mathsf{D}}|$

Using Equations 4.46 and 4.47 we have for $|\tilde{\mathsf{D}}|$:

$$|\tilde{\mathsf{D}}^{\mathsf{s}}| = \left(\prod_{l=1}^{n}\Lambda_l\right)|\mathsf{X_n}+\mathsf{Y_n}| \tag{4A.1}$$

$$|\tilde{\mathsf{D}}^{\mathsf{f}}| = \left(\prod_{l=1}^{n}\phi_l\right)|\mathsf{W_n}\mathsf{X_n}+\mathsf{Z_n}| \tag{4A.2}$$

The subscript n refers to the dimension of the square matrices. The matrices $\mathsf{W_n}$, $\mathsf{X_n}$, $\mathsf{Y_n}$, and $\mathsf{Z_n}$ have elements defined by

$$w_{ii} = \tilde{B}_i, \quad w_{ij} = 0 \quad \forall j \neq i \tag{4A.3}$$

$$x_{ij} = \left(\frac{\partial\mu_i}{\partial\phi_j}\right)_{\phi_{m\neq j,n+1}} \tag{4A.4}$$

$$y_{ij} = \sum_{k=1}^{n+1}\frac{1}{\Lambda_k}\sum_{l=1}^{n}(\tilde{B}_{n+1}-\tilde{B}_l)\phi_l x_{lj} \tag{4A.5}$$

$$z_{ij} = \sum_{l=1}^{n}(\tilde{B}_{n+1}-\tilde{B}_l)\phi_l x_{lj} \tag{4A.6}$$

Note that all rows of $\mathsf{Y_n}$ are identical, which is also the case for $\mathsf{Z_n}$.

We define the matrix $\mathsf{A_n}(k,l)$ as the one that is obtained by replacing rows k and l in $\mathsf{A_n}$ with the corresponding rows of matrix $\mathsf{B_n}$. For example, matrix $\mathsf{A_4}(1,2)$ is identical to matrix $\mathsf{B_4}(3,4)$. From $|\mathsf{A_n}+\mathsf{B_n}| = \sum_{k=1}^{n}(a_{1k}+b_{1k})|(\mathsf{A_{1k}})_{n-1}+(\mathsf{B_{1k}})_{n-1}|$ it can be shown by induction that $|\mathsf{A_n}+\mathsf{B_n}|$ may be calculated as

$$|\mathsf{A_n}+\mathsf{B_n}| = |\mathsf{A_n}|+|\mathsf{B_n}| \quad \text{for } n=1 \tag{4A.7}$$

$$|\mathsf{A_n}+\mathsf{B_n}| = |\mathsf{A_n}|+|\mathsf{B_n}|+|\mathsf{A_n}(1)|+|\mathsf{B_n}(1)| \quad \text{for } n=2 \tag{4A.8}$$

$$\begin{aligned}|\mathsf{A_n}+\mathsf{B_n}| = {} & |\mathsf{A_n}|+\sum_{i_1=1}^{n}|\mathsf{A_n}(i_1)|+\sum_{i_2=1}^{n-3}\sum_{i_1=i_2+1}^{n}|\mathsf{A_n}(i_2,i_1)| \\ & +\sum_{i_3=1}^{n-4}\sum_{i_2=i_3+1}^{n-3}\sum_{i_1=i_2+1}^{n}|\mathsf{A_n}(i_3,i_2,i_1)|+\cdots+ \\ & +\sum_{i_1=n-2}^{n}|\mathsf{A_n}(1,2,3,\cdots,n-3,i_1)|+|\mathsf{B_n}|+\sum_{i_1=1}^{n}|\mathsf{B_n}(i_1)| \\ & +\cdots+\sum_{i_1=n-2}^{n}|\mathsf{B_n}(1,2,3,\cdots,n-3,i_1)| \quad \text{for } n\geq 3.\end{aligned} \tag{4A.9}$$

We will focus on the most complex systems with $n \geq 3$. Fortunately, most terms in Equation 4A.9 vanish if this equation is applied to $|\mathsf{X_n}+\mathsf{Y_n}|$ or to $|\mathsf{W_n}\mathsf{X_n}+\mathsf{Z_n}|$ (the determinants in Equation 4A.1 and 4A.2). This is due to the fact that $|\mathsf{A_n}| = 0$ if $\mathsf{A_n}$ has

at least two identical rows. Applying Equation 4A.9 we obtain for $|\tilde{\mathsf{D}}|$:

$$|\tilde{\mathsf{D}}^{\mathsf{s}}| = \left(\prod_{l=1}^{n} \Lambda_l\right)\left(|\mathsf{X}_{\mathsf{n}}| + \sum_{i_1=1}^{n} |\mathsf{X}_{\mathsf{n}}(i_1)|\right) \tag{4A.10}$$

$$|\tilde{\mathsf{D}}^{\mathsf{f}}| = \left(\prod_{l=1}^{n} \phi_l\right)\left(|\mathsf{W}_{\mathsf{n}}\mathsf{X}_{\mathsf{n}}| + \sum_{i_1=1}^{n} |(\mathsf{WX})_{\mathsf{n}}(i_1)|\right) \tag{4A.11}$$

Equations 4.48 and 4.49 are now readily computed by substituting

$$|\mathsf{X}_{\mathsf{n}}(i_1)| = \left(\sum_{k=1}^{n+1} \frac{1}{\Lambda_k}\right)(\tilde{B}_{n+1} - \tilde{B}_{i_1})\phi_{i_1} \tag{4A.12}$$

$$|(\mathsf{WX})_{\mathsf{n}}(i_1)| = \left(\prod_{l=1}^{n} \tilde{B}_l\right)\frac{1}{\tilde{B}_{i_1}}(\tilde{B}_{n+1} - \tilde{B}_{i_1})\phi_{i_1} \tag{4A.13}$$

into Equations 4A.10 and 4A.11.

Chapter 5

Wetting transitions in symmetrical polymer blends

The characteristics of wetting in polymer blends are investigated by a self-consistent-field theory. A symmetrical system is chosen: the interface between two homopolymer liquids A_N and B_N is wetted by a third homopolymer C_N which is equally insoluble in both liquids. All components have the same chain length ($N_A = N_B = N_C = N = 10$ or 100). The emphasis of this study is on the wetting transitions induced by varying the interactions between the components. Cahn's argument, which predicts complete wetting near the critical temperature of two system components, is verified in this context. We show that it is necessary to consider the effective interaction parameters $\chi^{\rm eff}_{\rm AC} = \chi^{eff}_{\rm BC}$ to establish the validity of Cahn's argument. Since we vary the solubility of C (given by $\chi_{\rm AC} = \chi_{\rm BC}$) and the thickness of the A/B-interface (determined by $\chi_{\rm AB}$) independently we have a two-dimensional parameter space. In this parameter space we can distinguish three regimes representing wetting transitions with different characteristics. One of these regimes indeed shows Cahn-type transitions. A key observation is that the wetting transitions near the simultaneous critical point of mixtures A/C and B/C are of a second-order type. A second regime in the parameter space represents wetting transitions which are understood from the high surface tension of the A/B-interface. In many cases these wetting transitions are also of a second-order type, but become first order when $N\chi_{\rm AB} > 8$. In the third regime we find what might be called 'pseudo wetting': from inspection of the adsorption isotherms it follows that C seems to wet the A/B-interface, but upon increasing the amount of C in the system, the wetting layer is suddenly destroyed. The reason for this is clear. Here the apparent wetting point $\chi^{\rm wet}_{\rm AC}$ is close to $\chi^{\rm eff,crit}_{\rm AC}$, but $\chi_{\rm AB} < \chi_{\rm AC} = \chi_{\rm BC}$, the wetting film is unstable. As a result, while at first Cahn's argument seems to be fulfilled, it eventually fails in this region of the parameter space.

Published in Journal of Chemical Physics **114**, 4267 (2001).

5.1 Introduction

In the field of wetting the development of a new phase at the interface between two other phases is studied. Since wetting occurs in numerous systems and under many conditions, the study of wetting is of great interest for a large variety of applied research topics. One example is the development of new coatings. A coating should, for example, protect a surface against another (wetting) compound. There are also many examples in which two materials should remain in contact with each other, not allowing a third component to intervene. Adhesive tape for instance should not easily be removed by moisture. Recently, it was proposed that wetting also plays an important role in protein organization in cell membranes [139]. Obviously, this is important for the investigation of membranes or protein functions. In the literature there is a special interest for systems which may display second-order type wetting transitions, alternatively called critical wetting. Systems showing second-order wetting transitions are so attractive from an experimental point of view since uniform layer thicknesses can easily be achieved in such systems. However, in experimental studies, second-order transitions are rarely observed. Recently the wetting transitions of only three experimental liquid systems have been identified as being critical. Two of these experimental systems are of interest for petroleum engineering: with increasing temperature both pentane and octane films grow continuously onto the water-vapour interface [140, 141]. The third experimental observation of critical wetting concerned the methanol/nonane system in which methanol wetted the nonane liquid/vapour interface [142]. In theoretical studies it is possible to investigate wetting characteristics for a large parameter space, for example for a range of molecular weights, as has been done by Pereira and Wang in Monte Carlo simulations [143], by Ragil et al. in Cahn-type calculations [144] and by Leermakers and Van Eijk in self-consistent-field Scheutjens-Fleer calculations [145, 146]. Ragil's calculations led to the experimental observation of critical wetting by pentane.

The present theoretical study can be viewed as a continuation of the work of Leermakers [145] and Van Eijk [146]. In contrast to the previous self-consistent-field wetting studies our focus is on a mixture of three homopolymers. The solvents are denoted by A and B, and the wetting component by C. The system is chosen as symmetrical as possible: all polymers have the same degree of polymerization ($N_A = N_B = N_C = N$) and the wetting component is equally soluble in both solvents ($\chi_{\mathrm{AC}} = \chi_{\mathrm{BC}}$ where χ is the well-known Flory-Huggins parameter). The advantage of using such a symmetrical system is that curvature effects of the macroscopic interface are not present; the interface remains flat. By avoiding curved interfaces many complications like curvature-dependent surface tensions are eliminated, which facilitates the prediction of trends. Moreover, in our self-consistent-field calculations simple flat lattices can be used for non-curved interfaces.

The emphasis is on the wetting transitions occurring in the ternary system by varying the solubility of the wetting component (keeping $\chi_{\mathrm{AC}} = \chi_{\mathrm{BC}}$) and the mutual miscibility of the solvents χ_{AB}. As a consequence of the variation in the miscibility the width of the interface which will be wetted is varied as well. Our results show that for this simple system there exists a large parameter space for the interaction parameters which give rise to second-order wetting transitions (if the long-range Van der Waals contributions are negligible). We also check the occurrence of complete wetting close to the critical point as predicted by Cahn. Cahn's argument holds a special position in the field of wetting as it is the only general statement available to search for wetting transitions. The argument

is based on considerations of temperature effects. Here we study the effect of interaction parameters instead of temperature. We indeed find Cahn wetting, and the associated transitions are of second-order type. If we enter the region where $\chi_{\mathrm{AB}} < \chi_{\mathrm{AC}} = \chi_{\mathrm{BC}}$, Cahn wetting at first instance seems to occur, but real wetting is never found. The *wetting-like* transitions which do occur in the metastable regime of this region can be investigated in small finite systems and are associated with what might be called 'pseudo wetting', which has unusual behaviour. The Cahn wetting argument thus fails for a set of systems. This means that the Cahn argument is not as generally true as claimed in the literature.

In the following, we will first explain which wetting transitions can be expected if the interaction parameters are varied. We therefore position Cahn's argument in the context of interaction parameters. We do not review the general aspects of wetting, but refer to Schick [147], who introduces wetting transitions in terms of adsorption isotherms and wetting phase diagrams. We then briefly explain those aspects of the self-consistent-field method of Scheutjens and Fleer which are of importance for this study. In the subsequent section the results are presented and discussed, where we distinguish three different regimes in our two-dimensional parameter space spanned by χ_{AB} and $\chi_{\mathrm{AC}} = \chi_{\mathrm{BC}}$. In the last section the conclusions are summarized.

5.2 Wetting transitions by χ-variation

Cahn's argument states that a wetting transition from partial to complete wetting must take place before the critical temperature T^{crit} is reached [148, 149]. At the critical temperature the phase boundary between two phases ceases to exist and the three-phase system turns into a two-phase system. Cahn's argument is based upon a consideration of the temperature dependence of the surface tensions for systems in which the long-range forces are less important than the short-range forces. Suppose that we have a situation of partial wetting in a solid-liquid-vapour system. According to Young's equation [150] ($\sigma_{sv} = \sigma_{sl} + \sigma_{lv}\cos\alpha$) we then have for the surface tensions: $\sigma_{lv} > \sigma_{sv} - \sigma_{sl}$. The surface tension of the interface which becomes critical (σ_{lv} in this example system) decreases more rapidly with ($T^{\mathrm{crit}} - T$) than the difference between the surface tensions of the non-critical interfaces ($\sigma_{sv} - \sigma_{sl}$) does. Consequently, at a certain moment σ_{lv} will no longer exceed $\sigma_{sv} - \sigma_{sl}$ so that Young's condition for complete wetting by the liquid phase ($\sigma_{sv} = \sigma_{sl} + \sigma_{lv}$) is met. This phenomenological consideration of the temperature dependencies does not only apply to the wetting of a solid wall. It is also applicable in the case of three liquids: if the temperature approaches the critical temperature at which phases α and β will become miscible, either α will wet the β/γ-interface (if $\sigma_{\alpha\gamma} < \sigma_{\beta\gamma}$) or β will wet the α/γ-interface (if $\sigma_{\alpha\gamma} > \sigma_{\beta\gamma}$).

Cahn's argument does not predict the order of the wetting transition which has to occur before the critical temperature is reached. It only states that the interface will be completely wetted before $T = T^{\mathrm{crit}}$ and this can occur either after prewetting or after a continuous growth of the layer. It has been shown that Cahn's argument can be violated if long-range forces have to be taken into account and if short-range forces favour wetting, but the long-range forces do not [151, 152]. In that case, the wetting phase γ might form a layer at the interface between phases α and β, but this layer will not grow to an infinite thickness as is the case for complete wetting. Its thickness will be bounded by

the long-range forces which attract the β/γ-interface to the α/γ-interface. The thickness of the wetting layer will therefore be comparable to the bulk correlation length so that only at the critical point the layer can grow to macroscopic thicknesses. Thus instead of $T^{\text{wet}} < T^{\text{crit}}$, as stated by Cahn, long-range forces could lead to $T^{\text{wet}} = T^{\text{crit}}$.

In this study, we assume that the polymers are long enough to describe their wetting behaviour by short-rage forces only. Pereira and Wang have shown that it follows from numerical calculations that the Van der Waals (long-range) model give similar results to the short-range model if the effective range of the Van der Waals interaction is much smaller than the size of the polymer chains [153]. The wetting temperature in one of the experimental observations of a second-order transition was very close to the critical temperature of the nonane-methanol mixture under consideration [142]. If long-range forces would be important for this mixture, no second-order transition would be found. (The other second-order transitions observed where not close to the critical point [140, 141], but also in these cases it was assumed by the analysis of the Hamaker constant that the short-range forces became more important than the long-range forces near the wetting temperature).

Temperature is of course not the only parameter influencing the surface tensions. The interactions between the components are other examples of surface tension-determining variables. These variables are also experimentally accessible, for example by varying the concentration of an additional solute [141]. The Flory-Huggins interaction parameters χ are the variables of interest in the present study. The effect of a decreasing value for χ is similar to the effect of an increasing temperature: the interface becomes less sharp and the separate phases cannot exist anymore if χ becomes critical. From the Flory-Huggins free energy expression, it can easily be derived that for a three-component system the critical χ for two components P and Q depends on the volume fraction of the other component R as

$$\chi_{\text{PQ}}^{\text{crit}} = \frac{1}{2(1-\phi_R)} \left(\frac{1}{\sqrt{N_P}} + \frac{1}{\sqrt{N_Q}} \right)^2 \tag{5.1}$$

which reduces for our system to

$$\chi_{\text{PQ}}^{\text{crit}} = \frac{2}{N(1-\phi_R)} \tag{5.2}$$

While the temperature is the only variable in Cahn's argument, the interaction parameters between each pair of components ($\chi_{\text{AB}}/\chi_{\text{AC}}/\chi_{\text{BC}}$) can in principle be chosen independently from each other. However, the resulting (triangular) phase composition diagram depends on the combination of all χ-parameters. Like the temperature influences the mutual miscibilities of all components collectively, the value of each χ-parameter also changes all miscibilities collectively. Thus each value of $\chi_{\text{AC}} = \chi_{\text{BC}}$ will have a corresponding critical χ_{AB}. Cahn's argument can therefore easily be translated in terms of interaction parameters instead of temperature. Before χ_{AC} becomes critical either the A-rich phase or the C-rich phase will wet the interface between the two other phases depending on the relative values of σ_{AC} and σ_{BC}. If both χ_{AC} and χ_{BC} become critical, the only possible outcome is that the C-rich phase will wet the solvent-rich phases.

Thus according to Cahn's argument, decreasing the value of χ_{AC} (keeping χ_{BC} equal to χ_{AC}) should give rise to a wetting transition. However, if we consider the *effective* interaction parameter $\chi_{\text{AC}}^{\text{eff}} = \chi_{\text{BC}}^{\text{eff}}$, it can be seen that this wetting transition should also

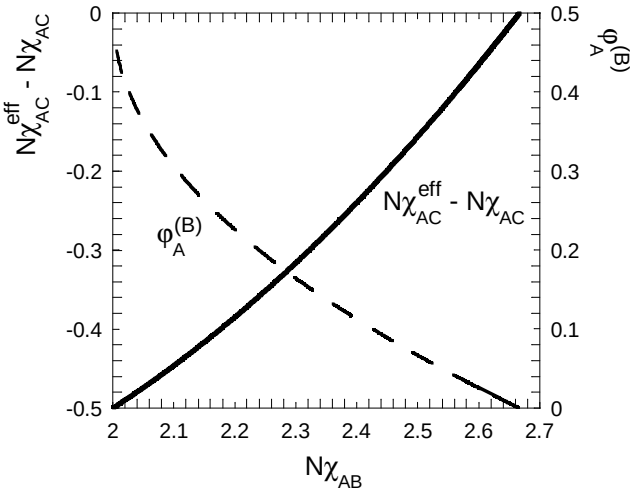

Figure 5.1. The effective interaction parameter $N\chi_{\mathrm{AC}}^{\mathrm{eff}}$ ($= N\chi_{\mathrm{BC}}^{\mathrm{eff}}$) as function of the real $N\chi_{\mathrm{AB}}$. For small χ_{AB} the effective interaction between the wetting component and the solvents can already be close to the critical value $\chi_{\mathrm{AC}}^{\mathrm{crit}}$ if the real value of χ_{AC} is still relatively far from $\chi_{\mathrm{AC}}^{\mathrm{crit}}$. The diagram also shows the volume fraction $\phi_A^{(B)}$ of component A in the B-rich solvent phase as function of $N\chi_{\mathrm{AB}}$.

be found by decreasing the value of χ_{AB} [145]. By the effective interaction parameter the wetting component is considered as being in contact with just one solvent which combines the properties of both solvent A and solvent B. To first order we can make the simplification of neglecting the volume fraction of C in the solvent-rich phases. The effective interaction parameter can then be written as

$$\chi_{\mathrm{AC}}^{\mathrm{eff}} = \chi_{\mathrm{AC}} - \chi_{\mathrm{AB}}\phi_A^{(B)}(1-\phi_A^{(B)}) \tag{5.3}$$

Obviously $\phi_A^{(B)}$, which is the volume fraction of A in the B-rich phase, is dependent on χ_{AB}: the larger the interactions between A and B, the smaller the volume fraction of A in B. If χ_{AB} is sufficiently close to the critical point of A and B, the quantitative relation between $\phi_A^{(B)}$ and χ_{AB} can be derived from the Van der Waals theory for liquid/liquid-interfaces [134]:

$$\phi_A^{(B)} = \frac{1}{2} - \sqrt{\frac{3}{8}\left(N\chi_{\mathrm{AB}} - 2\right)} \tag{5.4}$$

This can be substituted into Equation 5.3 and the resulting $\chi_{\mathrm{AC}}^{\mathrm{eff}}$ as function of χ_{AB} is plotted in Figure 5.1. It is seen that $\chi_{\mathrm{AC}}^{\mathrm{eff}} < \chi_{\mathrm{AC}}$ and that $\chi_{\mathrm{AC}}^{\mathrm{eff}}$ decreases with decreasing χ_{AB}. This means that if we have a certain combination of χ_{AB} and $\chi_{\mathrm{AC}} > \chi_{\mathrm{AC}}^{\mathrm{crit}}$ giving rise to partial wetting, the effective interactions $\chi_{\mathrm{AC}}^{\mathrm{eff}}$ can become equal to $\chi_{\mathrm{AC}}^{\mathrm{crit}}$ with constant $\chi_{\mathrm{AC}} = \chi_{\mathrm{BC}}$ and decreasing χ_{AB}, while χ_{AB} remains non-critical. Thus we can expect the Cahn-type wetting transition to occur also by decreasing the value of χ_{AB} instead of decreasing χ_{AC}. As a consequence, the larger the value for χ_{AC}, the smaller the value for χ_{AB} for which $\chi_{\mathrm{AC}}^{\mathrm{eff}}$ equals $\chi_{\mathrm{AC}}^{\mathrm{crit}}$. From all of this, it still remains impossible to predict

the conditions, i.e. the exact values of the interaction parameters, for Cahn-type wetting transitions. It is only known that their values should be such that $\chi_{\mathrm{AC}}^{\mathrm{eff}}$ is sufficiently close to $\chi_{\mathrm{AC}}^{\mathrm{crit}}$. It should be emphasized again that Equation 5.4 and Figure 5.1 can only be used as indications since they are only directly applicable for systems in which $\chi_{\mathrm{AB}} \approx \chi_{\mathrm{AB}}^{\mathrm{crit}}$ and $\chi_{\mathrm{AC}} = \chi_{\mathrm{BC}} \gg \chi_{\mathrm{AC}}^{\mathrm{crit}} = \chi_{\mathrm{BC}}^{\mathrm{crit}}$, so that the volume fractions of C in A and B are negligible. Therefore, we use Equation 5.4 only to indicate the trends which could be expected. In the self-consistent field calculations, performed to create the adsorption isotherms, we do not neglect the amount of C in the solvents.

An additional type of wetting transition can be expected to occur. The Cahn-type wetting transition from partial to complete wetting occurs for decreasing χ_{AB}. If however χ_{AB} is increased, the polymeric solvent A-solvent B interactions become more and more unfavourable. (Note that an increasing χ_{AB} is not accompanied by a proportional increase in σ_{AB}, since χ_{AB} only concerns the enthalpic effects and σ_{AB} also has entropic contributions). A polymer film between the solvents can help to avoid these unfavourable contacts. Indeed, this type of wetting transition has been found for a system of two monomeric solvents wetted by a polymer [145].

Consequently it is possible to have at a fixed value for $\chi_{\mathrm{AC}} = \chi_{\mathrm{BC}}$ a window of partial wetting in terms of χ_{AB}. Both with increasing and decreasing χ_{AB} a wetting transition occurs.

5.3 SF-SCF in wetting study

To study the wetting characteristics of the homopolymers, the lattice mean field method developed by Scheutjens and Fleer [9, 10, 15] is applied. The Scheutjens-Fleer self-consistent-field (SF-SCF) method provides an easy way to calculate volume fraction profiles for (multicomponent) systems at equilibrium and their corresponding partition functions. For our non-curved interfaces we can use a simple one-dimensional lattice. Partial and complete wetting are distinguished by constructing adsorption isotherms: the excess amount of C at the A/B-interface is plotted versus the chemical potential of the wetting component. Both quantities can be calculated from the volume fraction profiles:

$$\theta_C^{\mathrm{exc}} = \sum_{z=1}^{M} \left(\phi_C(z) - \phi_C^{\mathrm{bulk}} \right) \tag{5.5}$$

$$\frac{\mu_C - \mu_C^{\mathrm{bulk}}}{k_B T} = \ln \phi_C^{\mathrm{bulk}} - \frac{N}{2} \sum_{XY} (\phi_X^{\mathrm{bulk}} - \delta_{CX}) \chi_{\mathrm{XY}} (\phi_Y^{\mathrm{bulk}} - \delta_{CY}) \tag{5.6}$$

δ_{CX} is the Kronecker delta which equals one for $X = C$ and zero otherwise. In the following we denote the total amount of C in the system by θ_C.

As a result of the mean-field method, the adsorption isotherms show Van der Waals loops indicating metastable states. For example Figure 5.2*a* shows a typical isotherm for partial wetting as calculated by the SF-method. This isotherm could simply be cut off at the coexistence line ($\Delta\mu_C = 0$, where $\Delta\mu_C$ is the difference between the actual chemical potential of the wetting component and its value at coexistence). Isotherms which represent prewetting steps have loops already before coexistence is reached, see Figure 5.2*b*. The prewetting step can be located by an equal-area method as indicated

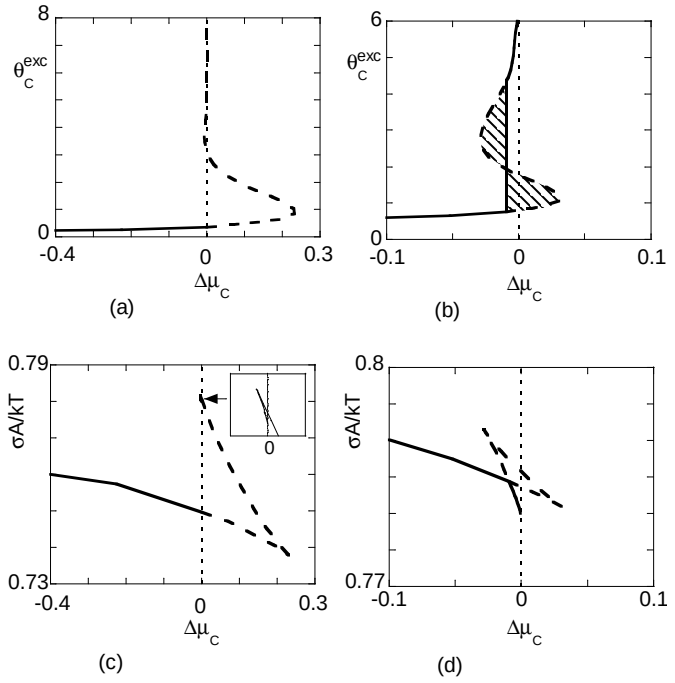

Figure 5.2. Typical examples of adsorption isotherms following from mean-field calculations. The dashed lines represent the metastable states, not found in experiments. Mean-field isotherms for partial wetting are like the isotherm in *(a)*. They can simply be cut off at the coexistence line ($\Delta\mu_C = 0$). The corresponding surface tension, plotted in *(c)*, decreases continuously until coexistence is reached from $\Delta\mu_C < 0$. Mean-field isotherms with prewetting steps are similar to the isotherm in *(b)*. One way to find the $\Delta\mu_C$ corresponding with the prewetting step is to apply the equal-area method. Another way is to use the corresponding plot of the surface tension as in *(d)*, where $\Delta\mu_C(\text{kink}) = \Delta\mu_C(\text{prewetting, step})$.

in that figure, but it is more convenient to use the surface free energy σ as function of $\Delta\mu_C$, see for example Figure 5.2*d*. For our system σ can be calculated by the equilibrium volume fraction profiles as

$$\begin{aligned}\frac{\sigma A}{k_B T} &= \sum_{z,X} \phi_X(z) \ln G_X(z) \\ &\quad + \frac{1}{2} \sum_{z,X,Y} \chi_{\mathrm{XY}} \left(\phi_X(z) \left\langle \phi_Y(z) \right\rangle - 2\phi_X(z)\phi_Y^{\mathrm{bulk}} + \phi_X^{\mathrm{bulk}}\phi_Y^{\mathrm{bulk}} \right)\end{aligned} \tag{5.7}$$

In this equation $G_X(z) = \exp\{-u_X(z)/k_B T\}$, where $u_X(z)$ is the potential felt by segments of type X; the angular brackets represent a three-layer average.

σ is higher for the metastable state than for the equilibrium state. Figures 5.2*c* and 5.2*d* show examples of curves for σ as function of $\Delta\mu_C$. In the partial wetting regime, there is no intersection point for $\Delta\mu_C \leq 0$. The surface tension decreases continuously until coexistence is reached as in Figure 5.2*c*. In case of prewetting, there is a discontinuity

in the first derivative of the surface tension as function of $\Delta\mu_C$. This discontinuity occurs if the curve for the stable state intersects with that of the metastable state (for $\Delta\mu_C \leq 0$) as in Figure 5.2*d*. It means that there is a transition from one stable state (microscopically thick film) to another stable state (mesoscopically thick film). Thus the prewetting step occurs at $\Delta\mu_C$ corresponding with this intersection point. The critical prewetting point is that T or χ for which the kink disappears because the loop in the figure shrinks to a point.

5.4 Results and discussion

The calculations are performed for two different chain lengths: either all polymers in the system have length $N = 10$, or they all have $N = 100$. Since the results for both values of N are nearly identical when the values for the interaction parameters are changed in order to keep $N\chi$ constant, we can generally write the results in terms of $N\chi_{\mathrm{AC}} = N\chi_{\mathrm{BC}}$ and $N\chi_{\mathrm{AB}}$. However, the analyses around critical points are carried out for systems in which $N = 10$ only, to reduce computation time. Therefore, the results for systems near critical points are presented in terms of χ and it has to be reminded that for these results N equals 10.

As has been outlined in the discussion of the effective interaction parameter, it is not possible to predict a priori the exact values of the interaction parameters for which Cahn-type wetting transitions occur. What we can predict from the effective interaction parameter is that Cahn-type transitions occur for decreasing $N\chi_{\mathrm{AB}}$. Detailed numerical analysis around critical points must be done carefully and a large number of lattice layers (i.e. a large system) is needed, leading to time-consuming trials to find the wetting transitions.

If we consider the two-dimensional parameter space given by the interaction parameters χ_{AB} and $\chi_{\mathrm{AC}} = \chi_{\mathrm{BC}}$, we find three different regimes, each with their own characteristics for the wetting transitions. In one of these regimes (where $\chi^{\mathrm{wet}} \approx \chi^{\mathrm{crit}}$ and $\chi^{\mathrm{wet}}_{\mathrm{AB}} > \chi^{\mathrm{wet}}_{\mathrm{AC}} = \chi^{\mathrm{wet}}_{\mathrm{BC}}$) Cahn-type wetting transitions are found. Another regime ($\chi^{\mathrm{wet}} \gg \chi^{\mathrm{crit}}$ and $\chi^{\mathrm{wet}}_{\mathrm{AB}} > \chi^{\mathrm{wet}}_{\mathrm{AC}} = \chi^{\mathrm{wet}}_{\mathrm{BC}}$) shows wetting transitions which are not associated with any critical state and which must therefore be *additional to* Cahn-transitions. In the third regime ($\chi^{\mathrm{wet}} \approx \chi^{\mathrm{crit}}$ and $\chi^{\mathrm{wet}}_{\mathrm{AB}} < \chi^{\mathrm{wet}}_{\mathrm{AC}} = \chi^{\mathrm{wet}}_{\mathrm{BC}}$) unusual 'hidden pseudo-wetting transitions' occur *instead of* Cahn's transitions and these transitions are thus violating Cahn's argument. We will discuss these three regimes separately.

5.4.1 First regime: additional to Cahn

These results concern a type of wetting transition which is additional to Cahn's wetting transition. In Figure 5.3 two collections of adsorption isotherms are presented as calculated by SF-SCF; for two values of $N\chi_{\mathrm{AC}} = N\chi_{\mathrm{BC}}$ the isotherms were calculated for a range of $N\chi_{\mathrm{AB}}$-values. Cahn's wetting transition is expected to occur if the interface between the solvents A and B becomes less sharp, i.e. if χ_{AB} is decreased. However Figure 5.3 shows that we find wetting transitions by *increasing* χ_{AB} (at constant χ_{AC}). This kind of wetting transitions has also been found for a monomer/monomer-interface wetted by a polymer [145]. Wetting for increasing χ_{AB} can be explained by the fact that the developing layer of C at the interface between A and B screens the A/B- interactions

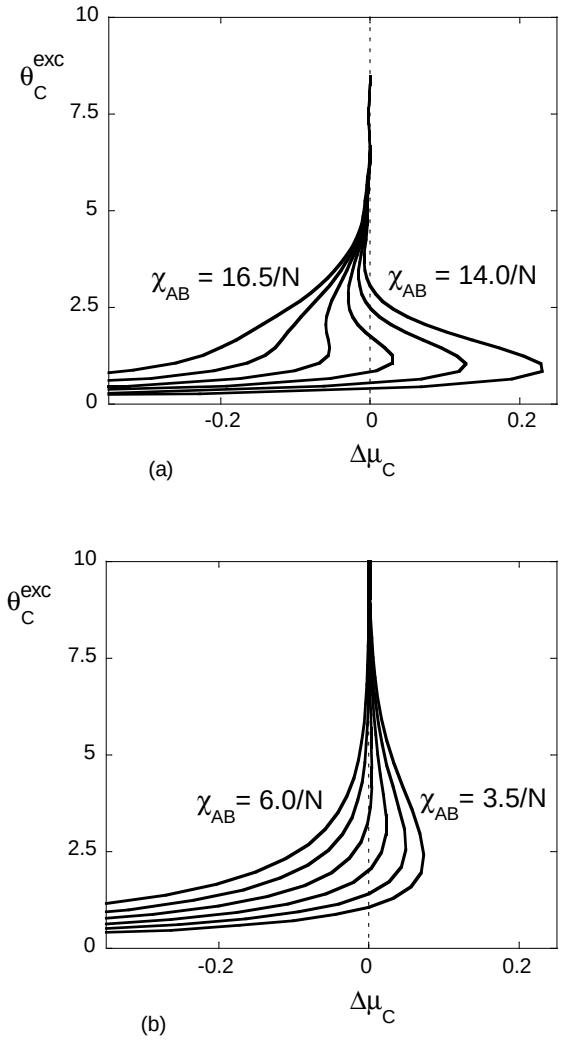

Figure 5.3. Examples of the adsorption isotherms obtained for $\chi_{\mathrm{AC}} = \chi_{\mathrm{BC}} = 7/N$ and $\chi_{\mathrm{AB}} = \chi_{\mathrm{BC}} = 3/N$, respectively. Diagram *(a)*is a typical example of a first-order wetting transition. Diagram *(b)* presents a second-order wetting transition. The wetting transitions for these polymer-solvent interactions are induced by *increasing* the value for χ_{AB}. (In these pictures, the isotherms are given for χ_{AB} incremented by $0.5/N$).

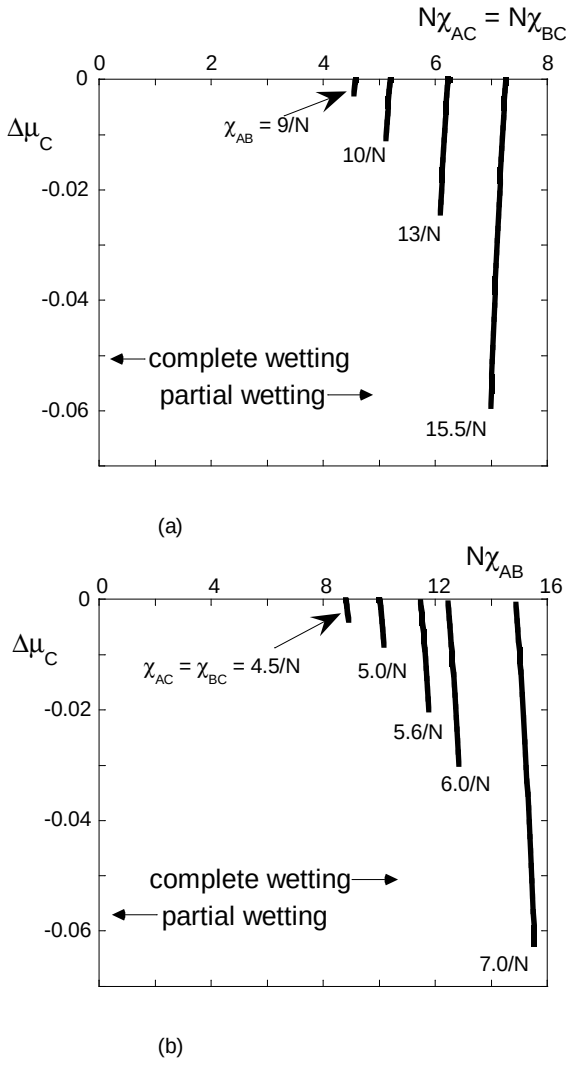

Figure 5.4. Phase diagrams showing the prewetting lines as function of χ_{AC} *(a)* and as function of χ_{AB} *(b)*. Extrapolating the line connecting the critical prewetting points predicts a tricritical point for $\chi_{\mathrm{AC}} = \chi_{\mathrm{BC}} \approx 4.3/N$ and $\chi_{\mathrm{AB}} \approx 8/N$. For smaller values of interaction parameters, second-order wetting transitions occur.

which become more and more unfavourable with increasing χ_{AB}. From Figure 5.3 it can also be seen that it is possible to find either first or second-order wetting transitions. Figure 5.3*a* presents a family of adsorption isotherms for $\chi_{\mathrm{AC}} = \chi_{\mathrm{BC}} = 7.0/N$ which proofs the presence of first-order wetting transitions. In Figure 5.3*b* another set of adsorption isotherms for $\chi_{\mathrm{AC}} = \chi_{\mathrm{BC}} = 3.0/N$ clearly shows a second-order character of the wetting transition. For several combinations of interaction parameters the prewetting lines have been localised by the μ-dependence of the surface free energy. The prewetting lines are shown in the wetting phase diagrams collected in Figure 5.4. Usually the temperature T or $T - T^{\mathrm{crit}}$ is used as control parameter instead of χ. Since $\chi \propto 1/T$, the relative

positions of wetting point, critical prewetting point and critical point are reversed with respect to standard wetting phase diagrams [147, 154] where $T^{\text{wet}} < T^{\text{cpr}} < T^{\text{crit}}$. In Figure 5.4*a* the control parameter is $N\chi_{\text{AC}} = N\chi_{\text{BC}}$. The wetting transition from partial to complete wetting occurs with decreasing control parameter; component C will wet the A/B-interface if the repulsive interactions between the wetting component and the solvents are sufficiently low. In Figure 5.4*b* the control parameter is $N\chi_{\text{AB}}$ which (as already shown in Figure 5.3) has to be increased to find a wetting transition. From the steepness of the prewetting lines it can be concluded that small variations in the value of the interaction parameters have relatively large effects. Focusing on the region near coexistence (not shown), it appears that the prewetting lines approach the coexistence line tangentially, as should be expected [154]. It is seen that the prewetting lines will disappear if both $\chi_{\text{AC}} = \chi_{\text{BC}}$ and χ_{AB} are sufficiently low, namely for $\chi_{\text{AC}} = \chi_{\text{BC}} \approx 4/N$ and $\chi_{\text{AB}} \approx 8/N$. These χ's mark the tricritical point, at which the wetting transitions change from first order to second order. Note that for binary systems the critical χ equals $2/N$, which is far from our tricritical point. Thus in our system second-order transitions occur for a relatively large range of χ-values. Replacing our polymeric solvents by monomeric solvents would result in a system showing the same kind of wetting transitions additional to Cahn wetting, but these are generally first-order [145].

If one would not consider the effective interaction $\chi^{\text{eff}}_{\text{AC}}$, but only the interaction χ_{AC} itself, one could incorrectly conclude from the results above, especially from the upper diagram in Figure 5.4, that Cahn's argument has been verified: complete wetting occurs for smaller χ_{AC}, partial wetting for larger χ_{AC}. However, from the consideration of the effective interaction, it is expected that complete wetting will also occur for smaller χ_{AB} and partial wetting for larger χ_{AB}. The lower diagram in Figure 5.4 shows the contrary. Thus these wetting transitions found for sharp interfaces between the solvents (i.e. large χ_{AB}) must be additional to Cahn-type transitions.

5.4.2 Second regime: Cahn-type transitions

We now discuss the wetting transitions found in our system near the critical points. As said before, each value of χ_{AB} will give rise to its own value for $\chi^{\text{crit}}_{\text{AC}}$. The easiest way to find an indication for a combination of critical interaction parameters is to calculate the binodals of a system in which $\chi = \chi_{\text{AB}} = \chi_{\text{AC}} = \chi_{\text{BC}}$. We then have only one parameter which controls the existence of three-phase coexistence. The three phase region in ternary phase diagrams arises from overlap of the binodals. The critical χ is that χ for which the three-phase region just disappears, thus for which the binodals do not overlap but are just tangential to each other. Because of the symmetry in a system with $\chi_{\text{AB}} = \chi_{\text{AC}} = \chi_{\text{BC}} = \chi$ and $N_A = N_B = N_C = N$, the binodals are then also tangent to the equimolar lines $\phi_A = \phi_B$, $\phi_B = \phi_C$, and $\phi_A = \phi_C$ in the ternary phase diagram. If we know that the three phase region just disappears for χ^{crit}, we can expect that in a system with $\chi_{\text{AC}} = \chi_{\text{BC}} = \chi^{\text{crit}}$ and $\chi_{\text{AB}} > \chi^{\text{crit}}$ the mixtures A/C and B/C will become critical if χ_{AB} is decreased, but according to Cahn, C will first wet the A/B-interface.

The binodals are calculated numerically by the generalised Flory-Huggins free-energy density expression, which coincides with the Scheutjens-Fleer result for homogeneous systems and which for $\chi = \chi_{\text{AB}} = \chi_{\text{AC}} = \chi_{\text{BC}}$ reads:

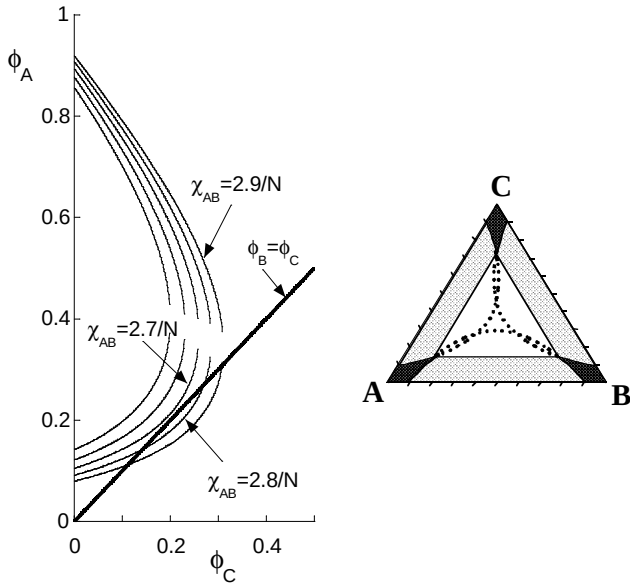

Figure 5.5. Binodals for a system with $N_A = N_B = N_C = N$ and $\chi_{\rm AB} = \chi_{\rm AC} = \chi_{\rm BC} = \chi$, calculated by minimization of the Flory-Huggins free energy. If $\chi_{\rm AB}$ is close to $2.7/N$, the binodal will be tangential to the (straight) line $\phi_B = \phi_C$. The ternary phase composition diagram for $\chi = 2.8/N$ shows that the three-phase region (white triangle) results from overlap of the (dotted) binodals. The dark areas in this diagram are the one-phase regions, the light grey areas are two-phase regions.

$$\begin{aligned} f_{\rm FH} &= \frac{\phi_A}{N}\ln\phi_A + \frac{1-\phi_A-\phi_C}{N}\ln(1-\phi_A-\phi_C) + \frac{\phi_C}{N}\ln\phi_C \\ &\quad +\chi\phi_A(1-\phi_A-\phi_C) + \chi\phi_C(1-\phi_A-\phi_C) + \chi\phi_A\phi_C \end{aligned} \tag{5.8}$$

Figure 5.5*a* shows the results for different values of χ. (Only binodals of the mixture A/B are shown, but the same figure applies for mixtures A/C and B/C if all subscripts in the figure are changed accordingly). If χ exceeds the value of about $2.7/N$, the binodals overlap and three phases can coexist. If χ is smaller than about $2.7/N$, the ternary phase diagram has only one- and two-phase regions bounded by three separate binodals. Choosing for the interaction parameters $\chi_{\rm AC} = \chi_{\rm BC} \approx 2.7/N$ should give rise to a wetting transition according to Cahn's argument with complete wetting for $\chi_{\rm AB} < \chi_{\rm AB}^{\rm wet}$. Indeed, this is found as shown in Figure 5.6. Note that for a clearer picture, the isotherms are not plotted against $\Delta\mu_C$ but against μ_C itself. In this figure a set of adsorption isotherms is given for $\chi_{\rm AC} = \chi_{\rm BC} = 0.27$ and different values of $\chi_{\rm AB}$ (note that $N = 10$). If $\chi_{\rm AB}$ equals 0.35 component C will partially wet the A/B-interface. Increasing $\chi_{\rm AB}$ up to $\chi_{\rm AB}^{\rm wet} \approx 0.40$ results in a second-order wetting transition which is similar to the wetting transitions in the first regime presented above and in Figure 5.4*b*. Another wetting transition is found in agreement with Cahn's argument by decreasing $\chi_{\rm AB}$ from 0.35. This wetting transition occurred for $\chi_{\rm AB}^{\rm wet} \approx 0.287$. It is also seen that Cahn's wetting transition is of second order. Summarizing: a window of partial wetting exists for $0.287 < \chi_{\rm AB} < 0.40$.

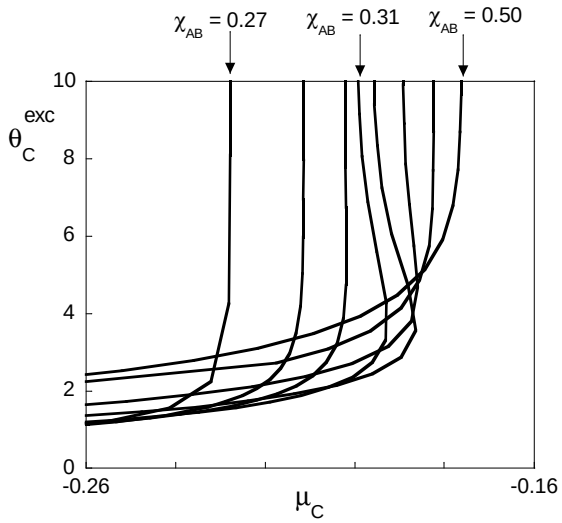

Figure 5.6. Adsorption isotherms for $N_A = N_B = N_C = 10$ and $\chi_{\rm AC} = \chi_{\rm BC} = 0.27$. From left to right the adsorption isotherms have $\chi_{\rm AB}$-values of 0.27, 0.28, 0.29, 0.31, 0.35, 0.40, 0.45, and 0.50. Note that $\theta_C^{\rm exc}$ is plotted versus μ_C instead of $\Delta\mu$. It is easy to see that the system is in the partial wetting regime for $\chi_{\rm AB} = 0.35$, whereas it is in the complete wetting regime both for $\chi_{\rm AB} = 0.27$ and $\chi_{\rm AB} = 0.50$. Both wetting transitions are of a second-order type.

$\chi_{\rm AC} = \chi_{\rm BC}$	$\chi_{\rm AB}^{\rm wet}$
0.270	0.287
0.274	0.282
0.277	0.279

Table 5.1. If $\chi_{\rm AC} = \chi_{\rm BC}$ is increased, Cahn's (second-order) wetting transitions are found for decreasing $\chi_{\rm AB}$.

If now the value of $\chi_{\rm AC}$ is increased, the critical value for $\chi_{\rm AB}$ can be expected to decrease. This can be understood by Figure 5.1: the larger $\chi_{\rm AC} = \chi_{\rm BC}$, the larger the difference between $\chi_{\rm AC} = \chi_{\rm BC}$ and $\chi_{\rm AC}^{\rm crit} = \chi_{\rm BC}^{\rm crit}$. Therefore, if $\chi_{\rm AC} = \chi_{\rm BC}$ is increased, the difference between $\chi_{\rm AC} = \chi_{\rm BC}$ and $\chi_{\rm AC}^{\rm eff} = \chi_{\rm BC}^{\rm eff}$ must also be increased to achieve $\chi_{\rm AC}^{\rm eff} = \chi_{\rm AC}^{\rm crit}$ $(= \chi_{\rm BC}^{\rm eff} = \chi_{\rm BC}^{\rm crit})$. According to Figure 5.1, $\chi_{\rm AB}$ must then be smaller. Indeed, as shown in Table 5.1 we find decreasing values for $\chi_{\rm AB}^{\rm wet}$ if $\chi_{\rm AC} = \chi_{\rm BC}$ is increased.

5.4.3 Third regime: instead of Cahn transitions (pseudo wetting)

From Table 5.1 it is seen that Cahn's wetting transitions are found for situations in which all interaction parameters have almost the same values, but still $\chi_{\rm AB}^{\rm wet} > \chi_{\rm AC}^{\rm wet} = \chi_{\rm BC}^{\rm wet}$. As mentioned before, if we increase $\chi_{\rm AC} = \chi_{\rm BC}$, Cahn's wetting transition is expected to be found for decreasing $\chi_{\rm AB}$. This means that at some point the value of $\chi_{\rm AB}^{\rm wet}$ would equal

that of $\chi_{\mathrm{AC}}^{\mathrm{wet}} = \chi_{\mathrm{BC}}^{\mathrm{wet}}$. If we imagine a system in which $\chi_{\mathrm{AB}} = \chi_{\mathrm{AC}} = \chi_{\mathrm{BC}}$, all components may act as the wetting component, because all interfaces have the same surface tensions. However, due to the way in which we perform our calculations, we always pre-assume C as the wetting component. We start with an 'empty' A/B-interface and use this as an initial guess for the self-consistent-field calculation for a system in which C is the minority component. With this initial guess C will accumulate at the interface. Then, the total amount of C in the system is incremented by small steps, each time using the previous step as initial guess.

If we cross the line $\chi_{\mathrm{AB}} = \chi_{\mathrm{AC}} = \chi_{\mathrm{BC}}$ in the two-dimensional parameter space, we arrive in the third regime where $\chi_{\mathrm{AB}} < \chi_{\mathrm{AC}} = \chi_{\mathrm{BC}}$. Here, unexpected wetting-like transitions are observed. In this regime the surface energy of the A/B-interface is lower than that of either the A/C- or the B/C-interface. Complete wetting by component C can therefore not be expected although the critical point is approached. Thus, for macroscopic systems, it is obvious that Cahn's argument is violated in this regime. As long as C would not wet the A/B-interface completely, it is energetically more favourable to have a droplet of C at the interface than to have a droplet of C either in the A or the B-rich phases. However, in our numerical calculations we have access to the metastable states, due to the fact that we (only) do calculations on finite sized systems. It turns out that we are able to see what could happen if wetting experiments are carefully performed in microscopically small and closed systems: at first instance the systems seem to act in agreement with Cahn's argument, but eventually the argument also fails in these microscopic systems.

Figure 5.7 shows a collection of isotherms for the case $\chi_{\mathrm{AB}}^{\mathrm{wet}} < \chi_{\mathrm{AC}}^{\mathrm{wet}} = \chi_{\mathrm{BC}}^{\mathrm{wet}}$. In this example $\chi_{\mathrm{AC}} = \chi_{\mathrm{BC}} = 0.30$ (and still $N = 10$). Decreasing the value for χ_{AB} down to 0.30 results in regular isotherms for partial wetting. The excess amount θ_C^{exc} at coexistence is still decreasing: the system does not show any approach to complete wetting. If we decrease χ_{AB} further below $\chi_{\mathrm{AC}} = \chi_{\mathrm{BC}}$, the characteristics of the isotherms change. θ_C^{exc} at coexistence ($\Delta\mu_C = 0$) still decreases, but unexpectedly a vertical part in the isotherm occurs in the meta-stable region, i.e. where $\Delta\mu_C > 0$. Consider for example the isotherm for $\chi_{\mathrm{AB}} = 0.265$ in Figure 5.7. With increasing θ_C, the isotherm first resembles isotherms of complete wetting: θ_C^{exc} increases without changing the chemical potential. However, we should call this 'pseudo wetting' instead of complete wetting, since if θ_C in the system has sufficiently increased, the volume fractions of C in the A-rich and B-rich phases suddenly decrease, and θ_C^{exc} increases discontinuously. This is reflected of course by a sudden decrease in the chemical potential μ_C and $\Delta\mu_C \to 0$. Associated with this there is a very pronounced change in the volume fraction profile of the C component at the A/B-interface (not shown). The jump from pseudo wetting back to the coexistence line is presented by the dashed line in Figure 5.7. (It is particularly difficult to find the exact shape of this kind of isotherms). For the isotherm with $\chi_{\mathrm{AB}} = 0.265$, the value of χ_{AB} is smaller than that of $\chi_{\mathrm{AC}} = \chi_{\mathrm{BC}}$, thus the pseudo wetting must be meta-stable. The smaller the value of χ_{AB}, the longer the vertical part in the isotherm, i.e. the more pronounced the pseudo wetting: compare the isotherms for $\chi_{\mathrm{AB}} = 0.265$ and $\chi_{\mathrm{AB}} = 0.260$. Before the system changes from regular partial wetting to pseudo wetting, we see 'pseudo partial wetting' as presented by the isotherm for $\chi_{\mathrm{AB}} = 0.27$ in Figure 5.7. This isotherm differs from the regular partial wetting isotherms, since it is less curved at maximum μ_C.

This wetting-like behaviour can be explained by the fact that our microscopic systems can maintain a situation of supersaturation as long as the amount of C is not sufficient to

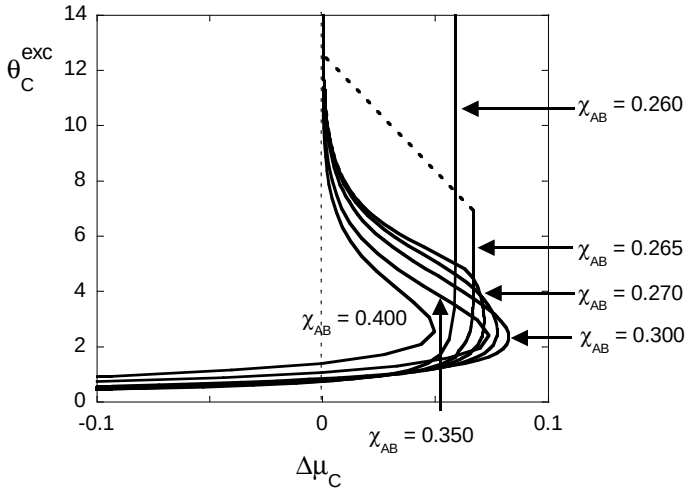

Figure 5.7. Adsorption isotherms for $N_A = N_B = N_C = 10$ and $\chi_{\mathrm{AC}} = \chi_{\mathrm{BC}} = 0.30$. As long as χ_{AB} is larger than $\chi_{\mathrm{AC}} = \chi_{\mathrm{BC}}$, the isotherms show regular partial wetting behaviour. If χ_{AB} becomes smaller, no Cahn wetting but pseudo wetting is found. Component C seems to wet the interface in the meta-stable region ($\Delta\mu > 0$), but suddenly the system finds its state of coexistence. The smaller χ_{AB}, the longer the pseudo wetting persists. Also the isotherm $\chi_{\mathrm{AB}} = 0.260$ will jump to $\Delta\mu_C = 0$, but this occurs for values of $\theta_C^{\mathrm{exc}} > 14$.The transition from pseudo partial to pseudo wetting is of a second-order type.

form a third (C-rich) phase in coexistence with the A- and B-rich phases. In Figure 5.8 it is shown how the volume fraction of C in the solvents A and B ($\phi_C^{(A)} = \phi_C^{(B)}$) develops with increasing θ_C^{exc}. At coexistence ($\Delta\mu_C = 0$) the solvents A and B are saturated with C. If $\Delta\mu_C > 0$, the solvents are supersaturated. If we enter the region where $\Delta\mu_C > 0$ by increasing the total amount of C in the system, first the volume fractions of C in the supersaturated solvents ($\phi_C^{(A)} = \phi_C^{(B)}$) continue to increase, but at a certain point of supersaturation, $\phi_C^{(A)}$ and $\phi_C^{(B)}$ do not change any more and $\Delta\mu_C$ has a constant (positive) value. From that moment, the excess amount of C at the A/B-interface (θ_C^{exc}) still increases if more C is added to the system. This is the moment where the isotherms behave as if wetting occurs. Suddenly, a sufficient amount of C has been added to the system to form three phases at coexistence, and the wetting-like behaviour turns out to be pseudo wetting. Since the supersaturated system is in a meta-stable state, it can be expected that hysteresis will occur if now the amount of C in the system is decreased. This has indeed been found as shown in Figure 5.9.

We can conclude that we have hidden (second-order) wetting-like transitions for systems in which C is the wetting component while $\chi_{\mathrm{AB}} < \chi_{\mathrm{AC}} = \chi_{\mathrm{BC}}$. At these hidden transitions the system changes from pseudo partial to pseudo wetting. These wetting transitions can only be found if one is able to keep the solvents supersaturated with wetting component C. This could happen in microscopic closed systems. However, since we are very close to the critical point, where molecular fluctuations have relatively large

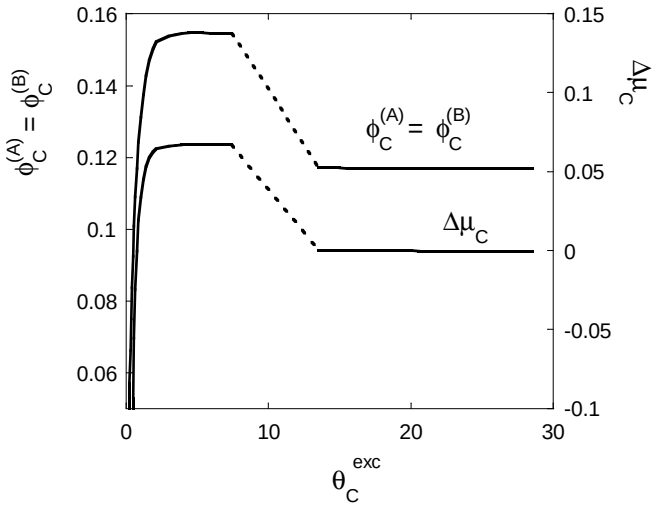

Figure 5.8. The volume fractions of C in solvents A and B as function of the excess amount of C at the interface and the (rotated) adsorption isotherm for $\chi_{AC} = \chi_{BC} = 0.30$, $\chi_{AB} = 0.265$ and $N = 10$. During pseudo wetting, $\phi_C^{(A)}$ and $\phi_C^{(B)}$ are constant, but the solvents are supersaturated with C, since at coexistence $\phi_C^{(A)} = \phi_C^{(B)} \approx 0.12$.

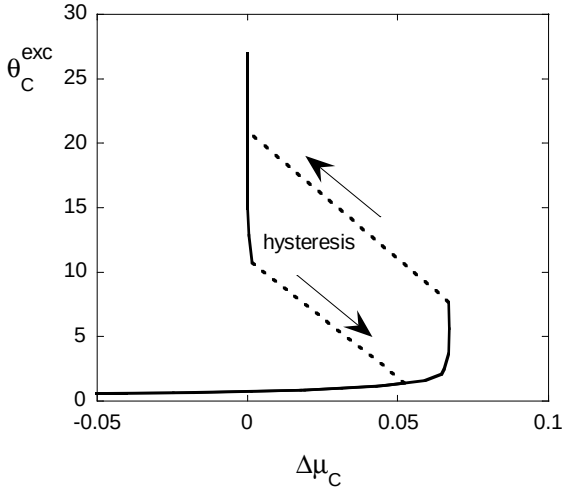

Figure 5.9. Pseudo wetting is related to supersaturation. No pseudo wetting is found if the adsorption isotherm is obtained by decreasing the total amount of C in the system. ($\chi_{AC} = \chi_{BC} = 0.30$, $\chi_{AB} = 0.265$, $N = 10$)

effects, this regime is difficult to explore.

If χ_{AC} is chosen too large, no hidden wetting transition is found anymore. For large χ_{AC}, the interaction parameter χ_{AB} approaches its critical value faster than its value for which χ_{AC}^{eff} equals $\chi_{AC}^{crit} = 2/N$. We find for example if $\chi_{AC} = 0.50$ that (pseudo) partial wetting occurs for $0.23 < \chi_{AB} < 1.0$. The wetting transition for $\chi_{AB} = 1.0$ has already been presented in Figure 5.4*b*. If χ_{AB} equals 0.23, the wetting component accumulates at the A/B-interface for small amounts of C, but before the amount of C is large enough to reach three-phase coexistence, the A/B-interface disappears. This occurs if ϕ_C obeys Equation 5.2 for $\chi_{AB} = 0.23$.

5.4.4 Combination of results

Since we had two control parameters in this study ($N\chi_{AB}$ and $N\chi_{AC} = N\chi_{BC}$) we can combine all wetting characteristics of our system in a two-dimensional plot with each of the control parameters along the axes, as in Figure 5.10. The solid line in this picture represents the combinations of interaction parameters which give rise to first-order or second-order wetting transitions. The critical prewetting points which are associated with the first-order wetting transitions are represented by the dashed line. It is seen that for first-order transitions both $N\chi_{AB}$ and $N\chi_{AC} = N\chi_{BC}$ must be very large. For smaller values of the control parameters second-order transitions occur. For points above the wetting line in this figure partial wetting is found, for points under the lines complete wetting or a phase transition to a one-phase system is found. The picture clearly indicates that indeed a transition to complete wetting can be found both for decreasing and increasing $N\chi_{AB}$. The wetting transitions at the right-hand side of the diagram (region I) are transitions to avoid unfavourable contacts between the A- and the B-rich phases. This type of transitions are also found in a system with monomer solvents [145]. The lower part of the left-hand side of the diagram (region II) is associated with Cahn-type wetting transitions, because they occur close to the critical point of the mixtures A/C and B/C. Cahn-type transitions must exist for all three-phase systems. (The wetting transitions in the left part of region I may also be due to Cahn-wetting, since the wetting occurs not too far before the value of $\chi_{AC} = \chi_{BC}$ has diminished to its critical value. Therefore, the boundary between region I and II should not be considered sharp). Region III contains the hidden wetting transitions from pseudo partial wetting to pseudo wetting which occur instead of the Cahn-type transitions. Interestingly, this means a failure of the Cahn argument for parameters corresponding to region III. Note that in our systems the long ranged Van der Waals interactions are not included. Therefore, the failure of the Cahn argument is of special interest. Our results show that the Cahn argument can not be as general as claimed in the literature. The pseudo-wetting transitions lie on a line that smoothly continues the line representing the Cahn-transitions. These hidden wetting transitions can in principle occur in other systems as well, but it is more difficult to predict where they occur if the system is less symmetrical. The fact that they have not been found before, for example by Leermakers et al. in their study of interfaces between two monomeric components [145], might be due to the part of parameter space which has been investigated.

These results are in agreement with simple considerations, which we collect for convenience in Table 5.2, concerning the relative size of the interaction parameters. As long as

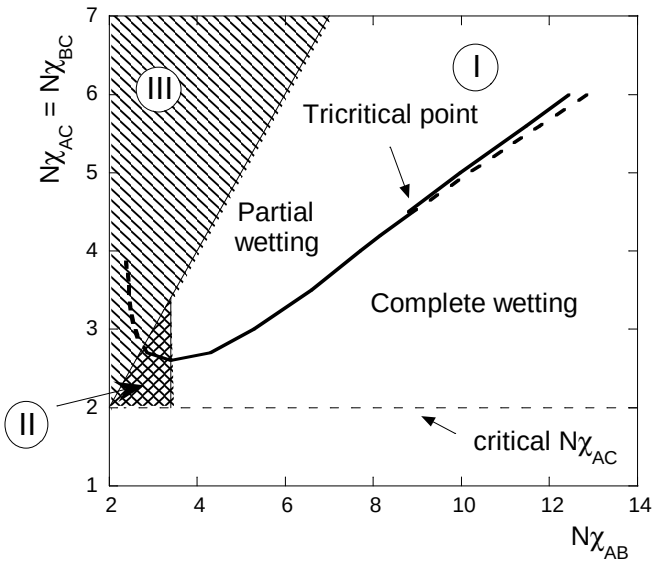

Figure 5.10. The wetting behaviour for all combinations of χ_{AB} and χ_{AC} ($= \chi_{\mathrm{BC}}$) collected in one figure. Three regimes can be distinguished in this parameter space. Region I ($\chi_{\mathrm{AC}}^{\mathrm{wet}} \gg \chi_{\mathrm{AC}}^{\mathrm{eff,crit}}$ and $\chi_{\mathrm{AB}} > \chi_{\mathrm{AC}} = \chi_{\mathrm{BC}}$) contains wetting transitions which are not associated with any critical point. The dashed line in region I indicates the critical prewetting points, which are associated with first-order wetting transitions. The critical prewetting points are absent for smaller values of interaction parameters, which means that for these values second-order transitions are found. Region II ($\chi_{\mathrm{AC}}^{\mathrm{wet}} \approx \chi_{\mathrm{AC}}^{\mathrm{eff,crit}}$ and $\chi_{\mathrm{AB}} > \chi_{\mathrm{AC}} = \chi_{\mathrm{BC}}$) includes Cahn-type wetting transitions which occur since $\chi_{\mathrm{AC}}^{\mathrm{eff}} \approx \chi_{\mathrm{AC}}^{\mathrm{crit}}$. In region III ($\chi_{\mathrm{AC}}^{\mathrm{wet}} \approx \chi_{\mathrm{AC}}^{\mathrm{eff,crit}}$ and $\chi_{\mathrm{AB}} < \chi_{\mathrm{AC}} = \chi_{\mathrm{BC}}$) pseudo-wetting transitions are found. Second-order transitions are found for a large parameter space. All Cahn-type wetting transitions and pseudo-wetting transitions are of a second-order type.

$\chi_{\mathrm{AB}} > \chi_{\mathrm{AC}} = \chi_{\mathrm{BC}}$	$0^\circ \leq \alpha < 60^\circ$
$\chi_{\mathrm{AB}} = \chi_{\mathrm{AC}} = \chi_{\mathrm{BC}}$	$\alpha = 60^\circ$ or $\sigma_{AB} = \sigma_{AC} = \sigma_{BC} = 0$
$\chi_{\mathrm{AB}} < \chi_{\mathrm{AC}} = \chi_{\mathrm{BC}}$	$60^\circ < \alpha \leq 90^\circ$

Table 5.2. The effects of the relative size of interaction parameters on the contact angle.

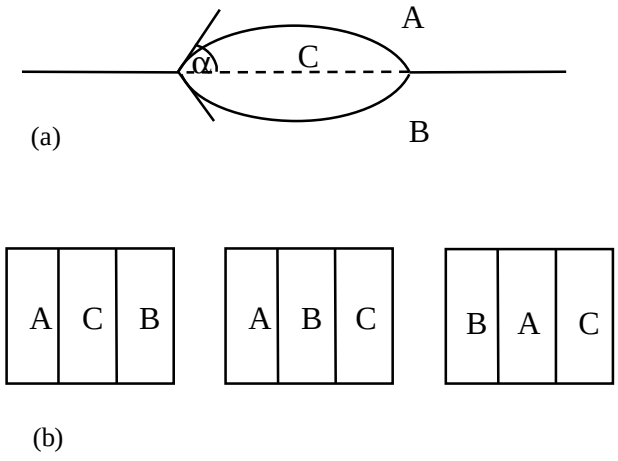

Figure 5.11. If $\chi_{\mathrm{AB}} = \chi_{\mathrm{AC}} = \chi_{\mathrm{BC}}$ and $\theta_A = \theta_B = \theta_C$ the system can choose between different equilibrium states which will have the same energy: the contact angle α must equal 60° *(a)*, or $\sigma_{AB} = \sigma_{AC} = \sigma_{BC} = 0$: α can take every value, each of the components may act as wetting component *(b)*.

$\chi_{\mathrm{AB}} > \chi_{\mathrm{AC}} = \chi_{\mathrm{BC}}$, it may be favourable to form a macroscopic layer of C to avoid the existence of an energetically unfavourable A/B-interface, and complete wetting may occur. If $\chi_{\mathrm{AB}} < \chi_{\mathrm{AC}} = \chi_{\mathrm{BC}}$, it is always unfavourable to create new A/C- and B/C-interfaces. Complete wetting will not occur. Still, component C will adsorb at the A/B-interface (as long as three phases may coexist) to compensate the newly formed interfaces by eliminating A/B-contacts. The contact angle will not exceed 90°, otherwise less A/B-contacts are eliminated than possible. If all interaction parameters are equal ($\chi_{\mathrm{AB}} = \chi_{\mathrm{AC}} = \chi_{\mathrm{BC}}$), none of the components A, B or C is preferred as the wetting component: all interfaces A/B, A/C and B/C have the same surface energies. As a consequence of Young's equation either the contact angle α will be equal to 60° or all surface tensions will equal zero. The first possibility means that partial wetting will occur, but the second possibility allows every possible behaviour between complete wetting ($\alpha = 0°$) and complete drying ($\alpha = 180°$) (see Figure 5.11). Because of our choice of system, it is still component C which adsorbs at the A/B-interface ($0 \leq \alpha \leq 90°$). Indeed we find complete wetting for $\chi_{\mathrm{AB}} = \chi_{\mathrm{AC}} = \chi_{\mathrm{BC}} = 0.278$ in combination with $\frac{\sigma A}{k_B T}$ approaching zero. Physically, this indicates the formation of a micro-emulsion without the presence of a classical amphiphilic surfactant.

5.5 Conclusions

The Scheutjens-Fleer method is a powerful tool to study systematically the wetting characteristics of a variety of systems. In the present study a system of three homopolymers was investigated, but we could also have chosen a system containing monomeric components or copolymers. Although we had a very simple system with $N_A = N_B = N_C$ and $\chi_{\mathrm{AC}} = \chi_{\mathrm{BC}}$, we still found a rich wetting behaviour. Close to the critical points of the A/C- and B/C-mixtures, approached by decreasing the effective interaction parameters,

the A/B-interface is completely wetted by C as long as $\chi_{AB} > \chi_{AC} = \chi_{BC}$. This is in agreement with Cahn's argument which was based on considerations of the temperature-dependence of surface tensions. In our homopolymer blends Cahn's wetting transitions are found to be of second-order type. However, Cahn's transitions occur only for a very small part of our two-dimensional parameter space. We see two characteristics of Cahn's transitions in our system. First: if, starting in a Cahn wetting transition point, the value of $\chi_{AC} = \chi_{BC}$ is increased, the next wetting transition point according to Cahn will be found by decreasing χ_{AB}. Secondly: in our system with three polymers of the same length these transitions are found if all interaction parameters are almost equal. As a result of these two facts, very soon the value of $\chi_{AC} = \chi_{BC}$ exceeds the value of χ_{AB} for which Cahn's transition would be expected. In that case it is energetically unfavourable for component C to wet the interface between A and B and indeed Cahn's argument fails. We then find hidden wetting transitions occurring in the metastable regime. In those situations, C seems to wet the A/B-interface, but suddenly the volume fraction of C in the solvents decreases and the system jumps to another state. We call this pseudo wetting. It is emphasized again that these transitions are not found in real macroscopic systems, but may only exist in finite systems. For macroscopic systems there is no wetting transition available in this region of parameter space, even though the system is close to a critical point.

In addition to Cahn's wetting transition and pseudo-wetting transitions another wetting transition was found by increasing χ_{AB}. This wetting transition could be explained by the screening effect of the developing C-layer. If the effective interactions are not taken into account, these wetting transitions could incorrectly be considered as Cahn-type wetting transitions, since complete wetting is found for $\chi_{AC} < \chi_{AC}^{wet}$. This type of transitions is not violating Cahn's argument. Second-order wetting transitions are found for a large parameter space. Only for relatively large χ_{AC} first-order wetting transitions occur.

Chapter 6

Steady-state analysis of polymer adsorption at off-equilibrium polymer interfaces

We consider an interface of two immiscible polymer liquids A_N and B_N at which a third polymer C_N may adsorb. Equilibrium characteristics of this system, in which all polymer lengths N are the same, were discussed in Chapter 5. In the present chapter, we study these interfaces in a stationary off-equilibrium state: due to imposed chemical-potential gradients, polymer A_N diffuses from the A-rich bulk phase through the interface to the A-poor bulk phase. Polymer B_N diffuses in the opposite direction. We select symmetric conditions for which the polymer C_N that accumulates at the A/B-interface has no net diffusion in the stationary state. This system is described by the Mean-Field Stationary Diffusion model, an approach that incorporates the transport of polymer segments and has the well-known Scheutjens-Fleer Self-Consistent-Field (SF-SCF) results as its limits (i.e., when the chemical-potential gradients vanish). From this method we obtain the stationary volume fraction profiles and segmental fluxes. We select the governing interaction parameters such that *at equilibrium* a macroscopically thick wetting layer of C develops at three-phase coexistence, i.e., the complete wetting case as described in Chapter 5. Here we focus on the *off-equilibrium* system where C has a *sub*-saturation concentration in the bulk phases and thick wetting films are thus not expected. We vary the driving forces for diffusion by variation of the concentration gradients and of the interactions between the polymers. By increasing the concentration gradients (the system is put further from three-phase coexistence), an unexpected sudden increase in the adsorbed amount of C is observed. A similar transition from microscopic to mesoscopic adsorbed amounts at the off-equilibrium interface is observed by increasing the interactions between the polymers. We study the susceptibility of the fluxes of A and B with respect to the imposed concentrations gradients and the interactions. The susceptibility changes simultaneously with the transitions in the adsorbed amounts. This means that upon variation of the concentration gradients, the fluxes of A and B are enhanced by the accumulation of C at the interface. Another interesting phenomenon is that the fluxes may vary even if the driving forces remain constant.

6.1 Introduction

Most theoretical studies on adsorption at interfaces focus on equilibrium. This is not surprising since the equilibrium is a well-defined state to which all ergodic systems tend to evolve. However, it may take a very long time before true equilibrium is achieved. Moreover, during the evolution from off-equilibrium to equilibrium, systems may encounter local minima in the free energy landscape, which may cause a system to be 'frozen' into an off-equilibrium state for a long time. Apart from such aspects that may prevent a system to reach equilibrium, there exist processes that never reach the equilibrium state. Cells in the human body, for example, constantly maintain concentration gradients over their membranes at the expense of an energy input. In catalysed reactions, reactants may be converted into products by interacting with the catalyst surface. The maintenance of a concentration gradient for the reactants towards the catalyst surface is essential to prevent the reaction rate to decrease. To analyse these and related systems it is relevant to study systems in stationary off-equilibrium states. Understanding the behaviour of stationary systems is a necessary step towards describing dynamic processes since the properties of a stationary state are governed by the dynamics and the state is well-defined.

We investigate the steady state of adsorption at and transport across an off-equilibrium interface between two immiscible polymer liquids A_N and B_N. The interface is off-equilibrium by imposing and maintaining driving forces to these polymers. The interface is due to the mutual immiscibility of A_N and B_N, but there is transport across this interface due to imposed gradients in chemical potentials. A similar system, but in equilibrium state, was studied in Chapter 5. There we were interested in the transitions from thin to thick adsorption layers induced by variation of the intermolecular interactions. The results of that study can be used to select the relevant systems for a steady-state analysis.

The equilibrium adsorption was studied in Chapter 5 by means of the Scheutjens-Fleer Self-Consistent Field (SF-SCF) method [15]. This lattice mean-field method has proven to be a powerful tool to investigate a variety of inhomogeneous polymer systems at equilibrium. For off-equilibrium interfaces we use an extension of the SF-SCF method, namely the Mean-Field Stationary Diffusion (MFSD) method. The details of this method were outlined in Chapter 2. The SF-SCF and MFSD methods use the same language in the description of the system, the polymers, and the interactions. The methods differ in the input requirements. In the equilibrium SF-SCF calculations the composition of a bulk system that is in equilibrium with the interface is uniquely defined. For the MFSD calculations one can select arbitrary bulk compositions, from which the driving forces for each component in the system follow. If these driving forces happen to be zero the solutions of the MFSD and SF-SCF calculations coincide. The MFSD method selects a solution in which the material fluxes are constant throughout the system, whereas the SF-SCF method focuses on the homogeneity of intensive variables. The fluxes in MFSD calculations are related to the free energy functional of SF-SCF calculations through the definition of the chemical potentials.

In Chapter 2 we illustrated the performance of the MFSD method by comparing the resulting diffusion profiles with analytic results for the simplest systems possible. The MFSD profiles matched the analytic profiles exactly. In the present chapter, we study diffusion profiles in a system that does not allow analytical solutions. This is due to the presence of energetic interactions between the components. In Chapter 4 it was shown that analytic calculations of the diffusion profiles fail even for simple binary systems.

Although fluxes were computed in these systems, they were not analysed in depth. In this chapter we will discuss both the steady state profiles as well as the stationary fluxes.

In the next section we first introduce our system. A connection is made to the equilibrium study of adsorption and wetting (Chapter 5) since the results of that study were used to select the appropriate boundary conditions for the stationary-state analysis. The stationary diffusion occurs between two bulk mixtures. The driving forces are defined by choosing the compositions of these bulk mixtures. The compositions were chosen such that the mixtures are stable, i.e., within these mixtures no phase separation will occur. Section 6.3 presents the necessary details of the MFSD method. The relation between the composition of the bulk mixtures and the driving forces (the chemical potential differences) is given. We distinguish three ways to vary the chemical potentials in the bulk mixtures. The consequences of these three variations for the adsorption layer and on the stationary fluxes are shown and discussed subsequently in Sections 6.4.1 to 6.4.3. In Section 6.5 we present a short outlook on further studies that may start from the results presented here. The conclusions are summarised in Section 6.6.

6.2 System

6.2.1 Equilibrium

We study an off-equilibrium interface between polymer components A_N and B_N. The adsorbing component C_N is also polymeric. The chain lengths N are chosen to be the same for the three polymers. In the corresponding equilibrium situation C_N would be referred to as the wetting component, that would either partially or completely wet the A/B-interface. In equilibrium the surface tensions between the three coexisting phases determine whether the C-rich phase forms a lens or a thick layer at the interface. These surface tensions depend on the (conformational) entropy of the chains at the interface and on the segmental interactions which we quantify by the Flory-Huggins parameters χ_{AB}, χ_{AC} and χ_{BC}. Two components i and j with equal chain lengths N are completely miscible if $N\chi_{ij} < 2$. An example of a concentration profile across an interface very close to three-phase coexistence in the case of complete wetting is shown in Figure 6.1*a*. It presents the volume fractions ϕ for all three components as a function of position z for $N\chi_{\mathrm{AB}} = 3.4$ and $N\chi_{\mathrm{AC}} = N\chi_{\mathrm{BC}} = 2.3$. The phase diagram in Figure 5.10 shows that for this combination of interaction parameters we are in the complete wetting regime. The profiles in Figure 6.1*a* were calculated by use of the SF-SCF method. The details of the calculation were given in Chapter 5. At the left side of the system in Figure 6.1*a* (low z-values) we have an A-rich phase α, at the right a B-rich phase β, and in the centre the wetting phase γ which is enriched in C. The A- and B-rich phases contain equal volume fractions of C since $\chi_{\mathrm{AC}} = \chi_{\mathrm{BC}}$. For the same reason we have $\phi_A = \phi_B$ in the C-rich phase. Due to the fact that $\chi_{\mathrm{AB}} > \chi_{\mathrm{AC}}$ the A-rich phase contains more C than B. From these volume fraction profiles, we can easily extract the compositions of the three coexisting phases α, β, and γ. (Note that the phase compositions in Figure 6.1*a* are calculated for a mesoscopic system. This means that these phases are actually only (good) approximations for the *macroscopic* phases that coexist at equilibrium). By separate numerical calculations we can obtain the compositions of coexisting phases in binary A_N/B_N, A_N/C_N, and B_N/C_N mixtures as explained in Chapter 4. Thus in total

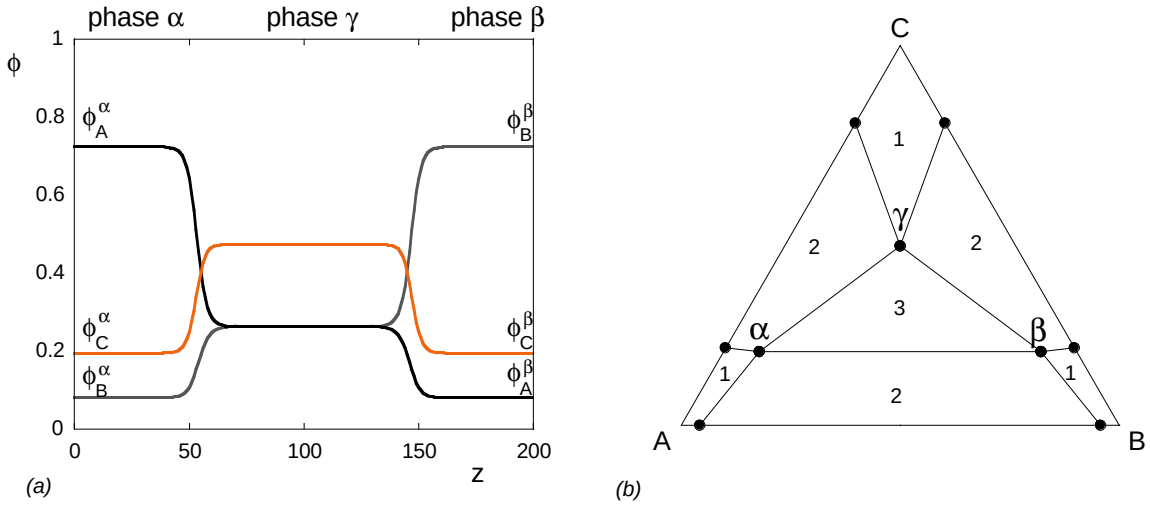

Figure 6.1. Ternary system with $N_A = N_B = N_C = 10$, $\chi_{AB} = 0.34$, $\chi_{AC} = \chi_{BC} = 0.23$. ($a$): Equilibrium volume fraction profiles for complete wetting of the A/B interface by C extremely close to three-phase coexistence. See Chapter 5 for more information on the wetting transition in this system. (b): Approximate phase composition diagram. The nine dots are numerically calculated compositions. The numbers 1, 2, and 3 refer to the number of phases that coexist for a certain overall composition within the system. (Thus they refer to one-phase, two-phase, and three-phase regions). The three phases α, β, and γ coexist.

we can easily generate nine phase composition points (the dots in Figure 6.1b), which allows us to construct an approximate phase composition diagram as given in Figure 6.1b. The coexisting phases in binary mixtures are represented by the six points on the three sides of the triangle. As an approximation for the binodals in the phase composition diagram we simply connect the coexisting phases in binary systems to the the three-phase coexistence points. We note that it is possible to generate a more accurate phase diagram but this approximated version is sufficient for our present purpose.

6.2.2 Stationary state

To study adsorption at off-equilibrium interfaces, we put the wetting system of Figure 6.1a into an (off-equilibrium) steady state condition. This is done by defining two infinitely large bulk mixtures each with a composition corresponding to a one-phase region of the phase composition diagram (Figure 6.1b). An example of such a system is shown in Figure 6.2. Mixture I is rich in A_N with concentrations $\phi_A^{\mathrm{I}} > \phi_A^{\alpha}$, $\phi_B^{\mathrm{I}} < \phi_B^{\alpha}$, and $\phi_C^{\mathrm{I}} < \phi_C^{\alpha}$. Mixture II is rich in B_N with $\phi_A^{\mathrm{II}} < \phi_A^{\beta}$, $\phi_B^{\mathrm{II}} > \phi_B^{\beta}$, and $\phi_C^{\mathrm{II}} < \phi_C^{\beta}$. The composition differences between mixtures I and II for A_N and B_N are denoted by $\Delta\phi = |\phi^{\mathrm{II}} - \phi^{\mathrm{I}}|$. We restrict ourselves to the situation that $\phi_C^{\mathrm{I}} = \phi_C^{\mathrm{II}}$, thus $\Delta\phi_C = 0$. The bulk mixtures are brought into contact. Since their compositions do not correspond to coexisting phases, the polymer components will start to diffuse in order to make mixtures I and II identical

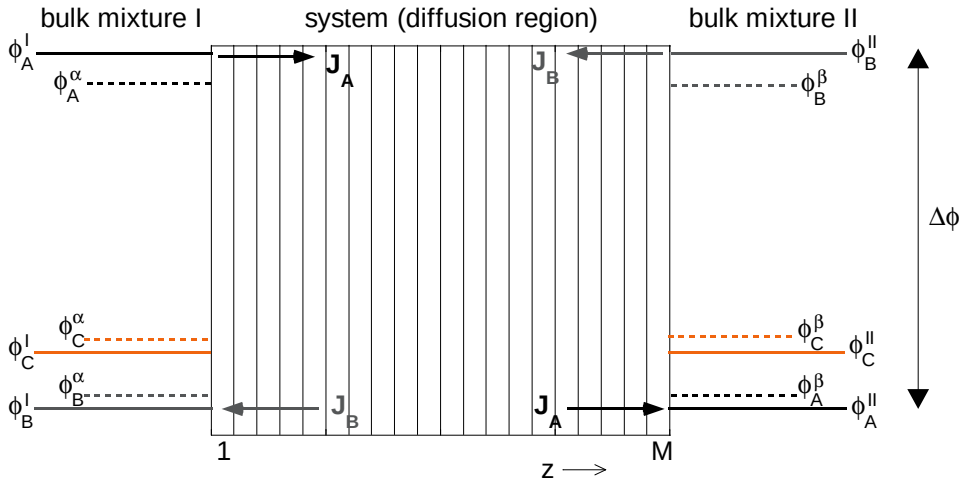

Figure 6.2. The system as used to study adsorption of C at off-equilibrium AB-interfaces and the associated stationary material fluxes, with imposed concentrations in I and II corresponding to the levels indicated by the solid horizontal lines. A symmetric system, typical for this study, is shown with $\Delta\mu_A = -\Delta\mu_B$ and $\Delta\mu_C = 0$. The dashed levels are the coexistence concentrations of Figure 6.1.

or coexisting. However, we keep the compositions of mixtures I and II constant (ideal sink-source system). Eventually, a steady state will occur, where all components diffuse with a flux that is constant in time and space. Although the dynamics of the system developing towards this steady state is certainly highly interesting, we limit ourselves to the steady state itself.

The steady state is studied by means of the Mean-Field Stationary Diffusion (MFSD)-method. This method yields the stationary volume fraction profiles, chemical potential profiles, material fluxes and chain conformations. That information is obtained for the region between bulk mixtures I and II as depicted in Figure 6.2. The region is described by a one-dimensional lattice, whose layers lie perpendicular to the diffusion direction. As in Figure 6.1*a* these layers are numbered by $z = 1, 2, 3, ...M$ ($M = 200$ in Figure 6.1*a*). The flux of segments A through layer z is denoted by $J_A(z)$. Due to the imposed volume fraction gradients and the constraints $\nabla J_A = \nabla J_B = \nabla J_C = 0$, the C-rich wetting layer (*cf.* Figure 6.1) is replaced by a C-rich adsorption layer that has a different width and composition. For example, the mesoscopically thick wetting layer may shrink to a small accumulation of C_N at the interface. The presence of an adsorption layer highly influences the material fluxes. Intuitively it reduces the available space for the diffusing components and may thereby act as a barrier. The effect of a similar, but static, barrier on the chain conformations was studied in Chapter 3. We will show in Section 6.4 that in the case of a 'dynamic' barrier it is highly nontrivial to relate the fluxes of A and B to the amount of C at the A/B-interface.

Note that we have chosen a system with a high degree of symmetry: $N_A = N_B = N_C = N$, $\phi_C^{\mathrm{I}} = \phi_C^{\mathrm{II}}$, and $\chi_{\mathrm{AC}} = \chi_{\mathrm{BC}}$. (In the following, we will write χ_{C} for χ_{AC} and χ_{BC}). The choice for this system allows comparison with our equilibrium wetting study

described in Chapter 5. In the results that we present we have chosen the compositions of mixtures I and II such that $\Delta\phi_A = -\Delta\phi_B$. Then, due to the other symmetric properties, $\Delta\mu_A = -\Delta\mu_B$, $\Delta\mu_C = 0$, and the adsorption layer will be situated exactly in the centre of the system. Even for such symmetric systems we obtain a rich adsorption behaviour.

6.3 Concepts of the method

The Mean-Field Stationary Diffusion method [96] was outlined in Chapter 2. The system is described by a lattice and the polymers are described by chains of segments. Each segment takes one lattice site. In the case of a three-dimensional lattice, each site would contain one segment. However, it suffices to divide the system in lattice layers perpendicular to the diffusion direction, as depicted in Figure 6.2. For a segment in such one-dimensional lattice, the precise identities of surrounding segments are unknown. The interactions between segments are calculated by using the average compositions of lattice layers. This is the so-called mean field approach.

Our systems contain three polymer components, A_N, B_N and C_N. All polymer chains have equal numbers of segments, which is the chain length N. We only consider homopolymers so that component A_N only consists of segments of type A. We may therefore refer to any component just by its constituent segment type.

The MFSD-method starts, as the SF-SCF method [15], with a guess for the segment potentials $u_A(z)$ [96]. These potentials can be expressed in terms of Boltzmann-weighting factors $G_A(z)$ through the relation $u_A(z) = -\ln G_A(z)$. (In this Chapter, we express the segment potentials and chemical potentials in units of k_BT). The segment potentials depend on the volume fractions ϕ of all other segments since energetic interactions, quantified by the Flory-Huggins parameters χ_{ij}, chain connectivities, and space filling determine the possibility to find segment A in layer z. Thus $u_A = u_A[\phi]$. On the other hand, the volume fraction $\phi_A(z)$ of segments A depends on the Boltzmann-weighting factors and therefore on the segment potentials: $\phi_A = \phi_A[u]$. The MFSD-calculation converges if self-consistency is obtained between the potentials and the volume fractions. When the weighting factors or segment potentials are known, the volume fractions ϕ_i and chemical potentials μ_i of all segments can be calculated as a function of position z. From these, we may calculate other system properties such as adsorbed amounts and stationary segment fluxes.

In the MFSD-method the segment weighting factors are calculated under the constraints of incompressibility and stationary volume fractions. Moreover, the solution of the MFSD-calculation must obey the desired compositions for bulk mixtures I and II located at $z = 0$ and $z = M$. By defining the compositions of bulk mixtures I and II we fix the chemical potentials for the segments at both sides of the system. We thus impose a certain driving force $\Delta\mu_i = \mu_i^{\mathrm{II}} - \mu_i^{\mathrm{I}}$ to each segment type. As derived in Appendix 2A the segment chemical potential for segment type A in bulk mixture I is given by:

$$\mu_A^{\mathrm{I}} = \frac{1}{N_A}\ln\phi_A^{\mathrm{I}} + \chi_{\mathrm{AB}}\phi_B^{\mathrm{I}} + \chi_{\mathrm{AC}}\phi_C^{\mathrm{I}}. \tag{6.1}$$

In the following, we will vary the chemical potentials in bulk mixtures I and II in three ways: (i) by variation of the compositions of mixtures I and II at constant χ-parameters, such that $\Delta\phi_A = -\Delta\phi_B$ and $\Delta\phi_C = 0$, (ii) by variation of χ_{AB} at constant composition

and constant $\chi_{\mathrm{C}} = \chi_{\mathrm{AC}} = \chi_{\mathrm{BC}}$, (iii) by variation of χ_{C} at constant composition and constant χ_{AB}. Of interest to the diffusion are the consequences of these variations for the imposed driving forces $|\Delta\mu_A|$ and $|\Delta\mu_B|$. In all three cases we have $|\Delta\mu_C| = 0$ due to the symmetry of our system. With the varying compositions of mixtures I and II (case (i)) $|\Delta\mu_A|$ and $|\Delta\mu_B|$ are rather complex functions of these compositions. However, as long as both bulk mixtures have a stable composition, i.e. if they fall into the one-phase region of a phase composition diagram, the driving forces increase monotonously with increasing $|\Delta\phi_A|$ and $|\Delta\phi_B|$. For varying χ_{AB} (case (ii)), the driving forces $|\Delta\mu_A|$ and $|\Delta\mu_B|$ are linear functions of χ_{AB}. The driving forces decrease with increasing χ_{AB}, since mixtures I and II approach coexistent phases if χ_{AB} is increased for a fixed composition of mixtures I and II. Case (iii), the variation of χ_{C}, has no effect on the driving forces due to our choice that ϕ_C^{I} equals ϕ_C^{II}. In this case, $|\Delta\mu_A| = |\Delta\mu_B|$.

We study the effect of varying driving forces on the adsorption and on the stationary segment fluxes. These fluxes were derived for multicomponent systems in Chapter 2. Two different diffusion mechanisms were put forward, the so-called slow-mode and fast-mode diffusion. According to the slow-mode model, the diffusion occurs through swapping the positions of two different segments [19]. According to the fast-mode model the slow-mode diffusion mechanism must be accompanied by a drift flux [20, 21]. In terms of Onsager coefficients Λ_i, the slow-mode flux and fast-mode flux are given by, respectively,

$$J_A^s = -\frac{\Lambda_A}{\sum_i \Lambda_i} k_B T \sum_j \Lambda_j \nabla \left(\mu_A - \mu_j\right) \tag{6.2a}$$

$$J_A^f = -k_B T \sum_j \left(\phi_j \Lambda_A \nabla\mu_A - \phi_A \Lambda_j \nabla\mu_j\right). \tag{6.2b}$$

The Onsager coefficient Λ_i equals $\tilde{B}_i\phi_i$, where $\tilde{B}_i$ is the mobility of segment type i. We assume equal mobilities for all types of segments ($\tilde{B}_i = \tilde{B}\ \forall i$), so that the slow-mode and fast-mode fluxes become identical:

$$J_A^s = J_A^f = -\tilde{B} k_B T \sum_j \phi_A \phi_j \nabla \left(\mu_A - \mu_j\right). \tag{6.3}$$

We do not specify the conversion factor between our (dimensionless) fluxes and real fluxes. We are only interested in the trends of the flux behaviour. Values for stationary fluxes given in graphs are only specified to illustrate such trends.

6.4 Results and Discussion

6.4.1 Variable $\Delta\phi$

Composition profiles

Figure 6.3 presents the stationary volume fraction profiles for two distinct situations in very similar systems. Figure 6.3*a* and 6.3*b* both refer to a system with $N = 10$, $\chi_{\mathrm{AB}} = 0.34$, and $\chi_{\mathrm{C}} = 0.23$. Moreover, we have chosen for both systems $\phi_C^{\mathrm{I}} = \phi_C^{\mathrm{II}} = 0.15$ and $\Delta\phi = -\Delta\phi_A = \Delta\phi_B$. There is no net diffusion of C-segments ($J_C = 0$). The only difference between the two cases is the value for $\Delta\phi$. In Figure 6.3*a* the imposed driving

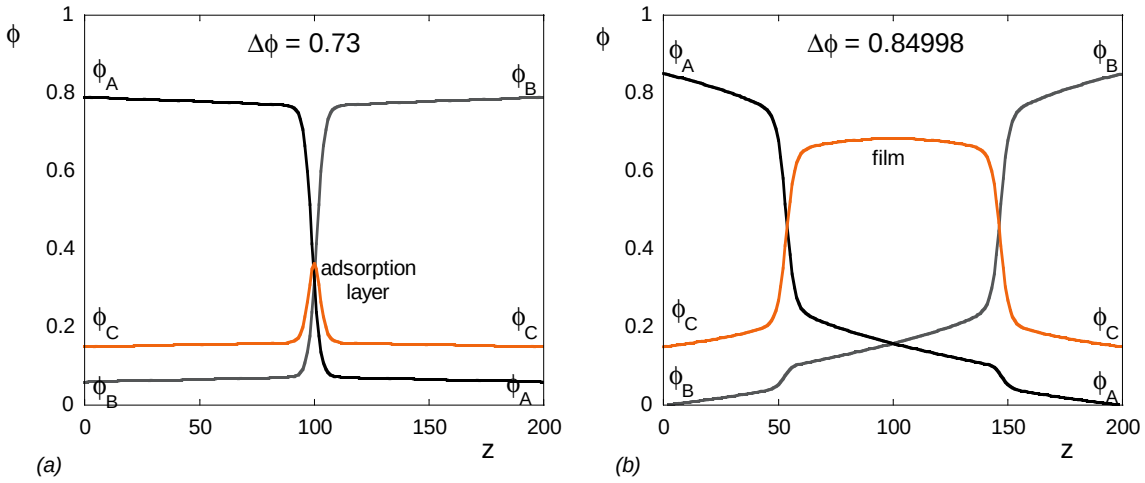

Figure 6.3. Stationary volume fraction profiles for adsorption at off-equilibrium interfaces in two similar systems; $N = 10$, $\chi_{AB} = 0.34$, $\chi_C = 0.23$, $\phi_C^{I} = \phi_C^{II} = 0.15$, $\phi_A^{I} = \phi_B^{II}$, $\phi_A^{II} = \phi_B^{I}$. (a): $\Delta\phi = -\Delta\phi_A = \Delta\phi_B = 0.73$. (b): $\Delta\phi = -0.84998$.

forces are substantially smaller than in Figure 6.3b: $\Delta\phi = 0.73$ and 0.84998 respectively. In fact, the true measure for the driving force is $\Delta\mu_A$ instead of $\Delta\phi_A$, but in the present system $\Delta\mu_A$ grows monotonously with $\Delta\phi_A$ (see the inset of Figure 6.7a). For the smaller driving force, the volume fraction profiles of all components are nearly flat up to a small distance from the interface. Despite the fact that the system is nearly at equilibrium and (with respect to the χ-values) identical to the system in Figure 6.1, the adsorption layer of C_N remains microscopically small. Presumably, the system is closer to a two-phase coexistence with an A- and B-rich phase than to the three-phase coexistence with phases α, β, and γ. In other words, the system remains subsaturated with C. The larger driving force in Figure 6.3b significantly changes the adsorption layer. It grows to mesoscopic scales (a liquid film develops) and the volume fraction of C within this film exceeds the value of ϕ_C^{γ} in the equilibrium γ-phase.

The origin of this quite different behaviour for seemingly similar systems is clarified by Figure 6.4. In this figure the volume fraction profiles of Figures 6.3a and 6.3b are plotted as composition profiles in the equilibrium phase composition diagram. Each point in Figure 6.4 corresponds to the composition of one lattice layer in Figure 6.3. The starting point to the left of a composition profile in Figure 6.4 is the composition of mixture I in the A-rich phase. The end point to the right corresponds to the composition of mixture II in the B-rich phase. The composition profile for small driving forces (Figure 6.3a and grey dots in Figure 6.4) runs through the A/B-binodals and the three-phase coexistence region. The profile does not cross the C-rich one-phase region; therefore there is only a (microscopic) adsorption layer. From the small number of points within the three-phase region it is clear that only a few layers have a composition which would be unstable in homogeneous macroscopic systems. These layers form the interface between the two stable portions of the system that are rich in A and B respectively. The gradients of ϕ within the interface stabilize the instability, as in Van der Waals' theory of liquid/liquid interfaces.

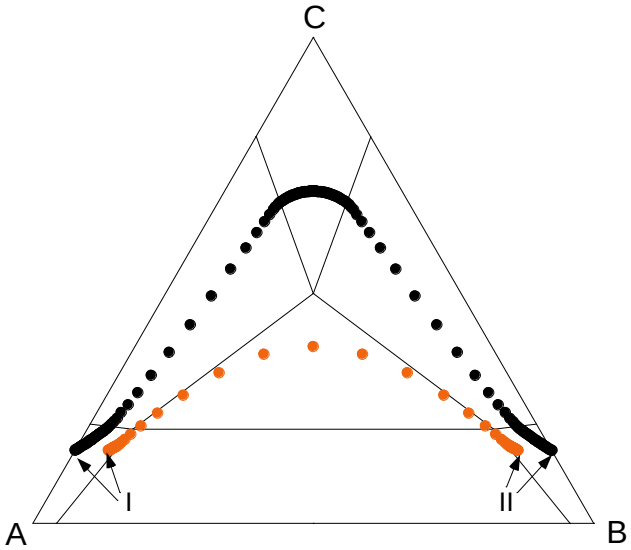

Figure 6.4. The composition profiles of Figure 6.3 plotted in the equilibrium phase composition diagram. The grey curve corresponds to Figure 6.3*a*, the black curve to Figure 6.3*b*. Each dot is the composition of one lattice layer.

For a larger driving force (Figure 6.3*b* and black dots in Figure 6.4) the composition profile first crosses the A/C-binodals so that a stable C-rich phase develops, which is the liquid film at the A/B interface. Then the B/C-binodals are crossed to arrive in the stable B-rich phase. Within the one-phase regions the composition profiles 'travel' more slowly through the composition diagram than within two- or three-phase regions. We conclude that whether a mesoscopic film will develop at the A/B interface or not depends in general on the location of one-phase regions in the phase composition diagram and on the driving forces between two points in this diagram. When the C-rich one-phase region or the driving forces are small, or when mixtures I and II are far from the A/C and B/C binodals, the adsorption layer will remain of microscopic size. We call the adsorption layer a 'film' when the composition profile enters the stable C-rich phase region of the phase composition diagram.

Adsorbed amount

From the composition profiles in Figure 6.4 it can be anticipated that when these profiles cross a phase barrier, that is, when they reach the stable C-rich phase, the adsorbed amount of C may increase faster. Figure 6.5 shows how the film develops with increasing driving force. The black curve presents a measure for the excess adsorbed amount θ_C^{ex} of component C at the interface. This quantity is calculated as

$$\theta_C^{\mathrm{ex}} = \sum_z \left[\phi_C(z) - \phi_C^{\mathrm{I}}\right] = \sum_z \left[\phi_C(z) - \phi_C^{\mathrm{II}}\right]. \tag{6.4}$$

This is only an approximation for the adsorbed amount, since the ϕ_C-gradients in the A- and B-rich phases also contribute (to a minor extent) to θ_C^{ex}. We define the susceptibility

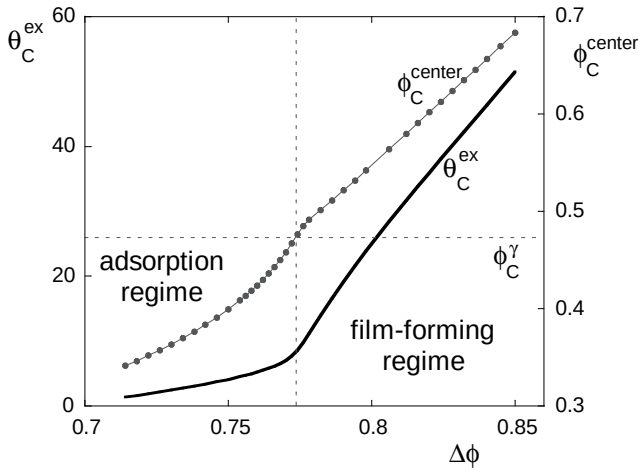

Figure 6.5. The excess amount of C (compared to the amount in the bulk mixtures) and the volume fraction of C in the centre of the system as a function of the imposed volume fraction gradient $\Delta\phi$. (In all cases $|\Delta\phi_A| = |\Delta\phi_B|$). The system is the same as in Figures 6.3 and 6.4.

of θ_C^{ex} with respect to a change in $\Delta\phi$ as

$$X^{\theta}_{\Delta\phi} = \frac{\partial\theta_C^{\text{ex}}}{\partial\Delta\phi}, \tag{6.5}$$

so that $X^{\theta}_{\Delta\phi}$ follows immediately from the slopes in Figure 6.5. In this figure it is seen that the excess amount of C grows continuously with increasing $\Delta\phi$, but the susceptibility $X^{\theta}_{\Delta\phi}$ changes suddenly for $\Delta\phi \approx 0.77$. We can distinguish three contributions to the increase of θ_C^{ex}: (i) the volume fraction of C within the adsorption layer is higher, (ii) the adsorption layer widens, (iii) the gradients of ϕ_C near the system boundaries increase. The first contribution to θ_C^{ex} is related to the concentration ϕ_C^{center} in the middle of the adsorption layer; this quantity is plotted as the grey curve in Figure 6.5. It is seen that as soon as ϕ_C^{center} exceeds the value of ϕ_C^{γ}, in other words, as soon as the composition profiles enter the stable C-rich phase region, the adsorbed amount starts to grow faster. This supports the observations from Figure 6.4. The transition that occurs in Figure 6.5 for $\Delta\phi \approx 0.77$ could be seen as a dynamic phase transition.

Fluxes

In Figure 6.6 the stationary flux of A segments, J_A, is plotted as a function of the imposed volume fraction differences. As expected, the flux increases with increasing driving force. The susceptibility of the flux with respect to $\Delta\phi$, $X^{J}_{\Delta\phi} = \partial J_A/\partial\Delta\phi_A$, suddenly increases at $\Delta\phi = 0.77$ (the value at which ϕ_C^{center} reaches ϕ_C^{γ}). This is shown by the slopes of the two dotted lines that are linear fits to the upper and lower part of the J_A-curve. The slopes differ by a factor 1.7. The same flux is plotted as a function of $\Delta\mu$ (defined as $|\Delta\mu_A| = |\Delta\mu_B|$) in Figure 6.7*a*. Whereas the susceptibility $X^{J}_{\Delta\phi}$ suddenly changes at $\Delta\phi_A = 0.77$ (where $\Delta\mu \approx 0.04$), the susceptibility $X^{J}_{\Delta\mu} = \partial J_A/\partial\Delta\mu$ hardly changes at

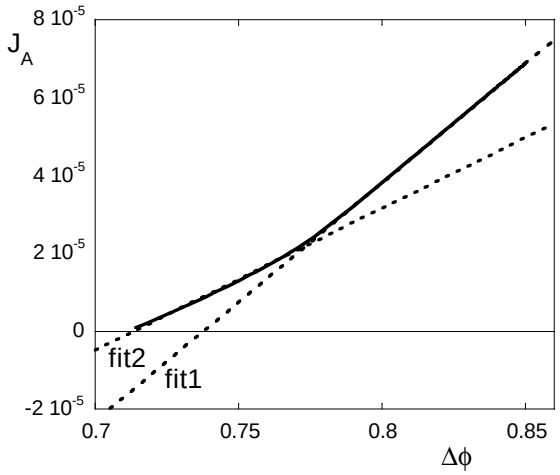

Figure 6.6. Stationary flux of segments A as a function of the imposed $\Delta\phi$ with two linear fits (dotted lines).

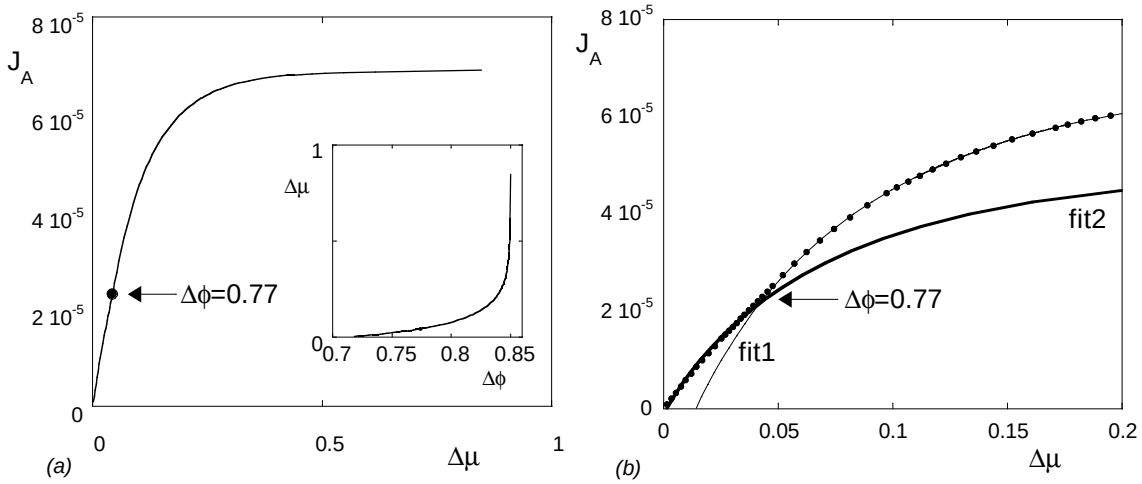

Figure 6.7. (a): Stationary flux J_A of segments A as a function of the imposed $\Delta\mu = |\Delta\mu_A| = |\Delta\mu_B|$. The dot indicates the flux for which $X^J_{\Delta\phi}$ suddenly changes. The inset shows the relation between $\Delta\mu$ and $\Delta\phi$. (b): The same curve $J_A(\Delta\mu)$ for small $\Delta\mu$ (dots). The thin curve is the flux as predicted by fit 1 in Figure 6.6, the thick curve is the same with fit 2 in Figure 6.6. With increasing $\Delta\mu$ the flux smoothly crosses over between both predictions so that $X^J_{\Delta\mu}$ and $X^J_{\Delta\phi}$ do not change at the same moment.

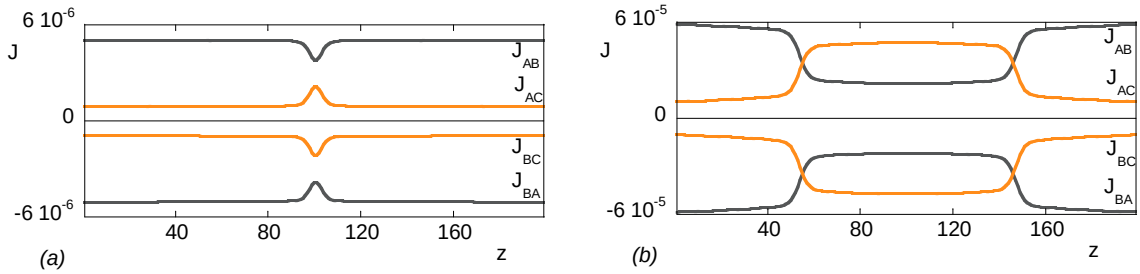

Figure 6.8. (a): The contributions J_{AB} and J_{AC} to the flux of A and the contributions J_{BA} and J_{BC} to the flux of B as a function of z for $\Delta\phi = 0.73$ (*cf.* Figure 6.3a). (b): the same for $\Delta\phi = 0.84998$ (*cf.* Figure 6.3b).

$\Delta\mu \approx 0.04$. This is because $\Delta\mu$ is only a weak function of $\Delta\phi$ in this part of parameter space, as shown by the inset in Figure 6.7a. When the flux would be a linear function of $\Delta\phi$ according to either one of the dashed lines in Figure 6.6, the flux would either follow the thick curve or the thin curve in Figure 6.7b. These curves cross, as they should, at $\Delta\mu \approx 0.04$. The initial part of the flux is plotted again in Figure 6.7b (dots). The flux follows the thick curve for small $\Delta\mu$ and the thin curve for larger $\Delta\mu$. Around $\Delta\mu \approx 0.04$ a smooth transition between both curves occurs so that $X^J_{\Delta\mu}$ remains almost constant around the cross-over.

Combination of Figures 6.5 and 6.6 indicates that the flux increases with the growing adsorption layer that accompanies the increasing driving force. Apparently, the adsorption layer does not act as a barrier to the segmental fluxes. This result shows that the C-segments participate in the swap-diffusion mechanism. The flux of segments A can be decomposed through Equation 6.3 into two partial fluxes J_{AB} and J_{AC} which denote the contributions of A/B and A/C position swaps to the overall diffusion of A:

$$J_A = \sum_i J_{Ai} \tag{6.6a}$$

$$J_{Ai} = -\tilde{B} k_B T \phi_A \phi_i \nabla (\mu_A - \mu_i) \tag{6.6b}$$

Although the overall flux J_A is independent of z, the partial fluxes J_{AB} and J_{AC} may strongly vary. Figures 6.8a and 6.8b show the separate contributions to J_A as a function of z for $\Delta\phi = 0.73$ and $\Delta\phi = 0.84998$, respectively. It is clearly seen that segments C have an important contribution to the overall flux of A. This contribution even exceeds the contribution of A/B-swaps in the film in Figure 6.8b. Figures 6.8a and 6.8b also show that $J_{AB} = -J_{BA}$, as it should according to the definition in Equation 6.6b. Moreover, $J_{AC} = -J_{BC}$ due to equal interactions ($\chi_{AC} = \chi_{BC}$) and the symmetry of mixtures I and II. As a consequence, $J_C = 0$ and $J_A = -J_B$. Figure 6.6 would change significantly if we would only allow position swaps between segments A and B so that $J_{AC} = J_{BC} = 0$. Polymer C_N would statically occupy a part of the diffusion space. The adsorption layer or film would then act as a barrier and reduce the fluxes of A and B. In the static-C_N case $\Delta\phi$ must be larger than 0.77 (as in Figure 6.5) in order to have a thick adsorption layer. The static-C_N case may be approximated by choosing the segment mobilities $\tilde{B}_A$ and $\tilde{B}_B$ much larger than $\tilde{B}_C$. Here we do not consider the static-C_N case any further.

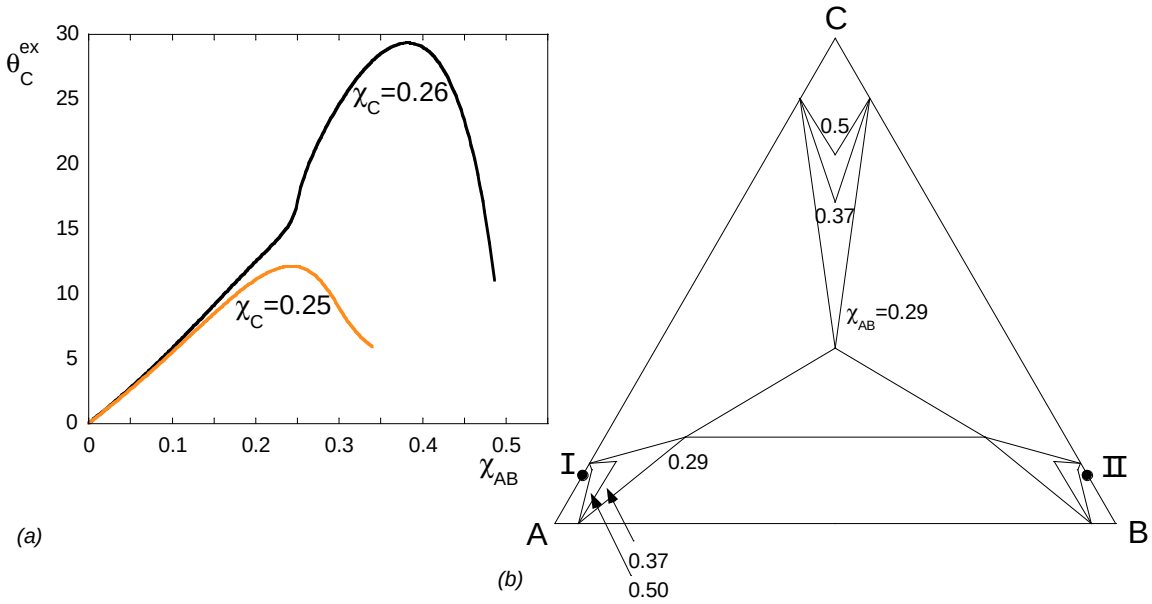

Figure 6.9. Results for varying χ_{AB} and $N = 10$, $\phi_A^{\mathrm{I}} = \phi_B^{\mathrm{II}} = 10^{-5}$, $\phi_C^{\mathrm{I}} = \phi_C^{\mathrm{II}} = 0.10$. (a): The excess amount of C as a function of χ_{AB} for two values of χ_{C}. (b): Phase composition diagrams for $\chi_{\mathrm{C}} = 0.26$ and three different values of χ_{AB}. The dots present the compositions of mixtures I and II. Boundaries of the three-phase regions have been omitted for $\chi_{\mathrm{AB}} = 0.37$ and $\chi_{\mathrm{AB}} = 0.5$.

6.4.2 Variable χ_{AB}

Adsorbed amount

In this section we vary the interactions between components A_N and B_N while keeping the compositions of I and II constant, such that these mixtures remain sub-saturated with C_N. As can be verified from Equation 6.1, the driving forces $|\Delta\mu_A|$ and $|\Delta\mu_B|$ decrease linearly with increasing χ_{AB}. Despite this simple relation between χ_{AB} and the driving forces, the systems show rich behaviour upon variation of χ_{AB} as can be seen in Figure 6.9*a*. This figure gives the excess amount of C as a function of χ_{AB}, for two values of χ_{C}. Let us first consider the curve for $\chi_{\mathrm{C}} = 0.26$ in Figure 6.9*a*. For $\chi_{\mathrm{AB}} \approx 0.25$ the susceptibility $X^{\theta}_{\chi_{\mathrm{AB}}} = \partial\theta_C^{\mathrm{ex}}/\partial\chi_{\mathrm{AB}}$ suddenly increases in a way similar to the susceptibility $X^{\theta}_{\Delta\phi}$ in Figure 6.5. In contrast to the curve in Figure 6.5, the adsorbed amount now exhibits a maximum (at $\chi_{\mathrm{AB}} \approx 0.38$). Such a maximum is also observed if χ_{C} is diminished to a value of 0.25, but the suddenly increasing growth rate is not observed for this χ_{C}.

In Section 6.4.1 we have explained the suddenly increasing susceptibility $X^{\theta}_{\Delta\phi}$ by the observation that at some moment the system is able to reach the C-rich one-phase region of the composition diagram. We now find that $X^{\theta}_{\chi_{\mathrm{AB}}}$ suddenly increases as soon as the composition profiles start to cross the two-phase regions that are bounded by A/C and B/C binodals. The three-phase region in the phase composition diagram may be absent for small values of χ_{AB} so that the phase composition diagram only contains one 1-phase

region and three 2-phase regions. Crossing the 2-phase regions still allows the occurrence of thick adsorption layers. For example, Figure 6.9*a* reveals the existence of a thick adsorption layer for $\chi_{\mathrm{AB}} = 0.25$ and $\chi_{\mathrm{C}} = 0.26$, whereas the three-phase region will only appear when $\chi_{\mathrm{AB}} > 0.26$ (see the discussion on binodals in symmetric three-component systems in Section 5.4.2).

Despite the maximum in θ_C^{ex} we found that ϕ_C^{center} remains an increasing function of χ_{AB}. The maximum in θ_C^{ex} reflects a maximum in the width of the adsorption layer. The width of the adsorption layer decreases as a result of diminishing driving forces: upon increasing χ_{AB}, mixtures I and II approach the coexistent phases α and β (*cf.* Figure 6.1*b*) or any other combination of coexistent points on the A/B binodals. This is seen from the collection of phase composition diagrams in Figure 6.9*b*. The boundaries of two three-phase regions have been omitted in this figure for the sake of clarity. For $\chi_{\mathrm{AB}} = 0.37$ or $\chi_{\mathrm{AB}} = 0.5$ (and $\chi_{\mathrm{C}} = 0.26$) only the one-phase regions are depicted. For $\chi_{\mathrm{AB}} = 0.29$ and $\chi_{\mathrm{C}} = 0.26$ the two-phase regions and the three-phase region are plotted as well. From the evolution of the A and B-rich regions with increasing χ_{AB} it is understood that mixtures I and II approach phase coexistence. Due to subsaturation of C within the bulk mixtures, the adsorption layer must become microscopically thick upon approach of coexistence. Figure 6.9*a* shows that the maximum of θ_C^{ex} for $\chi_{\mathrm{C}} = 0.25$ occurs before the composition profiles cross any two-phase region. For $\chi_{\mathrm{C}} = 0.25$ the A/C and B/C two-phase regions are smaller than for $\chi_{\mathrm{C}} = 0.26$.

Fluxes

Figure 6.10*a* shows that the stationary flux of A decreases with increasing χ_{AB}, that is (according to Equation 6.1) with decreasing driving force. There is no direct correlation between the excess amount of C and the flux of A. The maximum in θ_C^{ex} (Figure 6.9*b*) is not related to some special feature in the flux curve. For $\chi_{\mathrm{C}} = 0.26$ and $\chi_{\mathrm{AB}} < 0.38$ the flux decreases whereas the adsorption of C increases. In Section 6.4.1 it was shown that the adsorption layer does not act as a barrier since $X^J_{\Delta\phi}$ and $X^\theta_{\Delta\phi}$ increase simultaneously. Figure 6.10*b* gives the contribution of C to the total flux of A for $z = M/2$, i.e. $J_{AC}(M/2) = J_{AC}^{\mathrm{center}}$. Note that, due to the symmetry of the system, $\nabla\mu_C^{\mathrm{center}} = 0$, $\nabla\mu_A^{\mathrm{center}} = -\nabla\mu_B^{\mathrm{center}}$ and $\phi_A^{\mathrm{center}} = \phi_B^{\mathrm{center}}$. Therefore Equation 6.6 yields $J_{AC}^{\mathrm{center}}/J_A = \phi_C^{\mathrm{center}}$. The contribution J_{AC} and the volume fraction ϕ_C^{center} simultaneously have a sharp increase for $\chi_{\mathrm{AB}} \approx 0.25$. The volume fraction ϕ_C^{center} continues to grow for larger χ_{AB}. This growth is insufficient to compensate for the diminishing driving force $\nabla\mu$ so that J_{AC} and J_A must decrease.

6.4.3 Variable χ_{C}

Equation 6.1 reveals that upon variation of χ_{C} ($= \chi_{\mathrm{AC}} = \chi_{\mathrm{BC}}$) the driving forces between mixtures I and II remain constant since $\phi_C^{\mathrm{I}} = \phi_C^{\mathrm{II}}$. Even so, the stationary flux is an interesting function of χ_{C}. This is illustrated by Figure 6.11 where we plotted both the flux of A and the excess adsorbed amount of C versus χ_{C}. Whereas in Figures 6.9*a* and 6.10*a* we observed a maximum in θ_C^{ex} and a monotonic behaviour of the flux as a function of χ_{AB}, we now see a monotonic increase of θ_C^{ex} and a maximum in the flux as a function of χ_{C}. Figure 6.11*a* shows again that the flux behaviour changes simultaneously with the transition between the adsorption regime and the film-forming regime for $\chi_{\mathrm{C}} \approx 0.254$.

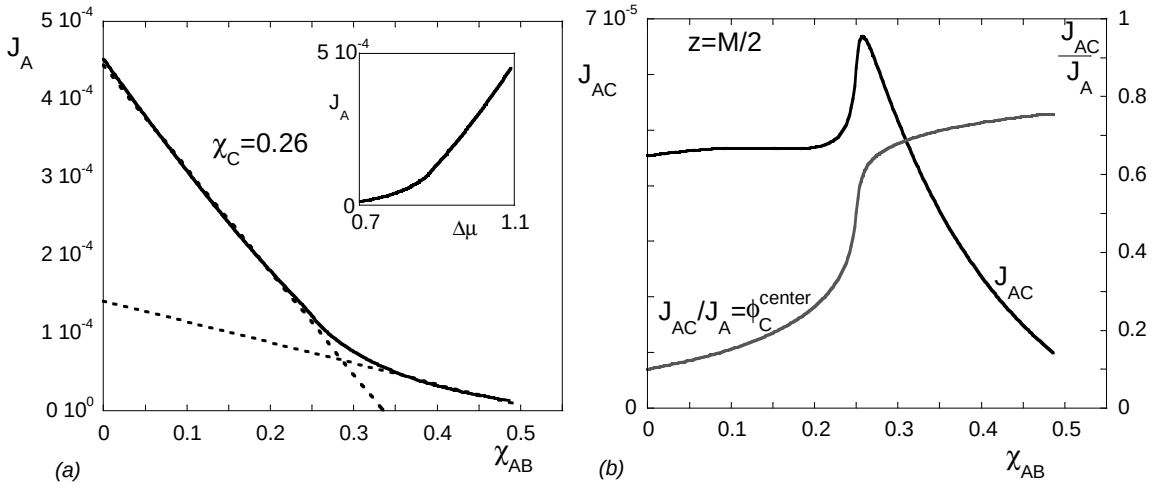

Figure 6.10. Results for varying $\chi_{\rm AB}$ and $\chi_{\rm C} = 0.26$, $N = 10$, $\phi_A^{\rm I} = \phi_B^{\rm II} = 10^{-5}$, $\phi_C^{\rm I} = \phi_C^{\rm II} = 0.10$. (a): The stationary flux of A-segments as a function of $\chi_{\rm AB}$ (main figure) and as a function of the driving force $\Delta\mu_A$ (inset). The dotted lines are linear fits; their slopes differ by a factor 4.9. (b): The contribution of C to the flux of A in the centre of the system ($z = M/2$) as a function of $\chi_{\rm AB}$, plotted as J_{AC} (left scale) and as $J_{AC}/J_A = \phi_C^{\rm center}$ (right scale).

The one-phase regions in the phase composition diagram become smaller for increasing $\chi_{\rm C}$ (see Figure 6.11b). The A/C and B/C binodals approach the compositions of mixtures I and II. Although the driving forces remain constant, the difference between $\mu_A^{\rm I}$ and $\mu_A^{\rm coex}$ decreases upon increasing $\chi_{\rm C}$. For $\chi_{\rm C} = 0.254$ the binodals are sufficiently close to be crossed by the composition profiles so that the stable C-rich phase is reached and a faster increase in $\theta_C^{\rm ex}$ (or a larger susceptibility $X_{\chi_{\rm C}}^{\theta}$) is observed.

With increasing $\chi_{\rm C}$ the width of the adsorption layer continues to increase; the A/C and B/C interfaces move towards $z = 0$ and $z = M$ respectively, since the bulk mixtures approach the binodal compositions associated with the A/C and B/C interfaces. Despite the continuously increasing width and increasing $\phi_C^{\rm center}$ the stationary flux has a maximum for a relatively high value of $\chi_{\rm C}$ (Fig. 6.11a). The maximum in J_A shifts to lower $\chi_{\rm C}$ for higher values of $\phi_C^{\rm I} = \phi_C^{\rm II}$ (not shown). The origin of this flux behaviour is illustrated in Figure 6.12 for $\phi_C^{\rm I} = \phi_C^{\rm II} = 0.10$. In Figure 6.12$a$ the μ_A-profiles are shown for different values of $\chi_{\rm C}$. Although the driving force $\Delta\mu_A = \mu_A^{\rm II} - \mu_A^{\rm I}$ is constant for varying $\chi_{\rm C}$, the profile of μ_A is not. The peaks in the μ_A profiles occur at the interfaces. It is seen that locally $\nabla\mu_A(z)$ may be positive although $\mu_A^{\rm II} < \mu_A^{\rm I}$. The profile of μ_A thus makes a 'detour' to arrive eventually for $z = M$ at the imposed value of $\mu_A^{\rm II}$. For increasing $\chi_{\rm C}$ this detour initially extends over a longer distance through the system. Putting it differently, the layer $z*$ for which $\mu_A(z*) = \mu_A^{\rm I}$ initially increases with increasing $\chi_{\rm C}$. This is shown in Figure 6.12b where we have plotted the value of $z*$ as a function of $\chi_{\rm C}$. A larger flux J_A compensates for the detour to overcome $\Delta\mu_A$. The detour of $\mu_A(z)$ is caused by the relatively high chemical potential within the adsorption layer. This potential

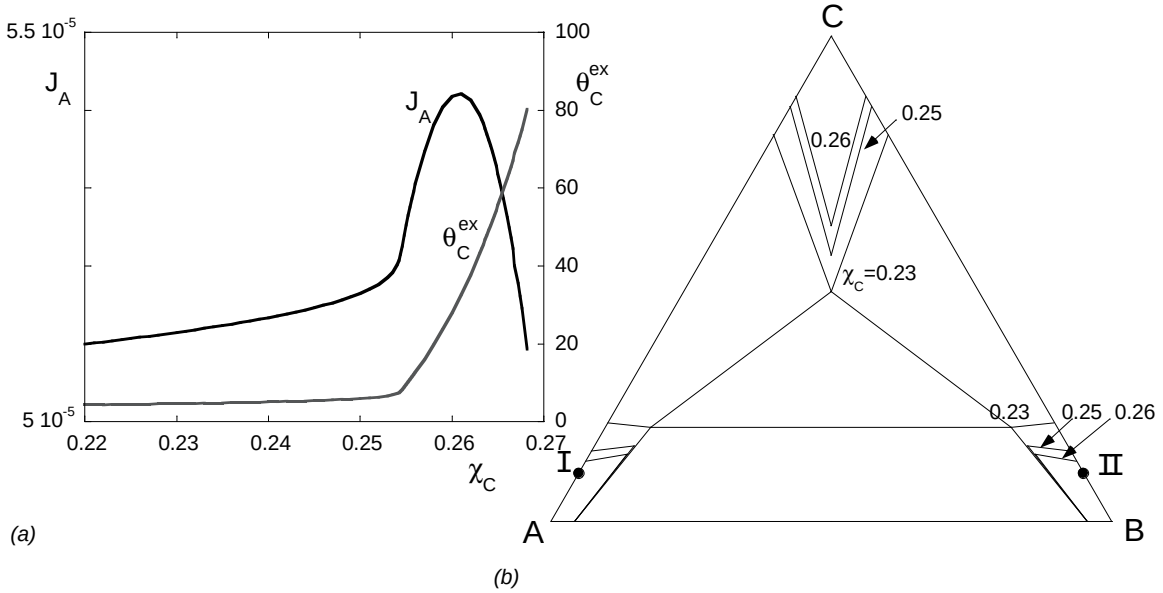

Figure 6.11. Results for varying χ_{C}, for constant $\Delta\mu = |\Delta\mu_A| = |\Delta\mu_B|$, $\Delta\mu_C = 0$, $\chi_{\mathrm{AB}} = 0.34$, $N = 10$, $\phi_C^{\mathrm{I}} = \phi_C^{\mathrm{II}} = 0.10$, and $\phi_A^{\mathrm{I}} = \phi_B^{\mathrm{II}} = 10^{-5}$. (a): The stationary flux of A and the excess amount of C. (b): Phase composition diagrams for three different values of χ_{C}. The dots present the compositions of mixtures I and II. Boundaries of the three-phase regions have been omitted for $\chi_{\mathrm{C}} = 0.25$ and $\chi_{\mathrm{C}} = 0.26$.

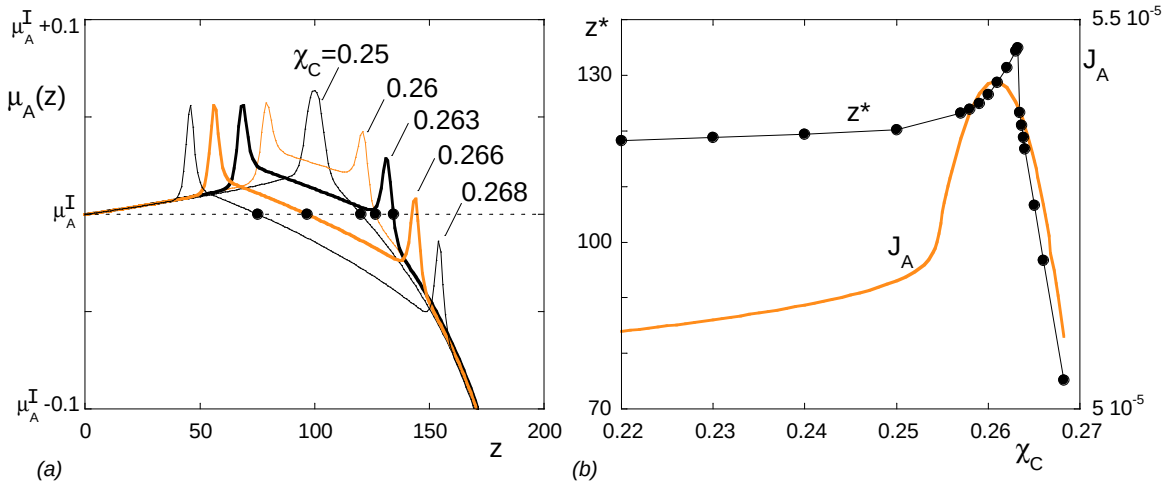

Figure 6.12. Results for varying χ_{C}, for constant $\Delta\mu = |\Delta\mu_A| = |\Delta\mu_B|$, $\Delta\mu_C = 0$, $\chi_{\mathrm{AB}} = 0.34$, $N = 10$, $\phi_C^{\mathrm{I}} = \phi_C^{\mathrm{II}} = 0.10$, and $\phi_A^{\mathrm{I}} = \phi_B^{\mathrm{II}} = 10^{-5}$. (a): Profiles of μ_A for five values of χ_{C}: 0.25 - 0.26 - 0.263 - 0.266 - 0.268. The dots indicate the values for $z*$ for which $\mu_A(z*) = \mu_A^{\mathrm{I}}$. (b): The value of $z*$ for which $\mu_A(z*) = \mu_A^{\mathrm{I}}$ and the stationary flux of A as functions of χ_{C}.

decreases with increasing χ_{C} and eventually $z*$ falls within the adsorption layer. From this moment, the value of $z*$ decreases with increasing χ_{C} (see Figure 6.12a). The detour of $\mu_A(z)$ shortens which means that lower fluxes are sufficient to overcome the imposed drop in μ_A between mixtures I and II. One would expect a direct correlation between $z*$ and J_A. However, in Figure 6.12b the maximum in J_A does not exactly coincide with the maximum in $z*$. This is due to the inaccurate calculation of $z*$ near its maximum: for $\chi_{\mathrm{C}} \approx 0.26$ we find that $z*$ is positioned at the μ_A peak occurring at the B/C interface.

6.5 Outlook

Our three-component system could be used to study the diffusion over a barrier that consists of polymers. The adsorption layer acts as a barrier to the diffusion of A and B if the polymer segments that constitute the adsorption layer do not contribute to the fluxes of A and B. These fluxes should then be calculated as $J_A = -\tilde{B}\phi_A\phi_B\nabla\left(\mu_A - \mu_B\right) = -J_B$. The polymer chain conformations of the barrier material may still respond to the diffusing segments. Cell membranes are natural barriers that consist of short chains, namely lipids. During transport of substances through these membranes, the structure of the membrane or the conformations of the lipids may change. Transport through cell membranes is a vital process in life, for example in the communication between brains and muscles, but also in the secretion of waste products by the kidneys or in drug delivery. It is therefore interesting to study the transport through a polymer layer that responds to the transport by conformational adjustments but that does not necessarily support the transport. The systems studied in this chapter may thus form the basis for further investigations in biological systems.

6.6 Conclusions

We have shown that off-equilibrium interfaces in simple symmetric systems exhibit a very rich adsorption behaviour. The adsorption and associated material fluxes have been studied in stationary three-component homopolymer systems. Two of these components, A_N and B_N, formed an interface at which the third component, C_N, adsorbed. (N is the chain length, which was the same for all three components). Due to imposed concentration gradients, the systems were off-equilibrium. Polymers A_N diffused from the A-rich phase through the interface to the B-rich phase. Polymers B_N diffused in the opposite direction. Polymer C_N did not have any net-diffusion since we imposed symmetric driving forces to A_N and B_N such that the driving force on C_N remained zero. The driving force was expressed in terms of $\Delta\mu = |\Delta\mu_A| = |\mu_A^{\mathrm{II}} - \mu_A^{\mathrm{I}}| = |\Delta\mu_B|$. The symmetry arose from the symmetric compositions at both sides of the interface ($\Delta\phi = |\Delta\phi_A| = |\phi_A^{\mathrm{II}} - \phi_A^{\mathrm{I}}| = |\Delta\phi_B|$, $\Delta\phi_C = 0$), from symmetric Flory-Huggins interaction parameters ($\chi_{\mathrm{AC}} = \chi_{\mathrm{BC}} = \chi_{\mathrm{C}}$), and from the equal chain lengths and segment mobilities. The interaction parameters were chosen such that all systems studied would display complete wetting in equilibrium. We quantified the adsorbed amount of C by θ_C^{ex}, i.e. the excess amount of C compared to the bulk mixtures. In short we can conclude the following:

- The excess amount of C increases with increasing $\Delta\phi$ or χ_{C}. The susceptibilities $X_{\Delta\phi}^{\theta} = \partial\theta_C^{\mathrm{ex}}/\partial\Delta\phi$ and $X_{\chi_{\mathrm{C}}}^{\theta} = \partial\theta_C^{\mathrm{ex}}/\partial\chi_{\mathrm{C}}$ increase if the composition in the centre of

the adsorption layer corresponds to the composition of a stable C-rich phase. From phase composition diagrams it can be verified that this should occur for sufficiently large values of $\Delta\phi_A$ or χ_{C}. The changing susceptibilities of θ_C^{ex} indicate a transition from molecular adsorption to film formation (in other words, from thin to thick adsorption layers).

- The excess amount of C as a function of χ_{AB} exhibits a maximum. This maximum can occur in both regimes of adsorption and film formation. The maximum in θ_C^{ex} reflects a maximum in the width of the adsorption layer. For large χ_{AB} the bulk mixtures approach coexistence between an A-rich and a B-rich phase so that the adsorbed amount of C must decline, because for our choice of $\phi_C^{\mathrm{I}} = \phi_C^{\mathrm{II}}$ the A and B-phases are subsaturated with C in equilibrium.

- The stationary segment fluxes decrease, as expected, with decreasing driving forces. The fluxes and θ_C^{ex} decrease simultaneously for varying $\Delta\phi_A$. However, for varying χ_{AB} the fluxes decrease while θ_C^{ex} increases.

- The stationary segment fluxes are a function of χ_{C} even if the driving forces between the two bulk mixtures are constant for all χ_{C}. This is due to the μ-profiles that must be followed to keep the fluxes constant throughout the system. For example, $\nabla\mu_A$ may be positive for some values of z, even though $\mu_A^{\mathrm{II}} < \mu_A^{\mathrm{I}}$.

Bibliography

[1] A. Spillman. *Ultrasound: an environmentally friendly tool for the textile industry.* Agricultural Research Magazine, **51**, 10 (2003).

[2] J. Han and H.G. Craighead. *Characterization and optimization of an entropic trap for DNA separation.* Analytical Chemistry, **74**, 394 (2002).

[3] J. Han and H.G. Craighead. *Separation of long DNA molecules in a microfabricated entropic trap array.* Science, **288**, 1026 (2000).

[4] S.E. Henrickson, M. Misakian, B. Robertson, and J.J. Kasianowicz. *Driven DNA transport into an asymmetric nanometer-scale pore.* Physical Review Letters, **85**, 3057 (2000).

[5] M. Akeson, D. Branton, J.J. Kasianowicz, E. Brandin, and D.W. Deamer. *Microsecond time-scale discrimination among polycytidylic acid, polyadenylic acid, and polyuridylic acid as homopolymers or as segments within single RNA molecules.* Biophysical Journal, **77**, 3227 (1999).

[6] J.J. Kasianowicz, E. Brandin, D. Branton, and D.W. Deamer. *Characterization of individual polynucleotide molecules using a membrane channel.* Proceedings of the National Academy of Sciences of the USA, **93**, 13770 (1996).

[7] P.J. Flory. *Thermodynamics of high polymer solutions.* Journal of Chemical Physics, **10**, 51 (1942).

[8] M.L. Huggins. *Some properties of solutions of long-chain compounds.* Journal of Physical Chemistry, **46**, 151 (1942).

[9] J.M.H.M. Scheutjens and G.J. Fleer. *Statistical theory of the adsorption of interacting chain molecules 1. Partition function, segment density distribution, and adsorption isotherms.* Journal of Physical Chemistry, **83**, 1619 (1979).

[10] J.M.H.M. Scheutjens and G.J. Fleer. *Statistical theory of the adsorption of interacting chain molecules 2. Train, loop, and tail size distribution.* Journal of Physical Chemistry, **84**, 178 (1980).

[11] J.M.H.M. Scheutjens and G.J. Fleer. *Interaction between two adsorbed polymer layers.* Macromolecules, **18**, 1882 (1985).

[12] F.A.M. Leermakers and J.M.H.M. Scheutjens. *Statistical thermodynamics of association colloids, I. Lipid bilayer membranes.* Journal of Chemical Physics, **89**, 3264 (1988).

[13] F.A.M. Leermakers and J.M.H.M. Scheutjens. *Statistical thermodynamics of association colloids, III. The gel to liquid phase transition of lipid bilayer membranes.* Journal of Chemical Physics, **89**, 6912 (1988).

[14] O.A. Evers, J.M.H.M. Scheutjens, and G.J. Fleer. *Statistical thermodynamics of block copolymer adsorption 1. Formulation of the model and results for the adsorbed layer structure.* Macromolecules, **23**, 5221 (1990).

[15] G.J. Fleer, J.M.H.M. Scheutjens, M.A. Cohen Stuart, T. Cosgrove, and B. Vincent. *Polymers at interfaces.* Chapman & Hall, London (1993).

[16] R. Israels, J.M.H.M. Scheutjens, and G.J. Fleer. *Adsorption of ionic block copolymers: self-consistent field analysis and scaling predictions.* Macromolecules, **26**, 5405 (1993).

[17] C.M. Wijmans, F.A.M. Leermakers, and G.J. Fleer. *Chain stiffness and bond correlations in polymer brushes.* Journal of Chemical Physics **101**,8214 (1994).

[18] P.J. Flory. *Principles of Polymer Chemistry.* Cornell University Press, Ithaca (1953).

[19] F. Brochard, J. Jouffroy, and P. Levinson. *Polymer-polymer diffusion in melts.* Macromolecules, **16**, 1638 (1983).
[20] E.J. Kramer, P. Green, and C.J. Palmstrøm. *Interdiffusion and marker movements in concentrated polymer-polymer diffusion couples.* Polymer, **25**, 473 (1984).
[21] H. Sillescu. *Relation of interdiffusion and self-diffusion in polymer mixtures.* Makromolecular Chemistry, Rapid Communication, **5**, 519 (1984).
[22] M.G. Brereton, E.W. Fischer, G. Fytas, and U. Murschall. *Mutual diffusion in binary polymer mixtures as measured by dynamic light scattering.* Journal of Chemical Physics, **86**, 5174 (1987).
[23] M.G. Brereton. *The dynamics of polymer blends: interdiffusion and the glass transition.* Progress in Colloid & Polymer Science, **91**, 8 (1993).
[24] P.F. Green, C.J. Palmstrøm, J.W. Mayer, and E.J. Kramer. *Marker displacement measurements of polymer-polymer interdiffusion.* Macromolecules, **18**, 501 (1985).
[25] R.J. Composto, E.J. Kramer, and D.M. White. *Mutual diffusion in the miscible polymer blend polystyrene/poly(xylenyl ether).* Macromolecules, **21**, 2580 (1988).
[26] T.E. Shearmur, A.S. Clough, D.W. Drew, M.G.D. van der Grinten, and R.A.L. Jones. *Interdiffusion of deuterated and protonated poly(methyl methacrylate).* Polymer, **39**, 2155 (1998).
[27] M. Geoghegan, R.A.L. Jones, M.G.D. van der Grinten, and A.S. Clough. *Interdiffusion in blends of deuterated polystyrene and poly(α-methylstyrene).* Polymer, **40**, 2323 (1999).
[28] S.M. Engels and F.A.M. Leermakers. *Wetting transitions in symmetrical polymer blends.* Journal of Chemical Physics, **114**, 4267 (2001).
[29] E.P.K. Currie, M. Wagemaker, M.A. Cohen Stuart, and A.A. van Well. *Structure of monodisperse and bimodal brushes.* Macromolecules, **32**, 9041 (1999).
[30] F.A.M. Leermakers and J.M.H.M. Scheutjens. *Statistical thermodynamics of association colloids II. Lipid vesicles.* Journal of Physical Chemistry, **93**, 7417 (1989).
[31] G.T. Pickett and A.C. Balazs. *Conformations of bridging polyelectrolytes in poor solvent: single-chain self-consistent field calculations.* Langmuir, **17**, 5111 (2001).
[32] J. van Male. *De dynamica van polymeeradsorptie.* Msc-thesis, Wageningen Agricultural University (1995).
[33] E. Reister, M. Muller, and K. Binder. *Spinodal decomposition in a binary polymer mixture: dynamic self-consistent-field theory and Monte Carlo simulations.* Physical Review E, **64**, 041804 (2001).
[34] J.G.E.M. Fraaije. *Dynamic density functional theory for microphase separation kinetics of block coploymer melts.* Journal of Chemical Physics, **99**, 9202 (1993).
[35] J.G.E.M. Fraaije, B.A.C. van Vlimmeren, N.M. Maurits, M. Postma, O.A. Evers, C. Hoffmann, P. Altevogt, and G. Goldbeck-Wood. *The dynamic mean-field density functional method and its application to the mesoscopic dynamics of quenched block copolymer melts.* Journal of Chemical Physics, **106**, 4260 (1997).
[36] R. Hasegawa and M. Doi. *Adsorption dynamics. Extension of self-consistent field theory to dynamical problems.* Macromolecules, **30**, 3086 (1997).
[37] C. Yeung and A.C. Shi. *Formation of interfaces in incompatible polymer blends: a dynamical mean field study.* Macromolecules, **32**, 3637 (1999).
[38] L.J.D. Frink, A. Thompson, and A.G. Salinger. *Applying molecular theory to steady-state diffusing systems.* Journal of Chemical Physics, **112**, 7564 (2000).
[39] G.H. Fredrickson, V. Ganesan, and F. Drolet. *Field-theoretic computer simulation methods for polymers and complex fluids.* Macromolecules, **35**, 16 (2002).
[40] F. Brochard and P.G. de Gennes. *Polymer-polymer interdiffusion* Europhysics Letters, **1**, 221 (1986).
[41] G. Foley and C. Cohen. *Diffusion in polymer-polymer mixtures.* Journal of Polymer Science: Part B: Polymer Physics, **25**, 2027 (1987).
[42] W. Jilge, I. Carmesin, K. Kremer, and K. Binder. *A Monte Carlo simulation of polymer-polymer interdiffusion.* Macromolecules, **23**, 5001 (1990).

[43] E. Jabbari and N.A. Peppas. *A model for interdiffusion at interfaces of polymers with dissimilar physical properties.* Polymer, **36**, 575 (1995).

[44] A.Z. Akcasu. *The 'fast' and 'slow' mode theories of interdiffusion in polymer mixtures: resolution of a controversy.* Macromolecular Theory and Simulations, **6**, 679 (1997).

[45] I.Y. Erukhimovich and Y.V. Kudryavtsev. *Interdiffusion in polymer blends: the effect of compressibility.* Macromolecular Theory and Simulations, **8**, 247 (1999).

[46] E. Pardo, J.P. Tomba, and J.M. Carella. *A generalized method to calculate diffusion rates in polydisperse systems. Application to miscible polymer pair in the concetrated regime.* Computational and Theoretical Polymer Science, **10**, 523 (2000).

[47] P.F. Green and B.L. Doyle. *'Thermodynamic slowing down' of mutual diffusion in isotopic polymer mixtures.* Macromolecules, **20**, 2471 (1987).

[48] T.E. Shearmur, A.S. Clough, D.W. Drew, M.G.D. van der Grinten, and R.A.L. Jones. *Interdiffusion of low molecular weight deuterated polystyrene and poly(methyl methacrylate).* Macromolecules, **29**, 7269 (1996).

[49] T.E. Shearmur, A.S. Clough, D.W. Drew, and M.G.D. van der Grinten. *Temperature dependence of the mutual diffusion coefficient of deuterated polystyrene and poly(methyl methacrylate).* Physical Review E, **55**, R3840 (1997).

[50] H. Qiu and M. Bousmina. *Determination of mutual diffusion coefficients at nonsymmetric polymer/polymer interfaces from rheometry.* Macromolecules, **33**, 6588 (2000).

[51] P.R. Rouse Jr. *The theory of linear viscoelastic properties of dilute solutions of coiling polymers.* Journal of Chemical Physics, **21**, 1272 (1953).

[52] P.G. de Gennes. *Reptation of a polymer chain in the presence of fixed obstacles.* Journal of Chemical Physics, **55**, 572 (1971).

[53] M. Doi and S.F. Edwards. *The Theory of Polymer Dynamics*, Volume 73 of *International series of monographs on physics.* Clarendon Press, Oxford (1986).

[54] A.Z. Akcasu, G. Nägele, and R. Klein. *Remarks on the 'fast' and 'slow' mode theories of interdiffusion.* Macromolecules, **28**, 6680 (1995).

[55] H. Morita, T. Kawakatsu, and M. Doi. *Dynamic density functional study on the structure of thin polymer blend films with a free surface.* Macromolecules, **34**, 8777 (2001).

[56] N.M. Maurits and J.G.E.M. Fraaije. *Mesoscopic dynamics of copolymer melts. From density dynamics to external potential dynamics using nonlocal kinetic coupling.* Journal of Chemical Physics, **107**, 5879 (1997).

[57] R.M. Barrer. *Measurement of diffusion and thermal conductivity 'constants' in non-homogeneous media, and in media where these 'constants' depend respectively on concentration or temperature.* Proceedings of the Physics Society, **58**, 321 (1946).

[58] J. Crank. *The mathematics of diffusion.* Oxford University Press, Oxford (1967).

[59] S. Chakraborty, D.B. Dingwell, and D.C. Rubie. *Multicomponent diffusion in ternary silicate melts in the system K_2O-Al_2O_3-SiO_2: I. Experimental measurements.* Geochimica et Cosmochimica Acta, **59**, 255 (1995).

[60] Y. Liang, F.M. Richter, and E.B. Watson. *Diffusion in silicate melts: II. Multicomponent diffusion in CaO-Al_2O_3-SiO_2 at 1500 C and 1 GPa.* Geochimica et Cosmochimica Acta, **60**, 5021 (1996).

[61] P.C. Tortorici and M.A. Dayananda. *Interdiffusion and diffusion structure development in selected refractory metal silicides.* Materials Science and Engineering A, **261**, 64 (1999).

[62] K. MacEwan and D.G. Leaist. *Incongruent diffusion (negative main mutual diffusion coefficient) for a ternary mixed surfactant system.* Journal of Physical Chemistry B, **106**, 10296 (2002).

[63] T. Nishiyama. *Uphill diffusion and a new nonlinear diffusion equation in ternary nonelectrolyte system.* Physics of the Earth and Planetary Interiors, **107**, 33 (1998).

[64] H. Salman, D. Zbaida, Y. Rabin, D. Chatenay, and M. Elbaum. *Kinetics and mechanism of DNA uptake into the cell nucleus.* Proceedings of the National Academy of Sciences of the USA, **98**, 7247 (2001).

[65] S. Mitragotri. *Modeling skin permeability to hydrophilic and hydrophobic solutes based on four permeation pathways.* Journal of Controlled Release, **86**, 69 (2003).

[66] F. Tihminlioglu, R.P. Danner, N. Lützow, and J.L. Duda. *Solvent diffusion in amorphous polymers: polyvinyl acetate-toluene system.* Journal of Polymer Science, Part B: Polymer Physics, **38**, 2429 (2000).

[67] M. Sahimi. *Transport of macromolecules in porous media.* Journal of Chemical Physics, **96**, 4718 (1992).

[68] A. Meller, L. Nivon, E. Brandin, J. Golovchenko, and D. Branton. *Rapid nanopore discrimination between single polynucleotide molecules.* Proceedings of the National Academy of Sciences of the USA, **97**, 1079 (2000).

[69] S. Howorka, S. Cheley, and H. Bayley. *Sequence-specific detection of individual DNA strands using engineered nanopores.* Nature Biotechnology, **19**, 636 (2001).

[70] M.A.M. Beerlage, J.M.M. Peeters, J.A.M. Nolten, M.H.V. Mulder, and H. Strathmann. *Hindered diffusion of flexible polymers through polyimide ultrafiltration membranes.* Journal of Applied Polymer Science, **75**, 1180 (2000).

[71] M.A.M. Beerlage, M.L. Heijnen, M.H.V. Mulder, C.A. Smolders, and H. Strathmann. *Non-aqueous retention measurements: ultrafiltration behaviour of polystyrene solutions and colloidal silver particles.* Journal of Membrane Science, **113**, 259 (1996).

[72] J. Han, S.W. Turner, and H.G. Craighead. *Entropic trapping and escape of long DNA molecules at submicron size constriction.* Physical Review Letters, **83**, 1688 (1999).

[73] W.D. Volkmuth and R.H. Austin. *DNA electrophoresis in microlithographic arrays.* Nature, **358**, 600 (1992).

[74] A.M. Skvortsov, L.I. Klushin, J. van Male, and F.A.M. Leermakers. *First-order coil-to-flower transition of a polymer chain pinned near a step-wise external potential: numerical, analytical and scaling analysis.* Journal of Chemical Physics, **115**, 1586 (2001).

[75] F.A.M. Leermakers, J. van Male, and A.M. Skvortsov. *Coil-to-flower transition of a polymer chain pinned near a stepwise external potential: finite size effects.* Macromolecules, **34**, 8294 (2001).

[76] A.M. Skvortsov, L.I. Klushin, and F.A.M. Leermakers. *Exactly solved polymer models with conformational escape transitions of a coil-to-flower type.* Europhysics Letters, **58**, 292 (2002).

[77] G.F. Hermsen, B.A. de Geeter, N.F.A. van der Vegt, and M. Wessling. *Monte Carlo simulation of partially confined flexible polymers.* Macromolecules, **35**, 5267 (2002).

[78] P. Cifra, Y. Wang and I. Teraoka. *Comparison of partitioning of a bimodal polymer mixture into micropores in good and Θ solvents. A Monte Carlo study.* Macromolecules, **35**, 1446 (2002).

[79] Z. Skrinarova and P. Cifra. *Partitioning of semiflexible macromolecules into a slit in good solvents.* Macromolecular Theory and Simulations, **10**, 523 (2001).

[80] D. Viduna, Z. Limpouchová, and K. Procházka. *Monte Carlo simulation of polymer brushes in narrow pores.* Journal of Chemical Physics, **115**, 7309 (2001).

[81] E. Manias, V. Kuppa, D.-K. Yang, and D.B. Zax. *Relaxation of polymers in 2 nm slit-pores: confinement induced segmental dynamics and suppression of the glass transition.* Colloids and Surfaces A, **187-188**, 509 (2001).

[82] I. Teraoka and P. Cifra. *Mean-field Gaussian chain theory for semidilute theta chains in a slit.* Journal of Chemical Physics, **115**, 11362 (2001).

[83] D. Viduna, Z. Limpouchová, and K. Procházka. *Conformation of chains in cores of block copolymer micelles with solubilized homopolymer: a Monte Carlo study.* Macromolecular Theory and Simulations, **10**, 165 (2001).

[84] G. Xu, J. Ding, and Y. Yang. *Monte Carlo simulation of self-avoiding lattice chains under slit flow.* Rheologica Acta, **38**, 562 (1999).

[85] P.G. de Gennes. *Flexible polymers in nanopores.* Advances in Polymer Science, **138**, 91 (1999).

[86] C. Gay and E. Raphaël. *Comb-like polymers inside nanoscale pores.* Advances in Colloid and Interface Science, **94**, 229 (2001).

[87] J.Y. Lee, A.R.C. Baljon, D.Y. Sogah, and R.F. Loring. *Molecular dynamics study of the intercalation of diblock copolymers into layered silicates.* Journal of Chemical Physics, **112**, 9112 (2000).

[88] A.R.C. Baljon, J.Y. Lee, and R.F. Loring. *Molecular view of polymer flow into a strongly attractive slit.* Journal of Chemical Physics, **111**, 9068 (1999).

[89] H. Yoon and J.M. Deutsch. *Dynamics of a polymer in the presence of permeable membranes.* Journal of Chemical Physics, **102**, 9090 (1995).

[90] K.K. Kumar and K.L. Sebastian. *Adsorption-assisted translocation of a chain molecule through a pore.* Physical Review E, **62**, 7536 (2000).

[91] F. Tessier, J. Labrie, and G.W. Slater. *Electrophoretic separation of long polyelectrolytes in submolecular-size constrictions: a Monte Carlo study.* Macromolecules, **35**, 4791 (2002).

[92] A. Milchev, V. Yamakov, and K. Binder. *Escape transition of a compressed polymer mushroom under good solvent conditions.* Europhysics Letters, **47**, 675 (1999).

[93] M. Muthukumar. *Theory of sequence effects on DNA translocation through proteins and nanopores.* Electrophoresis, **23**, 1417 (2002).

[94] J. Chuang, Y. Kantor, and M. Kardar. *Anomalous dynamics of translocation.* Physical Review E, **65**, 011802 (2002).

[95] S.-S. Chern, A.E. Cárdenas, and R.D. Coalson. *Three-dimensional dynamic Monte Carlo simulations of driven polymer transport through a hole in a wall.* Journal of Chemical Physics, **115**, 7772 (2001).

[96] S.M. Scheinhardt-Engels, F.A.M. Leermakers, and G.J. Fleer. *Lattice mean-field method for stationary polymer diffusion.* Physical Review E, **68**, 011802 (2003).

[97] S.M. Scheinhardt-Engels, F.A.M. Leermakers, and G.J. Fleer. *Stationary dynamics approach to analytical approximations for polymer coexistence curves.* Physical Review E, **69**, 021808 (2004).

[98] P.G. De Gennes. *Scaling Concepts in Polymer Physics.* Cornell University Press, Ithaca, 1979.

[99] G.J. Fleer, A.M. Skvortsov, and R. Tuinier. *Mean-field equation for the depletion thickness.* Macromolecules, **36**, 7857 (2003).

[100] P.J. Flory. *Thermodynamics of high polymer solutions* Journal of Chemical Physics, **9**, 660 (1941).

[101] I.C. Sanchez and R.H. Lacombe. *Statistical thermodynamics of polymer solutions.* Macromolecules, **11**, 1145 (1978).

[102] J.W. Kennedy, M. Gordon, and R. Koningsveld. *Generalization of the Flory-Huggins treatment of polymer solutions.* Journal of Polymer Science, Part C, **39**, 43 (1972).

[103] T. Dobashi, M. Nakata, and M. Kaneko. *Coexistence curve of polystyrene in methylcyclohexane II. Comparison of coexistence curves observed and calculated from classical free energy.* Journal of Chemical Physics, **72**, 6692 (1980).

[104] D. Schwahn, K. Hahn, J. Streib, and T. Springer. *Critical fluctuations and relaxation phenomena in the isotopic blend polystyrene/deuteropolystyrene investigated by small angle neutron scattering.* Journal of Chemical Physics, **93**, 8383 (1990).

[105] F. Scheffold, E. Eiser, A. Budkowski, U. Steiner, J. Klein, and L.J. Fetters. *Surface phase behavior in binary polymer mixtures. I. Miscibility, phase coexistence, and interactions in polyolefin blends.* Journal of Chemical Physics, **104**, 8786 (1996).

[106] C. Krause and B.A. Wolf. *Shear effects on the phase diagrams of solutions of highly incompatible polymers in a common solvent. 1. Equilibrium behavior and rheological properties.* Macromolecules, **30**, 885 (1997).

[107] W.W. Maurer, F.S. Bates, T.P. Lodge, K. Almdal, K. Mortensen, and G.H. Fredrickson. *Can a single function for χ account for block copolymer and homopolymer blend phase behavior?* Journal of Chemical Physics, **108**, 2989 (1998).

[108] S.L. Shmakov. *Phase equilibrium in solutions of star-shaped macromolecules: an improved Okada-Numasawa model.* Polymer, **43**, 1491 (2002).
[109] K.S. Schweizer and J.G. Curro. *Integral equation theories of the structure, thermodynamics and phase transitions of polymer fluids.* Advances in Chemical Physics, **98**, 1 (1997).
[110] G.H. Fredrickson, A.J. Liu, and F.S. Bates. *Entropic corrections to the Flory-Huggins theory of polymer blends: architectural and conformational effects.* Macromolecules, **27**, 2503 (1994).
[111] J. Dudowicz, K.F. Freed, and J.F. Douglas. *Beyond Flory-Huggins theory: New classes of blend miscibility associated with monomer structural asymmetry.* Physical Review Letters, **88**, 095503 (2002).
[112] J. Dudowicz and K.F. Freed. *Effect of monomer structure and compressibility on the properties of multicomponent polymer blends and solutions: 1. Lattice cluster theory of compressible systems.* Macromolecules, **24**, 5076 (1991).
[113] P.D. Gujrati and M. Chhajer. *New statistical mechanical treatment of systems near surfaces. I. Theory and principles.* Journal of Chemical Physics, **106**, 5599 (1997).
[114] P.D. Gujrati. *A binary mixture of monodisperse polymers of fixed architectures, and the critical and the theta states.* Journal of Chemical Physics, **108**, 5104 (1998).
[115] J.J. de Pablo, Q. Yan, and F.A. Escobedo. *Simulation of phase transitions in fluids.* Annual Review of Physical Chemistry, **50**, 377 (1999).
[116] A.Z. Panagiotopoulos. *Direct determination of phase coexistence properties of fluids by Monte Carlo simulation in a new ensemble.* Molecular Physics, **61**, 813 (1987).
[117] A.Z. Panagiotopoulos, N. Quirke, M. Stapleton, and D.J. Tildesley. *Phase equilibria by simulation in the Gibbs ensemble, alternative derivation, generalization, and application to mixture and membrane equilibria.* Molecular Physics, **63**, 527 (1988).
[118] A.D. Mackie, A.Z. Panagiotopoulos, and S.K. Kumar. *Monte Carlo simulations of phase equilibria for a lattice homopolymer model.* Journal of Chemical Physics, **102**, 1014 (1995).
[119] A. Poncela, A.M. Rubio, and J.J. Freire. *Phase separation of binary homopolymer and ternary homopolymer-copolymer mixtures through Gibbs ensemble simulations.* Journal of Chemical Physics, **114**, 8174 (2001).
[120] M. Laso, J.J. de Pablo, and U.W. Suter. *Simulation of phase equilibria for chain molecules.* Journal of Chemical Physics, **97**, 2817 (1992).
[121] J.I. Siepmann, S. Karaborni, and B. Smit. *Simulating the critical behaviour of complex fluids.* Nature, **365**, 330 (1993).
[122] F.A. Escobedo. *Simulation and extrapolation of coexistence properties with single-phase and two-phase ensembles.* Journal of Chemical Physics, **113**, 8444 (2000).
[123] J.K. Brennan and W.G. Madden. *Phase coexistence curves for off-lattice polymer-solvent mixtures: Gibbs-ensemble simulations.* Macromolecules, **35**, 2827 (2002).
[124] D.A. Kofke. *Gibbs-Duhem integration: a new method for direct evaluation of phase coexistence by molecular simulation.* Molecular Physics, **78**, 1331 (1993).
[125] D.A. Kofke. *Direct evaluation of phase coexistence by molecular simulation via integration along the saturation line.* Journal of Chemical Physics, **98**, 4149 (1993).
[126] M. Mehta and D.A. Kofke. *Coexistence diagrams of mixtures by molecular simulation.* Chemical Engineering Science, **49**, 2633 (1994).
[127] Q. Yan, H. Liu, and Y. Hu. *Simulation of phase equilibria for lattice polymers.* Macromolecules, **29**, 4066 (1996).
[128] T. Chen, H. Liu, and Y. Hu. *Monte Carlo simulation of phase equilibria for random copolymers.* Macromolecules, **33**, 1904 (2000).
[129] W.G. Madden, A.I. Pesci, and K.F. Freed. *Phase equilibria of lattice polymer and solvent: tests of theories against simulations.* Macromolecules, **23**, 1181 (1990).
[130] A.Z. Panagiotopoulos, V. Wong, and M.A. Floriano. *Phase equilibria of lattice polymers from histogram reweighting Monte Carlo simulations.* Macromolecules, **31**, 912 (1998).
[131] A. Indrakanti, J.K. Maranas, A.Z. Panagiotopoulos, and S.K. Kumar. *Quantitative lattice simulations of the structure and thermodynamics of macromolecules.* Macromolecules, **34**, 8596 (2001).

[132] R. Shetty and F.A. Escobedo. *On the application of virtual Gibbs ensembles to the direct simulation of fluid-fluid and solid-fluid phase coexistence.* Journal of Chemical Physics, **116**, 7957 (2002).
[133] L.A. Rodriguez-Guadarrama and V.R. Vasquez. *Phase behavior of amphiphile-solvent systems from lattice Monte Carlo simulations.* Fluid Phase Equilibria, **179**, 193 (2001).
[134] S.A. Safran. *Statistical thermodynamics of surfaces, interfaces, and membranes*, volume 90 of *Frontiers in physics.* Addison-Wesley, Reading, Massachusetts (1994).
[135] I.C. Sanchez. *Corresponding states in polymer mixtures.* Macromolecules, **17**, 967 (1984).
[136] D.Q. He, S. Kwak, and E.B. Nauman. *On phase equilibria, interfacial tension and phase growth in ternary polymer blends.* Macromolecular Theory and Simulations, **5**, 801 (1996).
[137] R. Horst and B.A. Wolf. *Phase diagrams calculated for quaternary polymer blends.* Journal of Chemical Physics, **103**, 3782 (1995).
[138] J.W. Gibbs. *The scientific papers of J. Willard Gibbs*, Volume I. OX BOW Press, Woodbridge, Conneticut (1993).
[139] T. Gil, M.C. Sabra, J.H. Ipsen, and O.G. Mouritsen. *Wetting and capillary condensation as means of protein organization in membranes.* Biophysical Journal, **73**, 1728 (1997).
[140] K. Ragil, J. Meunier, D. Broseta, J.O. Indekeu, and D. Bonn. *Experimental observation of critical wetting.* Physical Review Letters, **77**, 1532 (1996).
[141] T. Pfohl and H. Riegler. *Critical wetting of a liquid/vapor interface by octane.* Physical Review Letters, **82**, 783 (1999).
[142] D. Ross, D. Bonn, and J. Meunier. *Observation of short-range critical wetting.* Nature, **400**, 737 (1999).
[143] G.G. Pereira and J.-S. Wang. *Wetting transitions in polymer blends: comparison between simulation and theory.* Journal of Chemical Physics, **105**, 3849 (1996).
[144] K. Ragil, D. Bonn, D. Broseta, and J. Meunier. *Wetting of alkanes on water from a Cahn-thype theory.* Journal of Chemical Physics, **105**, 5160 (1996).
[145] F.A.M. Leermakers, C. Dorrepaal, and N.A.M. Besseling. *Wetting of a fluid interface by a homopolymer: a system with a rich prewetting behavior.* Journal of Chemical Physics, **111**, 2797 (1999).
[146] M.C.P. van Eijk and F.A.M. Leermakers. *Wetting by polymers of a liquidliquid interface: effects of short-range interactions and of chain stiffness.* Journal of Chemical Physics, **110**, 6491 (1999).
[147] M. Schick. *Introduction to wetting phenomena.* In: J. Charvolin, J.F. Joanny, and J. Zinn-Justin, editors, *Les Houches, Session XLVIII, 1988 - Liquides aux interfaces/ Liquids at interfaces*, Elsevier Scence Publishers, 415 (1990).
[148] J.W. Cahn. *Critical point wetting.* Journal of Chemical Physics, **66**, 3667 (1977).
[149] M.R. Moldover and J.W. Cahn. *An interface phase transition: complete to partial wetting.* Science, **207**, 1073 (1980).
[150] T. Young. *An essay on the cohesion of fluids.* Philosophical Transactions of the Royal Society of London, **95**, 65 (1805).
[151] M.P. Nightingale and J.O. Indekeu. *Examination of the necessity of complete wetting near critial points in systems with long-range forces.* Physical Review B, **32**, 3364 (1985).
[152] C. Ebner and W.F. Saam. *Effect of long-range forces on wetting near bulk critical temperatures: An Ising-model study.* Physical Review B, **35**, 1822 (1987).
[153] G.G. Pereira and J.-S. Wang. *Effect of van der Waals surface interaction on wetting transitions in polymer blends.* Physical Review E, **54**, 3040 (1996).
[154] E.H. Hauge and M. Schick. *Continuous and first-order wetting transition from the van der Waals theory of fluids.* Physical Review B, **27**, 4288 (1983).

Summary

Theoretical models for the study of polymers mainly deal with equilibrium properties, such as the compositions of coexisting phases, the morphology of micro-phase separated mixtures, or the conformations of polymer chains near phase boundaries. In practice however, it may take a long time before equilibrium is obtained in polymer systems. Moreover, many polymer processes in industry, biology, and research occur off-equilibrium, since driving forces are maintained by the reactions that take place (for example at catalyst surfaces) or by the continuous input of mechanical energy (for example to transport polymer liquids through industrial pipes). Therefore it is necessary to go beyond the equilibrium considerations. This thesis presents a new theoretical model, as well as its applications, for the study of polymer systems in stationary off-equilibrium states.

The new model, outlined in Chapter 2, is called the Mean-Field Stationary Diffusion model. It provides more insight into the steady state behaviour of polymers that diffuse between two bulk mixtures with different compositions. Calculations with this new model yield information about the stationary concentration profiles, sometimes showing interface formation, and stationary fluxes. The polymers are studied on the length scale of a few monomers so that their conformational changes can be followed during the diffusion.

The basis for the Mean-Field Stationary Diffusion (MFSD) model is the equilibrium Scheutjens-Fleer (SF) model. As a result, when the two bulk mixtures that determine the driving force for diffusion in the MFSD-model have equal compositions, the system is in equilibrium and the results of the MFSD and SF calculations coincide. The SF model has already been applied for a wide variety of interfacial systems, including solid surfaces, liquid/liquid interfaces, and self-assembling interfaces such as membranes and vesicles composed of (charged) amphiphilic molecules. The MFSD model might be used to study all these systems in stationary off-equilibrium situations.

The basic result of an SF or MFSD calculation is the average distribution of molecules in the system under the appropriate constraints and boundary conditions. The boundary condition for the SF calculations is given by the composition of a bulk mixture that must be in equilibrium with the system under consideration. The constraints for the SF model are minimum free energy and incompressibility of the system. In the MFSD model the boundary conditions are the compositions of the two bulk mixtures between which the stationary diffusion occurs. The constraints for the molecular distribution in MFSD calculations are system incompressibility and concentrations that are constant in time on every position in the system. Both methods provide only the *average* molecular distributions in contrast to simulation methods in which, in principle, the location of every particle is exactly known at any moment. The average distribution is calculated more efficiently in the SF and MFSD models and it provides statistical information about a large collection of molecules without any statistical noise.

The development of the MFSD model requires an assumption about the diffusion mechanism. We adopt two diffusion theories from the literature: the slow-mode and fast-mode theories, which both assume a 'swap' mechanism where particles move by interchanging their positions with others. The parameters for the MFSD calculations are the Flory-Huggins interaction parameters, the chain lengths of the polymers, and the mobilities of the constituent segments. If desired, the slowing-down effect of entanglements between chains may be taken into account by defining the entanglement length of the chains. The numerical MFSD calculations are found to converge rapidly and smoothly to the average molecular distributions as long as the bulk mixtures are stable, in the sense that they do not feel a driving force for phase separation into two or more coexisting phases.

For athermal homopolymer mixtures and solutions we find from MFSD calculations that the stationary concentration profiles can be very asymmetrical as a result of different chain mobilities. A shorter polymeric component has a larger chain mobility than a longer polymer; when the chains are equal in length, there may be a different chain mobility due to a difference in segmental mobilities. The stationary concentration profile is a stronger function of position for those locations that are occupied by larger amounts of relatively mobile chains.

In Chapter 3 we apply the MFSD model to study hindered polymer diffusion, a frequently occurring process in biology. Chains diffusing from one bulk mixture to another encounter a barrier that has the characteristics of a fluid film. This means that the chains experience a reduction in the available space for diffusion, but that the barrier material has no structural pore morphology. The barrier may resemble a lipid bilayer by subdividing the barrier into regions and choosing the appropriate interaction parameters. The ideal coil conformations of the polymer chains are dramatically disturbed when they approach or cross the barrier. The chains are found to adopt inhomogeneous flower conformations when they reside partly in the barrier and partly in unconfined space. The part of the chain within the barrier (the stem of the flower) is stretched to allow the remaining coil part of the chain (the crown) to escape from the barrier. This result is particularly important for the experimental characterisation of membrane morphologies, whereby the maximum pore size of a membrane is derived from the size of the largest polymers that are able to cross the membrane. It is thereby usually assumed that the chains retain a spherical coil conformation. Our results show that this assumption is incorrect.

The stretching of the confined chains is quantified by the notion of 'blob sizes'. The smaller the blob size, the stronger the stretching. We find that the blob size decreases if the barrier occupies more space or if the repulsive interactions between the polymer and the barrier are made stronger. The blob sizes are independent of chain length or barrier width. However, the shorter the chains, the smaller the fraction of chains that adopt a flower conformation. These finding are in agreement with the predictions from a Gaussian scaling model.

As mentioned above, the bulk mixtures that in the MFSD model determine the driving force for polymer diffusion need to be stable, at least one of them. The limits of stability are given by the compositions of coexisting phases. When both bulk mixtures have a different, but coexistent composition, all components have equal chemical potentials in both mixtures. This means that all fluxes between these mixtures remain zero. This observation is the basis of a new analytical approximation for the compositions of coexisting

phases in homopolymer systems that we present in Chapter 4. We use the MFSD-flux expressions to calculate the conditions for vanishing fluxes. For binary mixtures the fluxes not only vanish when the bulk mixtures have equal or coexistent (also called binodal) compositions, but more generally if the driving force on molecules A is the same (equal and in the same direction) as the driving force on molecules B. This is due to the constraint of incompressibility. As a result, the condition of vanishing fluxes between two mixtures is only a necessary and not a sufficient condition for phase coexistence. We therefore use an additional condition to find an analytical approximation for coexistent phases. This condition is that the flux between two mixtures also vanishes when one of these mixtures has a binodal composition and the other has the critical composition. The critical composition is defined as the composition for which both the second and the third derivative of the Gibbs free energy with respect to the composition vanish: $\partial^2 G/\partial\phi^2 = \partial^3 G/\partial\phi^3 = 0$. This assumption is motivated by results for symmetrical homopolymer blends and from numerical MFSD calculations of the stationary flux between a binodal composition and unstable compositions. When our stationary dynamics approach is applied to the Flory-Huggins free energy functional the result is an analytical expression for the coexisting phase compositions in terms of chain lengths and interaction parameters. We compare our approximation with numerically calculated binodal compositions. Our approximation is more accurate than the Van der Waals approximation, the 'pure-phase' approximation for polymer solutions and the so-called root-three rule. Our stationary dynamics approach to obtain analytical approximations for coexisting compositions is not only applicable to binary homopolymer mixtures, but also to symmetrical multicomponent homopolymer mixtures in which all components have equal chain lengths and interaction parameters. However, results are more satisfactory for binary mixtures.

Two coexisting phases are separated by an interface. When the two phases are stable but not coexistent, the interface is off-equilibrium and molecules will diffuse through this interface. We study polymer adsorption both at equilibrium (Chapter 5 and off-equilibrium interfaces (Chapter 6. The interface separates an A-rich phase from a B-rich phase, where A and B are homopolymers with length N. The adsorbing component C is also a polymer with length N and it is equally soluble in A and B. The corresponding Flory-Huggins interaction parameters are: $\chi_{\mathrm{AC}} = \chi_{\mathrm{BC}} = \chi_{\mathrm{C}} \neq \chi_{\mathrm{AB}}$, with all $\chi_{\mathrm{ij}} > 2/N$.

In Chapter 5 the Scheutjens-Fleer model is used for the study of equilibrium adsorption. When the adsorption layer is a coexisting phase with the A- and B-rich phases, the phenomenon is also called wetting. Depending on the solubility of C (the value of χ_{C}) and on the miscibility of A and B (the value of χ_{AB}), the wetting will be partial or complete. In partial wetting only a finite amount of C accumulates at the interface. In practice, we would see droplets of C at the interface. In complete wetting a thick film of C may develop at the interface, thereby minimising the unfavourable A/B contacts. Upon variation of the interaction parameters a transition may occur between partial and complete wetting. This is analogous to the transition that occurs from partial to complete wetting upon increasing temperature. When this transition occurs gradually so that the wetting film grows continuously, the transition is called second order. This is rarely seen in experiments. We find second-order transitions for a large parameter space.

Cahn's argument states that a wetting transition must occur at a temperature below the critical temperature. In other words, at the critical temperature the wetting must be complete. This can be explained by considering the temperature dependence of the surface

tensions. In order to verify Cahn's argument in terms of interaction parameters instead of temperature, we need to express the interaction between the wetting component and the solvents as an effective interaction parameter which also incorporates the miscibility of A and B. Cahn's argument is then translated to the statement that a wetting transition must occur either upon decreasing the solubility of C in A and B (χ_{C}) or upon decreasing the miscibility of A and B (χ_{AB}). We indeed find wetting transitions as predicted by Cahn's argument.

The wetting behaviour becomes more complex when it is unfavourable to screen the A/B contacts by a wetting layer consisting of C, that is if $\chi_{\mathrm{AB}} < \chi_{\mathrm{C}}$. In this case we find so-called pseudo-wetting, where a thick wetting film develops while the A and B-rich phases become supersaturated with C. The supersaturation is finite so that, upon increasing the amount of component C, the wetting film eventually breaks down.

Cahn's argument predicts a transition from partial to complete wetting upon decreasing χ_{AB}, but we find an additional wetting transition by increasing the value of χ_{AB}. This is readily explained, since the screening of A/B contacts, as is possible by the development of a wetting layer, becomes more important with increasing χ_{AB}.

The equilibrium adsorption study is followed in Chapter 6 by a study of adsorption with stationary diffusion. From the equilibrium wetting results we select the conditions for the complete wetting regime by the appropriate choice for χ_{AB} and χ_{C}. We also choose the compositions of the bulk mixtures on both sides of the interface such that they are stable, but not coexisting, and sub-saturated with C. This results in an off-equilibrium interface. Polymer A diffuses from the A-rich phase through the interface to the B-rich phase and B diffuses in the opposite direction. The A-rich and B-rich phases are chosen to contain equal amounts of C, so that there exists no driving force on this component. The adsorption and stationary fluxes in this system are studied by use of the MFSD model. Although the system is rather simple it shows rich adsorption behaviour together with interesting variations in the stationary fluxes.

We first follow the adsorption of C at the off-equilibrium interface during variation of the concentration gradients of A and B. For small gradients, only little adsorption occurs, as would also occur at equilibrium interfaces due to the choice for sub-saturation of the bulk mixtures. However, when the concentration gradients are increased a thick adsorption layer develops at the off-equilibrium interface. This means that a third phase develops which is rich in C. This third phase is able to contain a large amount of C so that the adsorption becomes a stronger function of concentration gradients. The stationary fluxes of A and B become stronger functions of the concentration gradients as well. The fluxes increase with increasing adsorption, indicating that component C facilitates the swapping diffusion mechanism.

The adsorption also grows for increasing χ_{AB} and constant concentration gradients. Again, the adsorption becomes a stronger function of the variable when a C-rich phase exists at the off-equilibrium interface. However, the adsorption shows a maximum for some value of χ_{AB}. As can be explained from ternary phase composition diagrams, this maximum occurs since the bulk mixtures that determine the driving force for diffusion approach phase coexistence upon increasing χ_{AB}. At phase coexistence, the mixtures are sub-saturated with C and the adsorbed amount is only small. As expected, the stationary fluxes are found to decrease to zero upon approach of phase coexistence.

For increasing χ_{AB} and constant concentration gradients we thus find a maximum in

the adsorbed amount of C. For increasing χ_C we find a maximum in the stationary fluxes although the driving forces remain constant. The stationary flux first increases with increasing χ_C, supported by the development of a C-rich phase at the off-equilibrium interface. When the width of the adsorption layer is sufficiently large, there exists a place somewhere within the adsorption layer where the composition is such that component A has the same chemical potential as in the A-rich bulk mixture. The stationary flux of A (and therefore also of B) depends on the distance between that place and the A-rich bulk mixture. That distance decreases with increasing χ_C and the stationary fluxes decrease accordingly.

This thesis shows the performance and broad applicability of the Mean-Field Stationary Diffusion method. It provides insight into the diffusion profiles and flux characteristics for stationary diffusion between two stable polymer mixtures. Future applications could be in the field of biological transport of (charged) molecules through membranes. These membranes could consist of polymer chains that may facilitate the diffusion through the swapping mechanism, but on the other hand act as barriers through the occupation of space. It would be of interest to study the conformational changes of these chains during diffusion of molecules. The mixtures at both sides of the membrane could have compositions that are not coexisting, so that some of the features observed for off-equilibrium adsorption will also occur for transport through a membrane.

The equilibrium Scheutjens-Fleer model was developed to study the equilibrium in polymer systems. The Mean-Field Stationary Diffusion model developed in this thesis allows calculations for stationary off-equilibrium polymer systems. This is a step forward towards the development of a 'Mean-Field Dynamics model' that would enable the efficient study of dynamic processes in polymer systems that evolve from any arbitrary initial state to either a stationary off-equilibrium or an equilibrium state.

Samenvatting

1 Doel van het onderzoek

De eindtoestand van alle processen is een systeem in evenwicht. Wanneer een systeem in evenwicht verkeert, zijn alle eigenschappen zoals temperatuur, druk en volume constant in de tijd en in de ruimte. Uiteindelijk zullen alle geïsoleerde systemen een evenwicht bereiken. Dit, en het feit dat de evenwichtstoestand goed te begrijpen is, verklaart waarom in onderzoek vaak evenwichtssystemen worden bestudeerd.

Het kan echter geruime tijd duren voordat evenwicht wordt bereikt, met name in systemen die polymeren bevatten. Polymeren zijn lange moleculen die opgevat kunnen worden als aaneenschakelingen van kleinere moleculen, de monomeren. Als gevolg van de grootte van de polymeren zijn veel processen in polymeersystemen traag. Veel systemen die van belang zijn in de industrie, in de biologie of in het onderzoek verkeren helemaal niet in evenwicht; in veel processen worden systemen juist uit hun evenwicht gehouden doordat er reacties plaatsvinden (zoals aan katalysatoroppervlakken) of doordat er voortdurend energie aan het systeem wordt toegevoegd (bijvoorbeeld om vloeistoffen door fabrieksleidingen te pompen). Het is daarom ook nodig om in het onderzoek verder te kijken dan de evenwichtstoestand.

Het doel van het onderzoek dat beschreven is in dit proefschrift is het ontwikkelen van een theoretisch model waarmee polymeersystemen kunnen worden bestudeerd die niet in evenwicht verkeren. Het is wat ambitieus om de volledige dynamica van een willekeurige begintoestand naar het evenwicht te beschrijven, vandaar dat we ons beperkt hebben tot zogenaamde stationaire niet-evenwichtssystemen. In een stationaire toestand kunnen bijvoorbeeld concentraties afhankelijk zijn van positie, maar niet van de tijd.

In de natuur vinden we veel voorbeelden van processen die (in goede benadering) stationair zijn. Er kan (en moet) bijvoorbeeld een stationair verschil in concentratie bestaan van kaliumionen aan de binnenkant en de buitenkant van een cel. Dit zorgt er onder andere voor dat spieren kunnen samentrekken. Omdat er binnen de cel veel meer kaliumionen zijn dan buiten de cel, hebben ze de neiging naar buiten te diffunderen. Als deze diffusie het enige proces zou zijn, zou uiteindelijk een evenwichtstoestand ontstaan waarin de kaliumionen binnen en buiten de cel gelijke concentratie hebben; het functioneren van de cel in het metabolisme is dan onmogelijk. De natuur zorgt voor een constante energietoevoer via een pompmechanisme in de celwand waardoor het concentratieprofiel van de kaliumionen stationair blijft op de gewenste waarde. Om een systeem in een stationaire niet-evenwichtstoestand te houden is altijd een *constante* aanvoer van energie of materiaal naar het systeem nodig. Eigenlijk is de evenwichtstoestand een bijzondere stationaire toestand; hier is namelijk de aanvoer van energie of materiaal *constant* en *gelijk aan nul*.

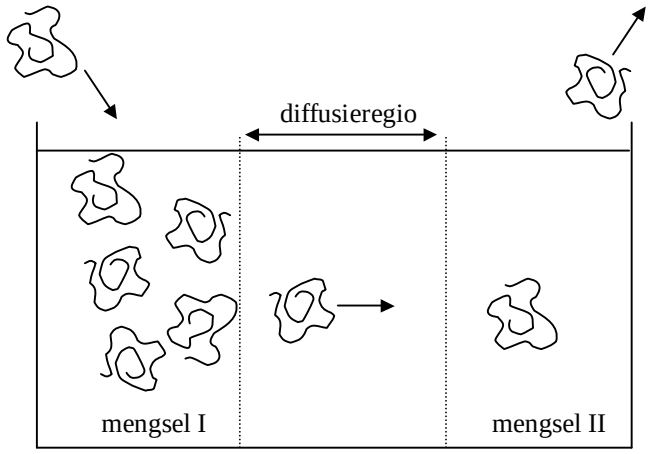

Figure I. Het stationaire polymeersysteem dat in dit proefschrift wordt bestudeerd.

In dit proefschrift bestuderen we een specifiek stationair polymeersysteem, zoals in Figuur I weergegeven. Twee bulkmengsels met verschillende samenstelling worden met elkaar in contact gebracht. Er zullen dan polymeermoleculen van de geconcentreerde oplossing naar de verdunde oplossing diffunderen. Door continue aanvulling van de geconcentreerde oplossing met nieuwe polymeer en door continue afvoer vanuit de verdunde oplossing blijven de twee bulkmengsels constant van samenstelling. Tussen de twee bulkmengsels zal na verloop van tijd een stationaire concentratiegradiënt van polymeren ontstaan. Hoe die gradiënten eruit zien voor complexere systemen waarbij meerdere componenten in verschillende richtingen diffunderen is niet eenvoudig te voorspellen, maar wel met ons theoretische model te berekenen. Het systeem in Figuur I kan dienen als een model voor diffusie-gelimiteerde katalyse: de reactanten diffunderen vanuit de bulk naar het katalysatoroppervlak waar de concentratie van reactanten laag wordt gehouden als gevolg van de reactie die er plaatsvindt.

We kunnen het systeem van Figuur I nog wat complexer maken door tussen de bulkoplossingen een barrière te plaatsen, zodat de diffusie van polymeren bemoeilijkt wordt. Die barrière zou bijvoorbeeld een membraan kunnen voorstellen. We hebben dan een model voor nicotinepleisters of voor vergelijkbare methoden van medicijnafgifte. Nicotinepleisters bevatten moleculen die vanuit de pleister door de huid (bestaande uit diverse barrières) naar het lichaam moeten diffunderen waar ze omgezet worden. Bij een dergelijke methode van medicijnafgifte wordt gestreefd naar een stationaire diffusie van moleculen door de huid heen. Het ontwerp van zulke pleisters vereist onderzoek naar de juiste samenstelling van het pleistermateriaal en naar het transportmechanisme door de huid. Ons model, waarin polymeerdiffusie ook gehinderd kan worden door een barrière, helpt bij het ophelderen van dit soort transportmechanismen.

Een andere toepassing van gehinderde diffusie is een veelbelovende techniek om de monomeervolgorde in DNA-moleculen te ontrafelen. DNA-moleculen zijn polymeren die in iedere levende cel aanwezig zijn en die genetische informatie bevatten. Deze informatie is gecodeerd in de vorm van een voor ieder individu specifieke volgorde van vier verschillende monomeren. Elk van de vier bouwstenen is in grote aantallen aanwezig in een

DNA-molecuul. Kasianowicz heeft laten zien dat bij diffusie van een synthetisch DNA-molecuul door een speciaal ontworpen membraan de transporteigenschappen afhankelijk zijn van de monomeervolgorde [6]. Als we meer zouden begrijpen van het transportgedrag van polymeren door een membraan, dan zouden we mogelijk uit het transportgedrag conclusies kunnen trekken over de volgorde van monomeren in een echt DNA-molecuul. Het model dat in dit proefschrift beschreven wordt geeft een eerste aanzet tot meer begrip van gehinderd polymeertransport.

Transportbarrières worden ook veelvuldig gebruikt in de industrie: zeven met zeer kleine poriën worden gebruikt om stoffen met verschillende molecuulgrootte van elkaar te scheiden. Bij het maken van deze zeven (technische membranen) is het van groot belang om te weten hoe groot de poriën zijn. Vaak wordt de poriegrootte vastgesteld door polymeren van verschillende lengte door het membraan te laten diffunderen. Daarbij wordt aangenomen dat iedere polymeerketen is opgevouwen als een bolvormige kluwen. De grootte van die kluwen hangt af van de lengte van de keten. Van de langste polymeerketens die nog net door de poriën kunnen diffunderen wordt de afmeting van de kluwen geschat. De poriegrootte wordt dan gelijk gesteld aan deze afmeting. De vraag is echter of de ketens wel hun kluwenvorm behouden tijdens de gehinderde diffusie. Als de ketens in staat zijn om zich te strekken, dan wordt de poriegrootte (veel) te groot ingeschat. Het is dus interessant om te onderzoeken hoe polymeerketens zich vouwen tijdens diffusie door een barrière. Ons theoretische model maakt dit mogelijk.

2 Het model (Hoofdstuk 2)

Het nieuw ontwikkelde theoretische model wordt het 'Gemiddeld-veld Stationaire Diffusie'-model genoemd, of in het Engels het 'Mean-Field Stationary Diffusion' (MFSD) model. Hoofdstuk 2 van dit proefschrift beschrijft alle (technische) details van dit model. De basis is een bestaande evenwichtstheorie ontwikkeld door Scheutjens en Fleer (SF) [15]. Het SF-model is een geschikt startpunt voor de ontwikkeling van het MFSD-model omdat de SF-resultaten al ruimschoots geverifieerd en onderbouwd zijn met experimentele bevindingen, echter alleen voor evenwichtssituaties. In tegenstelling tot het gangbare Flory-Hugginsmodel staat het SF-model toe dat het systeem niet homogeen hoeft te zijn. Dat wil zeggen dat bijvoorbeeld het grensvlak tussen twee niet-mengbare fasen bestudeerd kan worden (mits de fasen met elkaar in evenwicht zijn). Er mogen dus concentratie-verschillen in het systeem bestaan. Ook in een niet-evenwichtsmodel moeten er concentratie-verschillen kunnen bestaan, vandaar dat het SF-model geschikt is als basis voor het MFSD-model.

Het doel van SF-berekeningen is het vinden van de gemiddelde verdeling van moleculen in de ruimte voor de evenwichtstoestand. Door middel van een iteratief proces worden de moleculen steeds herverdeeld tijdens de berekening totdat de vrije energie van het systeem minimaal is. Deze toestand met minimale vrije energie is per definitie de evenwichtstoestand. De krachten die een molecuul in het systeem ondervindt hangen af van de posities van alle andere moleculen. Een SF-berekening (waarvoor altijd een computer nodig is) start met een beginschatting voor de verdeling van de moleculen. Deze verdeling levert een krachtenveld op dat ervoor zorgt dat de moleculen zich herschikken om de vrije energie te verminderen. De herschikking levert weer een nieuw krachtenveld op zodat opnieuw een herverdeling nodig kan zijn. De SF-berekening stopt zodra het krachtenveld consistent is

met de moleculaire verdeling met minimale vrije energie: verdere herschikking verlaagt de vrije energie niet meer.

Het MFSD-model doet iets soortgelijks: door middel van een iteratieve procedure worden de moleculen steeds herschikt totdat het krachtenveld consistent is met de opgelegde eis dat voor iedere component de flux overal in het systeem gelijk is, gegeven de samenstelling van de bulkmengsels. In een stationaire toestand is namelijk per definitie voor iedere component de flux constant. Het verschil met SF-berekeningen is tweeledig. Terwijl in een evenwichtssysteem de chemische potentialen van de moleculen overal gelijk zijn, is dat bij MFSD niet het geval: de concentraties in de beide bulkfasen (zie Figuur I) zijn niet gelijk of met elkaar in evenwicht maar worden (op een verschillend niveau) vastgelegd. Vervolgens moeten we in het MFSD-model vergelijkingen voor de moleculaire fluxen hebben; die spelen geen rol in het SF-model (de flux is immers nul). Zoals in Hoofdstuk 2 wordt beschreven gebruiken we twee verschillende theorieën uit de literatuur voor het opstellen van de fluxvergelijkingen.

Het is zowel voor SF- als voor MFSD-berekeningen nodig om enkele trucs toe te passen zodat de computer niet al te lang bezig is om de uiteindelijke moleculaire verdeling te vinden, terwijl we toch voldoende gedetailleerde informatie over die verdeling willen hebben, namelijk op de schaal van monomeren. Ten eerste worden de polymeerketens beschreven als een soort kralenketting. Ieder polymeermolecuul bestaat uit segmenten (de 'kralen'), waarbij ieder segment een klein aantal monomeren representeert. Homopolymeren bestaan uit identieke segmenten, terwijl copolymeren twee of meer soorten segmenten kunnen bevatten. Een segment beschrijft dus op efficiënte manier de eigenschappen van een klein aantal monomeren. Deze eigenschappen zijn de plaats in de polymeerketen en de interacties met andere segmenten.

Ook de ruimte wordt in de SF- en MFSD-berekeningen vereenvoudigd, namelijk door middel van een rooster. Een rooster maakt snellere discrete berekeningen mogelijk. We zouden een rooster kunnen gebruiken waarin op iedere roosterplaats precies één segment past zoals in Figuur II*a*. De berekeningen gaan echter nog sneller als we het rooster in roosterlagen verdelen, waarbij we alleen kijken naar de gemiddelde concentratie van ieder segmenttype in zo'n laag. Een dergelijk rooster (als in Figuur II*b*) wordt in dit proefschrift gebruikt. Een gevolg van deze aanpak is dat we niet precies weten welke segmenten buren van elkaar zijn in het rooster. Om interacties tussen segmenten te berekenen moeten we dus gebruik maken van hun *gemiddelde* verdeling over het rooster. Hier komt de naam 'Mean-Field' vandaan: er wordt aangenomen dat elk segment van een bepaald type in een gegeven roosterlaag hetzelfde krachtenveld voelt, ongeacht de precieze positie in de roosterlaag.

In het MFSD-model gaan we ervan uit dat polymeren door het systeem diffunderen door middel van een uitwisselingsmechanisme. Dat wil zeggen dat een segment van de ene polymeerketen van plaats verwisselt met een ander segment van dezelfde keten of met een segment van een andere keten. Gedurende de diffusie zal dus steeds de vouwing (ruimtelijke structuur) van de polymeerketen veranderen.

In Hoofdstuk 2 wordt niet alleen de MFSD-methode beschreven, maar ook geëvalueerd. Dit doen we door voor enkele eenvoudige systemen de resultaten van de MFSD-methode te vergelijken met analytische resultaten. De resultaten blijken goed met elkaar overeen te komen. Het voordeel van MFSD-berekeningen is dat ook hele ingewikkelde systemen onderzocht kunnen worden waarvoor geen analytische berekeningen mogelijk zijn.

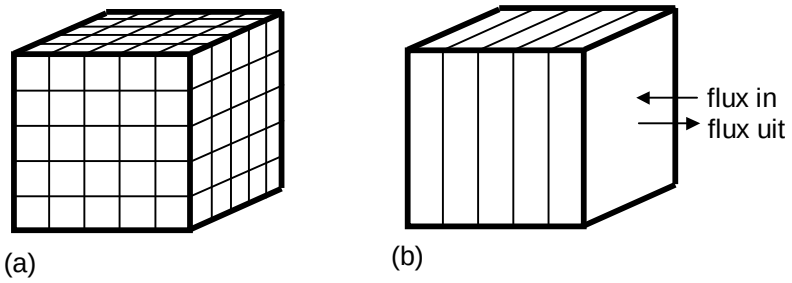

Figure II. Het MFSD-model beschrijft de ruimte door middel van een rooster. In ieder roostervakje van Figuur (a) past precies één segment. Om nog effiëntere berekeningen mogelijk te maken, kijken we in dit proefschrift alleen naar de gemiddelde vulling van een aantal roostervlakjes die samen in dezelfde roosterlaag liggen (Figuur (b)).

3 Vouwing van polymeren in gehinderde diffusie (Hoofdstuk 3)

In Hoofdstuk 3 bestuderen we met behulp van de MFSD-methode de diffusie van polymeren door een barrière. De barrière is een vloeistoflaag waarin de polymeren minder ruimte tot hun beschikking hebben en/of waarin ze maar moeizaam oplossen. We bekijken hoe de barrière de concentratieprofielen beïnvloedt. Dit blijkt sterk af te hangen van de dichtheid van de vloeistoflaag. We bestuderen ook met behulp van verschillende parameters hoe de polymeerketens zich vouwen tijdens hun diffusie. In de bulkmengsels zijn de ketens als kluwens opgevouwen. Zodra ze echter de barrière naderen, vervormt de kluwen om de keten zo min mogelijk in contact te laten zijn met de barrière. Bevindt een segment van de keten zich in de barrière, dan strekt de keten zich om toch voor een groot deel buiten de barrière te blijven. De keten heeft dan de vorm van een bloem: de gestrekte steel bevindt zich in de barrière, de kluwenvormige kroon erbuiten.

We kunnen de barrière laten lijken op het omhulsel van een lichaamscel (een membraan) door drie (of meer) verschillende gebieden in de barrière te definiëren. De twee buitenste gebieden worden slecht toegankelijk gemaakt voor olie-oplosbare stoffen (de hydrofiele gebieden), het binnenste gebied wordt juist slecht toegankelijk gemaakt voor water-oplosbare stoffen (dit gebied is hydrofoob). We bekijken in Hoofdstuk 3 polymeren die olie-oplosbaar zijn en vinden grote veranderingen in hun vouwing als ze door de barrière heen moeten bewegen.

De resultaten van Hoofdstuk 3 zijn onder andere van belang voor het maken van technische membranen en de bepaling van de poriegrootte daarvan door middel van polymeerdiffusie. Vaak wordt aangenomen dat de polymeren hun kluwenvorm behouden, maar deze aanname blijkt incorrect.

4 De samenstelling van mengsels in evenwicht (Hoofdstuk 4)

Het MFSD-model beschrijft polymeerdiffusie tussen twee bulkmengsels met een gegeven samenstelling. Er is een beperking aan de keuzevrijheid voor deze samenstelling: de mengsels mogen niet allebei instabiel zijn, want dan komt de MFSD-methode niet tot een eenduidige oplossing. Een mengsel is instabiel als het wil ontmengen in twee fasen, bijvoorbeeld een olie- en een waterrijke fase die met elkaar in evenwicht zijn. Een oververzadigde oplossing is een voorbeeld van een instabiel mengsel.

Voor het gebruik van de MFSD-methode is het daarom handig als we snel kunnen inschatten welke mengsels stabiel zijn. In Hoofdstuk 4 ontwikkelen we een analytische vergelijking waarmee we een benadering hebben voor de samenstelling van twee polymeermengsels (een verdunde en een geconcentreerde fase) die met elkaar in evenwicht zijn. Alle mengsels die meer verdund zijn dan de verdunde evenwichtsfase en alle mengsels die geconcentreerder zijn dan de geconcentreerde evenwichtsfase zijn stabiel; alle samenstellingen tussen de evenwichtssamenstellingen in noemen we hier instabiel.

Onze analytische benadering voor evenwichtsmengsels is gebaseerd op de fluxvergelijkingen die in het MFSD-model worden gebruikt. Het komt erop neer dat we berekenen voor welke samenstelling van de bulkmengsels alle fluxen gelijk aan nul worden. Dit gebeurt natuurlijk als de bulkmengsels gelijke samenstelling hebben, maar ook als ze met elkaar in evenwicht zijn; in beide gevallen is het SF-model van toepassing. De vergelijkingen die afgeleid worden door de MFSD-flux nul te stellen blijken nauwkeuriger te zijn dan benaderingen uit de literatuur.

5 Bevochtiging van grensvlakken tussen evenwichtsmengsels (Hoofdstuk 5)

In Hoofdstuk 5 maken we gebruik van het SF-model, waarop ons MFSD-model is gebaseerd, en we kijken dus alleen naar evenwicht. We bestuderen het grensvlak tussen twee mengsels die met elkaar in evenwicht zijn. Ieder mengsel bestaat uit drie verschillende homopolymeercomponenten A, B en C. Het ene mengsel is rijk in A, het andere is rijk in B. Homopolymeer C is niet goed oplosbaar in A en B en zal zich daarom ophopen aan het grensvlak tussen de twee evenwichtsmengsels. Met toenemende hoeveelheid C zal deze ophoping steeds groter worden, zodat uiteindelijk drie fasen met elkaar in evenwicht zijn; er is nu ook een C-rijke fase. Nu hangt het van de interacties tussen A, B en C af of de C-rijke fase een dikke vloeistoflaag vormt of dat er druppeltjes, bestaande uit de C-rijke fase, op het grensvlak ontstaan. Iets dergelijks kun je ook zien op vaste waterminnende oppervlakken: als het oppervlak wat vettig is dan zal water in druppeltjes op het oppervlak blijven liggen. Op schone oppervlakken spreidt het water zich juist uit als een dunnen film.

In Hoofdstuk 5 variëren we de interacties tussen A, B en C. Hierdoor kunnen de druppeltjes (bestaande uit de C-rijke fase) overgaan in een dikke laag of vice versa. Meestal verloopt de overgang heel plotseling. Er zijn maar een paar experimenten bekend waarbij de overgang geleidelijk verloopt. Voor ons systeem met drie polymeercomponenten vinden we juist wel vaak geleidelijke overgangen.

6 Adsorptie aan niet-evenwichtsgrensvlakken (Hoofdstuk 6)

De resultaten van Hoofdstuk 5 worden gebruikt in Hoofdstuk 6 waarin we met behulp van het MFSD-model de adsorptie aan niet-evenwichtsgrensvlakken bestuderen. In Hoofdstuk 5 zijn de twee mengsels aan weerszijden van het grensvlak met elkaar in evenwicht (de fluxen zijn nul), in Hoofdstuk 6 zijn de mengsels stabiel, maar niet in evenwicht. Het gevolg is dat in Hoofdstuk 6 polymeer A vanuit de A-rijke fase door het grensvlak naar de B-rijke fase diffundeert, terwijl polymeer B in tegengestelde richting diffundeert. De twee mengsels hebben zodanige samenstelling dat polymeer C geen drijvende kracht voor diffusie ondervindt.

Polymeer C hoopt zich weer op aan het grensvlak. De interacties tussen de polymeren en de samenstellingen van de bulkmengsels worden zo gekozen (op basis van de resultaten in Hoofdstuk 5) dat zich in de evenwichtstoestand een kleine hoeveelheid van de C-rijke fase op het grensvlak ophoopt. Voor de stationaire niet-evenwichtstoestand vinden we dat de hoeveelheid C op het grensvlak sterk afhangt van de drijvende krachten op polymeren A en B. Wanneer de drijvende krachten voldoende groot zijn, kan er een dikke adsorptielaag ontstaan. We vinden een abrupte verandering in de groeisnelheid van de adsorptielaag als we de drijvende krachten op A en B laten toenemen. Het relatief eenvoudige evenwichtssysteem dat we in Hoofdstuk 6 bestuderen levert al een zeer gevarieerd gedrag op voor de fluxen van A en B en voor de adsorptie van C als we het systeem uit evenwicht brengen. We vinden een vorm van dynamische adsorptie-overgangen.

7 Verder onderzoek

In dit proefschrift demonstreren we de brede toepasbaarheid van het MFSD-model. Het model verschaft inzicht in de diffusieprofielen en fluxeigenschappen voor stationaire diffusie tussen twee stabiele polymeermengsels. Het model zou ook gebruikt kunnen worden voor de bestudering van biologische systemen, waarin (al dan niet geladen) moleculen door membranen diffunderen. Die membranen zouden zelf uit polymeerketens kunnen bestaan die hun vouwing aanpassen aan het diffusieproces. Enerzijds kan dit bijdragen aan versneld transport, anderszijds kunnen de polymeerketens een barrière voor transport vormen omdat ze ruimte innemen.

Wanneer het MFSD-model verder wordt uitgebreid zodat ook berekeningen in twee-dimensionale roosters mogelijk zijn, dan zouden speciale transportkanalen in de membranen ingebouwd kunnen worden. Twee-dimensionale roosters zouden het ook mogelijk maken om barrières te bestuderen die een specifieke poriestructuur hebben. Dit is van belang voor verder onderzoek naar het vouwingsgedrag van diffunderende polymeren.

Het MFSD-model vormt een noodzakelijke stap tussen evenwicht- en dynamica-studies. Uitbreiding naar een 'Mean-Field Dynamics model' zou een efficiënte bestudering mogelijk maken van dynamische processen in polymeersystemen. Uit hoofdstuk 6 van dit proefschrift blijkt al dat inzichten verkregen uit het bestuderen van systemen in evenwicht nuttig zijn voor het begrijpen van systemen in een steady state. Op dezelfde manier vormen de steady-state resultaten uit dit proefschrift een opstapje om de resultaten van een volledig dynamisch model te gaan doorgronden.

Levensloop

Sonja Maria Engels werd op 3 oktober 1974 in Haarlem geboren. Haar hele schoolcarrière bracht ze door in Alkmaar, waar ze in 1993 haar diploma op het Murmellius Gymnasium behaalde. In datzelfde jaar begon ze aan de studie Chemische Technologie aan de Universiteit Twente te Enschede. In 1997 verbleef ze enkele maanden in Zweden voor een onderzoeksstage bij de Universiteit van Uppsala, waar ze onder leiding van professor Kersti Hermansson het effect van kristalfouten op de oppervlaktestructuur van metaaloxiden onderzocht. In 1998 studeerde ze (cum laude) af bij professor Wim Briels van de leerstoel Chemische Fysica, later omgedoopt tot Computational Chemistry. Ze deed bij deze leerstoel onderzoek naar een nieuwe simulatie-aanpak om kristalgroei te bestuderen. Voor dit onderzoek ontving zij in 1999 de Unilever Research prijs. Vanaf november 1998 tot september 2003 was zij in dienst van de Nederlandse Organisatie voor Wetenschappelijk Onderzoek als onderzoeker in opleiding en gedetacheerd bij het Laboratorium voor Fysische Chemie en Kolloïdkunde van Wageningen Universiteit. Zij werd begeleid door dr.ir. Frans Leermakers en professor Gerard Fleer. Het onderzoek dat in deze periode werd verricht staat beschreven in dit proefschrift en werd eerder gepresenteerd op enkele conferenties in Turku (Finland), Cardiff (Wales), Rostock (Duitsland) en verschillende gelegenheden in Nederland. Tijdens haar promotieperiode verbleef ze in 1999 en 2000 gedurende enkele maanden in Australië waar ze in het Ian Wark Research Institute te Adelaide in samenwerking met dr. Phil Attard onderzoek deed aan hydrofobe interacties. Vanaf december 2003 is zij werkzaam als klinisch chemicus in opleiding bij de Ziekenhuisgroep Twente te Almelo.

This research was financially supported by the Council for Chemical Sciences of the Netherlands Organisation for Scientific Research (CW-NWO) via the program Computational Materials Science.